University of Oviedo
Department of Electrical, Electronics,
Communications and Systems Engineering

Universidad de Oviedo

Ph.D. Thesis
PhD Program in Energy and Process Control

Coordinated control of distributed resources in hybrid AC/DC mesh distribution networks

Carlos Gómez-Aleixandre Tiemblo

Gijón, December 2022

Universidad de Oviedo
Departamento de Ingeniería Eléctrica,
Electrónica, de Comunicaciones y de Sistemas

Universidad de Oviedo

Tesis Doctoral
Programa de Doctorado en Energía y Control de Procesos

Control coordinado de recursos distribuidos en redes de distribución híbridas AC/DC malladas

Carlos Gómez-Aleixandre Tiemblo

Gijón, Diciembre 2022

University of Oviedo
Department of Electrical, Electronics, Communications and Systems Engineering

Universidad de Oviedo

Ph.D. THESIS DISSERTATION

Coordinated control of distributed resources in hybrid AC/DC mesh distribution networks

Dissertation submitted in fulfilment of the requirements for the degree of Doctor of Philosophy in the Energy and Process Control PhD program of the University of Oviedo with International Mention

Carlos Gómez-Aleixandre Tiemblo

Supervisors: Pablo García Fernández and José Manuel Cano Rodríguez.
Department of Electrical, Electronics,
Communications and Systems Engineering

Gijón, December 2022

Universidad de Oviedo

RESUMEN DEL CONTENIDO DE TESIS DOCTORAL

1.- Título de la Tesis	
Español/Otro Idioma: Control coordinado de recursos distribuidos en redes de distribución híbridas AC/DC malladas	Inglés: Coordinated control of distributed resources in hybrid AC/DC mesh distribution networks

2.- Autor	
Nombre:Carlos Gómez-Aleixandre Tiemblo	DNI/Pasaporte/NIE:
Programa de Doctorado: Energía y Control de Procesos	
Órgano responsable: Centro Internacional de Postgrado	

RESUMEN (en español)

El desarrollo de la electrónica y las comunicaciones durante las últimas décadas ha permitido incrementar las capacidades de control del sistema eléctrico. Esta evolución presenta algunas ventajas, pero también algunos retos debido al número de elementos a controlar de forma coordinada. Esto ha llevado a un creciente interés en microrredes y su control coordinado.

Aunque la corriente alterna se utiliza tradicionalmente para distribución, la creciente presencia de convertidores electrónicos ha desencadenado un interés cada vez mayor hacia la distribución de corriente continua, debido a su mayor eficiencia en algunos de los usos prácticos actuales. Sin embargo, su uso debe combinarse con la infraestructura de corriente alterna ya existente. Las microrredes híbridas AC/DC han recibido un creciente interés de investigación, también exploradas en esta tesis.

Esta tesis está enfocada en el diseño de un control coordinado para recursos distribuidos en redes híbridas de distribución malladas, partiendo de las tradicionales redes de distribución radial, proponiendo un diseño que pueda ser replicado en el laboratorio. Basada en el concepto de microrred y control jerárquico, la arquitectura de control está diseñada para aprovechar al máximo la flexibilidad y fiabilidad de la arquitectura propuesta. El control propuesto tiene una dependencia reducida de las comunicaciones en términos de estabilidad, a pesar de que se utilizan para una operación óptima.

Se propone un control secundario para el control primario basado en droop, caracterizado por su flexibilidad y robustez frente a retrasos en la comunicación o pérdida de datos. El método comienza con el cálculo de la solución óptima de flujo de energía atendiendo a cualquier criterio, como la minimización de pérdidas. Las variables que intervienen en el droop se obtienen a partir de esa solución de flujo de potencia y la característica de droop se mueve de modo que contenga el punto definido por la solución. La posibilidad de combinar este control con problemas de optimización debido a la mencionada flexibilidad se demuestra mediante un problema de optimización económica.

Se desarrolla un droop basado en las ecuaciones de flujo de potencia en la descomposición dq. En lugar de las funciones trigonométricas normalmente utilizadas para la obtención de los droops clásicos, se utiliza el equivalente dq. El droop se aplica a ambos componentes de la tensión en lugar de la frecuencia y la amplitud. Esto permite lograr que no haya desviación de frecuencia en régimen permanente. Además, se considera el acoplamiento entre la ecuación de potencia activa y reactiva cuando las líneas no son puramente inductivas/resistivas. El droop se compara con los clásicos P/f+Q/V y P/V+Q/f para diferentes valores de relación R/X, mostrando un buen

desempeño. Se analiza el efecto de los desajustes en la estimación R/X, con un desempeño razonablemente bueno.

Finalmente, se ha diseñado una propuesta para el control interno para convertidor DC/DC. El control se basa en el concepto de generador virtual de corriente continua. El esquema básico del generador virtual solo se enfoca en uno de los lados del convertidor, pero en los convertidores que interconectan dos redes, ambos lados pueden ser de interés para el control. Para usar la misma arquitectura de control para controlar tensión del otro lado, solo se requiere una adaptación de las variables que involucran el control de tensión. Luego, se aplica un promedio ponderado de cada control lateral. En la propuesta de tesis, los pesos para hacer el promedio se eligen para que sean proporcionales a la desviación de tensión con respecto al valor nominal. Este control proporciona al convertidor de interconexión la capacidad de operar como formador de red en ambos lados al mismo tiempo, requiriendo solo un elemento de soporte de red en cualquiera de los lados, lo que reduce los requisitos con respecto a los convertidores formadores de red.

RESUMEN (en Inglés)

The development of electronics and communications during the last decades has allowed an increase in the control capabilities for the electric system. This evolution presents some advantages, but also some challenges due to the important number of elements to be coordinated. This has led to increasing research in microgrids and its coordinated control.

Although AC is traditionally used for distribution, the increasing presence of power electronic converters has triggered an increasing interest towards DC distribution, due to its higher efficiency in some of the practical uses. However, its use must be combined with the already existing AC infrastructure. For this reason, hybrid AC/DC microgrids have received a growing research interest.

This thesis is focused on the design of a coordinated control for distributed resources in hybrid mesh distribution networks, departing from traditional radial distribution networks. Based on the microgrid and hierarchical control concept, the control architecture is designed to take maximum advantage of the flexibility and reliability of the proposed architecture. Besides that, the proposed control has a reduced dependency on communications in terms of stability, even though they are used for optimum operation. The proposals of this thesis can be classified in the different layers of hierarchical control.

A secondary control for droop control is proposed. The most important characteristics for this secondary control is the flexibility, with the objective of exploiting the different alternatives for power flow, and robustness against communication delays or data loss. The method starts with the calculation of the optimum power flow solution attending to any criteria, like losses minimizationThe variables which are involved in the droop are obtained from that power flow solution and the droop characteristic is moved so that it contains the point defined by the solution. The possibility of combining this control with optimization problems due to the mentioned flexibility is tested by an economic optimization problem. The method is first tested for P/V droop, but it can be adapted to other droops.

A droop based on the power flow equations in dq reference frame is developed. Instead of using trigonometric functions typically used for the derivation of classical droops, the dq equivalent is used. The droop is applied to both components of the voltage instead of frequency and amplitude. This allows to achieve no frequency deviation in steady-state. Besides that, the coupling between active and reactive power equation when lines are not purely inductive/resistive is considered for the droop. The droop is compared with the classical P/f+Q/V and P/V+Q/f for different values of R/X ratio, showing a good performance. The effect of mismatches in R/X estimation is analysed, with a good performance even for extreme errors in the estimation. An adaptation of the proposed

Universidad de Oviedo

secondary control is used to eliminate voltage amplitude deviation.

Finally, a proposal for the inner control layer of interlinking DC/DC converter has been designed and tested. The control is based on the DC virtual generator concept. The basic DC virtual generator scheme just focuses on one of the sides of the converter, but in interlinking converters both sides can be of interest for the control. For using the same control architecture to control the other side voltage, it only requires an adaptation of variables involving voltage control (referring the variables to the other side voltage level). Then, a weighted average of each side control is applied. In the thesis proposal, the weights for doing the average are chosen to be proportional to the voltage deviation with respect to nominal value. This control provides the interlinking converter with the capability of operating as grid-forming in both sides at the same time, requiring only a grid-supporting element in any of the sides, lowering the requirements regarding grid-forming converters.

SR. PRESIDENTE DE LA COMISIÓN ACADÉMICA DEL PROGRAMA DE DOCTORADO EN ENERGÍA Y CONTROL DE PROCESOS

A mis padres, hermanos, familia, a mi novia y a mis amigos...

Agradecimientos

Dedicado a mis directores de tesis, mis compañeros de universidad, mi familia, mis amigos y mi novia.

Resumen

El desarrollo de la electrónica y las comunicaciones durante las últimas décadas ha permitido incrementar las capacidades de control del sistema eléctrico. Esta evolución presenta algunas ventajas, pero también algunos retos importantes debido al importante número de elementos a controlar de forma coordinada. Esto ha llevado a un creciente interés de investigación en microrredes y su control coordinado.

Aunque la corriente alterna se utiliza tradicionalmente para las redes de distribución, la creciente presencia de convertidores electrónicos de potencia ha desencadenado un interés cada vez mayor hacia la distribución de corriente continua, debido a su mayor eficiencia en algunos de los usos prácticos actuales. Sin embargo, su uso debe combinarse con la infraestructura de corriente alterna ya existente. Por esta razón, las microrredes híbridas AC/DC han recibido un creciente interés de investigación, también exploradas en esta tesis.

Esta tesis está enfocada en el diseño de un control coordinado para recursos distribuidos en redes híbridas de distribución en malla AC/DC, partiendo de las tradicionales redes de distribución radial, proponiendo un diseño que pueda ser replicado en el laboratorio. Basada en el concepto de microrred y control jerárquico, la arquitectura de control está diseñada para aprovechar al máximo la flexibilidad y confiabilidad de la arquitectura propuesta. Además, el control propuesto tiene una dependencia reducida de las comunicaciones en términos de estabilidad, a pesar de que se utilizan para una operación óptima. Las propuestas de esta tesis se pueden clasificar en las diferentes capas de control jerárquico.

Se propone un control secundario para el control primario basado en droop. Las características más importantes de este control secundario son la flexibilidad, con el objetivo de explotar las diferentes alternativas de flujo de energía, y la robustez frente a retrasos en la comunicación o pérdida de datos. El método comienza con el cálculo de la solución óptima de flujo de energía atendiendo a cualquier criterio, como la minimización de pérdidas o la utilización económica de los sistemas de almacenamiento de energía. Las variables que intervienen en el droop se obtienen a partir de esa solución de flujo de potencia y la característica de droop se mueve de modo que contenga el punto definido por la solución. La posibilidad de combinar este control con problemas de optimización debido a la mencionada flexibilidad se demuestra mediante un problema

de optimización económica que podría considerarse en la capa de control terciaria. El método primero se demuestra para droop P/V, pero se puede adaptar a otro tipo de droops.

Se desarrolla un droop basado en las ecuaciones de flujo de potencia en la descomposición *dq*. En lugar de utilizar las funciones trigonométricas normalmente utilizadas para la obtención de los droops clásicos, se utiliza el equivalente *dq*. El droop se aplica a ambos componentes de la tensión en lugar de la frecuencia y la amplitud. Esto permite lograr que no haya desviación de frecuencia en régimen permanent. Además, para el droop se considera el acoplamiento entre la ecuación de potencia activa y reactiva cuando las líneas no son puramente inductivas/resistivas. El droop se compara con los clásicos $P/f + Q/V$ (líneas inductivas) y $P/V + Q/f$ (líneas resistivas) para diferentes valores de relación R/X, mostrando un buen desempeño. Se analiza el efecto de los desajustes en la estimación R/X, con un desempeño razonablemente bueno incluso para errores extremos en la estimación.

Finalmente, se ha diseñado y probado una propuesta para la capa de control interna del convertidor DC/DC. El control se basa en el concepto de generador virtual de corriente continua. El esquema básico del generador virtual de corriente continua solo se enfoca en uno de los lados del convertidor, pero en los convertidores interconectando dos redes, ambos lados pueden ser de interés para el control. Para usar la misma arquitectura de control para controlar el tensión del otro lado, solo se requiere una adaptación de las variables que involucran el control de tensión (similar a referir las variables al nivel de tensión del otro lado). Luego, se aplica un promedio ponderado de cada control lateral. En la propuesta de tesis, los pesos para hacer el promedio se eligen para que sean proporcionales a la desviación de tensión con respecto al valor nominal. Este control proporciona al convertidor de interconexión la capacidad de operar como formador de red en ambos lados al mismo tiempo, requiriendo solo un elemento de soporte de red en cualquiera de los lados, lo que reduce los requisitos con respecto a los convertidores formadores de red.

Abstract

The development of electronics and communications during the last decades has allowed an increase in the control capabilities for the electric system. This evolution presents some advantages, but also some important challenges due to the important number of elements to be controlled in a coordinated way. This has led to an increasing research interest in microgrids and its coordinated control.

Although AC is traditionally used for distribution networks, the increasing presence of power electronic converters has triggered an increasing interest towards DC distribution, due to its higher efficiency in some of the practical nowadays uses. However, its use has to be combined with the already existing AC infrastructure. For this reason, hybrid AC/DC microgrids have received a growing research interest, also explored in this dissertation.

This thesis is focused on the design of a coordinated control for distributed resources in hybrid AC/DC mesh distribution networks, departing from traditional radial distribution networks, proposing a design that can be replicated in the laboratory. Based on the microgrid and hierarchical control concept, the control architecture is designed to take maximum advantage of the flexibility and reliability of the proposed architecture. Besides that, the proposed control has a reduced dependency on communications in terms of stability, even though they are used for optimum operation. The proposals of this thesis can be classified in the different layers of hierarchical control.

A secondary control for droop-based primary control is proposed. The most important characteristics for this secondary control is the flexibility, with the objective of exploiting the different alternatives for power flow, and robustness against communication delays or data loss. The method starts with the calculation of the optimum power flow solution attending to any criteria, like losses minimization or economic utilization of energy storage systems. The variables which are involved in the droop are obtained from that power flow solution and the droop characteristic is moved so that it contains the point defined by the solution. The possibility of combining this control with optimization problems due to the mentioned flexibility is tested by an economic optimization problem which could be considered in the tertiary control layer. The method is first tested for P/V droop, but it can be adapted to other droops as it is shown for the next contribution.

A droop based on the power flow equations in dq reference frame is developed. Instead of using the trigonometric functions typically used for the derivation of classical droops, the dq equivalent is used. The droop is applied to both components of the voltage instead of frequency and amplitude. This allows to achieve no frequency deviation in steady-state. Besides that, the coupling between active and reactive power equation when lines are not purely inductive/resistive is considered for the droop. The droop is compared with the classical $P/f + Q/V$ (inductive lines) and $P/V + Q/f$ (resistive lines) for different values of R/X ratio, showing a good performance. The effect of mismatches in R/X estimation is analysed, with a reasonably good performance even for extreme errors in the estimation. An adaptation of the proposed secondary control is used to eliminate voltage amplitude deviation.

Finally, a proposal for the inner control layer of interlinking DC/DC converter has been designed and tested. The control is based on the DC virtual generator concept. The basic DC virtual generator scheme just focuses on one of the sides of the converter, but in interlinking converters both sides can be of interest for the control. For using the same control architecture to control the other side voltage, it only requires an adaptation of variables involving voltage control (similar to referring the variables to the other side voltage level). Then, a weighted average of each side control is applied. In the thesis proposal, the weights for doing the average are chosen to be proportional to the voltage deviation with respect to nominal value. This control provides the interlinking converter with the capability of operating as grid-forming in both sides at the same time, requiring only a grid-supporting element in any of the sides, lowering the requirements regarding grid-forming converters.

Abbreviations and acronyms

AC	Alternating Current
CCL	Constant Current Load
CIL	Constant Impedance Load
CPL	Constant Power Load
DC	Direct Current
DCVG	DC Virtual Generator
DER	Distributed Energy Resource
dESS	Distributed Energy Storage System
DVC	Direct Voltage Control
ESS	Energy Storage System
FLL	Frequency Locked Loop
HPEC	Header Power Electronic Converter
IC	Interlinking Converter
IGBT	Insulated-Gate Bipolar Transistor
LV	Low-Voltage
NPC	Neutral-Point Clamped
PCB	Printed Circuit Board
PCC	Point of Common Coupling
PEC	Power Electronic Converter
PI	Proportional Integral
PLL	Phase Locked Loop
PR	Proportional Resonant
PV	Photovoltaic
PWDCVG	Proportionally Weighted DC Virtual Generator

QVC	Quadatric Voltage Control
RES	Renewable Energy Source
RPEC	Ring Power Electronic Converter
SRF	Synchronous Reference Frame
SST	Solid-State Transformer
TPEC	Tail Power Electronic Converter
VPP	Virtual Power Plant
WDCVG	Weighted DC Virtual Generator

Contents

Chapter 1

Introduction

1.1 Background and motivation

The fast development of electronics, communications and computational power during the last decades has brought the possibility for a change in the power system structure, especially at distribution level. From a traditional power system, with only relatively few large-scale power plants as producers, the power system has moved towards a scheme with much more producers, with some of them being really small-scale compared to the old ones.

This change towards smaller scale but more distributed generation is related to the development of renewable energy sources. In the traditional electricity grid, the presence of renewable energies was much smaller, mainly relying on fossil fuels, nuclear power plants or big hydropower plants. This type of generation was not feasible or desirable for distributed small-scale generation. In the case of fossil fuels, their use was preferred to be distant from consumers due to the pollution and large-scale was preferable due to the greater efficiency. For nuclear power plants, the handling of nuclear waste becomes a social issue, being a difficult political issue to find a proper location without public opposition; besides that, the safety requirements of a nuclear power plant make them not affordable for small-scale applications. In the case of hydropower plants, the problems arise from the need of wide areas for building dams.

Renewable energy sources, on the other hand, are much more beneficial when used in distributed generation. Firstly, they do not pollute during their operation, so bringing them closer to the consumer is not a problem and, in fact, could reduce line losses due to the reduction in the distance between generation and consumption. This can reduce the necessity of capacity for transmission lines, which can be interesting in a moment in which global demand is constantly increasing, especially in developing countries. However, the capacity of distribution lines to handle this production has to be analysed too.

Another important characteristic of the main renewable energy sources (solar and wind) for their use in distributed generation is that the reduction in efficiency conversion when using smaller-scale generators is not an important issue. From a global point of view, it is more important to cover wider areas, even if reducing the efficiency, since in the areas which are not covered the solar or wind energy is wasted.

So this development of energy resources, together with the increasing concern about greenhouse gases and the intention of reduction in fossil fuel consumption, because of their scarcity and to reduce energy dependency for the countries with need to import them, has led to a increasing interest of a change towards distributed generation paradigm.

These changes has been made possible due to the increase capacity of electronics, computation and communications. The new scheme has moved from large-scale synchronous generators with simpler control schemes to small-scale generation, not always in form of rotating machines, and almost always interfaced with a Power Electronic Converter.

Besides all of the mentioned advantages and possibilities, the new electricity grid presents very important challenges too. The traditional electric system presented high inertia elements, the already mentioned large-scale synchronous generators. This gives a really important increase in system robustness and stability, reducing the effect of mismatches during transients. For example, if a large power plant fails (or a significant and unforeseen demand appears), the system will require some extra production to compensate this effect. However, this will take some time, even if the faster technologies (hydro or gas) are used. This mismatch will cause a frequency drop, but the effect is reduced because of the inertia of the generators, which deliver some of the rotational energy to compensate the mismatch effect by reducing their rotational speed. This mechanism operates naturally, with no need of specific control for doing it.

However, this effect of natural stability support due to the inertia is lost in distributed generation. The rotating generators are much less and have much less combined inertia, due to their smaller-scale. Even for large wind turbines, they do not operate always at maximum speed, and some studies show that half of the time their are operating with half or less their maximum kinetic rotational energy. Some other technologies, like solar generation, has no kinetic energy at all. Besides the lost of the inertia present in the system, the rotating elements still present in this type of system (wind turbines or small-scale fossil fuel generators) lose their natural capacity of providing their energy during mismatches when they are interfaced with Power Electronic Converters.

Furthermore, solar and wind are normally desired to operate at their maximum capacity for the given weather conditions, leaving less space for power reserves to be used to compensate mismatches. Thus the control strategies have to be able to compensate both the reduction in inertia (both the actual reduction in inertia and the lost of the natural compensation mechanism when interfacing with Power Electronic Converters) and the interest in operating an important share of the production at full

capacity so that the system is still robust and with good disturbance rejection.

A key element to face this challenge are the Energy Storage System. Firstly, they allow to decouple generation from demand, reducing the negative effect of the dependency of the main renewable energy sources on weather and the importance of proper forecasting of renewable energy production and also of the expected demand. Secondly, they are needed to compensate the reduction of inertia. The positive effect of inertia is, in fact, because it is a way of storing energy that the generators have. Storing energy in any form (electrochemical in batteries, electrostatical in capacitors or supercapacitors, inertial in flywheels,...) can compensate the effect, although, as already mentioned, when these elements are interfaced with Power Electronic Converters the control has to provide their ability to support mismatches in transients.

Another challenge of the modern concept of grid is the coordination of many different and smaller producers. The traditional power system used to have much fewer producers, with much higher power rating and with few companies owning them. Nowadays, there are a lot of possible producers, in much lower scale, and less concentrated in a reduced number of owners. Thus the idea of aggregating a significant amount of producers (and, in some cases, also consumers) became an interesting approach in order to split the effort of coordinating the whole system. The small-scale producers are grouped to form a coordinated large-scale agent, easing the coordination of the grid in the upper level, and making it possible to coordinate everything in a similar way as the traditional power system.

However, this requires the development of a coordinated control of these small-scale producers so that they can behave as a single entity from the complete grid point of view. Microgrids or Virtual Power Plants (which have some similarities but are not equivalent) become an opportunity to face these challenges.

Microgrids are an aggregation of renewable and non-renewable energy sources, Energy Storage System and loads that can behave as a single entity. The reason to use non-renewable energy sources is to increase stability, since microgrids, due to the already mentioned lack of inertia, are weak grids. Besides that, both Energy Storage System and non-renewable energy sources increase autonomy for the microgrid, both in the sense of having less dependency on market fluctuations and having the possibility of operating disconnected from the rest of the grid. This is of especial interest for providing stable power supply to isolated areas (remote rural areas, islands,...), large vehicles (like aircrafts) or in any situation in which there is no easy power supply or this supply is not stable.

This thesis focuses in the coordinated control of microgrids, based on hierarchical control. Hierarchical control is a concept that was already applied to traditional power systems, although the application of the same concept to microgrids has some differences due to the special characteristics already mentioned. The fast development of communications and control makes possible to coordinate the significant amount of agents in a microgrid to behave as a single entity for the upper control, so that from the point of view of the whole grid, their coordination is not very different from traditional

power plants. This requires fast computation and communications, although they are now possible with the fast development of those. However, reducing the dependency on communications for a stable operation is an important research interest for this thesis, seeking for a method which does not rely on them for the stability, although communications will be required for optimizing the operation in larger time scales.

In particular, the proposed microgrid will have a hybrid AC/DC topology. DC is used to the many advantages that has, like the reduction in losses due to the absence of reactive current flow and skin effect. Besides that, the use of DC networks can reduce the number of conversion stages due to the increasing presence of DC distributed generators (like PV panels) and loads and also AC loads and generation interfaced with Power Electronic Converters, which normally require an AC/DC/AC topology when connected to an AC network. However, AC is still used, mainly for exploiting to the already existing infrastructure.

1.2 Thesis objectives

The objective of this work is the design of a hybrid AC/DC microgrid and its control architecture. The design of the microgrid is intended to obtain high flexibility and reliability, by means of ringed structures inside it that can provide different alternatives for power flow. The control has to be able to take advantage of the flexibility of the microgrid to optimally operate and help to enhance reliability.

In order to achieve all above, the following objectives are defined:

I. A complete review of the state of the art with especial focus on hybrid microgrid topologies alternatives and the different control architecture options. The main topics for state of the art will be:

   - Definition of microgrid, highlighting its advantages and challenges. Analysis of the difference between microgrids and the traditional transmission and distribution power systems. Explanation of the elements that compose the microgrid.
   - Definition of hierarchical control and its application to hybrid microgrids. Description of the different layers of the hierarchical control and a comparative analysis with the traditional view of hierarchical control applied to transmission and distribution power systems and the more modern paradigm applied to microgrids.
   - Detailed explanation of the different layers, including different alternatives presented in the literature. Analysis of the main deficits among the different options, with a especial focus in the characteristics of hybrid microgrids, giving especial importance to flexibility and reliability.
   - Explanation of the key role of interlinking converters and the control alternatives to increase their support to reliability of the microgrid.

II. Design of the proposed hybrid microgrid paradigm, including converter topologies and control structure based on existing literature. Simulation of the microgrid under different scenarios.

III. Design of a secondary control that eases the flexible operation of the microgrid, allowing the integration of different criteria for the power sharing among involved converters. Combination of the proposed method with the resolution of an optimization problem for the optimal operation of the microgrid.

IV. Design of a primary control based on a droop concept, intended to reduce frequency oscillations and eliminating its steady-state deviation. The proposed control should consider that distribution lines are mainly resistive, as compared to the inductive lines considered for the traditional droop equations, and analyse the coupling appearing due to the fact that lines are not purely resistive/inductive.

V. Design of a control for DC/DC interlinking converter in order to maximize reliability. The proposed control should be able to keep reasonable voltage levels in each network, lowering the requirements regarding the number of required grid-forming converters. This will increase the reliability of the microgrid, allowing the stable operation with only one grid-forming converter per network to be able to continue working even if any of those grid-forming converter fails.

1.3 Thesis contributions

The contributions of the work carried out during this thesis are presented below:

Design of a hybrid microgrid [CP3]

A hybrid microgrid was designed, deciding the topology of the involved converters and choosing appropriate control strategies from the literature. The microgrid departs from typical radial topologies to consider instead ring connections, allowing alternative paths for the power flow. The flexibility and the reliability are considered as the main design objectives. The operation of the microgrid has been verified through simulation, using MATLAB/Simulink. Different operation modes were demonstrated, considering outages of some Power Electronic Converters.

Part of the microgrid was built in the laboratory. This includes some commercial Power Electronic Converters and two NPC converters designed and built during the thesis development, including filters, protection and design of PCBs for the control platform. The converter operation was validated, first with programmable voltage sources and then grid-connected. The capability of the NPC converter to compensate unbalances in a bipolar DC bus was tested, based on a control found in the literature.

Flexible secondary control and its use in optimization [JP1, CP2]

A secondary control strategy for the microgrid was designed. The control is of especial interest for hybrid microgrids with redundant power flow options. The proposed algorithm gives total flexibility for the power sharing among the microgrid, allowing easy change between operating conditions attending to different criteria, like varying power sharing among the converters, coordinating the different networks that form the microgrid or its use with optimization problems. The proposed algorithm was combined with an economic optimization problem as a demonstration.

Since the control relies on a good knowledge of the parameters, its robustness against estimation mismatches were validated through simulation with a satisfactory result. Besides that, good knowledge of the grid parameters is required for proper optimization.

Primary control for AC with no frequency deviation in steady-state [CP1]

A method for primary control in AC networks was proposed and verified. The proposed method is derived from the power flow equations in dq-decomposition instead of the traditional formula in terms of trigonometric functions. This eases the analysis of the dynamic behaviour of the converter, as the power flow equations in dq-decomposition is linear, so no linearization is required for small-signal analysis. Besides that, this dq-decomposition is more in line with the widespread dq-decomposition used in Power Electronic Converter control. The proposed method considers the coupling between both droop equations when the network is not purely resistive/inductive, based on the R/X ratio.

The method was verified through simulations in MATLAB/Simulink and was compared with traditional $P/f+Q/V$ and $P/V+Q/f$ droops. The effect of R/X estimation mismatches was checked, even for extreme cases, and the operation was good enough.

Interlinking DC/DC converter control with dual grid-forming capability

A control for interlinking converters has been designed. The objective of the control was to enhance reliability by including the grid-forming capability in both sides. Besides that, achieving similar operating conditions (similar deviation from voltage reference levels) in both networks was desired. The proposed method is able to provide grid-forming capability to both networks at the same time, just requiring one grid-feeding converter with P/V droop in one of the sides, as it was verified both with MATLAB/Simulink and OPAL-RT. This characteristic enhances the reliability of the microgrid, being able to operate if the grid-forming converter normally present in each network fails, without requiring multiple grid-forming converters in each network to assure reliability. The proposed method achieves equal per unit voltage in both sides, thus achieving the most balanced situation between the networks considering interlinking converter local variables.

This fact of equal per unit voltage in both sides of the converter, allow the use of P/V droop for both networks to collaborate, making the converters in each network able to collaborate in change in the demand in the other network. The secondary control proposed and mentioned in one of the previous contributions was adapted and used with this sharing strategy, including a validation with MATLAB/Simulink.

1.4 Thesis publications

The work described in this thesis has resulted in the following journal and conference publications. Some of them [JP1, CP1, CP2, CP3] are strictly related with the content and contributions of this thesis. In the others, the author of this thesis has contributed by performing the experimental validation or in the writing and reviewing process

1.4.1 Peer-reviewed journal papers

JP1 **C. Gómez-Aleixandre**, Á. Navarro-Rodríguez, G. Villa, C. Blanco and P. García, "Adaptive Droop Controller for a Hybrid 375 Vdc/48 Vdc/400 Vac AC/DC Microgrid," in IEEE Transactions on Industry Applications, vol. 58, no. 4, pp. 5104-5116, July-Aug. 2022, doi: 10.1109/TIA.2022.3176597.

JP2 Á. Navarro-Rodríguez, P. García, **C. Gómez-Aleixandre** and C. Blanco, "Cooperative Primary Control of a Hybrid AC/DC Microgrid based on AC/DC Virtual Generators," in IEEE Transactions on Energy Conversion, 2022, doi: 10.1109/TEC.2022.3203770.

JP3 C. Blanco, A. Suárez, **C. Gómez-Aleixandre**, I. Peláez and P. García, "Passive and Online DC Bus Status Monitoring for Back-to-Back Converters Applied to Doubly Fed Induction Machines," in IEEE Transactions on Power Electronics, vol. 37, no. 4, pp. 4697-4707, April 2022, doi: 10.1109/TPEL.2021.3128021.

JP4 G. Villa, S. Saeed, P. García, **C. Gómez-Aleixandre** and R. Georgious, "Compensation Alternatives for Power Sharing Mismatch in Multiport DC–DC–AC Converters," in *IEEE Transactions on Industry Applications*, vol. 57, no. 6, pp. 6221-6236, Nov.-Dec. 2021, doi: 10.1109/TIA.2021.3115721.

1.4.2 Peer-reviewed conference papers

CP1 **C. Gómez-Aleixandre**, C. Blanco, A. Suárez-González, Á. Navarro-Rodríguez and P. García, "Analysis of a Complex-Valued Droop Method in AC Microgrids with Complete Steady-State Frequency Compensation Using dq-Decomposition," 2021 IEEE Energy Conversion Congress and Exposition (ECCE), 2021, pp. 1122-1127, doi: 10.1109/ECCE47101.2021.9595227.

CP2 **C. Gómez-Aleixandre**, Á. Navarro-Rodríguez, G. Villa, C. Blanco and P. García, "Sharing Control Strategies for a Hybrid 48V/375V/400Vac AC/DC Microgrid," *2020 IEEE Energy Conversion Congress and Exposition (ECCE)*, 2020, pp. 3900-3907, doi: 10.1109/ECCE44975.2020.9235472.

CP3 **C. Gómez-Aleixandre**, P. García, Á. Navarro-Rodríguez and G. Villa, "Design and Control of a Hybrid 48V/375V/400Vac AC/DC Microgrid," *IECON 2019 - 45th Annual Conference of the IEEE Industrial Electronics Society*, 2019, pp. 3977-3982, doi: 10.1109/IECON.2019.8926709.

CP4 **C. Gómez-Aleixandre**, G. Villa, P. García, A. Suárez-González and Á. Navarro-Rodríguez, "Homopolar harmonic injection and grid synchronization in distributed control systems for grid-tied intelligent power electronic blocks in 4-wire 3-phase converters," *IECON 2019 - 45th Annual Conference of the IEEE Industrial Electronics Society*, 2019, pp. 3906-3911, doi: 10.1109/IECON.2019.8927413.

CP5 G. Villa, S. Saeed, P. García, **C. Gómez-Aleixandre** and R. Georgious, "Compensation Alternatives for Power Sharing Errors in Multi-Port Converters for Hybrid DC/AC Microgrids," *2019 IEEE Energy Conversion Congress and Exposition (ECCE)*, 2019, pp. 6929-6939, doi: 10.1109/ECCE.2019.8912879.

CP6 C. Blanco, P. García, **C. Gómez-Aleixandre** and I. Peláez, "Online parameter estimator of the DC bus capacitor bank for Doubly-Fed Induction Generators," 2019 21st European Conference on Power Electronics and Applications (EPE '19 ECCE Europe), 2019, pp. P.1-P.9, doi: 10.23919/EPE.2019.8915563.

CP7 G. Villa, **C. Gómez-Aleixandre**, P. García and J. García, "Distributed Control Alternatives of Modular Power Converters for Hybrid DC/AC Microgrids," *2018 IEEE Energy Conversion Congress and Exposition (ECCE)*, 2018, pp. 6379-6386, doi: 10.1109/ECCE.2018.8557556.

1.5 Thesis outline

The thesis document is organized in six chapters and some appendices according to the following structure:

- **Chapter 1** introduces the thesis topic, explaining the background and motivation behind it. From that, thesis objectives are determined, followed by the thesis contributions, supported by an enumeration of the publications derived from this thesis work.
- **Chapter 2** presents a review of the existing literature related to microgrids and its control and coordination. Firstly, the microgrid concept is explained, with a

review on microgrid architectures, with their advantages and drawbacks, followed by a description of the elements present in microgrids, with a especial focus on Power Electronic Converters. Secondly, the concept of hierarchical control is explained, showing its layer decomposition, with a definition of each layer and a review of their state of the art. Finally, the key role of interlinking converters in microgrids is explained, with a especial focus in their contributions to flexibility and reliability. A final summary of the state of the art is included, analyzing the research opportunities related to the thesis contributions.

- **Chapter 3** introduces the hybrid AC/DC microgrid studied in this thesis. The basic control structure of the whole microgrid is explained, based on control schemes found in the literature. An explanation of the different operation modes is presented. These operation modes depend on the availability of the microgrid elements, taking advantage of the redundant power flow path alternatives to increase grid resiliency.

- **Chapter 4** presents a secondary control strategy designed for the characteristics of hybrid microgrids. Starting with an analysis of the state of the art secondary control, it explains the main drawbacks of them, with a special focus on the flexibility desired for a coordinated control in a complex microgrid with redundant power flows, besides the objective of increasing robustness against communication delays or data loss. The proposed control is validated with simulations of the complete proposed microgrid and a experimental validation in a partial implementation of the microgrid. Finally, the flexibility of the proposed method is demonstrated, combining it with an optimization problem, demonstrating its capacity to couple with the tertiary control.

- **Chapter 5** establishes an alternative for the $P/f + Q/V$ droop or its alternative $P/V + Q/f$ for resistive lines, named complex-valued droop. The method considers the coupling between droops when lines are not purely inductive/resistive, which implies a correction depending on R/X ratio (or impedance phase angle). Instead of the power flow equations based on trigonometric functions and its simplifications, the *dq*-decomposition is considered, more in line with the widespread *dq*-decomposition for converter control. The deviation caused by the proposed droop is analyzed, highlighting that frequency deviation is eliminated, meanwhile amplitude deviation is in the same range as for $P/f+Q/V$ and $P/V+Q/f$ droops for the same value of droop coefficient. A comparison between $P/f + Q/V$, $P/V + Q/f$ and the proposed complex-valued droops is performed by simulations for different values of $P/f + Q/V$ and $P/V + Q/f$ droops for different impedance phase angles. Finally, the proposed droop performance under significant impedance phase angle estimation errors is analysed.

- **Chapter 6** defines a control strategy for DC/DC interlinking converters, which main objective was to increase reliability. The objective was to find a control scheme with the reversible grid-forming capability, i.e., the capability of operate as grid-forming in either output depending on operating conditions and with

seamless transition. The proposed method is, in fact, capable of providing grid-forming capability to both sides at the same time, just requiring for a grid-feeding element with P/V droop in one of the sides. The proposed control was modelled and used for small-signal stability analysis, comparing the dynamic response to a widely used DC voltage control strategy.

- **Chapter 7** presents the conclusions of the thesis, supported by a summary of the results obtained during the thesis development, and presents some future work opportunities.

- The **Appendices** includethe journal and conference publications strictly related to the contents in the thesis document, flowcharts for the proposed secondary control algorithm and the state-space matrices of the dynamic model used in Chapter 6 for the small-signal analysis.

Chapter 2

Literature review and state of the art

2.1 Introduction

In this chapter, a review of the literature related to the topics addressed in the present thesis is presented. The thesis contributions which are going to be presented in the next paper are though for hybrid AC/DC microgrid applications, having flexibility and reliability as key objectives. A hierarchical control structure is chosen, based on inner control loops, primary, secondary and tertiary control. The different contributions are related to all the different layers mentioned before. Thus the state of the art will follow the next structure.

1. Definition of microgrid concept, characteristics and classification, attending to its types and topologies.

2. Hierarchical control: definition and explanation of the difference between the application to the traditional power system and to microgrids. Definition of the different layers (inner, primary, secondary and tertiary control), with a review of the most common solutions. Classification of the different alternatives based on different criteria, with a special focus in the communication requirements for the alternatives on each layer. Especial focus on the hierarchical control structure based on droop alternatives, due to its widespread use.

3. Interlinking converters: explanation of their key role in microgrid reliability and flexibility. Classification attending to their capacity to support voltage control in the networks it interconnects.

2.2 Microgrids

The first reference to microgrids appeared in [2.1], as a "cluster of micro-sources, storage systems and loads which presents itself to the grid as a single entity that can respond to central control signals." The idea aroused due to the increasing presence of "micro-sources", due, mainly, to some emerging technologies. By that moment, fuel cells and micro-turbines were at that moment the main technologies involved in distributed generation, although in the years after renewable resources (mainly solar panels) and Energy Storage System (ESS) became more important. Both distributed generation (with especial focus to renewable sources in order to fulfil environmental goals [2.2]) and ESSs give the possibility of acting autonomously from the grid, having the possibility of operating in islanded mode [2.3] or connected to the grid but acting as a single entity, arising to the concept of Virtual Power Plant (VPP) [2.4]. Although microgrids and VPPs have some similarities, they have differences too: microgrids are small-size and local, meanwhile VPPs can have high power rating and cover a wide geographical area [2.5]. Apart from that, VPPs tend to ignore local consumption, behaving just as an aggregator of the generation, meanwhile microgrids can include load in this aggregation when controllable loads are present.

These microgrids are seen as an opportunity for sustainable growth in urban areas [2.6]. The combination of renewable energy distributed resources and ESSs gives autonomy to the microgrid of using energy coming from renewable sources in other times of the day despite of being non-dispatchable. It also allows the microgrid to charge or discharge its ESSs depending on the energy price, being able to sell their production when the price is higher and charging when it is low, being less affected by price variations. Apart from that, the spatial distribution of the Distributed Energy Resources (DERs) eases its forecasting and the presence of ESSs reduce the dependency on forecasting accuracy [2.7–2.9]

However, this presents two challenges. First one is the optimum sizing and operation of the microgrid elements. Renewable distributed resources and ESSs need to be sized according to many parameters, as the expected consumption in the corresponding areas, expected production for the Renewable Energy Source (RES), as well as electricity prices [2.10, 2.11]. Normally, another traditional energy resource (fuel cells, micro-turbines, diesel generators,...) is present and also affects the optimum sizing problem [2.12].

Second one is the requirement for communications between all the elements in the microgrid to behave as a single entity [2.13]. However, with the fast development of communications during this century, this became feasible and affordable. The computational power present nowadays allows the integration of the microgrid elements and its coordination in order to optimize its operation involving complex optimization problems that were not feasible to solve in reasonable time some years ago [2.14]. Even the most modern technologies for communications, like Blockchain [2.15, 2.16], and computation, like machine learning [2.17], are research topics for their integration in the distribution network and, especially, microgrids.

This change in the electricity distribution system, in which the distributed generation becomes widespread and a communication structure becomes key for the optimum operation, lead to the concept of smart-grid. One of the first uses of this term [2.18] presenting the following advantages:

- Giving power systems plug-and-play capability.
- Easier diagnostic and monitoring for all the equipment.
- Electric power system operation as an adaptive system.
- Use of grid computing for optimizing the system operation (reliability, price, sustainability,...).
- Making the power system a self-healing network. System blackouts are easier to avoid and isolate due to the distributed agents. The presence of microgrids that could operate in islanded mode could also ease the recovery from a blackout.

However, this smart-grid concept present some challenges too, like the lack of transmission capability and the difficulty of coordination between the centralized and decentralized control [2.18]. Both challenges can be faced by using microgrids, bringing generation closer to consumption level and aggregating close agents into single entities (for example, in form of Virtual Power Plants) which are easier to coordinate. However, this still presents difficulties in the communication and control required for the coordination of this systems [2.19].

Microgrids and smart-grid concept are highly related. Microgrids are a key element of a complete smart-grid [2.20], dividing the complete grid in smaller parts that can be seen as a single entity from the Distribution System Operators. This eases the coordination of the complete system, alleviating the communication and computation requirements of the central controller with each microgrid controller contribution. Therefore, when talking about microgrids, it is usually supposed to have the characteristic of a smart-grid, but at lower scale. These characteristics can be summarized as [2.21]:

- Energy efficiency, sustainability and renewable energy sources.
- Reliability, security, ESSs and distributed generation units.
- Sensing, measurements and advanced control methods.
- Load usage awareness, real-time energy management systems and advanced load components.
- Integrated information and communication infrastructures.

As mentioned before, these are characteristics close related to the initial idea of microgrids, including the possibilities that communication and computational development aroused. For the grid, it eases the coordination and facilitates voltage and frequency regulation, as active agents in each microgrid will be in charge of this support due to the location, close to the demand (increasing efficiency too). For the customers, it can help improve voltage quality, optimize operation, reduce impact of energy price variation and offer uninterruptible power supply functions, both for critical loads [2.22] or difficult areas due to geographical issues [2.23], like real islands or rural areas [2.24].

However, the change from the conventional power system, with large-scale synchronous generators, to a system with important share of distributed generation, which are small-scale and not always coming from rotating generators, present an important challenge: the significant reduction in inertia.

This is due to many factors:

- A reduction in the inertia of all the elements in the microgrid. As just mentioned, the synchronous generators are much smaller and some generation does not come from rotating generators.
- RES are normally intended to produce the maximum power regarding weather conditions, but this power can be far from their rated power. This means that, for example, although wind turbines can have an inertia comparable to traditional generators, most of the time they will have a rotating speed lower than rated one. This means their rotational kinetic energy will be lower, so their contribution to the inertia of the system will be smaller too. An interesting analysis of this is presented in [2.25], showing that around 50 % of the time the turbine has 50 % the kinetic energy at rated wind speed or less (for a specific standard variable speed wind turbine). Furthermore, more than 10 % of the time the wind speed is below the cut-in speed, so the wind turbine would have no kinetic energy at all.
- Even if there is some inertia in the microgrid, like wind turbines, these elements are rarely directly connected to the grid, being most of them interfaced with Power Electronic Converters (PECs). AC transmission has an interesting natural behaviour, especially for low R/X values: when there is an excess in demanded power, the extra energy is obtained from the generator rotational energy, thus slowing it down. This increases the phase difference between generator and load, increasing the power delivered by the generator, which results in a natural compensation mechanism: no control action is required for making the generator start compensating the mismatches by using its inertia. Then, the speed governor will react to return to the desired frequency, returning to the original speed when the phase difference is so that the increase in delivered power is exactly the increase in demand [2.26]. As it will be explained later, this natural mechanism was the underlying idea for P/f droop control, although droop was not yet considered for this explanation. This natural mechanism is lost when working with PEC interfaced generators, because mechanical frequency of the generator is decoupled

from frequency at the output of the PEC. Because of this, a lot of research is done in imitating this behaviour with the control design, as it will be explained later.

- Apart from generators, loads can also provide inertia to the system [2.25], like motors directly connected to the grid. This is the reason why flywheels are used for supporting frequency regulation from long ago [2.27, 2.28]. However, as mentioned before in the case of generators, when they are interfaced with PEC, the control has to be designed in order to have the capability of using the stored energy to support regulation during transients. Estimation of system inertia becomes an important issue for microgrids in order to evaluate their disturbance rejection capability and assure stable operation [2.29].

A deep study of the effect of the reduction of the inertia is performed in [2.25, 2.30–2.32]. Apart from that, it is important to remark the equivalence between inertia in AC and capacitance in DC [2.33, 2.34]. This equivalence is shown in (2.1), where E represents the stored energy, C and V the capacitance and voltage across the capacitor and J and ω the inertia and angular frequency of the generator (or any rotating element, as flywheels).

$$(DC) \quad E = \frac{1}{2}CV^2 \quad \longleftrightarrow \quad (AC) \quad E = \frac{1}{2}J\omega^2 \tag{2.1}$$

In fact, capacitors in AC store energy too.However, most of the energy available in AC conventional power system was stored in form of rotational kinetic energy, giving robustness to the system and increasing the disturbance rejection by the use of this stored energy. This is the reason why sometimes the concept of inertia is used with a sense of total energy available in the system available for this purpose, regardless of being an actual inertia (like in rotating generators, motors or flywheels) or other kind of energy, like in capacitors or batteries, provided that this energy can be effectively used for this support during transients.

2.2.1 DC vs AC

The future electricity grid is gradually moving in the direction of Direct Current (DC) distribution, due the envisaged lower distribution losses compared with Alternating Current (AC) distribution and the more efficient integration of renewables and distributed resources [2.35–2.37].

The increasing importance of DER interfaced by power electronic converters has led to the appearance of microgrids [2.38]. Although AC was traditionally more used, the benefits of DC has caused a gradual move towards DC distribution. These benefits include the easiness of integration of intermittent DER due to renewable sources (which normally requires extra DC/AC conversion stages in AC microgrids) and the reduced

Table 2.1: DC distribution alternatives.

Standard	DC voltage (V)	Application
EMerge Alliance Standard for commercial buildings	24	DC power distribution in commercial buildings
EMerge Alliance Standard for data centres	380	Hybrid use of AC and DC power within data centres and telecom central offices
EU Telecom Standard ETSI EN 300 132-3-1	400	Distribution networks supplying telecom and datacom equipment
IEEE 802.3 Standard	50	Applications that receive both power and high-speed data through the same RJ45 connector
European directive EU LDV 2006/95EC	75 - 1500	Encourages manufacturers and other agents for harmonisation but without fixing any voltage level
SEG4 group, IEC60038	12/48/380	Provides a recommendation for different voltage levels
National Electrical Code (NEC) NFPA70	60	Low voltage low power devices like sensors or led lighting
MIL-STD-1399	28/155/270 /375/650	Shipboard applications

losses, due to the absence of reactive current flow, skin effect and the reduced number of conversion stages [2.39–2.43].

Due to the random behavior of such renewable generation units, a major challenge for a reliable grid performance is to increase the wind/solar power share, while achieving power balance and voltage and frequency stability. Such intermittent behavior of the renewable generators can be effectively compensated by the inclusion of ESSs in the distribution grid [2.37]. The evolution in power electronics and control technologies has enabled the development of DC Low-Voltage (LV) microgrids. This eases the integration of ESSs, also enhancing the performance of DC grids at building level, by reducing costs and increasing reliability [2.37, 2.44]. Although the pathway from traditional ac distribution systems to these new topologies integrating is not clear, it is reasonable to think that the new grids should take advantage of the already existing ac infrastructure, leading to the creation of hybrid AC/DC microgrids [2.35]. This hybrid approach should use PECs in order to provide redundancy of power flows, thus increasing the grid resiliency [2.45].

Table 2.1 shows the main conclusions arising from the current situation about DC distribution, given by regulations and directives, also considering associations and committees, as well as the experiences in some key facilities.

Therefore, it is reasonable to think that the change is not going to be a drastic switch from a contrasted AC system, with a history over 100 years, to a completely new distribution paradigm. The most feasible solution seems to be the adoption of hybrid AC/DC power system schemes with both AC and DC subsystems based on current AC infrastructures [2.35]. This hybrid approach has the following objectives: 1) use of PECs in order to provide redundancy of power flows and thus increasing the

grid resiliency [2.45], 2) reducing the number of required power conversion stages for the connection of loads and distributed resources, thus increasing the efficiency.

So far, a manifold of purely AC or DC microgrid topologies have been proposed, as well as some experiences dealing with hybrid topologies. In [2.46], DC and some existing hybrid microgrid topologies are analyzed. The most common hybrid structure is the typical AC/DC hybrid microgrid in which two different buses (AC and DC) are connected through one or more converters. DC loads and generators are connected to the DC bus, while AC loads and generators are coupled with the AC line. Usually, in these kinds of schemes, the AC line is connected to the main grid. Other proposals consider AC rings connected to a substation and AC/DC converters connected to this outer AC rings feeding DC small microgrids. There are few experiences considering complex topologies combining AC and DC structures [2.44, 2.46, 2.47]. The use of these kind of networks inside buildings is another trend that could lead to the massive use of such hybrid technologies. For instance in [2.48], the building main network is AC but there is a small DC radial microgrid for connecting the PV generation, ESSs and also dedicated DC loads. Regarding the control implementation in hybrid microgrids, it is critical to analyze the transient response and the power sharing among the DC and AC buses [2.49, 2.50].

2.2.2 AC microgrids

Based on the traditional electric system, its basic topology would be one or more AC feeders connected to the grid by a static switch that are coordinated in such a way that it can adapt its configuration, demand and generation, including a possible disconnection from the grid in case of failure.

The main advantage of this topology is the use of highly reliable and efficient elements for the connection to the grid, a static switch and, in some cases, a transformer, which use a very mature technology. The existing infrastructure can be easily adapted to AC microgrids, just requiring the coordination of an already existing area of the grid [2.51].

AC microgrids can be either single-phase or three-phase. In the case of three-phase, the neutral wire can be available or not, distinguishing between three-phase three-wire and three-phase four-wire.

2.2.3 DC microgrids

As already mentioned, the main reasons for the use of DC is the lower distribution losses, both in lines (no reactive current flow nor skin effect) and PECs, due to the reduction in the number of conversion stages. This is due to the presence of DC in ESSs (batteries, supercapacitors, fuel cells) and RES distributed generation, mainly in Photovoltaic (PV) panels. Besides that, nearly 30% of the generated AC power passes through a power electronic converter before it is utilized [2.52].

This reduction of conversion stages for the PECs also increases reliability of the system [2.53], since PECs are one of the main failure sources as compared to traditional AC distribution network elements.

DC microgrids are a good option to reduce the number of conversion stages, directly connecting the DC elements to the DC bus or avoiding the intermediate step of AC elements interfaced by PECs (normally done with a DC intermediate step when connected to AC in an AC/DC/AC structure). It also simplifies the conversion stage for DC elements interfaced by PECs, since DC/DC converters require less elements than those for AC/DC conversion.

The main disadvantage of DC microgrids is that it requires to build new distribution system, due to its incompatibility with the traditional AC one. Protection systems for DC present some challenges as compared to AC and are normally more expensive [2.54, 2.55].

The simplest version of DC microgrids [2.56] would be an Interlinking Converter (IC) connected to the grid, normally through a transformer, providing isolation and voltage level adaptation. This IC will control the DC bus (in the simpler control configuration) where loads and generators will be connected, directly or through a PEC (DC/DC or AC/DC). This IC has to be bidirectional. Its efficiency and reliability will be lower compared to AC microgrids interfaced (a transformer). Solid-State Transformer (SST) appears as an interesting option.

The term SST was first used in [2.57], although it did not include a real transformer. Nowadays idea of SST is closer to the ones proposed in [2.58] (although not using SST term) and [2.59] (which is the first official use of the term to the current idea of SST). The SST gives the possibility of drastically reducing the size of the transformer, by increasing its frequency of operation. This is done by combining the PEC, required as IC, and the transformer, required for isolation, using topologies in which the operates in a high-frequency.

To summarize, DC microgrids present the following advantages [2.60]:

- Less PEC stages, reducing topology complexity and increasing reliability.
- Easier coordination of controllers, since transient in AC are more complex due to the frequency.
- Stability and power quality control and estimation are easier, since frequency, phase angle and reactive power are not an issue. Harmonic mitigation is easier too.

On the other hand, they present also the following disadvantages or challenges:

- Since AC was traditionally more used, standards for AC are more mature, meanwhile in DC they are still under construction.

- Direct connection to the grid is not possible, requiring bidirectional converters for the interconnection. This reduces efficiency and reliability of this connection to the grid.
- Protection systems are more difficult and less mature.

Regarding the cost of the infrastructure, a completely new installation would be cheaper in DC due to the reduce number of PEC stages. However, the price for the AC alternative is reduced when some part of the existing AC infrastructure can be utilized.

2.2.3.1 Unipolar/Bipolar DC microgrids

DC microgrids can be also classified according to the number of wires and voltage level available [2.61]. Unipolar configuration consists on two cables, one positive and one negative, meanwhile bipolar configuration includes the neutral line too. The unipolar alternative is simpler and cheaper, but the presence of neutral line for bipolar configuration gives the possibility of accessing to different voltage levels (half or total DC bus voltage) and increases the reliability of the system, since in the event of fault in one of the DC poles, the power can still be supplied by the other two wires.

2.2.4 Hybrid AC/DC microgrids

In order to exploit the advantages of both DC and AC alternatives, hybrid AC/DC microgrids have become an interesting solution. They can provide the opportunity of an easier integration in the existing infrastructure, reusing AC components already available. The number of PECs staged is minimized, having possible direct connection to AC and DC depending on the application.

However, it still presents some of the challenges for DC application (like protections) and it has a higher complexity. Coordinated control between the different networks becomes another issue and it will be the main focus of this thesis.

2.2.4.1 Hybrid microgrid topologies

Some further classification can be one attending to the topology of hybrid microgrids. Some of these classifications could also apply to regular AC or DC microgrids (not only for the hybrid alternative).

- Coupled and decoupled AC topologies [2.62], depending on the interface with the grid. For coupled AC, the AC part of the hybrid microgrid is connected to the grid by a transformer. The DC part of the microgrid can be directly connected to the grid (partially isolated) or by the same transformer (completely

isolated), providing isolation to the DC grid but increasing the required power rating for the transformer. For decoupled AC, the AC network of the microgrid is decoupled by a DC stage, increasing controllability and easing fault management (being less sensitive to faults in the connection to the grid). On the other hand, reliability is decreased and cost and maintenance is increased, since the AC network is connected through a converter instead of just a transformer. An example of completely isolated coupled AC microgrid is shown in Fig. 2.1 and one of decoupled AC is shown in Fig. 2.2.

- Radial, ring or interconnected configurations [2.63]. For radial configuration, there is only one possible way for the energy flow for each load. Ring configuration forms a loop, allowing always two different paths for energy flow. In case of failure of any single component, it can be isolated and the rest of the components can consume energy from the other side of the loop. For further improvement of the reliability, interconnected configurations can be considered as well, with more than one connection to the main grid, and with interconnection between different points of the loop. A microgrid with only radial configuration is shown in Fig. 2.1 and Fig. 2.2 shows an example with both radial and ring configurations on it.

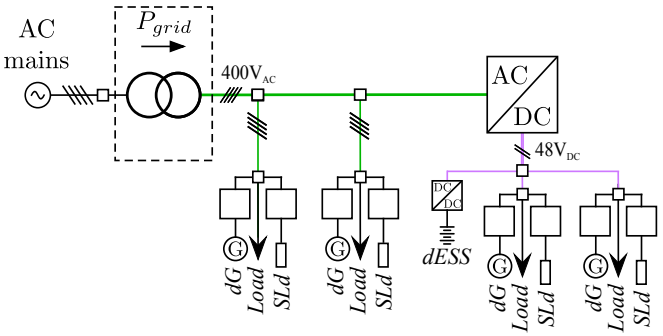

Figure 2.1: Example of a completely isolated coupled AC hybrid microgrid, with only radial networks.

2.2.5 Microgrid elements

2.2.5.1 Networks

As already mentioned, some microgrids can have more than one network. This distinction between grid, microgrid and network is going to be used throughout the thesis.

- Grid will refer to the mains, being microgrids one of its components.

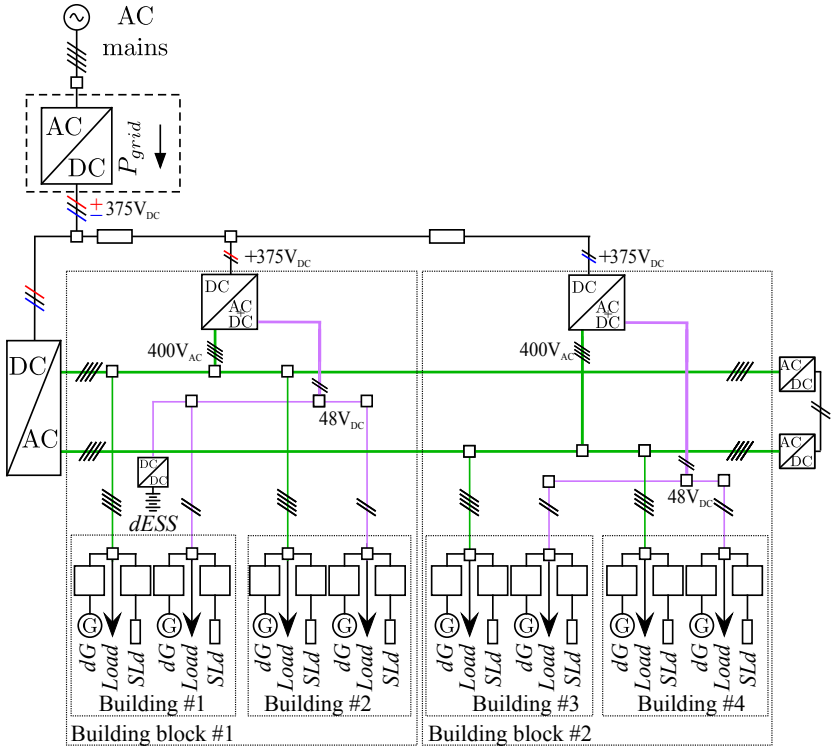

Figure 2.2: Example of a decoupled AC hybrid microgrid. The back-to-back converter in the right side form a ring giving more than one alternative for power flow, increasing reliability. 48 Vdc networks are radial, so they would be preferred for non-critical loads. A bipolar ±375 Vdc is created from the connection to the grid and elements can connect either between neutral and positive, neutral and negative or positive and negative, increasing reliability of the system.

- Microgrid, more precisely defined before, is a group of elements coordinated to behave as a single entity. A microgrid can have both AC and DC and different voltage levels.
- Network refers to all the elements in a microgrid which are directly connected through buses or wires. A PEC whose input is connected to only one energy source is considered to be completely inside the network to which the output is connected. For example, if a single 48 Vdc battery/capacitor is connected to a 375 Vdc network using a PEC, both PEC and battery/capacitor are considered to belong to the 375 Vdc network, since a network with only a battery/capacitor will make no sense. Bus (feeder) is going to be used as equivalent of network for DC (AC).

For example, a hybrid microgrid will have, at least, one DC and one AC networks. They are normally identified with their voltage level and specifying whether they are

AC or DC. However, there can be more than one network with the same voltage level in the same microgrid.

In general, the border between two different networks is an interlinking converter. For the purpose of this thesis, the most important feature of this division is the decoupling between both networks' voltages (an interlinking converter can control its output to a fixed value and maintain it even if the input voltage is varying).

Interlinking converters can be:

- AC/DC: normally present in any microgrid with a DC network, either in hybrid microgrids for connecting to the AC network or in DC microgrids for the connection to the grid.
- AC/AC or AC/DC/AC: for example, for interconnecting two AC microgrids.
- DC/DC: used for connecting more than one DC microgrid to increase stability by having the capacity of exchanging power [2.41] or to have different voltage levels in the same microgrid [2.42]).

2.2.5.2 Loads

They can be classified attending to a different number of criteria:

- Critical or non-critical: critical loads need continuous power with appropriate quality. This means that, in case of failures in the system, non-critical loads can be disconnected in order to guarantee the proper operation of critical loads. Non-critical loads can be used for load shedding [2.64] disconnecting non-critical loads for reducing the demand, either because an emergency, saturation of the capacity of any line or converter or due to economic reasons (in order to move demand to lower demand periods, where the price is lower).
- Directly connected or PEC interfaced: some loads can be directly connected to an AC feeder or DC bus, although the development of PEC and its advantages produced a reduction in the number of direct connections.
- Controllable or non-controllable loads: some loads, normally interfaced by a PEC, can be controlled. All PEC interfaced loads are somehow controlled, but, in this sense, controllable means both the capability of doing so and being an application in which this control is acceptable. For example, the slow dynamics of temperature as compared to electricity makes that any load regarding heating will not be very sensitive to a variation in their power consumption during transients, so this demand can be controlled in order to improve grid operation, especially when there are heat accumulators [2.65]. This makes that although load shedding has been used from long ago [2.66, 2.67], the flexibility of the modern grid, with a lot of controllable loads make it much more versatile.

- Constant Impedance Load (CIL), Constant Current Load (CCL) or Constant Power Load (CPL): depending on the behaviour of the load and its $V-I$ (voltage-current) characteristic. CILs have a positive linear relationship between both ($V \propto I$), being an example a electric heater (that can be simply a resistor). CCLs have a constant current independent on the voltage; it is the least common, although some especial cases can consider CCLs as part of their model (like some wireless electric vehicle charging systems [2.68]). For CPLs, voltage and current are inversely proportional ($V \propto 1/I$) and, nowadays, they are really common, since PEC interfaced loads are usually controlled to follow a power reference. In some cases, loads do not behave exactly as one of these three options. In this case, they can be modeled in different ways, like the exponential load model or the polynomial one [2.69], being this last one just a model with one load of each type in parallel. This is why this model is called ZIP mode, being Z, I and P the letters used to name impedance, current and active power, although this model is applied to reactive power too. This characterization of the load is really important, since it affects the stability of the system; meanwhile CIL reduce its current consumption during a voltage sag, helping to alleviate its effect, CPL does the opposite, increasing current consumption for withdrawing the same power. This effect is sometimes referred as "negative incremental input resistance" [2.70] and it has been a major concern during the last decade [2.71, 2.72], both for the stability analysis [2.73, 2.74] and control proposals for improving stability and disturbance rejection [2.75–2.78]

2.2.5.3 Distributed generation

According to the Institute of Electrical and Electronics Engineers (IEEE), distributed generation is the generation of electricity by facilities sufficiently smaller than central generating plants as to allow interconnection at nearly any point in a power system [2.79].

This distributed generators can be from renewable energy sources, like PV arrays or small wind turbines, since one of the main purposes of microgrids and distributed generation is, precisely, the environmental benefits. However, due to the intermittent nature of this RES, some small-scale distributed generators based on fossil fuels is normally used too, as diesel or gas generators [2.51]. They act as a backup, giving more flexibility to microgrids to adapt its production regardless of the weather conditions.

2.2.5.4 Energy Storage Systems (ESSs)

ESSs play a key role in microgrids. Most of the difficulties of the electric power system and electric market are related to the necessity of always balancing demand and production. Significant ESSs at grid level would be the ideal solution. However, ESSs at that level are not feasible yet. Pumped-storage hydropower is the most important option at grid level but, of course, is not suitable for microgrids.

Pumped-storage hydropower installed capacity was around 160 GW in 2021, meanwhile grid-scale battery storage was around 16 GW, being lithium-ion battery the most widely used [2.80]. Almost 15 GW out of the total 16 GW were installed after 2014. This capacity is being installed mainly in China (3.7 GW), the United States (5.2 GW) and Europe (3.1 GW). To see the impact of this at grid scale, this 3.1 GW installed capacity in Europe can be compared to the total generation capacity installed by 2020, which was around 963 GW [2.81]. So, at grid level, the impact is really small yet, although in the last 8 years the capacity increased more than 10 times.

However, at microgrid level ESSs play a key role and are a feasible solution, presenting two main contributions. First of all, they give flexibility to the microgrid, especially when combined when renewable energies, playing a similar role as the backup generation mentioned before. Nevertheless, they provide even more flexibility, due to their faster response and the possibility of charging/discharging the ESSs regarding electricity price at each moment.

In the present thesis, ESSs will be used to refer to a battery system, with lithium-ion due to their higher energy density, power density and efficiency [2.82], although the applications shown for the proposed control architectures are agnostic to the technology.

Apart from batteries, there are other elements that can belong to the ESSs, like supercapacitors and flywheels [2.83]. The objective of both of them is to provide the microgrid with inertia, since the small-scale, the predominance of RES and the absence of traditional generators (except the backup one) makes it much more sensitive to sudden changes in the demand. Supercapacitors are sometimes used combined with batteries, with the supercapacitors providing power during transients, to reduce stress in the battery.

Apart from that, controllable loads, like air conditioning, heating or electric vehicles, can be used combined with the battery (and supercapacitor) in order to form a generalized energy storage system [2.84]. This is just a coordinated control between the ESSs and the controllable loads, using the flexibility of those loads as a energy storage form.

2.2.5.5 Power Electronic Converter

As already mentioned, PEC are one of the essential part of the microgrids and smart-grids. In fact, their development and widespread presence were the main driver to the change in paradigm from a traditional centralized electric power system to the more distributed version nowadays.

Different switching devices can be used for PEC, like Insulated-Gate Bipolar Transistors (IGBTs) or MOSFETs. IGBTs are the most widely used for low voltage medium power applications [2.85] so they will be the choice for this thesis. However, with the development of wide bandgap semiconductors is making, some alternatives, like SiC MOSFETs are becoming more popular, although they are thought for higher frequencies [2.86, 2.87] than the one used for this thesis (10 kHz).

2.2.5.5.1 AC/DC converters

As mentioned before, AC can be single-phase, three-phase three-wire or three-phase four-wire. The same classification can be done for the PEC on them, although with further divisions. The present thesis will only study three-phase system, so the present analysis will focus on them.

When talking about three-phase PEC, they can be either three-wire or four-wire, as mentioned before. However, four-wire inverters can either be three or four leg [2.88]. Four-leg alternative has one branch of two IGBT per wire, including the neutral. Three-leg four-wire inverters have their neutral wire connected to the DC bus midpoint, being the neutral uncontrolled.

For the present thesis, four-leg four-wire PEC are going to be used for the AC feeders. This is because, although not in the scope of this thesis, the proposed microgrid is going to have unbalances, like single-phase loads, and the controllability of the neutral helps in managing them. Apart from that, four-leg four-wire can achieve around 15.5 % more output voltage by adding zero-sequence third harmonic term as compared to three-leg four-wire [2.89, 2.90].

The most basic controlled inverter topology is shown in Fig. 2.3, with a two-level four-leg four-wire inverter. All the converters are shown with LC filter, since it is going to be the most used throughout the thesis.

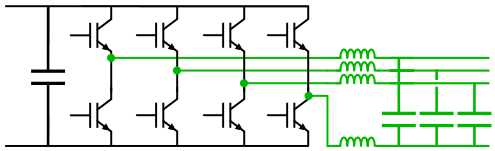

Figure 2.3: Two-level four-leg four-wire inverter.

Multilevel converters reduce harmonic content due to their higher equivalent switching frequency [2.88]. Apart from that, some multilevel topologies, like three-level Neutral-Point Clamped (NPC) present an interesting feature due to the extra degree of freedom o the third level. These converters have the capability of balancing both halves of their DC bus, even when the converter is not controlling the DC bus voltage [2.91]. Three-level four-leg four-wire NPC is shown in Fig. 2.4.

2.2.5.5.2 DC/DC converters

The simplest bidirectional DC/DC converter is just one of the branches with two IGBTs, similar to the ones used for the two-level inverter.The output terminals are connected to the midpoint of the IGBTs (through an inductor) and the negative terminal of the DC bus. This topology is shown in Fig. 2.5.

This is called a buck converter with synchronous operation [2.92], which means that both IGBTs are controlled to have complementary signals, instead of a simpler

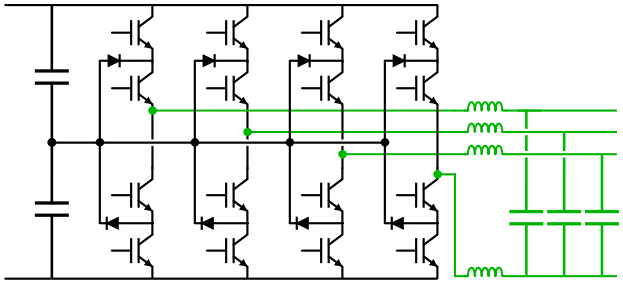

Figure 2.4: Three-level four-leg four-wire NPC converter.

unidirectional version with one IGBT and one diode. Boost synchronous converters have a completely equivalent scheme, where the only difference is which side of the converter is considered as the output whose variables are going to be controlled. Both terms are going to be used indistinctly, except for highlighting which one is the output if needed.

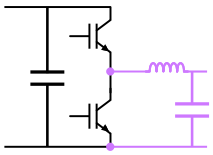

Figure 2.5: Buck converter with synchronous operation.

2.3 Hierarchical control

Due to the important presence of distributed generation and the significant increase of controllability due to the development of communication and computational power, the coordination of the modern grid is much more complex than the traditional ones.

Much more and smaller agents are present in the grid and a central coordination of all the elements is not feasible, even for microgrids, at some time scale levels. These microgrids, since they operate as a single entity, ease the coordination of the grid at a higher level, coordinating different elements so that they behave as only one from the point of view of the complete distribution system.

However, an only controller cannot perform all the control tasks in a microgrid, both for computational and communication issues. The optimum division of these control tasks is not straightforward, as it depends on many factors.

- Computation required: depends mainly of the number of nodes, complexity of the structure, accuracy required and number of variables to control. Depending on

the type of algorithm to be solved and its complexity, an increase in the size in the microgrid can affect on different manners. This means that, for example, for some optimization problems, if the number of nodes is doubled, the computational time is more than twice, increasing faster than linearly [2.93]. This means that, when the size of the microgrid is increased, it might be required to split the problem in smaller ones or to use approximations.

- Communications: the speed and reliability of the possible communication methods is key. A problem might be solvable by one affordable central controller, but with no possibility of sending commands to the involved converters at the required speed. Apart from that, some control tasks are critical and it is preferred to perform them without needing communication between different elements of the grid. When talking about communications using Internet, that might be the only feasible solution for distant elements, cibersecurity becomes an issue too. This is especially important at grid level, to coordinate microgrids or VPPs [2.94, 2.95], but it also has to be taken into account when using Internet for communication among microgrid elements.

- Common goals or interest: grouping different agents in the system is easier when they have common interests. For example, a microgrid for one industry with one single owner will not have conflict of interests that can appear in residential microgrids with different users with different characteristics.

Thus microgrids will act as a single entity, with a coordinated control, in which some of the control tasks are centralized and the rest are distributed. The distribution system operator will coordinate the different elements, such as big power plants or microgrids. How to optimally divide the grid in microgrids in order to take full advantage of the benefits of this division can be a complex problem too [2.96].

Different layers of control have to be established to do this division, leading to the concept of hierarchical control. The complete control scheme of the microgrid is divided into different layers (normally 3 or 4), from a more local and faster control, to a higher level, involving more coordinated elements and with slower response. The separation between layers is not always clear nor is the time scale assigned to each of them. Apart from that, the hierarchical control was already widely used in the conventional grid, in which the generation was done mainly by synchronous generators and with higher power rating, so the time constants changed from that hierarchical control conception in conventional grid as compared to microgrid application, with low inertia and fast response of PECs [2.97].

For example, in [2.98], three levels are considered: primary control (local level), secondary control (microgrid level) and tertiary control (global level). Some other classifications, like the ones in [2.99, 2.100], add an extra layer, called inner control loop, which was considered inside primary control layer in [2.98]. The inner control loop would be the one in charge of current and voltage control loops, meanwhile primary control will be in charge of the coordination between them, especially for avoiding

circulating currents between different generators. Apart from that, all the hierarchical control is considered to be inside the microgrid, so the tertiary control is in charge of the communication between the microgrid and the main grid, an it assures optimum power flow solution.

As explained in [2.100], this type of hierarchical division is not only needed in the electrical system and, in fact, the classification comes from a more general standard (ISA-95) for industrial domain for an automated interface between enterprise and control systems. This classification has more layers (or levels) and it is directly identified with increasing size aggregation of elements. For this thesis, the division proposed in [2.100] is going to be considered as the reference, although, as already mentioned, sometimes the border between different layers is not clear. This reference division is as follows:

- Level 0: inner control loop, derived from ISA-95 device level. Voltage and/or current control loop. It makes the PEC behave as a voltage/current source. Sometimes included in level 1, especially because these control loops were not required in the conventional grid with synchronous generators In fact, sometimes this level just imitates the operation of those generators, as it will be explained later.
- Level 1: primary control, derived from ISA-95 unit level. It allows the coordination between different voltage/current sources from level 0. Especially important for reducing circulating current between voltage sources and make the system more stable and damped. In conventional synchronous generators, it was the external local control which changes their references in order to regulate the contribution of different generators. Mainly done with droop control and/or virtual impedances. Due to the widespread use of droop control as primary control, the definition of the upper layers and its review is going to focus on droop related structures.
- Level 2: secondary control, derived from ISA-95 area level. Guarantees that the levels of electrical variables are within some acceptable range. It "corrects" the deviation from reference values caused by droop or virtual impedance. It also includes management of connection (requiring synchronization) and disconnection from the grid
- Level 3: tertiary control, derived from ISA-95 building level. It controls power flow between the microgrid and the grid, optimizing the microgrid complete operation, normally for cost minimizing.

These two different classifications, considering inner control loop as a layer or including it inside the primary control is understandable taking into account that the original classification was done for traditional power systems, mainly at transmission level. In that case, the level 0 had no sense, because it was simply the operation of the generators.

These differences between the traditional paradigm, completely dominated by rotating generators, to the modern microgrid concept, with PEC interfaced converters and much higher computation and communications capability, is noticeable in the timescales of each layer too. This is mainly due to two reasons. First of all, the first layer of the traditional paradigm was limited by the inertia. The time needed for a significant change in speed of a large generator is much higher than the time constants that a PEC can have for its inner control loops. Even if trying to compensate the lack of inertia in microgrids, the system dynamics would normally be much faster. Since the inner control layer corresponds to this device level behaviour, the fact that PEC control reacts much faster than generators makes possible that the rest of the layers are faster too. Second important reason is that the microgrid has to coordinate with other microgrids and other elements of the grid, like large power plants or Virtual Power Plants. Thus, in fact, microgrids can participate in wider area hierarchical control, so its internal control has to be faster the same way that the inner layer of the microgrids has to be faster than the rest.

For example, for the traditional system in [2.97, 2.101, 2.102], primary control is considered to lie in the range of seconds or tens of seconds, secondary control in minutes and tertiary control in tens of minutes.

On the other hand, for modern microgrids time ranges vary a bit more. In [2.103], the range for primary control is in the order of milliseconds, for secondary from milliseconds to seconds and for tertiary from minutes to hours. However, other classifications like the one in [2.104], specifies a range from seconds to minutes for tertiary control.

This important difference probably comes from different interpretation of the tertiary control in microgrids. Some classifications distinguish between these two concepts of tertiary control [2.105]. These two concepts could be understood as the tertiary control at microgrid level, with the microgrid trying to optimize its own operation attending to economic issues, and the participation of the microgrid in the complete power system tertiary control layer.

In Fig. 2.6, the timescales of both traditional power system and microgrid hierarchical control are shown. Microgrid tertiary control is considered at microgrid level, since the tertiary control layer of complete power system is also represented.

The global operation of the hierarchical control can be summarized in the following sequence, considering the increasing time scale when going to upper layers:

1. Inner control: just controls current or voltage to a given reference value with very fast operation to achieve stability against disturbances.

2. Primary control: modifies current or voltage references to the inner control as a power sharing mechanism, normally without requiring communication and with very fast operation, sometimes only depending on the electrical time constants. Mainly decentralized and with no communications, with a majority of solutions based on droop control. It makes the PECs share power production in the short-term, attending mainly to stability and voltage quality issues.

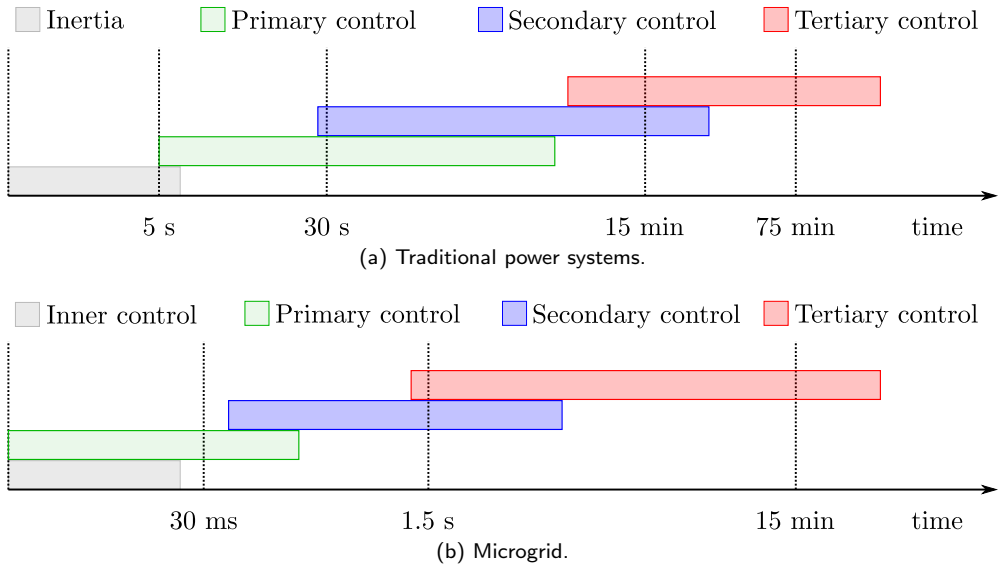

Figure 2.6: Comparison between timescales for hierarchical control in traditional power systems and microgrids [2.97, 2.104].

3. Secondary control: eliminates voltage deviation of the droop control by displacing all the curves, sometimes with exactly the same displacement so that the droop power sharing is not affected, or it is even corrected when it is not accurate due to the different voltage measurements. It can be centralized (communications and central controller), distributed (only communications) or decentralized (no communications nor central controller).

4. Tertiary control: modifies the references of the secondary control to achieve a given power exchange with the grid (only in grid-connected) and an optimum power sharing between the converters, given the desired total production of the microgrid (0 in islanded mode). It is always centralized, as it requires information from all the PECs for the optimization and communication with the grid. It makes the PECs share power production in the long-term, attending mainly to economic issues or ESS state of charge.

The complete hierarchical control structure is summarized in Fig. 2.7, where primary control is considered to be decentralized and secondary and tertiary control are considered as centralized. As already mentioned, for secondary control it is not rare to find distributed or decentralized solutions too.

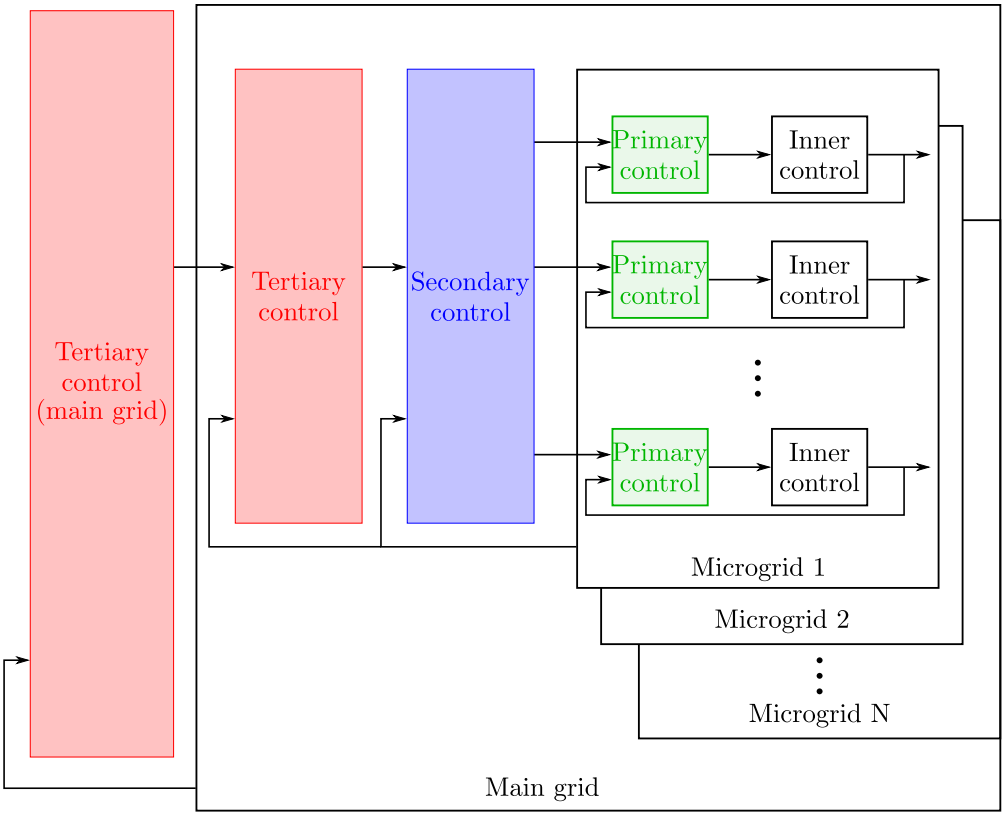

Figure 2.7: General scheme of typical microgrid hierarchical control structure [2.106].

2.3.1 Inner control layer

It is in charge of voltage and/or current control loops. It makes the PEC behave as a voltage or current source. Thus they can be divided in:

- Grid-forming converters behave as a voltage source connected with a series impedance to the Point of Common Coupling (PCC). The name comes from the fact that at least one of them is required on a network to provide a stable voltage. It is required for a microgrid to work in islanded mode. In fact, all the networks of the microgrid need a grid-forming converter, except AC feeders directly connected to mains.
- Grid-feeding converters behave as a current source connected to the PCC with a parallel impedance. Their control is normally simpler, especially when the output power wants to be controlled, like renewable energy sources extracting the maximum power regarding weather conditions.

Traditionally grid-forming and grid-feeding converters were referred to as grid-supporting when including a droop [2.107]. However, recently the trend has moved to distinguish just between grid-forming and grid-feeding, only attending to their behaviour as voltage or current source [2.108, 2.109]. This naming is going to be used throughout the thesis and the capacity of a converter to control the voltage in a given network is going to be referred as grid-forming capability [2.110]. This division is preferred to highlight that any network needs one grid-forming converter (or converter with grid-forming capability) to properly operate, although this converter can have a droop. Although only one grid-forming element is required for the operation of a network, having more than one improves stability and can compensate the low inertia by contributing to voltage control [2.111].

Grid-supporting term is going to be used for grid-feeding converters with support capability (for example, including a droop), as done in [2.112]. Grid-feeding with RES were traditionally thought to operate at maximum power, but some recent codes are encouraging participation of grid-feeding converters in grid support [2.113, 2.114]. However, the capability of grid-feeding converters of providing this support is lower than those of grid-forming [2.111, 2.115]. This justifies the presence of multiple grid-forming converters in the same network even though they present some challenges that grid-feeding converters do not [2.116].

This classification is shown in Fig. 2.8.

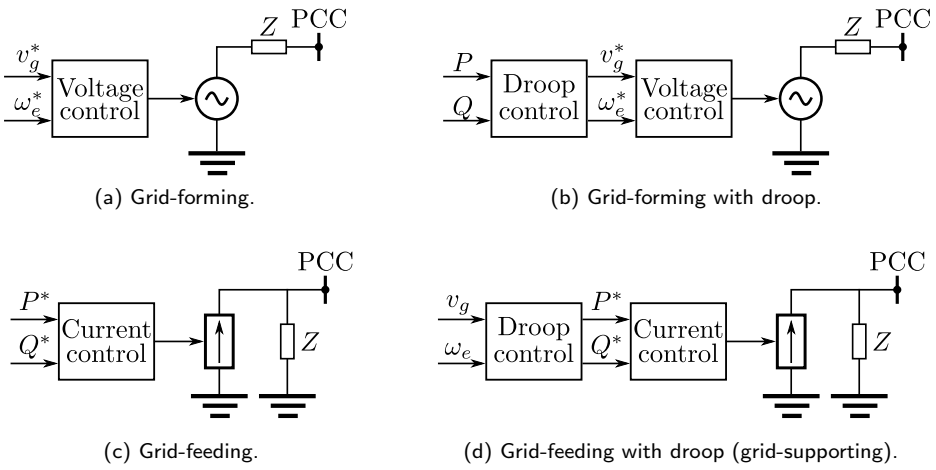

Figure 2.8: Classification of PEC depending on their inner control strategies.

2.3.1.1 Grid-feeding control

2.3.1.1.1 DC

The basic structure of a DC grid-feeding converter consists only on a Proportional Integral (PI) regulator as a current controller. The current reference normally is normally obtained from a power reference. Apart from that, it can help improving system inertia by implementing a virtual inertia or virtual capacitance, with the already mentioned equivalence between capacitance and inertia [2.33, 2.34].

The concept of virtual capacitance was first proposed in [2.117] and later generalized in [2.78] to AC. Sometimes completely equivalent schemes are referred to as virtual inertia because of the already mentioned equivalence [2.118].

When the grid-feeding control is designed for supporting the system, either with virtual capacitance/inertia or with primary control strategies, it is going to be referred to as grid-supporting.

2.3.1.1.2 AC

Control in AC is more complex than for DC, since control of sinusoidal variables is not as straightforward. PI regulators are suitable for controlling DC variables, since they eliminate steady-state error of DC component due to their integral action. However, this complete elimination of the error only happens in DC ($f = 0$ Hz), increasing the error when the frequency to be controlled increases.

Two main solutions appear as an adaptation of the DC case to be applied in AC [2.119]. They are presented for stationary $\alpha\beta$ and synchronous dq reference frame. 0 component is not considered, since unbalances are out of the scope of the thesis. Although the first one can be applied in abc reference frame too, $\alpha\beta$ is more convenient than abc since it eliminates one control variable for balanced systems.

- Use of Proportional Resonant (PR) controllers tuned at grid frequency (50 Hz for this thesis). The PR controller has a resonance frequency for which it has infinite gain, as does the PI regulator in DC, thus eliminating steady-state error at that given frequency. This can be applied both to abc or to $\alpha\beta$ reference frame, although, as already mentioned, the latter is more convenient in balanced systems.

- Use of PI regulators after applying abc to dq transformation. With the synchronous reference frame, the dq components behave as two DC components that can be controlled in a similar way as for DC current control already mentioned. The only difference is that both components are coupled, so instead of having two independent DC components to be controlled, each component is affecting the control of the other one. This can be solved by decoupling them, compensating the effect of each current in the control of the other one.

Both methods have equivalent behaviour at the fundamental frequency [2.120]. Besides these two alternatives, there are other control alternatives to control sine variables, like repetitive controllers [2.121]. For this thesis, *dq* decomposition will be used.

For grid-feeding converters in AC, it is generally needed to estimate the frequency of the grid, requiring a synchronization mechanism. The synchronization mechanism can either be open-loop or close-loop. A deep review on these synchronization methods is presented in [2.122]. However, closed-loop techniques are going to be used due to their better performance. They can be classified into two major groups, Phase Locked Loop (PLL) and Frequency Locked Loop (FLL) techniques. There are different alternatives for each group and the comparison between them has been a research interest since the PEC interfaced distributed generation became more popular [2.123–2.125]. Since the frequency estimation is not in the main scope of the thesis, the widespread Synchronous Reference Frame-PLL (SRF-PLL) is going to be used, as its performance is normally good enough for most applications [2.126].

There are methods which do not require direct estimation of the frequency [2.127]. Although some of them present really good performance in very weak grids, like [2.128], its scheme is much more complex, so they will not be considered for this thesis.

As mentioned for DC, both *d* and *q* components of the current reference normally come from power references (being AC, both active and reactive power) and virtual capacitance/inertia can be included, as well as primary control techniques, so that they support voltage and frequency regulation even if in grid-feeding mode.

The control variables for AC control are shown in Fig. 2.9 with the single-phase equivalent of the three-phase DC/AC converter. All the variables will have subscript *abc* or *dq* depending on the reference frame in which they are measured.

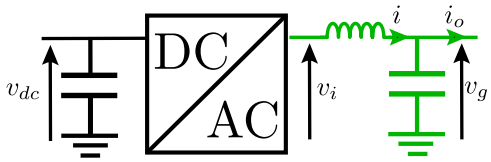

Figure 2.9: DC/AC converter control variables.

The explained grid-feeding control scheme for AC, using *dq* decomposition and SRF-PLL synchronization is shown in Fig. 2.10, including the already mentioned decoupling terms, together with the grid-voltage feedforward and the *dq* transformations. These details (PLL internal structure, *abc* to *dq* transformations, feedforward or decoupling) will be often omitted for simplifying figures.

2.3.1.2 Grid-forming control

There are many alternatives for grid-forming control in DC, although two main ones are going to be studied, both of them based on a cascaded current-voltage control. A

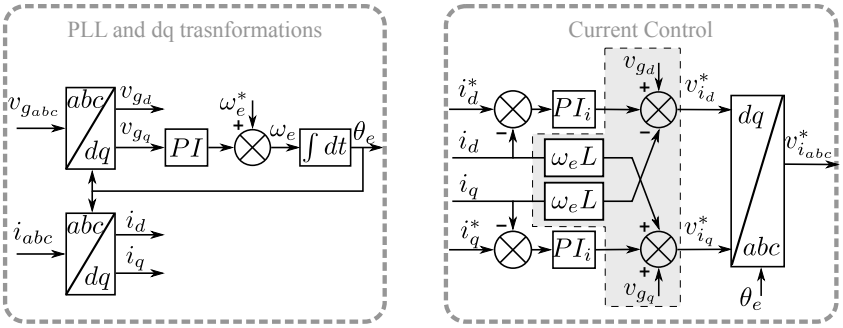

Figure 2.10: Grid-feeding control for AC converters, including SRF-PLL and *dq* transformation of the required variables. Grid-voltage feedforward and cross-coupling *dq* compensation appear in shadowed blocks.

voltage controller, whose two analyzed alternatives are going to be explained later, obtain a current reference that can be sent to the PI based current control explained before.

2.3.1.2.1 PI voltage regulator

The first alternative is to add another PI regulator for the voltage control. The control variables are shown in Fig. 2.11.

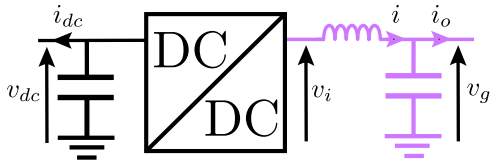

Figure 2.11: DC/DC converter control variables.

The control scheme for the buck configuration (controlling voltage on the side with lower voltage) is shown in Fig. 2.12. Two alternatives are shown for the voltage controller, Direct Voltage Control (DVC) and Quadatric Voltage Control (QVC). As explained in [2.78], the quadratic approximation, although it includes other nonlinearities, facilitates the study of the stability for CPLs due to the linear relationship between squared voltage and power and has an improved CPL disturbance rejection. Feedforward terms appear in shadowed blocks, as they are optional. Output current sensors are not always available; voltage feedforward is normally required for avoiding overcurrent during connection, except if it is a black start (capacitor initially discharged).

The control scheme for the boost configuration (controlling voltage on the side with higher voltage) is shown in Fig. 2.13. It can be seen that the control scheme is

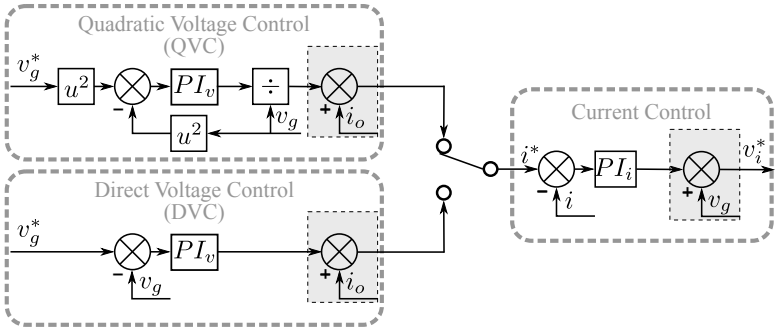

Figure 2.12: Buck control diagram. Both DVC and QVC are shown. Feedforward terms appear in shadowed blocks.

completely equivalent to the buck case, but adapting current reference obtained from voltage controller to the other side voltage (multiplying by v_{dc} and dividing by v_g), since it is the side whose current is being controlled.

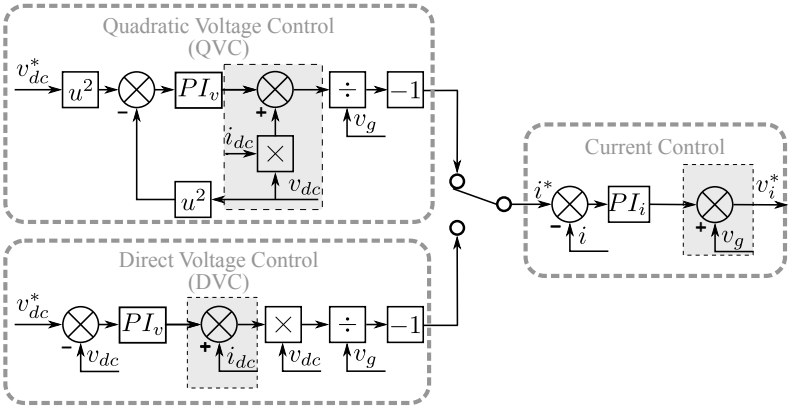

Figure 2.13: Boost control diagram. Both DVC and QVC are shown. Feedforward terms appear in shadowed blocks.

The same controller can be applied to AC, if dq decomposition is applied. This is shown in Fig. 2.14, for both DVC and QVC.

2.3.1.2.2 DC Virtual Generator (DCVG)

As already mentioned, the substitution of rotating generators by PEC interfaced converters meant a reduction in the inertia, which could lead to instabilities in the microgrid. Virtual capacitance can be added with the current control, as explained in [2.78], either for grid-feeding or grid-forming converters. In [2.129], another alternative for the virtual capacitance is added before the voltage controller. Due to the equivalence

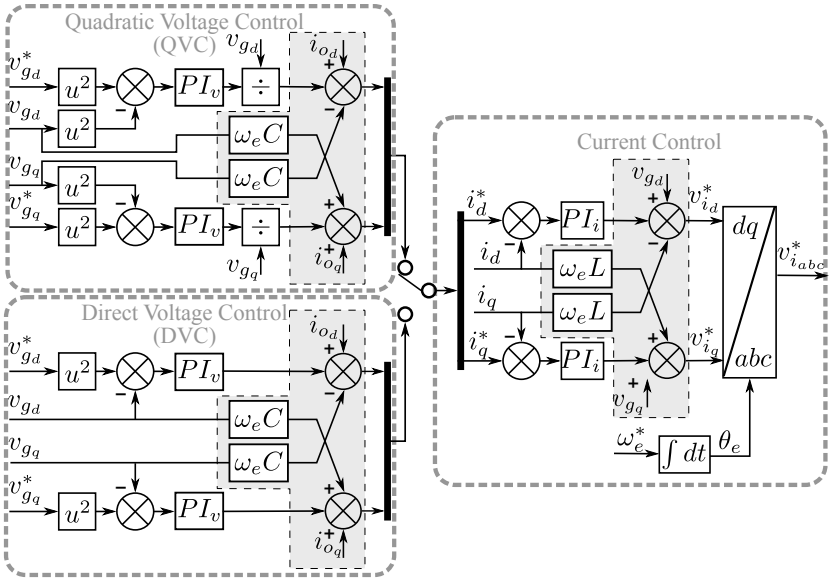

Figure 2.14: Grid-forming control for AC converters for both DVC and QVC. Grid-voltage feedforward and cross-coupling *dq* compensation appear in shadowed blocks. Angular frequency reference, ω_e^*, is either fixed or calculated in primary control.

between capacitance and inertia, both alternatives are the same as adding a virtual inertia.

Another option for adding the virtual inertia is to emulate the operation of a DC Virtual Generator (DCVG). Virtual generators where first used for AC, with the use of virtual synchronous generators or synchronverters [2.130, 2.131]. The same idea was used later on for DC with the idea of DCVG [2.132–2.138]. There are many different implementations, but they are all based in the DCVG equations.

In Fig. 2.15, the control scheme proposed in [2.138] is shown. It consists on a rotor model, with a chosen inertia and damping (J and b), driven by a speed regulator (the governor) and whose load torque is calculated with the virtual voltage and current. The virtual voltage is obtained with the virtual angular frequency and the back electromotive force constant; virtual current is calculated as the current that would flow through a virtual impedance between the virtual voltage and the voltage at the output of the converter.

In [2.139], an analysis about the equivalence of some droop applications with virtual generators if a first-order filter is applied is presented. However, virtual generators, both in AC and DC, can have an external and slower droop loop. This makes that the faster dynamics during transients are shared depending on the virtual inertia, meanwhile steady-state sharing is fixed by the droop coefficients, as shown in [2.138].

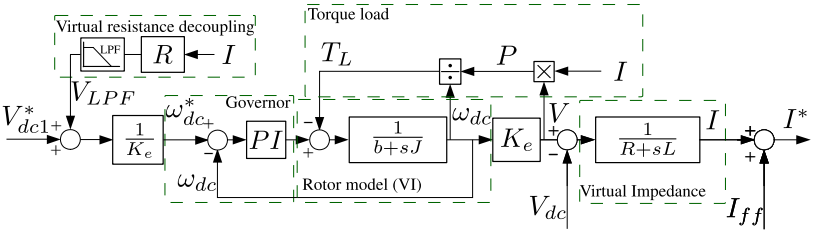

Figure 2.15: DCVG control diagram [2.138].

2.3.2 Primary control layer

As already explained, primary control allows the coordination between different elements behaving as current or voltage sources. In microgrids, this will normally mean grid-forming and grid-feeding converters (referred to as grid-supporting if participating in the power sharing with primary control). Primary control is especially important for reducing circulating current between voltage sources and make the system more stable and damped.

Although some classifications consider primary control based on communications, like in [2.106, 2.107], some definitions of primary control consider no communications at all. In any case, one of the objectives of the thesis is to reduce the dependency on communication for stable operation, so no communications are going to be considered for this level. However, some examples using communications can be found in [2.98, 2.103].

For the primary control strategies, the immense majority of examples are based on droop control and virtual impedances. Both strategies are used combined very often, as it will be explained later. Very few examples do not lie in one of these categories, like the one proposed in [2.140], based on the instantaneous power theory.

For the present thesis, only droop alternatives, combined with virtual impedance, are going to be considered.

2.3.2.1 Virtual impedance

As stated in [2.141–2.145] the virtual impedance can be used for many different purposes like active stabilization and disturbance rejection. Although virtual impedance can be applied to both AC and DC, most of the applications are related to AC problems that do not appear in DC.

In [2.146], the virtual impedance is used to avoid stability problems and to increase power quality, by eliminating flicker. In [2.147], an adaptive virtual impedance control scheme is proposed for overcome the unbalanced and harmonic power sharing in islanded microgrids. In [2.148], in order to reduce voltage harmonic distortion, capacitive virtual impedance for each harmonic is introduced, by applying resonant filters

to the capacitance to be applied to each harmonic. Variable virtual impedance is proposed for soft-start in [2.100]. There are two other applications for its combination with droop controllers which will be explained in the droop explanation.

Nevertheless, this virtual impedance has some unwanted side effects, like the voltage loss capability in the control system. The virtual impedance causes a voltage drop, that makes the effective total voltage drop greater, since the real output voltage of the converter is lower than the reference one (assuming that the converter is producing power). Some solutions can be found in the literature, like the use of a high-pass filter in the virtual impedance [2.142] to eliminate the effect of the virtual impedance in steady-state.

However, this solution is only valid when the use of the virtual impedance is needed because of its transient effect (like the active stabilization aforementioned). When the steady-state effects of the virtual impedance are also needed, this solution is not valid. Secondary control will be in charged of compensating this voltage drop.

2.3.2.2 Droop control

2.3.2.2.1 DC

A review on the main alternatives for droop in DC is shown in [2.149]. The basic DC droop is shown in Fig. 2.16a. This is sometimes called the direct droop, meanwhile the use of the inverse equivalent of this is called inverse droop [2.150] and can be seen in Fig. 2.16b. The main difference between both is more related with the inner control explained previously. They both achieve the same power sharing, although direct droop, applied to grid-forming converters, provides better support. This distinction between direct and inverse is sometimes omitted, specifying the grid-forming/feeding characteristic of the converter instead.

Droop control, as it happens for virtual impedance, cause a voltage deviation from steady-state. This depends on the droop coefficient choice, presenting a trade-off: the greater the droop coefficient, the better the power sharing, but the greater the voltage deviation. Some more complex droops are found to solve this issue. For example, in [2.151] the droop is not linear, presenting a lower droop coefficient for light loads (better voltage regulation) than for heavy loads (better load sharing).

Some other alternatives are found for the droop which consist on a region of the droop characteristic where voltage or power do not vary (i.e., the droop characteristic is vertical or horizontal), as shown in [2.152]. This is normally called a dead band and the idea is to make the converters not participate in the droop power sharing for some range, either controlling voltage to a certain level (grid-forming) or follow a power reference (grid-feeding) . Normally this is done for avoiding unneeded participation in droop sharing for elements that are more suitable to follow a power reference (like charging ESSs or extracting maximum power from renewable sources), unless the grid-forming elements are close to saturate or the voltage profile is not good enough.

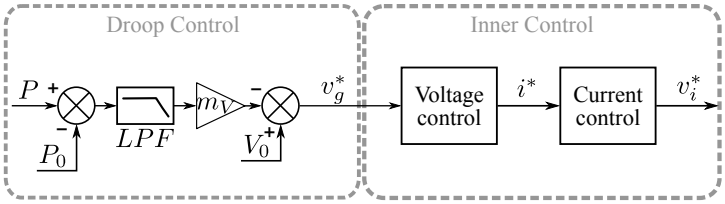

(a) Direct droop control.

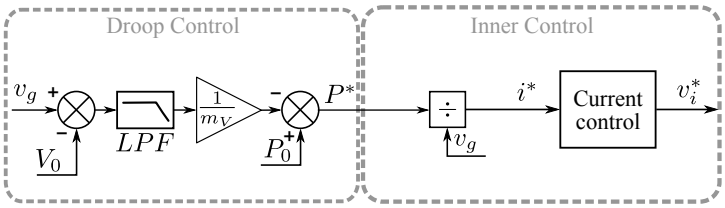

(b) Inverse droop control.

Figure 2.16: Droop control in DC. v_g and v_g^* are measured (inverse droop) and reference voltage (direct droop); P and $P*$ are measured (direct droop) and reference power output (inverse droop); m_V is the droop coefficient; P_0 and V_0 the offset power and voltage.

2.3.2.2.2 AC

In traditional power systems, $P/f + Q/V$ droop has been used for many years. As explained when the problem with inertia was introduced, there is a coupling between power and frequency due to the rotational energy of the generators. Besides that, in inductive power lines, like the transmission system with long lines, the active power transmission mainly depends on phase difference between the voltage, whereas reactive power transmission depends on voltage amplitudes. For resistive lines, it is the opposite, leading to the appearance of an alternative droop, $P/V + Q/f$ [2.107]. In both cases, for obtaining the final droop droop lines are assumed to be purely inductive/resistive and the other term of the impedance is neglected. Both options are shown in Fig. 2.17.

Neglecting resistive/inductive part can worsen the operation when R/X ratio is close to 1, thus the coupling term effect becoming significant. As mentioned before, virtual impedance can be included to increase the resistive/inductive component of the line impedance [2.153, 2.154], but with the possible drawbacks of virtual impedance already explained. In [2.155], a negative virtual resistance is used to try to eliminate the effect of the line resistance, instead of increasing the inductance term.

Some solutions can be found in the literature that consider the coupling terms, without requiring the use of virtual impedances. In [2.156, 2.157], an orthogonal linear rotational transformation matrix (obtained from impedance phase angle) is used to rotate P and Q so that the coupling terms are avoided. In [2.158, 2.159], the coupling terms are compensated. This is done by introducing in the formula for each droop output (voltage magnitude and frequency) a term to compensate the effect of the

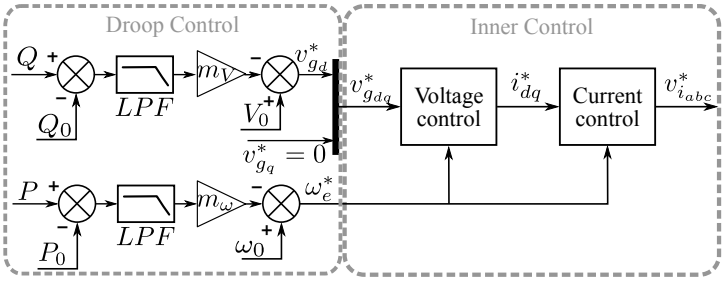

(a) $P/f + Q/V$ droop control.

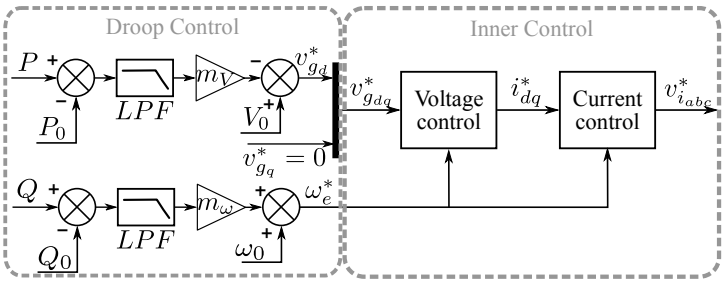

(b) $P/V + Q/f$ droop control.

Figure 2.17: Droop control in AC. ω_e^* and $v_{g_d}^*$ are reference frequency and voltage ($v_{g_d}^*$ is set to 0); P and Q are measured active and reactive power output; m_ω and m_V are the droop coefficient for voltage frequency and amplitude; P_0, Q_0, ω_0 and V_0 the offset active, reactive power, voltage frequency and amplitude.

deviation of the other output with respect to the nominal value.

Besides the already mentioned $P/f + Q/V$ and $P/V + Q/f$ droops and their variations considering the coupling terms, many different variations of the droop exist in the literature. A review is presented in [2.160]. Some solutions use angle instead of frequency as one of the droop outputs [2.159, 2.161–2.163], thus eliminating frequency deviation. No frequency deviation can be achieved with droops based on *dq* decomposition too, like the one in [2.164].

Clock drift might be a problem for these angle or *dq* droops, since each converter frequency will not match exactly. Solutions to this problem can be found, either using signals from global positioning system (GPS) [2.165, 2.166] or based on an implementation of the Precision Time Protocol (PTP), defined in IEEE Standard 1588-2008 [2.167, 2.168].

2.3.2.2.3 Virtual impedance for accurate power sharing

Since PECs are normally connected to different voltages, droop characteristic involving voltage will not achieve accurate power sharing. In AC, reactive power is not

shared accurately if $P/f + Q/V$ droop is used, meanwhile the same happens for active power for $P/V + Q/f$, as it does for the DC case. This problem is normally solved in upper control layers, but some solutions used virtual impedance to avoid this problem.

For example, in [2.169], an adaptive virtual impedance is used to compensate this effect in a small-scale DC network. It can be seen that the proposed algorithm achieves a virtual impedance which compensates the different between each PEC line impedances. The same procedure could be applied to more complex lines were the equivalent impedance for each PEC depends on grid situation.

Similar procedures could be done in AC, either for $P/f + Q/V$ or $P/V + Q/f$. In [2.155], where a negative inductance is used in order to achieve same reactive power sharing among the converters (Q/V droop). Negative inductance is used, in this case, for avoiding increasing the effective inductance and for reducing the virtual inductance effects to harmonics [2.170]. In [2.171], an adaptive complex virtual impedance method is proposed for the same purpose.

2.3.3 Secondary control layer

Secondary control is used to eliminate voltage and frequency deviation due to the droop. The explanation is going to focus on the P/V droop, due to its application to both AC and DC. However, the application to the other droops used in AC for its different alternatives are equivalent (P/f, Q/f, Q/V or any other variation).

Secondary control is typically based a displacement of the droop characteristic so that it eliminates voltage/frequency deviation but trying to maintain the same power sharing. The concept for this deviation elimination is shown in Fig. 2.18. For the example, P_0 is considered to be 0 and V_0 equal to the nominal voltage, varying P_0 to achieve $V = V_0$. Instead of a variation in P_0, the same operation could be done considering V_0 variation, but for this thesis V_0 (and w_0) are considered always equal to the nominal values.

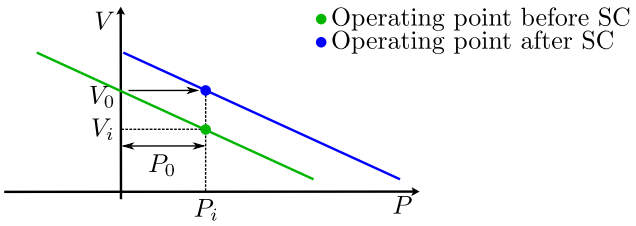

Figure 2.18: Droop characteristic and secondary control principle. P_i and V_i correspond to the initial operating point of a given converter. After the secondary control is applied, the same power output is achieved while obtaining nominal voltage.

Secondary control typically relies on integrators or PI regulators to eliminate this voltage/frequency deviation, both in AC [2.172] and DC [2.173]. This requires periodic

calculations for the integrator to operate, gradually reducing the error every cycle by varying P_0.

This type of secondary control is normally divided into three categories [2.174]:

- Centralized secondary control has a central controller with communications with the control of each involved converter and measures the area voltage in order to eliminate its deviation, normally with a PI regulator, sending the same reference to all the converters. [2.175, 2.176]. The central controller normally calculates the average of the variables to be restored (voltage amplitude and, in AC, also frequency) and applies a PI regulator until the average is equal to the reference value, sending the same command to all the converters, displacing all the droop characteristics in the same amount.

- Distributed secondary control operates in a similar way, but the PI regulator is implemented on each converter control, but with communication among the converters. In some cases, all the converters share with all others the measurement of the voltage amplitude/frequency at its terminal so that they calculate the average; then, every distributed PI regulator does the same procedure the central controller does in centralized secondary control [2.177]. Another option is that the converters do not communicate with every other one, but just with the closest ones, and apply the PI regulator to that value instead of the average of all the converters [2.173]; they are normally referred to as consensus-based.

- Decentralized control does not require neither central controller nor communications. Some applications rely on state estimation in order to estimate the data needed for the secondary control, estimating the information that distributed secondary control receives from communications. State estimators or observers has been used for wide variety of applications, like estimate variables which are not directly measurable (like magnetic flux in a electrical machine) or just to reduce the number of needed sensors [2.178–2.180]. The decentralized control can estimate and use average of all terminal voltages or the voltage at a terminal considered critical [2.181]. Other ones are consensus-based, estimating the average voltage considering only neighbours [2.182]. Instead of state estimation, some decentralized controls use predictive control [2.183].

Secondary control can also be used to achieve accurate active (reactive) power sharing in P/V (Q/V) droops [2.177]. However, these methods add some extra complexity to the secondary control, with an extra control loop with a PI regulator and they are not suitable for decentralized secondary control, since they use some communication between PECs.

The differences between the three types of distributed control are summarized in Table 2.2.

Table 2.2: Comparison between centralized, distributed and decentralized alternatives in the literature based on PI regulators [2.174].

	Centralized	Distributed	Decentralized
Central controller required	Yes	No	No
Communication required	Yes	Yes	No
Robustness against data loss, comm. delays or high latency	Low	Medium	Complete (no comm.)
Power sharing accuracy	Extra PI	Extra PI	No
Flexibility to change the power sharing	No	No	No

2.3.4 Tertiary control layer

Tertiary control layer delimitation is probably the least clear. As already mentioned, this comes from two different applications of the tertiary control concept in traditional power system. One considers the adaptation of the tertiary control to the microgrid concept, with the same objective as for the traditional power system, which is the optimum operation of the microgrid, especially in economic aspects. The second one is just the participation of the microgrid as a single entity in the tertiary control layer of the power system. In fact, some authors consider tertiary control only operates in grid-connected mode [2.100, 2.184]. This distinction between these two concepts are sometimes considered as different features of microgrid tertiary control layer [2.105].

Some other authors consider the economical operation of the microgrid inside the secondary control [2.106]. However, for this thesis the economic optimization of the operation of the microgrid is going to be considered inside the tertiary control, considering it more in line with the adaptation of the hierarchical concept to microgrid characteristics, since tertiary control is the only one in charge of economic aspects in traditional power systems.

The operational principle of tertiary control is similar to that of secondary control, but with slower response and, instead of restoring voltage amplitude/frequency levels, it controls the active/reactive power interchange with the microgrid, as well as the optimum power share between the elements in the microgrid. It is also mainly do with PI regulators.

2.4 Interlinking converters

Interlinking converters play a significant role in microgrids with more than one network since they allow power flow between those networks to help the weaker system. Weak/strong term is used here to refer not only to refer to design parameters, but also to the situation of each network in any given moment. For example, a network which is close to overload will be considered weaker than another one with more margin,

even if that one is clearly smaller. The purpose of a interlinking converter could be to attenuate these difference so that no network is in a clearly worse situation than the other, regarding voltage/frequency levels, margin for demand increase before overloading,... For that purpose, control strategies of interlinking converter should result in power flow from the stronger to the weaker network.

When dealing with interlinking converters, it is important to remark that, normally, when one of its sides acts as grid-forming in one network, it is seen as a load by the other network. They behave as a voltage source by a voltage control loop in one of the sides. This voltage control is done by controlling the converter current attending to the voltage control command. Since the voltage control is considering only the voltage of one of the sides, it is seen as a current or power source from the other side. So, normally, the interlinking converter will behave as grid-forming converter only with respect to one of the networks or even for none of them. Although providing grid-forming capability to only one side of the converter, the converter can provide support to one or both sides.

The analysis is going to focus especially on reliability. Thus the main focus of the analysis is going to focus on the inner control layer and the already mentioned grid-forming capability. The objective is to obtain an interlinking converter control strategy with the possibility of behaving as grid-forming in either output, without switching between different control strategies depending on microgrid conditions and without requiring communication for that purpose, although it can use communications for upper control layers. Although focusing mainly in the inner control layer, some alternatives involving primary and secondary control layers are going to be presented too, especially because the division is not always clear and many authors do not even separate inner from primary control layer.

In [2.112], a classification of the interlinking converters is done, together with a deep review of possible control methods. Focusing on the capability of contributing to both sides support, only *dual grid-supporting* and *single grid-forming + dual-grid supporting* are going to be mentioned.

2.4.1 Dual grid-supporting

Dual grid-supporting control architectures allow the interlinking converter to collaborate in both networks' support, although not providing grid-forming capability to any of those. It is probably the most widespread technique, together with the single *grid-forming* (like normal voltage control in one of the networks), due to their simplicity.

A simple approach is followed in [2.185], considering the production surplus on each network. If the interlinking converter is connected a region with production surplus and one with deficit, it will increase the power flow in the corresponding direction. The variation of power flow will only happen if the surplus and deficit of each network

is higher than a given threshold, as a hysteresis mechanism to avoid mode chattering. However, this method relies on a low bandwidth communication channel for this purpose.

In [2.186], a control strategy for an AC/DC interlinking converter uses a PI regulator applied to the per unit value of the frequency and the DC voltage, so that they end up being equal. In this case, the frequency for AC and the voltage for DC are considered as an indirect measure of the strength of the corresponding network.

In [2.187], a similar strategy is implemented for an AC/DC/AC interlinking converter. Instead of comparing per unit frequency and voltage, it applies a P/V (for DC) and a P/f (for AC) droop and compares both outputs. Then, it applies a PI regulator until both droop outputs are equal, using this droop active power demands as a measure of the strength of each network. It also includes an extra loop to control voltage in the intermediate DC link.

The method proposed in [2.186] can be considered a particular case of the alternative proposed in [2.187]. If the P/V (for DC) and the P/f (for AC) have the same per unit value for the droop coefficient, the difference between V and f would be proportional to the difference in the droop outputs that would be obtained with the previous methods, being the proportionality constant the droop coefficient. Thus adapting the PI regulator parameters with this droop coefficient will result in exactly the same result.

For DC/DC converters, very few options were found in the literature. In [2.188], the same strategy followed in [2.187] is used.

As mentioned in [2.112], the explained options of AC/DC interlinking converters could be applied to AC/DC due to the equivalence between inertia/capacitance and frequency/voltage between AC and DC networks [2.33, 2.34].

2.4.2 Single grid-forming + dual grid-supporting

Even if acting as grid-forming for one specific network, they can collaborate with voltage (or frequency) regulation in the other side. For this purpose, it is important that the interlinking converters are sensitive to variations in the conditions of both networks.

Some strategies apply inner and primary control layer to focus in one network, meanwhile the secondary control tries to balance both networks, like the one presented in [2.189].

Some others use inner control loop to control one side voltage, meanwhile the primary control (mainly, droop strategies) contributes to both sides. For example, some solutions can be found in the literature for DC/AC converters interfacing an AC microgrid with a DC link capacitor at the output of a converter connected to an energy source. This is done with a droop relating AC and DC voltage (V_g/V_{dc} droop) [2.190] or a dual droop, adding a DC voltage term to AC droop equations [2.191]. However,

they were analysed as an interface between one network and an energy source (not acting as interlinking between two networks).

In [2.192–2.196], a dual droop similar to the one mentioned for [2.191] is applied to an interlinking DC/AC converter. However, the control scheme is thought to operate only as grid-forming in one side.

2.4.3 Reversible grid-forming

The choice of which side voltage is to be controlled is not always straightforward. In some scenarios, it is clear which of the two networks is weaker, like in any microgrid in grid-connected mode. The connection to the grid will act as a slack for all the system, thus considering that the strongest network for the interlinking converter point of view is the one closer to the grid connection. The interlinking converters will normally withdraw the power from that side to control the other side voltage, which is considered weaker. For example, in Fig. 2.1, the most typical configuration would be that the AC/DC converter will operate as grid-forming in the DC network, since the grid is the strongest element and acts a slack for the system.

However, microgrids are though to work in islanded mode too. Thus a control capable of behaving as grid-forming in either side depending on the situation would be preferable. That would be referred to as reversible grid-forming.

Some interlinking AC/DC converter control schemes propose a complete change from DC side voltage control in grid-connected mode to AC side voltage control in islanded mode [2.197]. Thus islanding detection becomes an issue especially important for interlinking converters, as mentioned in [2.198].

In [2.199], four different operation modes are considered, two for each grid static switch state: one for voltage control (DC voltage control in grid-connected, AC voltage control in islanded) and another one for power flow control. For the grid-connected mode, the power flow is determined by the microgrid management system, meanwhile for islanded mode the power flow control tries to balance the situation of both grids in a similar power flow control strategy as the ones in [2.186, 2.187] already mentioned. The islanding detection for switching the operation mode relies on communication, with a poor performance during the transition.

Both previous methods require islanding detection and they do not present a seamless transition between operation modes. Some solutions are found both for AC/DC [2.200] and DC/DC [2.201] interlinking converters that can act as grid-forming units in either side, with no specific islanding detection and seamless transition. This makes that if one of the interconnected networks losses its grid-forming unit, the interlinking converter will give voltage control capability to that network with power coming from the grid-forming unit in the other network. This can be done without control scheme switching and operation mode detection. However, this method requires communications between the interlinking converter and the grid-forming units of each network and it needs a grid-forming unit in one of them.

A variation of voltage margin control [2.202, 2.203] can be used for the transition between operating modes too. The voltage margin control idea is to switch control scheme to a voltage control when a threshold for the voltage is reached avoiding that voltage to remain uncontrolled. The original idea, although proposed for interlining converters, neglected one of the outputs of the converter, just controlling variables on one of the sides. In that sense, the original application was agnostic of the interlinking nature of the converter.

As shown in Table 2.3, the idea of the original proposal was a complete switch between power injection mode to voltage control mode when the voltage reaches some limits ($V_{1,min}$ or $V_{1,max}$). The application of this idea to interlinking converters with reversible grid-forming capability is to control voltage of the weakest network (V_2) in normal conditions and change to control the other voltage (V_1) only when that voltage reaches the aforementioned limits.

Table 2.3: Control variables and reference values for different voltage margin control operation modes. V_1 is the voltage in the strongest side, being a network with a slack the most clear scenario. P_1 is the injected power to the

Voltage level (V_1)	Original case	Interlinking converters
$V_1 \leq V_{1,min}$	$V_1 = V_{1,min}$	$V_1 = V_{1,min}$
$V_{1,min} < V_1 < V_{1,max}$	$P_1 = P_1^*$	$V_2 = V_2^*$
$V_1 \geq V_{1,max}$	$V_1 = V_{1,max}$	$V_1 = V_{1,max}$

This method is very simple and straightforward. However, it is not suitable for cases in which the weakest network is not clear. In case, for example, V_1 is controlled by another converter (or grid-connection) operating as slack in normal operation, it might be a suitable solution. In that case, the operation mode switch will appear in emergency situations, when the slack fails or saturates. The restoration of normal operation is not so straightforward, although it could be done with communications when the slack gets back to normal operating conditions.

2.4.4 Dual grid-forming

Some converters can have the capability of providing grid-forming capability to both networks at the same time, just requiring a grid-supporting element in one of the networks (for example, a grid-feeding converter with droop).

In [2.138], a control based on virtual synchronous generators is used. The virtual synchronous generator is considered to be mechanically coupled to a virtual DC motor. This imposes a coupling between frequency of AC voltage and amplitude of DC voltage, making the converter sensitive to disturbances in the DC side. An increase in demand in the DC side will cause a voltage decrease, reducing the virtual DC motor current and torque. Thus the frequency will decrease, making the inertial elements in the AC side (like virtual synchronous generators or virtual inertia elements) to increase power

injection to compensate the frequency variation. This method can behave as grid-forming inverter for either side of the converter with no specific islanding detection or communication needed. It can also behave as grid-forming in both sides at the same time if combined with a grid-supporting element (a voltage-frequency compensator was used in the article). However, it presents many parameters to be tuned.

No DC/DC interlinking converter control strategy with similar characteristics was found in the literature. The deep review in [2.112] does not even consider that possibility for the classification.

2.5 Summary and research opportunities

This chapter has reviewed the main characteristics of microgrids and their classification attending to different criteria, showing the advantages they can provide, but also their control challenges. The hierarchical control concept has been explained, with a description of its control layers and its especial characteristics when applied to microgrids as compared to the traditional power system. This analysis has emphasized the communication requirement of the different layers, considering the necessity of a reduced dependence on them for stability purposes, as well as robustness against communication problems (delays, data loss, high latency) for optimum operation. The role of interlinking converters has been highlighted, due to their importance for versatile and reliable operation of the microgrid.

The thesis work will focus on the following topics, seen as an opportunity as lines of research:

- Design of a hybrid microgrid in order to exploit the possibility of both AC and DC. The use of AC will ease the integration with the already existing infrastructure and the use of many AC products that are widespread and mature. The use of DC will allow reduced number of conversion stages for PEC interfaced elements, like distributed generation and ESSs. Ring configuration is going to be considered inside the microgrid in order to increase reliability and flexibility of the system, also easing maintenance. Attending to the versatility of the proposed design, different operation modes will be considered depending on microgrid elements' availability. The design will require validation with simulation.
- Flexible secondary control structure that can fully exploit the possibilities of hybrid microgrids with mesh configurations. Some of the benefits of the use of microgrids present a challenge in the sense of coordinated control of the elements of the microgrid. The versatility of the hybrid AC/DC topology with different alternatives for power flow due to its mesh configuration requires a secondary control that can adapt to many different criteria for the final power flow solution. This includes the easiness for including agents with different participation in the power flow: slack bus, droop-controlled converters, controllable loads, elements with a fixed active power reference which can contribute to reactive power

sharing,... Some flexibility in terms of communication requirements will be considered of interest too, allowing a variation of periodicity of the application of the control and reduced sensitivity to delays or data losses: a reduction in the frequency of application of the proposed solution or data losses should not compromise the achievement of the optimum solutions, but just delay its application. An easy integration of the proposed secondary control solution with the upper layers (tertiary control, both at microgrid and main grid level) is sought too, so that the mentioned reduced communication requirements do not compromise the coordination with other elements of the power system. The application of the proposed structure to economic optimization problems of natural interest for microgrid operation will be considered too.

- Primary control for AC with no frequency deviation for application in different R/X scenarios. Since the appearance of microgrids and the increasing research interest on its control, the difference of application of droop-based primary control strategies to microgrid particular characteristics has been an important field of study. First primary control strategies were designed considering the coupling between frequency and active power due to: 1) the relationship between stored energy and frequency of the system due to the kinetic rotational energy due to the widespread use of synchronous generators directly connected to the AC feeder and 2) the fact that active power flow in inductive lines (typical in transmission level) mainly depends on phase difference between voltages. However, considering both the reduction of directly connected rotating generators to the AC feeders and the resistive characteristic of distribution lines (where active flow depend more on voltage amplitude than phase), the coupling between active power and frequency in AC control is less advantageous when referring to microgrid applications. Thus considering that frequency is an important source of instabilities, as well as control challenges (like proper estimation in weak microgrids), droops with no frequency variation have an increasing interest. Besides that, the possibility of using R/X knowledge for an optimum operation of the control needs to be considered. This parameter can be estimated with different methods, but a proper analysis of the robustness of the proposed control for estimation mismatches is required. Droop solutions based on *dq* decomposition appear as an interesting alternative, with some interesting solutions already in the literature, although with still an important gap in research about that type of droops. This strategy for droop design is considered as an interesting approach, moving from the traditional power system droop paradigm based on non-linear power flow equations with trigonometric functions which normally require linearization methods to its analysis in the *dq* reference frame, based on already linear functions and in-line with the widespread use of *dq* decomposition for the inner control loops. However, the already existing $P/f + Q/V$ and its alternative $P/V + Q/f$ (precisely designed for resistive networks) are very mature control strategies and a proper comparison with them needs to be considered for the whole range of R/X ratio.

- Design of DC/DC interlinking converter control with dual grid-forming capability

and allowing participation of PEC for support of voltage in the other network. No control has been found in the literature for DC/DC interlinking converter which demonstrated the capability of keeping stable voltage levels in both interconnected networks without any other grid-forming element in at least one of them. Besides that, it would be of great interest that the proposed control allows participation of PECs of both networks in voltage support of the other one. There are many alternatives that allow this capability for voltage support between networks, but a lot of them rely on communications, so they help alleviate and balance the necessities of both networks, but can be insufficient for significant changes in the microgrid situation like, for example, unforeseen transition to islanded operation mode due to component failure. Some control strategies rely on islanding detection microgrid and switching between control modes, although a seamless transition control architecture is a thesis objective.

References

[2.1] B. Lasseter, "Microgrids [distributed power generation]," in *2001 IEEE Power Engineering Society Winter Meeting. Conference Proceedings (Cat. No.01CH37194)*, vol. 1, Jan. 2001, pp. 146–149 vol.1.

[2.2] R. Schmalensee, "Evaluating Policies to Increase Electricity Generation from Renewable Energy," *Review of Environmental Economics and Policy*, Jan. 2012.

[2.3] D. Wu, F. Tang, T. Dragicevic, J. C. Vasquez, and J. M. Guerrero, "Autonomous Active Power Control for Islanded AC Microgrids With Photovoltaic Generation and Energy Storage System," *IEEE Transactions on Energy Conversion*, vol. 29, no. 4, pp. 882–892, Dec. 2014.

[2.4] K. Dielmann and A. van der Velden, "Virtual power plants (VPP) - a new perspective for energy generation?" in *Proceedings of the 9th International Scientific and Practical Conference of Students, Post-graduates Modern Techniques and Technologies, 2003. MTT 2003.*, Apr. 2003, pp. 18–20.

[2.5] N. Hatziargyriou, "The Microgrids Concept," in *Microgrids: Architectures and Control*. IEEE, 2014, pp. 1–24.

[2.6] C. Liu, R. J. Yang, X. Yu, C. Sun, P. S. P. Wong, and H. Zhao, "Virtual power plants for a sustainable urban future," *Sustainable Cities and Society*, vol. 65, p. 102640, Feb. 2021.

[2.7] G. Moreno, P. Martin, C. Santos, F. J. Rodríguez, and E. Santiso, "A Day-Ahead Irradiance Forecasting Strategy for the Integration of Photovoltaic Systems in Virtual Power Plants," *IEEE Access*, vol. 8, pp. 204 226–204 240, 2020.

[2.8] G. Moreno, C. Santos, P. Martín, F. J. Rodríguez, R. Peña, and B. Vuksanovic, "Intra-Day Solar Power Forecasting Strategy for Managing Virtual Power Plants," *Sensors*, vol. 21, no. 16, p. 5648, Jan. 2021.

[2.9] C. Santos-Perez, M. Tradacete-Ágreda, G. Moreno-Baeza, P. Martin-Sánchez, and F. J. Rodriguez-Sánchez, "Hybrid Photovoltaic Power Forecasting Algorithm for Managing Virtual Power Plants," in *2022 International Conference on Electrical, Computer and Energy Technologies (ICECET)*, Jul. 2022, pp. 1–7.

[2.10] T. A. Nguyen, M. L. Crow, and A. C. Elmore, "Optimal Sizing of a Vanadium Redox Battery System for Microgrid Systems," *IEEE Transactions on Sustainable Energy*, vol. 6, no. 3, pp. 729–737, Jul. 2015.

[2.11] L. H. Koh, P. Wang, F. H. Choo, K.-J. Tseng, Z. Gao, and H. B. Püttgen, "Operational Adequacy Studies of a PV-Based and Energy Storage Stand-Alone Microgrid," *IEEE Transactions on Power Systems*, vol. 30, no. 2, pp. 892–900, Mar. 2015.

[2.12] Bagen and R. Billinton, "Incorporating well-being considerations in generating systems using energy storage," *IEEE Transactions on Energy Conversion*, vol. 20, no. 1, pp. 225–230, Mar. 2005.

[2.13] C. Hauser, D. Bakken, and A. Bose, "A failure to communicate: Next generation communication requirements, technologies, and architecture for the electric power grid," *IEEE Power and Energy Magazine*, vol. 3, no. 2, pp. 47–55, Mar. 2005.

[2.14] H. S. V. S. K. Nunna and D. Srinivasan, "Multiagent-based transactive energy framework for distribution systems with smart microgrids," *IEEE Transactions on Industrial Informatics*, vol. 13, no. 5, pp. 2241–2250, Oct. 2017.

[2.15] A. Aderibole, A. Aljarwan, M. H. Ur Rehman, H. H. Zeineldin, T. Mezher, K. Salah, E. Damiani, and D. Svetinovic, "Blockchain Technology for Smart Grids: Decentralized NIST Conceptual Model," *IEEE Access*, vol. 8, pp. 43 177–43 190, 2020.

[2.16] D. Li, Q. Guo, D. Bai, and W. Zhang, "Research and Implementation on the Operation and Transaction System Based on Blockchain Technology for Virtual Power Plant," in *2022 International Conference on Blockchain Technology and Information Security (ICBCTIS)*, Jul. 2022, pp. 165–170.

[2.17] W. Ali, A. Ulasyar, M. U. Mehmood, A. Khattak, K. Imran, H. S. Zad, and S. Nisar, "Hierarchical Control of Microgrid Using IoT and Machine Learning Based Islanding Detection," *IEEE Access*, vol. 9, pp. 103 019–103 031, 2021.

[2.18] S. Massoud Amin and B. Wollenberg, "Toward a smart grid: Power delivery for the 21st century," *IEEE Power and Energy Magazine*, vol. 3, no. 5, pp. 34–41, Sep. 2005.

[2.19] T. Kazičková and B. Buhnova, "ICT architecture for the Smart Grid: Concept overview," in *2016 Smart Cities Symposium Prague (SCSP)*, May 2016, pp. 1–4.

[2.20] P. P. Varaiya, F. F. Wu, and J. W. Bialek, "Smart Operation of Smart Grid: Risk-Limiting Dispatch," *Proceedings of the IEEE*, vol. 99, no. 1, pp. 40–57, Jan. 2011.

[2.21] J. J. Justo, F. Mwasilu, J. Lee, and J.-W. Jung, "AC-microgrids versus DC-microgrids with distributed energy resources: A review," *Renewable and Sustainable Energy Reviews*, vol. 24, pp. 387–405, Aug. 2013.

[2.22] D. Salomonsson and A. Sannino, "Low-voltage DC distribution system for commercial power systems with sensitive electronic loads," *IEEE Transactions on Power Delivery*, vol. 22, no. 3, pp. 1620–1627, 2007.

[2.23] T. L. Vandoorn, B. Meersman, L. Degroote, B. Renders, and L. Vandevelde, "A Control Strategy for Islanded Microgrids With DC-Link Voltage Control," *IEEE Transactions on Power Delivery*, vol. 26, no. 2, pp. 703–713, Apr. 2011.

[2.24] H. Camblong, J. Sarr, A. T. Niang, O. Curea, J. A. Alzola, E. H. Sylla, and M. Santos, "Micro-grids project, Part 1: Analysis of rural electrification with high content of renewable energy sources in Senegal," *Renewable Energy*, vol. 34, no. 10, pp. 2141–2150, Oct. 2009.

[2.25] P. Tielens and D. Van Hertem, "The relevance of inertia in power systems," *Renewable and Sustainable Energy Reviews*, vol. 55, pp. 999–1009, Mar. 2016.

[2.26] Kundur, "Chapter 11 - Control of Active Power and Reactive Power," in *Power System Stability And Control*. McGraw-Hill, 1994.

[2.27] J. Bitterly, "Flywheel technology: Past, present, and 21st century projections," *IEEE Aerospace and Electronic Systems Magazine*, vol. 13, no. 8, pp. 13–16, Aug. 1998.

[2.28] M. Lazarewicz and J. Arseneaux, "Status of pilot projects using flywheels for frequency regulation," in *2006 IEEE Power Engineering Society General Meeting*, Jun. 2006, pp. 3 pp.–.

[2.29] M. R. B. Tavakoli, M. Power, L. Ruttledge, and D. Flynn, "Load Inertia Estimation Using White and Grey-Box Estimators for Power Systems with High Wind Penetration," *IFAC Proceedings Volumes*, vol. 45, no. 21, pp. 399–404, Jan. 2012.

[2.30] G. Delille, B. Francois, and G. Malarange, "Dynamic Frequency Control Support by Energy Storage to Reduce the Impact of Wind and Solar Generation on Isolated Power System's Inertia," *IEEE Transactions on Sustainable Energy*, vol. 3, no. 4, pp. 931–939, Oct. 2012.

[2.31] A. Ulbig, T. Rinke, S. Chatzivasileiadis, and G. Andersson, "Predictive control for real-time frequency regulation and rotational inertia provision in power systems," in *52nd IEEE Conference on Decision and Control*, Dec. 2013, pp. 2946–2953.

[2.32] F. M. Uriarte, C. Smith, S. VanBroekhoven, and R. E. Hebner, "Microgrid Ramp Rates and the Inertial Stability Margin," *IEEE Transactions on Power Systems*, vol. 30, no. 6, pp. 3209–3216, Nov. 2015.

[2.33] E. Unamuno and J. A. Barrena, "Equivalence of Primary Control Strategies for AC and DC Microgrids," *Energies*, vol. 10, no. 1, p. 91, Jan. 2017.

[2.34] K. Rouzbehi, J. I. Candela, G. B. Gharehpetian, L. Harnefors, A. Luna, and P. Rodriguez, "Multiterminal DC grids: Operating analogies to AC power systems," *Renewable and Sustainable Energy Reviews*, vol. 70, pp. 886–895, Apr. 2017.

[2.35] P. Wang, L. Goel, X. Liu, and F. H. Choo, "Harmonizing AC and DC: A Hybrid AC/DC Future Grid Solution," *IEEE Power and Energy Magazine*, vol. 11, no. 3, pp. 76–83, May 2013.

[2.36] P. Fairley, "DC Versus AC: The Second War of Currents Has Already Begun [In My View]," *IEEE Power and Energy Magazine*, vol. 10, no. 6, pp. 104–103, Nov. 2012.

[2.37] A. Bindra, "Projecting the Evolution of Power Electronics: Highlights from FEPPCON VIII," *IEEE Power Electronics Magazine*, vol. 3, no. 1, pp. 32–44, Mar. 2016.

[2.38] M. Ahmed, L. Meegahapola, A. Vahidnia, and M. Datta, "Stability and Control Aspects of Microgrid Architectures-A Comprehensive Review," *IEEE access : practical innovations, open solutions*, vol. 8, pp. 144 730–144 766, 2020.

[2.39] F. S. Al-Ismail, "DC Microgrid Planning, Operation, and Control: A Comprehensive Review," *IEEE access : practical innovations, open solutions*, vol. 9, pp. 36 154–36 172, 2021.

[2.40] S. Ullah, A. M. Haidar, P. Hoole, H. Zen, and T. Ahfock, "The current state of Distributed Renewable Generation, challenges of interconnection and opportunities for energy conversion based DC microgrids," *Journal of Cleaner Production*, vol. 273, p. 122777, 2020. [Online]. Available: https://www.sciencedirect.com/science/article/pii/S0959652620328225

[2.41] T. Dragičević, X. Lu, J. C. Vasquez, and J. M. Guerrero, "DC Microgrids-Part II: A Review of Power Architectures, Applications, and Standardization Issues," *IEEE Transactions on Power Electronics*, vol. 31, no. 5, pp. 3528–3549, 2016.

[2.42] T. Dragičević, J. C. Vasquez, J. M. Guerrero, and D. Skrlec, "Advanced LVDC Electrical Power Architectures and Microgrids: A step toward a new generation of power distribution networks." *IEEE Electrification Magazine*, vol. 2, no. 1, pp. 54–65, 2014.

[2.43] B. T. Patterson, "DC, Come Home: DC Microgrids and the Birth of the "Enernet"," *IEEE Power and Energy Magazine*, vol. 10, no. 6, pp. 60–69, Nov. 2012.

[2.44] N. Eghtedarpour and E. Farjah, "Power Control and Management in a Hybrid AC/DC Microgrid," *IEEE Transactions on Smart Grid*, vol. 5, no. 3, pp. 1494–1505, May 2014.

[2.45] C. Marnay, H. Aki, K. Hirose, A. Kwasinski, S. Ogura, and T. Shinji, "Japan's Pivot to Resilience: How Two Microgrids Fared After the 2011 Earthquake," *IEEE Power and Energy Magazine*, vol. 13, no. 3, pp. 44–57, May 2015.

[2.46] L. Jia, Y. Zhu, and Y. Wang, "Architecture design for new AC-DC hybrid micro-grid," in *2015 IEEE First International Conference on DC Microgrids (ICDCM)*, Jun. 2015, pp. 113–118.

[2.47] A. A. Eajal, E. F. El-Saadany, M. F. Shaaban, and K. Ponnambalam, "Stochastic energy coordination in hybrid AC/DC smart grids," in *2015 IEEE Electrical Power and Energy Conference (EPEC)*, Oct. 2015, pp. 158–163.

[2.48] P. Arboleya, P. Garcia, B. Mohamed, and C. Gonzalez-Moran, "Distributed resources coordination inside nearly-zero energy buildings providing grid voltage support from a symmetrical component perspective," *Electric Power Systems Research*, vol. 144, pp. 208 – 214, 2017. [Online]. Available: http://www.sciencedirect.com/science/article/pii/S0378779616304862

[2.49] Á. Navarro-Rodríguez, P. García, R. Georgious, and J. García, "Adaptive Active Power Sharing Techniques for DC and AC Voltage Control in a Hybrid DC/AC Microgrid," *IEEE Transactions on Industry Applications*, vol. 55, no. 2, pp. 1106–1116, Mar. 2019.

[2.50] Á. Navarro-Rodríguez, P. García, C. Blanco, R. Georgious, and J. García, "Cooperative Control in a Hybrid DC/AC Microgrid based on Hybrid DC/AC Virtual Generators," in *2018 IEEE Energy Conversion Congress and Exposition (ECCE)*, Sep. 2018, pp. 1156–1163.

[2.51] I. Patrao, E. Figueres, G. Garcerá, and R. González-Medina, "Microgrid architectures for low voltage distributed generation," *Renewable and Sustainable Energy Reviews*, vol. 43, pp. 415–424, Mar. 2015.

[2.52] H. Gabbar, *Smart Energy Grid Engineering*. Academic Press, 2016.

[2.53] S. Harb and R. S. Balog, "Reliability of Candidate Photovoltaic Module-Integrated-Inverter (PV-MII) Topologies—A Usage Model Approach," *IEEE Transactions on Power Electronics*, vol. 28, no. 6, pp. 3019–3027, Jun. 2013.

[2.54] N. Yousefpoor, S. Kim, and S. Bhattacharya, "Control of voltage source converter based multi-terminal DC grid under DC fault operating condition," in *2014 IEEE Energy Conversion Congress and Exposition (ECCE)*, Sep. 2014, pp. 5703–5708.

[2.55] M. H. Rahman, L. Xu, and L. Yao, "DC fault protection strategy considering DC network partition," in *2016 IEEE Power and Energy Society General Meeting (PESGM)*, Jul. 2016, pp. 1–5.

[2.56] X. She, A. Q. Huang, S. Lukic, and M. E. Baran, "On Integration of Solid-State Transformer With Zonal DC Microgrid," *IEEE Transactions on Smart Grid*, vol. 3, no. 2, pp. 975–985, Jun. 2012.

[2.57] J. C. Bowers, S. J. Garrett, H. A. Nienhaus, and J. L. Brooks, "A solid state transformer," in *1980 IEEE Power Electronics Specialists Conference*, Jun. 1980, pp. 253–264.

[2.58] M. Kang, P. Enjeti, and I. Pitel, "Analysis and design of electronic transformers for electric power distribution system," *IEEE Transactions on Power Electronics*, vol. 14, no. 6, pp. 1133–1141, Nov. 1999.

[2.59] S. D. Sudhoff, "Solid state transformer," US Patent US5 943 229A, Aug., 1999.

[2.60] H. Abdelgawad and V. K. Sood, "A Comprehensive Review on Microgrid Architectures for Distributed Generation," in *2019 IEEE Electrical Power and Energy Conference (EPEC)*, Oct. 2019, pp. 1–8.

[2.61] G. S. Rawat and Sathans, "Survey on DC microgrid architecture, power quality issues and control strategies," in *2018 2nd International Conference on Inventive Systems and Control (ICISC)*, Jan. 2018, pp. 500–505.

[2.62] E. Unamuno and J. A. Barrena, "Hybrid ac/dc microgrids—Part I: Review and classification of topologies," *Renewable and Sustainable Energy Reviews*, vol. 52, pp. 1251–1259, Dec. 2015.

[2.63] D. Kumar, F. Zare, and A. Ghosh, "DC Microgrid Technology: System Architectures, AC Grid Interfaces, Grounding Schemes, Power Quality, Communication Networks, Applications, and Standardizations Aspects," *IEEE Access*, vol. 5, pp. 12 230–12 256, 2017.

[2.64] "Emergency Control and Load Shedding in Microgrids," in *Microgrid Dynamics and Control*. John Wiley & Sons, Ltd, 2017, ch. 11, pp. 561–587.

[2.65] A. Odukomaiya, J. Woods, N. James, S. Kaur, K. R. Gluesenkamp, N. Kumar, S. Mumme, R. Jackson, and R. Prasher, "Addressing energy storage needs at lower cost via on-site thermal energy storage in buildings," *Energy & Environmental Science*, vol. 14, no. 10, pp. 5315–5329, Oct. 2021.

[2.66] J. O. Swanson and J. P. Jolliffe, "Load Shedding Program in the Pacific Northwest," *Transactions of the American Institute of Electrical Engineers. Part III: Power Apparatus and Systems*, vol. 73, no. 2, pp. 1655–1668, Jan. 1954.

[2.67] L. L. Fountain and J. L. Blackburn, "Application and Test of Frequency Relays for Load Shedding," *Transactions of the American Institute of Electrical Engineers. Part III: Power Apparatus and Systems*, vol. 73, no. 2, pp. 1660–1668, Jan. 1954.

[2.68] B. Esteban, M. Sid-Ahmed, and N. C. Kar, "A Comparative Study of Power Supply Architectures in Wireless EV Charging Systems," *IEEE Transactions on Power Electronics*, vol. 30, no. 11, pp. 6408–6422, Nov. 2015.

[2.69] "Load representation for dynamic performance analysis (of power systems)," *IEEE Transactions on Power Systems*, vol. 8, no. 2, pp. 472–482, May 1993.

[2.70] X. Liu, A. J. Forsyth, and A. M. Cross, "Negative Input-Resistance Compensator for a Constant Power Load," *IEEE Transactions on Industrial Electronics*, vol. 54, no. 6, pp. 3188–3196, Dec. 2007.

[2.71] E. Hossain, R. Perez, A. Nasiri, and S. Padmanaban, "A Comprehensive Review on Constant Power Loads Compensation Techniques," *IEEE Access*, vol. 6, pp. 33 285–33 305, 2018.

[2.72] T. Dragičević, X. Lu, J. C. Vasquez, and J. M. Guerrero, "DC Microgrids—Part I: A Review of Control Strategies and Stabilization Techniques," *IEEE Transactions on Power Electronics*, vol. 31, no. 7, pp. 4876–4891, Jul. 2016.

[2.73] S. Sanchez, R. Ortega, R. Griño, G. Bergna, and M. Molinas, "Conditions for Existence of Equilibria of Systems With Constant Power Loads," *IEEE Transactions on Circuits and Systems I: Regular Papers*, vol. 61, no. 7, pp. 2204–2211, Jul. 2014.

[2.74] D. Karimipour and F. R. Salmasi, "Stability Analysis of AC Microgrids With Constant Power Loads Based on Popov's Absolute Stability Criterion," *IEEE Transactions on Circuits and Systems II: Express Briefs*, vol. 62, no. 7, pp. 696–700, Jul. 2015.

[2.75] J. Zeng, Z. Zhang, and W. Qiao, "An Interconnection and Damping Assignment Passivity-Based Controller for a DC–DC Boost Converter With a Constant Power Load," *IEEE Transactions on Industry Applications*, vol. 50, no. 4, pp. 2314–2322, Jul. 2014.

[2.76] P. Liutanakul, A.-B. Awan, S. Pierfederici, B. Nahid-Mobarakeh, and F. Meibody-Tabar, "Linear Stabilization of a DC Bus Supplying a Constant Power Load: A General Design Approach," *IEEE Transactions on Power Electronics*, vol. 25, no. 2, pp. 475–488, Feb. 2010.

[2.77] M. Gutierrez, P. A. Lindahl, and S. B. Leeb, "Constant Power Load Modeling for a Programmable Impedance Control Strategy," *IEEE Transactions on Industrial Electronics*, vol. 69, no. 1, pp. 293–301, Jan. 2022.

[2.78] A. Navarro-Rodríguez, P. García, J. M. Cano, and M. Sumner, "Limits, stability and disturbance rejection analysis of voltage control loop strategies for grid forming converters in DC and AC microgrids with high penetration of constant power loads," in *2017 19th European Conference on Power Electronics and Applications (EPE'17 ECCE Europe)*, Sep. 2017, pp. P.1–P.10.

[2.79] V. K. Sood and H. Abdelgawad, "Chapter 1 - Microgrids architectures," in *Distributed Energy Resources in Microgrids*, R. K. Chauhan and K. Chauhan, Eds. Academic Press, Jan. 2019, pp. 1–31.

[2.80] "Grid-Scale Storage – Analysis," https://www.iea.org/reports/grid-scale-storage.

[2.81] "Electricity and heat statistics," https://ec.europa.eu/eurostat/statistics-explained/index.php?title=Electricity_and_heat_statistics.

[2.82] X. Li and S. Wang, "Energy management and operational control methods for grid battery energy storage systems," *CSEE Journal of Power and Energy Systems*, vol. 7, no. 5, pp. 1026–1040, Sep. 2021.

[2.83] H. Jiayi, J. Chuanwen, and X. Rong, "A review on distributed energy resources and MicroGrid," *Renewable and Sustainable Energy Reviews*, vol. 12, no. 9, pp. 2472–2483, Dec. 2008.

[2.84] Z. Zhang, M. Song, H. Liu, C. Wang, L. Li, and W. Liu, "Review of Typical Energy Storage Resources From the Perspective of Generalized Energy Storage System," in *2022 IEEE 5th International Electrical and Energy Conference (CIEEC)*, May 2022, pp. 4733–4738.

[2.85] C. Meyer and R. De Doncker, "Power electronics for modern medium-voltage distribution systems," in *The 4th International Power Electronics and Motion Control Conference, 2004. IPEMC 2004.*, vol. 1, Aug. 2004, pp. 58–66 Vol.1.

[2.86] D. Woldegiorgis, M. M. Hossain, Z. Saadatizadeh, Y. Wei, and H. Alan Mantooth, "Hybrid Si/SiC Switches: A Review of Control Objectives, Gate Driving Approaches and Packaging Solutions," *IEEE Journal of Emerging and Selected Topics in Power Electronics*, pp. 1–1, 2022.

[2.87] J. Srijeeth, S. Mohanrajan, and A. Vijayakumari, "Performance comparison of Si-IGBT and SiC-MOSFET in an inverter application using DPT," in *2021 IEEE 2nd International Conference on Smart Technologies for Power, Energy and Control (STPEC)*, Dec. 2021, pp. 1–5.

[2.88] F. Rojas, R. Cárdenas, C. Burgos-Mellado, E. Espina, J. Pereda, C. Pineda, D. Arancibia, and M. Díaz, "An Overview of Four-Leg Converters: Topologies, Modulations, Control and Applications," *IEEE Access*, vol. 10, pp. 61 277–61 325, 2022.

[2.89] J. A. Houldsworth and D. A. Grant, "The Use of Harmonic Distortion to Increase the Output Voltage of a Three-Phase PWM Inverter," *IEEE Transactions on Industry Applications*, vol. IA-20, no. 5, pp. 1224–1228, Sep. 1984.

[2.90] J. Liang, T. C. Green, C. Feng, and G. Weiss, "Increasing Voltage Utilization in Split-Link, Four-Wire Inverters," *IEEE Transactions on Power Electronics*, vol. 24, no. 6, pp. 1562–1569, Jun. 2009.

[2.91] C. Wang, Z. Li, X. Si, and H. Xin, "Control of neutral-point voltage in three-phase four-wire three-level NPC inverter based on the disassembly of zero level," *CPSS Transactions on Power Electronics and Applications*, vol. 3, no. 3, pp. 213–222, Sep. 2018.

[2.92] S. Kapat and P. T. Krein, "A Tutorial and Review Discussion of Modulation, Control and Tuning of High-Performance DC-DC Converters Based on Small-Signal and Large-Signal Approaches," *IEEE Open Journal of Power Electronics*, vol. 1, pp. 339–371, 2020.

[2.93] N. Hatziargyriou, "Microgrids Control Issues," in *Microgrids: Architectures and Control*. IEEE, 2014, pp. 25–80.

[2.94] F. Si, N. Zhang, Y. Wang, P.-Y. Kong, and W. Qiao, "Distributed Optimization for Integrated Energy Systems with Secure Multi-Party Computation," *IEEE Internet of Things Journal*, pp. 1–1, 2022.

[2.95] X. Jiang, A. Sun, Y. Sun, H. Luo, and M. Guizani, "A Trust-Based Hierarchical Consensus Mechanism for Consortium Blockchain in Smart Grid," *Tsinghua Science and Technology*, vol. 28, no. 1, pp. 69–81, Feb. 2023.

[2.96] M. Rosenberg, J. Fletcher, M. Reynolds, T. French, and L. While, "Identifying Isolated Microgrids in Rural Areas : An Evolutionary Algorithm Approach for a Graph Clustering Problem," in *2019 IEEE Congress on Evolutionary Computation (CEC)*, Jun. 2019, pp. 2498–2505.

[2.97] F. Milano, F. Dörfler, G. Hug, D. J. Hill, and G. Verbič, "Foundations and Challenges of Low-Inertia Systems (Invited Paper)," in *2018 Power Systems Computation Conference (PSCC)*, Jun. 2018, pp. 1–25.

[2.98] E. Unamuno and J. A. Barrena, "Hybrid ac/dc microgrids—Part II: Review and classification of control strategies," *Renewable and Sustainable Energy Reviews*, vol. 52, pp. 1123–1134, Dec. 2015.

[2.99] O. Palizban and K. Kauhaniemi, "Hierarchical control structure in microgrids with distributed generation: Island and grid-connected mode," *Renewable and Sustainable Energy Reviews*, vol. 44, pp. 797–813, Apr. 2015.

[2.100] J. M. Guerrero, J. C. Vasquez, J. Matas, L. G. de Vicuna, and M. Castilla, "Hierarchical Control of Droop-Controlled AC and DC Microgrids—A General Approach Toward Standardization," *IEEE Transactions on Industrial Electronics*, vol. 58, no. 1, pp. 158–172, Jan. 2011.

[2.101] E. Ela, M. Milligan, and B. Kirby, "Operating Reserves and Variable Generation," https://digital.library.unt.edu/ark:/67531/metadc839479/, Jan. 2011.

[2.102] U. , "P1 Load-Frequency Control and Performance," in *Operation Handbook*.

[2.103] K. Ahmed, M. Seyedmahmoudian, S. Mekhilef, N. M. Mubarak, and A. Stojcevski, "A Review on Primary and Secondary Controls of Inverter-interfaced Microgrid," *Journal of Modern Power Systems and Clean Energy*, vol. 9, no. 5, pp. 969–985, Sep. 2021.

[2.104] X. Feng, A. Shekhar, F. Yang, R. E. Hebner, and P. Bauer, "Comparison of Hierarchical Control and Distributed Control for Microgrid," *Electric Power Components and Systems*, vol. 45, no. 10, pp. 1043–1056, Jun. 2017.

[2.105] T. L. Vandoorn, B. Zwaenepoel, J. D. M. De Kooning, B. Meersman, and L. Vandevelde, "Smart microgrids and virtual power plants in a hierarchical control structure," in *2011 2nd IEEE PES International Conference and Exhibition on Innovative Smart Grid Technologies*, Dec. 2011, pp. 1–7.

[2.106] D. E. Olivares, A. Mehrizi-Sani, A. H. Etemadi, C. A. Cañizares, R. Iravani, M. Kazerani, A. H. Hajimiragha, O. Gomis-Bellmunt, M. Saeedifard, R. Palma-Behnke, G. A. Jiménez-Estévez, and N. D. Hatziargyriou, "Trends in Microgrid Control," *IEEE Transactions on Smart Grid*, vol. 5, no. 4, pp. 1905–1919, Jul. 2014.

[2.107] J. Rocabert, A. Luna, F. Blaabjerg, and P. Rodríguez, "Control of Power Converters in AC Microgrids," *IEEE Transactions on Power Electronics*, vol. 27, no. 11, pp. 4734–4749, Nov. 2012.

[2.108] M. Paolone, T. Gaunt, X. Guillaud, M. Liserre, S. Meliopoulos, A. Monti, T. Van Cutsem, V. Vittal, and C. Vournas, "Fundamentals of power systems modelling in the presence of converter-interfaced generation," *Electric Power Systems Research*, vol. 189, p. 106811, 2020. [Online]. Available: https://www.sciencedirect.com/science/article/pii/S037877962030482X

[2.109] T. Qoria, Q. Cossart, C. Li, X. Guillaud, F. Colas, F. Gruson, and X. Kestelyn, "WP3 - Control and Operation of a Grid with 100 % Converter-Based Devices. Deliverable 3.2: Local control and simulation tools for large transmission systems," H2020 Migrate Project, Tech. Rep., 2018. [Online]. Available: https://www.h2020-migrate.eu/

[2.110] T. Qoria, E. Rokrok, A. Bruyere, B. François, and X. Guillaud, "A PLL-Free Grid-Forming Control With Decoupled Functionalities for High-Power Transmission System Applications," *IEEE access : practical innovations, open solutions*, vol. 8, pp. 197 363–197 378, 2020.

[2.111] J. Matevosyan, B. Badrzadeh, T. Prevost, E. Quitmann, D. Ramasubramanian, H. Urdal, S. Achilles, J. MacDowell, S. H. Huang, V. Vital, J. O'Sullivan, and R. Quint, "Grid-Forming Inverters: Are They the Key for High Renewable Penetration?" *IEEE Power and Energy Magazine*, vol. 17, no. 6, pp. 89–98, Nov. 2019.

[2.112] A. Ordoño, E. Unamuno, J. A. Barrena, and J. Paniagua Amillano, "Interlinking converters and their contribution to primary regulation: A review," *International Journal of Electrical Power & Energy Systems*, vol. 111, pp. 44–57, Apr. 2019.

[2.113] "IEEE Standard for Interconnection and Interoperability of Distributed Energy Resources with Associated Electric Power Systems Interfaces," *IEEE Std 1547-2018 (Revision of IEEE Std 1547-2003)*, pp. 1–138, Apr. 2018.

[2.114] A. Singhal, T. L. Vu, and W. Du, "Consensus Control for Coordinating Grid-Forming and Grid-Following Inverters in Microgrids," *IEEE Transactions on Smart Grid*, vol. 13, no. 5, pp. 4123–4133, Sep. 2022.

[2.115] G. Song, B. Cao, and L. Chang, "Review of Grid-forming Inverters in Support of Power System Operation," *Chinese Journal of Electrical Engineering*, vol. 8, no. 1, pp. 1–15, Mar. 2022.

[2.116] R. Rosso, X. Wang, M. Liserre, X. Lu, and S. Engelken, "Grid-forming converters: An overview of control approaches and future trends," in *2020 IEEE Energy Conversion Congress and Exposition (ECCE)*, Oct. 2020, pp. 4292–4299.

[2.117] P. Dahono and R. Mulyadi, "A new control method of DC-DC converters based on virtual capacitance concept," in *4th IEEE International Conference on Power Electronics and Drive Systems. IEEE PEDS 2001 - Indonesia. Proceedings (Cat. No.01TH8594)*, vol. 1, Oct. 2001, pp. 121–125 vol.1.

[2.118] D. Wu, F. Tang, T. Dragicevic, J. M. Guerrero, and J. C. Vasquez, "Coordinated Control Based on Bus-Signaling and Virtual Inertia for Islanded DC Microgrids," *IEEE Transactions on Smart Grid*, vol. 6, no. 6, pp. 2627–2638, Nov. 2015.

[2.119] F. Blaabjerg, R. Teodorescu, M. Liserre, and A. Timbus, "Overview of Control and Grid Synchronization for Distributed Power Generation Systems," *IEEE Transactions on Industrial Electronics*, vol. 53, no. 5, pp. 1398–1409, Oct. 2006.

[2.120] C. Zou, B. Liu, S. Duan, and R. Li, "Stationary Frame Equivalent Model of Proportional-Integral Controller in dq Synchronous Frame," *IEEE Transactions on Power Electronics*, vol. 29, no. 9, pp. 4461–4465, Sep. 2014.

[2.121] G. Villa, C. Gómez-Aleixandre, P. García, and J. García, "Distributed Control Alternatives of Modular Power Converters for Hybrid DC/AC Microgrids," in *2018 IEEE Energy Conversion Congress and Exposition (ECCE)*, Sep. 2018, pp. 6379–6386.

[2.122] P. Gawhade and A. Ojha, "Recent advances in synchronization techniques for grid-tied PV system: A review," *Energy Reports*, vol. 7, pp. 6581–6599, Nov. 2021.

[2.123] L. Mathe, F. Iov, D. Sera, L. Török, and R. Teodorescu, "Implementation of PLL and FLL trackers for signals with high harmonic content and low sampling frequency," in *2014 International Conference on Optimization of Electrical and Electronic Equipment (OPTIM)*, May 2014, pp. 633–638.

[2.124] W. Zhu, "IEEE 1588 implementation with FLL vs. PLL," in *2013 IEEE International Symposium on Precision Clock Synchronization for Measurement, Control and Communication (ISPCS) Proceedings*, Sep. 2013, pp. 71–76.

[2.125] V. Valouch, P. Šimek, and J. Škramlík, "New three phase PLL and FLL techniques for converters used in distributed sources," in *2015 16th International Scientific Conference on Electric Power Engineering (EPE)*, May 2015, pp. 94–99.

[2.126] W. Du, F. K. Tuffner, K. P. Schneider, R. H. Lasseter, J. Xie, Z. Chen, and B. Bhattarai, "Modeling of Grid-Forming and Grid-Following Inverters for Dynamic Simulation of Large-Scale Distribution Systems," *IEEE Transactions on Power Delivery*, vol. 36, no. 4, pp. 2035–2045, Aug. 2021.

[2.127] N. Mohammed, W. Zhou, and B. Bahrani, "Comparison of PLL-Based and PLL-Less Control Strategies for Grid-Following Inverters Considering Time and Frequency Domain Analysis," *IEEE Access*, vol. 10, pp. 80 518–80 538, 2022.

[2.128] M. Zarif Mansour, M. H. Ravanji, A. Karimi, and B. Bahrani, "Linear Parameter-Varying Control of a Power-Synchronized Grid-Following Inverter," *IEEE Journal of Emerging and Selected Topics in Power Electronics*, vol. 10, no. 2, pp. 2547–2558, Apr. 2022.

[2.129] E. Unamuno and J. A. Barrena, "Design and small-signal stability analysis of a virtual-capacitor control for DC microgrids," in *2017 19th European Conference on Power Electronics and Applications (EPE'17 ECCE Europe)*, Sep. 2017, pp. P.1–P.10.

[2.130] H.-P. Beck and R. Hesse, "Virtual synchronous machine," in *2007 9th International Conference on Electrical Power Quality and Utilisation*, Oct. 2007, pp. 1–6.

[2.131] Q.-C. Zhong and G. Weiss, "Synchronverters: Inverters That Mimic Synchronous Generators," *IEEE Transactions on Industrial Electronics*, vol. 58, no. 4, pp. 1259–1267, Apr. 2011.

[2.132] N. Zhi, Y. Ding, and L. Du, "Virtual DC Generator Control Strategy Based on Differential Compensation," in *2019 IEEE Energy Conversion Congress and Exposition (ECCE)*, Sep. 2019, pp. 1454–1458.

[2.133] W. Yi, D. Yi, X. Hu, X. Wang, and F. Shi, "Modeling and simulation of DC micro-grid based on virtual motor control," in *2017 IEEE Transportation Electrification Conference and Expo, Asia-Pacific (ITEC Asia-Pacific)*, Aug. 2017, pp. 1–6.

[2.134] T. Shucheng, D. Ge, Z. Hui, Z. Na, and X. Xi, "Virtual DC machine control strategy of energy storage converter in DC microgrid," in *2016 IEEE Electrical Power and Energy Conference (EPEC)*, Oct. 2016, pp. 1–5.

[2.135] H. Hu, M. Zhu, X. Li, and X. Cai, "Virtual DC machine based islanding detection method in DC distribution system and stability enhancement," in *IECON 2020 The 46th Annual Conference of the IEEE Industrial Electronics Society*, Oct. 2020, pp. 3277–3282.

[2.136] D. Huang, S. Fan, and B. Fan, "Virtual DC Generator Control Strategy for Load DC-DC converter," in *2015 International Symposium on Computers & Informatics*. Atlantis Press, Jan. 2015, pp. 1359–1368.

[2.137] Y. Guo, J. Meng, Y. Wang, and C. Wang, "A Virtual DC Machine Control Strategy for Dual Active Bridge DC-DC Converter," in *2019 IEEE Innovative Smart Grid Technologies - Asia (ISGT Asia)*, May 2019, pp. 2384–2388.

[2.138] A. Navarro-Rodríguez, P. García, C. Gómez-Aleixandre, and C. Blanco, "Cooperative Primary Control of a Hybrid AC/DC Microgrid based on AC/DC Virtual Generators," *IEEE Transactions on Energy Conversion*, pp. 1–14, 2022.

[2.139] J. Liu, Y. Miura, and T. Ise, "Comparison of Dynamic Characteristics Between Virtual Synchronous Generator and Droop Control in Inverter-Based Distributed Generators," *IEEE Transactions on Power Electronics*, vol. 31, no. 5, pp. 3600–3611, May 2016.

[2.140] A. Ovalle, G. Ramos, S. Bacha, A. Hably, and A. Rumeau, "Decentralized Control of Voltage Source Converters in Microgrids Based on the Application of Instantaneous Power Theory," *IEEE Transactions on Industrial Electronics*, vol. 62, no. 2, pp. 1152–1162, Feb. 2015.

[2.141] X. Wang, Y. W. Li, F. Blaabjerg, and P. C. Loh, "Virtual-Impedance-Based Control for Voltage-Source and Current-Source Converters," *IEEE Transactions on Power Electronics*, vol. 30, no. 12, pp. 7019–7037, 2015.

[2.142] Z. Liu, S. Ouyang, and W. Bao, "An improved droop control based on complex virtual impedance in medium voltage micro-grid," in *2013 IEEE PES Asia-Pacific Power and Energy Engineering Conference (APPEEC)*, 2013, pp. 1–6.

[2.143] A. Micallef, M. Apap, C. Spiteri-Staines, and J. M. Guerrero, "Performance comparison for virtual impedance techniques used in droop controlled islanded microgrids," in *2016 International Symposium on Power Electronics, Electrical Drives, Automation and Motion (SPEEDAM)*, Jun. 2016, pp. 695–700.

[2.144] A. D. Paquette and D. M. Divan, "Virtual Impedance Current Limiting for Inverters in Microgrids With Synchronous Generators," *IEEE Transactions on Industry Applications*, vol. 51, no. 2, pp. 1630–1638, 2015.

[2.145] J. He and Y. W. Li, "Analysis, Design, and Implementation of Virtual Impedance for Power Electronics Interfaced Distributed Generation," *IEEE Transactions on Industry Applications*, vol. 47, no. 6, pp. 2525–2538, 2011.

[2.146] B. Keyvani-Boroujeni, B. Fani, G. Shahgholian, and H. H. Alhelou, "Virtual Impedance-Based Droop Control Scheme to Avoid Power Quality and Stability Problems in VSI-Dominated Microgrids," *IEEE Access*, vol. 9, pp. 144 999–145 011, 2021.

[2.147] B. Liu, Z. Liu, J. Liu, R. An, H. Zheng, and Y. Shi, "An Adaptive Virtual Impedance Control Scheme Based on Small-AC-Signal Injection for Unbalanced and Harmonic Power Sharing in Islanded Microgrids," *IEEE Transactions on Power Electronics*, vol. 34, no. 12, pp. 12 333–12 355, Dec. 2019.

[2.148] A. Micallef, M. Apap, C. Spiteri-Staines, J. M. Guerrero, and J. C. Vasquez, "Reactive Power Sharing and Voltage Harmonic Distortion Compensation of Droop Controlled Single Phase Islanded Microgrids," *IEEE Transactions on Smart Grid*, vol. 5, no. 3, pp. 1149–1158, May 2014.

[2.149] A. Ashok Kumar and N. Amutha Prabha, "A comprehensive review of DC microgrid in market segments and control technique," *Heliyon*, vol. 8, no. 11, p. e11694, Nov. 2022.

[2.150] Y. Han, G. Zhang, Q. Li, Z. You, W. Chen, and H. Liu, "Hierarchical energy management for PV/hydrogen/battery island DC microgrid," *International Journal of Hydrogen Energy*, vol. 44, no. 11, pp. 5507–5516, Feb. 2019.

[2.151] F. Chen, R. Burgos, D. Boroyevich, J. C. Vasquez, and J. M. Guerrero, "Investigation of Nonlinear Droop Control in DC Power Distribution Systems: Load Sharing, Voltage Regulation, Efficiency, and Stability," *IEEE Transactions on Power Electronics*, vol. 34, no. 10, pp. 9404–9421, Oct. 2019.

[2.152] Y. Che, J. Zhou, T. Lin, W. Li, and J. Xu, "A Simplified Control Method for Tie-Line Power of DC Micro-Grid," *Energies*, vol. 11, no. 4, p. 933, Apr. 2018.

[2.153] J. C. Vasquez, J. M. Guerrero, M. Savaghebi, J. Eloy-Garcia, and R. Teodorescu, "Modeling, Analysis, and Design of Stationary-Reference-Frame Droop-Controlled Parallel Three-Phase Voltage Source Inverters," *IEEE Transactions on Industrial Electronics*, vol. 60, no. 4, pp. 1271–1280, 2013.

[2.154] E. Lenz, D. J. Pagano, A. Ruseler, and M. L. Heldwein, "Two-Parameter Stability Analysis of Resistive Droop Control Applied to Parallel-Connected Voltage-Source Inverters," *IEEE Journal of Emerging and Selected Topics in Power Electronics*, vol. 8, no. 4, pp. 3318–3332, 2020.

[2.155] C. Dou, Z. Zhang, D. Yue, and M. Song, "Improved droop control based on virtual impedance and virtual power source in low-voltage microgrid," *IET Generation, Transmission & Distribution*, vol. 11, no. 4, pp. 1046–1054, 2017.

[2.156] K. De Brabandere, B. Bolsens, J. Van den Keybus, A. Woyte, J. Driesen, and R. Belmans, "A Voltage and Frequency Droop Control Method for Parallel Inverters," *IEEE Transactions on Power Electronics*, vol. 22, no. 4, pp. 1107–1115, 2007.

[2.157] T. Qunais and M. Karimi-Ghartemani, "Systematic Modeling of a Class of Microgrids and Its Application to Impact Analysis of Cross-Coupling Droop Terms," *IEEE Transactions on Energy Conversion*, vol. 34, no. 3, pp. 1632–1643, 2019.

[2.158] Z. Peng, J. Wang, D. Bi, Y. Wen, Y. Dai, X. Yin, and Z. J. Shen, "Droop Control Strategy Incorporating Coupling Compensation and Virtual Impedance for Microgrid Application," *IEEE Transactions on Energy Conversion*, vol. 34, no. 1, pp. 277–291, 2019.

[2.159] K. Lao, W. Deng, J. Sheng, and N. Dai, "PQ-Coupling Strategy for Droop Control in Grid-Connected Capacitive-Coupled Inverter," *IEEE access : practical innovations, open solutions*, vol. 7, pp. 31 663–31 671, 2019.

[2.160] A. K. Sahoo, K. Mahmud, M. Crittenden, J. Ravishankar, S. Padmanaban, and F. Blaabjerg, "Communication-Less Primary and Secondary Control in Inverter-Interfaced AC Microgrid: An Overview," *IEEE Journal of Emerging and Selected Topics in Power Electronics*, vol. 9, no. 5, pp. 5164–5182, Oct. 2021.

[2.161] R. Majumder, B. Chaudhuri, A. Ghosh, R. Majumder, G. Ledwich, and F. Zare, "Improvement of Stability and Load Sharing in an Autonomous Microgrid Using Supplementary Droop Control Loop," *IEEE Transactions on Power Systems*, vol. 25, no. 2, pp. 796–808, 2010.

[2.162] H. Han, X. Hou, J. Yang, J. Wu, M. Su, and J. M. Guerrero, "Review of Power Sharing Control Strategies for Islanding Operation of AC Microgrids," *IEEE Transactions on Smart Grid*, vol. 7, no. 1, pp. 200–215, 2016.

[2.163] J. M. Guerrero, M. Chandorkar, T. Lee, and P. C. Loh, "Advanced Control Architectures for Intelligent Microgrids—Part I: Decentralized and Hierarchical Control," *IEEE Transactions on Industrial Electronics*, vol. 60, no. 4, pp. 1254–1262, 2013.

[2.164] R. M. Imran, S. Wang, and F. M. F. Flaih, "DQ-Voltage Droop Control and Robust Secondary Restoration With Eligibility to Operate During Communication Failure in Autonomous Microgrid," *IEEE Access*, vol. 7, pp. 6353–6361, 2019.

[2.165] R. E. Wilson and P. S. Sterlina, "GPS synchronized power system phase angle measurements," *International Journal of Satellite Communications*, vol. 12, no. 5, pp. 499–505, 1994.

[2.166] A. Carta, N. Locci, C. Muscas, and S. Sulis, "A Flexible GPS-based System for Synchronized Phasor Measurement in Electric Distribution Networks," in *2006 IEEE Instrumentation and Measurement Technology Conference Proceedings*, Apr. 2006, pp. 1547–1552.

[2.167] J. C. Eidson, M. Fischer, and J. White, "IEEE-1588™ Standard for a Precision Clock Synchronization Protocol for Networked Measurement and Control Systems," in *Proceedings of the 34th Annual Precise Time and Time Interval Systems and Applications Meeting*, Dec. 2002, pp. 243–254.

[2.168] J. Han and D.-K. Jeong, "A Practical Implementation of IEEE 1588-2008 Transparent Clock for Distributed Measurement and Control Systems," *IEEE Transactions on Instrumentation and Measurement*, vol. 59, no. 2, pp. 433–439, Feb. 2010.

[2.169] Y.-S. Lee, K.-M. Kang, M. Kim, H. Lee, C.-G. An, and C.-Y. Won, "Novel Adaptive Virtual Impedance-based Droop Control for Parallel Operation of AC-DC Converter for DC Distribution," in *2020 23rd International Conference on Electrical Machines and Systems (ICEMS)*, Nov. 2020, pp. 636–640.

[2.170] X. Wang, F. Blaabjerg, and Z. Chen, "Autonomous Control of Inverter-Interfaced Distributed Generation Units for Harmonic Current Filtering and Resonance Damping in an Islanded Microgrid," *IEEE Transactions on Industry Applications*, vol. 50, no. 1, pp. 452–461, Jan. 2014.

[2.171] F. Zandi, B. Fani, I. Sadeghkhani, and A. Orakzadeh, "Adaptive complex virtual impedance control scheme for accurate reactive power sharing of inverter interfaced autonomous microgrids," *IET Generation, Transmission & Distribution*, vol. 12, no. 22, pp. 6021–6032, 2018.

[2.172] J. W. Simpson-Porco, Q. Shafiee, F. Dörfler, J. C. Vasquez, J. M. Guerrero, and F. Bullo, "Secondary Frequency and Voltage Control of Islanded Microgrids via Distributed Averaging," *IEEE Transactions on Industrial Electronics*, vol. 62, no. 11, pp. 7025–7038, 2015.

[2.173] P. Wang, X. Lu, X. Yang, W. Wang, and D. Xu, "An Improved Distributed Secondary Control Method for DC Microgrids With Enhanced Dynamic Current Sharing Performance," *IEEE Transactions on Power Electronics*, vol. 31, no. 9, pp. 6658–6673, 2016.

[2.174] Y. Khayat, Q. Shafiee, R. Heydari, M. Naderi, T. Dragičević, J. W. Simpson-Porco, F. Dörfler, M. Fathi, F. Blaabjerg, J. M. Guerrero, and H. Bevrani, "On the Secondary Control Architectures of AC Microgrids: An Overview," *IEEE Transactions on Power Electronics*, vol. 35, no. 6, pp. 6482–6500, 2020.

[2.175] M. Savaghebi, J. M. Guerrero, A. Jalilian, and J. C. Vasquez, "Secondary control for voltage unbalance compensation in an islanded microgrid," in *2011 IEEE International Conference on Smart Grid Communications (SmartGridComm)*, Oct. 2011, pp. 499–504.

[2.176] M. Savaghebi, A. Jalilian, J. C. Vasquez, and J. M. Guerrero, "Secondary Control for Voltage Quality Enhancement in Microgrids," *IEEE Transactions on Smart Grid*, vol. 3, no. 4, pp. 1893–1902, Dec. 2012.

[2.177] Q. Shafiee, J. M. Guerrero, and J. C. Vasquez, "Distributed Secondary Control for Islanded Microgrids—A Novel Approach," *IEEE Transactions on Power Electronics*, vol. 29, no. 2, pp. 1018–1031, 2014.

[2.178] "Observers in Control Systems - 1st Edition," https://www.elsevier.com/books/observers-in-control-systems/ellis/978-0-12-237472-2.

[2.179] R. A. Liston, E. G. Carati, R. Cardoso, J. P. da Costa, and C. Marcelo de Oliveira Stein, "A Robust Design of Active Damping With a Current Estimator for Single-Phase Grid-Tied Inverters," *IEEE Transactions on Industry Applications*, vol. 54, no. 5, pp. 4672–4681, Sep. 2018.

[2.180] R. Ebrahimian and R. Baldick, "State estimation distributed processing [for power systems]," *IEEE Transactions on Power Systems*, vol. 15, no. 4, pp. 1240–1246, Nov. 2000.

[2.181] G. Lou, W. Gu, L. Wang, B. Xu, M. Wu, and W. Sheng, "Decentralised secondary voltage and frequency control scheme for islanded microgrid based on adaptive state estimator," *IET Generation, Transmission & Distribution*, vol. 11, no. 15, pp. 3683–3693, 2017.

[2.182] Y. Khayat, R. Heydari, M. Naderi, T. Dragicevic, Q. Shafiee, M. Fathi, H. Bevrani, and F. Blaabjerg, "Estimation-based Consensus Approach for Decentralized Frequency Control of AC Microgrids," in *2019 21st European Conference on Power Electronics and Applications (EPE '19 ECCE Europe)*, Sep. 2019, pp. 1–8.

[2.183] A. Morattab, O. Akhrif, and M. Saad, "Decentralised coordinated secondary voltage control of multi-area power grids using model predictive control," *IET Generation, Transmission & Distribution*, vol. 11, no. 18, pp. 4546–4555, 2017.

[2.184] O. Palizban, K. Kauhaniemi, and J. M. Guerrero, "Microgrids in active network management—Part I: Hierarchical control, energy storage, virtual power plants, and market participation," *Renewable and Sustainable Energy Reviews*, vol. 36, pp. 428–439, Aug. 2014.

[2.185] J. Ma, M. Zhu, X. Cai, and Y. W. Li, "Configuration and operation of DC microgrid cluster linked through DC-DC converter," in *2016 IEEE 11th Conference on Industrial Electronics and Applications (ICIEA)*, Jun. 2016, pp. 2565–2570.

[2.186] P. C. Loh, D. Li, Y. K. Chai, and F. Blaabjerg, "Autonomous Operation of Hybrid Microgrid With AC and DC Subgrids," *IEEE Transactions on Power Electronics*, vol. 28, no. 5, pp. 2214–2223, May 2013.

[2.187] I. U. Nutkani, P. C. Loh, and F. Blaabjerg, "Power flow control of intertied ac microgrids," *IET Power Electronics*, vol. 6, no. 7, pp. 1329–1338, 2013.

[2.188] A. S. Morais and L. A. Lopes, "Interlink Converters in DC nanogrids and its effect in power sharing using distributed control," in *2016 IEEE 7th International Symposium on Power Electronics for Distributed Generation Systems (PEDG)*, Jun. 2016, pp. 1–7.

[2.189] M. Panda, D. V. Bhaskar, and T. Maity, "A Fuzzy-Based Coordinated Power Management Strategy for Voltage Regulation and State-of-Charge Balancing in Multiple Subgrid-Based DC Microgrid," *International Transactions on Electrical Energy Systems*, vol. 2022, p. e1288985, Apr. 2022.

[2.190] T. L. Vandoorn, B. Renders, L. Degroote, B. Meersman, and L. Vandevelde, "Active Load Control in Islanded Microgrids Based on the Grid Voltage," *IEEE Transactions on Smart Grid*, vol. 2, no. 1, pp. 139–151, 2011.

[2.191] H. Liu, Y. Yang, X. Wang, P. C. Loh, F. Blaabjerg, W. Wang, and D. Xu, "An Enhanced Dual Droop Control Scheme for Resilient Active Power Sharing Among Paralleled Two-Stage Converters," *IEEE Transactions on Power Electronics*, vol. 32, no. 8, pp. 6091–6104, 2017.

[2.192] M. Baharizadeh, H. R. Karshenas, and J. M. Guerrero, "Control strategy of interlinking converters as the key segment of hybrid AC–DC microgrids," *IET Generation, Transmission & Distribution*, vol. 10, no. 7, pp. 1671–1681, 2016.

[2.193] F. Luo, K. H. Loo, and Y. M. Lai, "A hybrid AC/DC microgrid control scheme with voltage-source inverter-controlled interlinking converters," in *2016 18th European Conference on Power Electronics and Applications (EPE'16 ECCE Europe)*, Sep. 2016, pp. 1–8.

[2.194] D. Chen, Y. Xu, and A. Q. Huang, "Integration of DC Microgrids as Virtual Synchronous Machines Into the AC Grid," *IEEE Transactions on Industrial Electronics*, vol. 64, no. 9, pp. 7455–7466, Sep. 2017.

[2.195] Y. Xia, Y. Peng, P. Yang, M. Yu, and W. Wei, "Distributed Coordination Control for Multiple Bidirectional Power Converters in a Hybrid AC/DC Microgrid," *IEEE Transactions on Power Electronics*, vol. 32, no. 6, pp. 4949–4959, Jun. 2017.

[2.196] P. Yang, Y. Xia, M. Yu, W. Wei, and Y. Peng, "A Decentralized Coordination Control Method for Parallel Bidirectional Power Converters in a Hybrid AC–DC Microgrid," *IEEE Transactions on Industrial Electronics*, vol. 65, no. 8, pp. 6217–6228, Aug. 2018.

[2.197] J. Zhang, D. Guo, F. Wang, Y. Zuo, and H. Zhang, "Control strategy of interlinking converter in hybrid AC/DC microgrid," in *2013 International Conference on Renewable Energy Research and Applications (ICRERA)*, Oct. 2013, pp. 97–102.

[2.198] A. Gupta, S. Doolla, and K. Chatterjee, "Hybrid AC–DC Microgrid: Systematic Evaluation of Control Strategies," *IEEE Transactions on Smart Grid*, vol. 9, no. 4, pp. 3830–3843, Jul. 2018.

[2.199] J. Khajesalehi, K. Sheshyekani, M. Hamzeh, and E. Afjei, "Maximum constant boost approach for controlling quasi-Z-source-based interlinking converters in hybrid AC–DC microgrids," *IET Generation, Transmission & Distribution*, vol. 10, no. 4, pp. 938–948, 2016.

[2.200] J. Wang, C. Dong, C. Jin, P. Lin, and P. Wang, "Distributed Uniform Control for Parallel Bidirectional Interlinking Converters for Resilient Operation of Hybrid AC/DC Microgrid," *IEEE Transactions on Sustainable Energy*, vol. 13, no. 1, pp. 3–13, 2022.

[2.201] X. Li, L. Guo, Y. Li, C. Hong, Y. Zhang, Z. Guo, D. Huang, and C. Wang, "Flexible Interlinking and Coordinated Power Control of Multiple DC Microgrids Clusters," *IEEE Transactions on Sustainable Energy*, vol. 9, no. 2, pp. 904–915, 2018.

[2.202] T. Nakajima and S. Irokawa, "A control system for HVDC transmission by voltage sourced converters," in *1999 IEEE Power Engineering Society Summer Meeting. Conference Proceedings (Cat. No.99CH36364)*, vol. 2, Jul. 1999, pp. 1113–1119 vol.2.

[2.203] T. K. Vrana, J. Beerten, R. Belmans, and O. B. Fosso, "A classification of DC node voltage control methods for HVDC grids," *Electric Power Systems Research*, vol. 103, pp. 137–144, 2013. [Online]. Available: https://www.sciencedirect.com/science/article/pii/S0378779613001193

Chapter 3

Microgrid description

3.1 Introduction

Previous chapter presented the advantages of microgrids and the reasons for the increasing interest on its use. Different classifications attending to their topology and the use of AC or DC were explained, attending to the advantages of each alternative. The present chapter will propose the design of a hybrid AC/DC microgrid, with 4 different available voltage levels. A ±375 Vdc bus is going to be used for distribution from the connection to the mains, exploiting the advantages of DC distribution and the possibility of connection to two different voltage levels, 750 Vdc and 375 Vdc. The use of a bipolar configuration increases reliability in case of failure of one of the lines, allowing the connection to half the voltage in case of contingency. A LV level (48 Vdc) will be available for the users, since it is more suitable for the low power applications that a normal customer can require, using the higher DC voltage levels (750 Vdc and 375 Vdc) for loads with significant rated power. Finally, a 400 V AC feeder is included too due to its widespread use as a mature technology. The topology will provide different alternatives for power flow in order to increase its versatility and reliability.

3.2 Proposed Hybrid DC/AC microgrid

The hybrid AC/DC network architecture proposed in this thesis is shown in Fig. 3.1. In there, the hybrid distribution system departures from the output port of a three-port solid state transformer with one input port connected to the main AC grid and the other to a central energy storage system [3.1]. From there, a ±375 Vdc distribution line is connected. In parallel, a power converter (Header PEC, 60 kVA) generates two parallel 400 Vac feeders, which distribute the power downstream. The Header Power

Electronic Converter (HPEC) is built by two parallel-connected 3-level NPC converters which are also responsible of keeping the two DC buses (375 V each) balanced. From the main DC line two identical Ring Power Electronic Converters (RPECs) are connected, providing an alternative path for the AC distribution but also generating a 48 Vdc bus for the internal DC distribution inside a building block. These two RPEC shall be installed in the main connection of a set of buildings to the grid. Finally, the Tail Power Electronic Converter (TPEC) allows for generating a ring between the two feeders, thus enabling an alternative distribution path in the case the other feeder is disabled. The converters could be installed at the next transformation center in the distribution grid.

The DC line connecting the point of connection of the HPEC to the RPEC is considered as a pure resistive line with three identical conductors: one for the +375 DC bus rail of 500 m length and two for ground and −375 DC bus rail of 1000 m length. It is modelled for a maximum voltage drop of 3 % at the end of the 1000 m line, assuming Ring #2 PEC is working at full power. Both feeders are modelled for 1000 m length and for a maximum voltage drop of 3 % at the end of the line.

3.2.1 Header Power Electronic Converter

The header power electronic converter is the coordination converter for the hybrid DC/AC microgrid. Its functions include: 1) to provide a distributed ±375 Vdc for the main DC grid path; 2) to generate two different 4-wire 3-phase 400 V lines for the main AC grid distribution; 3) to deal with the load disturbances, both in the AC and DC grids. It will be of critical importance for the converter to be able to deal with unbalances in the distributed DC link, which is connected to the two Rings, Ring#1 and Ring#2 converters, shown in Fig. 3.1. As it can be seen these two converters provide an alternative path for the 400 Vac grid as well as they are the responsible of generating the 48 Vdc links. Considering the two converter can have different loads, the demanded energy from the two DC link rails, +375/gnd and gnd/−375 will be different. The reason of the dual DC link distribution instead of a single 750 Vdc link is to have a more reliable energy link path, being possible that even if one of the DC links presents a fault condition, the other to continue working.

According to the design constraints, the selected topology for the HPEC is a dual 3-level 4-wire 4-phase NPC converter. The reason about this topology is that is has a reasonable cost for the target power (60 kVA), it provides a split DC link to generate the two distribution 375 Vdc links and it allows for a balancing control method able to deal both with 3-phase and single phase loads and generation units.

The control system is shown in Fig. 3.3. The voltage controller uses Quadatric Voltage Control (QVC) [3.2], as does the rest of the voltage controllers in the rest of the chapter. The DC link balancing scheme is implemented according to the one developed in [3.3].

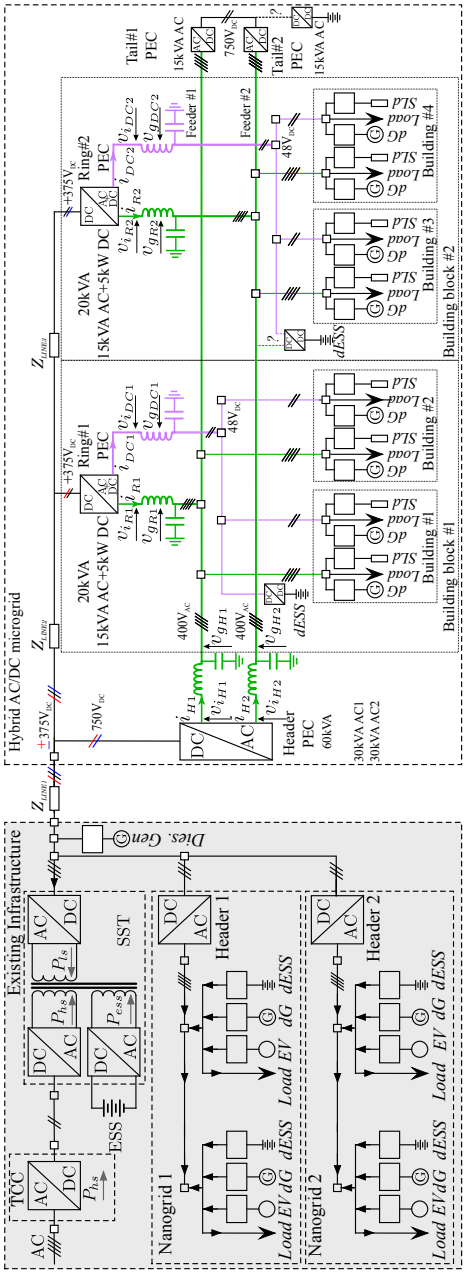

Figure 3.1: Proposed system level grid infrastructure.

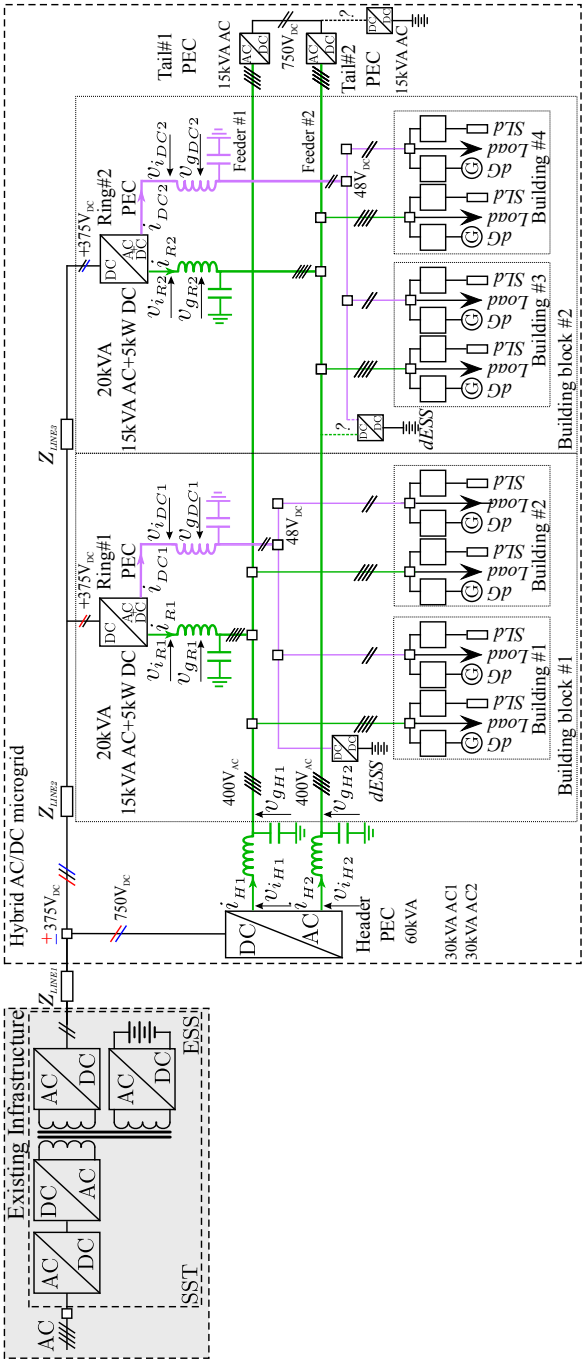

Figure 3.2: Proposed system level grid infrastructure.

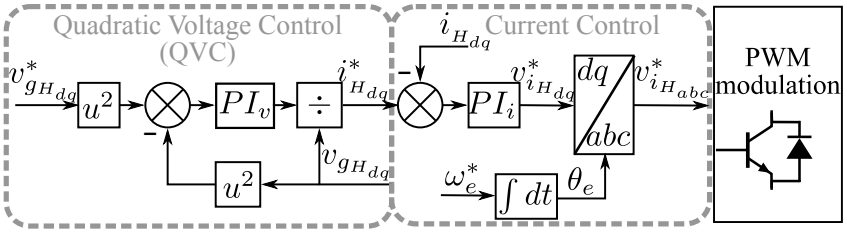

Figure 3.3: Header converter control diagram.

3.2.2 Ring converter

The two ring converters shown in Fig. 3.1 have the same rated power, 20 kVA, and they generate, from the two different main DC grid, a connection to the two 400 Vac feeders and two independent 48 Vdc grids. The converter has an internal bidirectional stage for generating a 750V DC link from the 375Vdc, a 2-level 4-wire 3-phase DC/AC stage for the interconnection with the AC grid and a bidirectional DC/DC 375/48 V for the generation of the 48 V internal building grid. Regarding the control system, Fig. 3.4 shows the required control loops. As it can be seen, the converter has to be able to synchronize with the AC grid generated by the HPEC, contributing to the energy demands. For the case of the 48 Vdc link, the control system generates an stiff bidirectional link, able to deal with the integration of small distributed generation and energy storage systems.

3.2.3 Tail converter

The TPEC shown in Fig. 3.1 is a 2-level 4-wire 3-phase back-to-back converter used for the interconnection of the two AC feeders, thus generating a ringed distribution system. It is worth noting that the operation of that converter, considers the isolated operation of the grid because of the shown local energy storage.

3.3 Microgrid operation modes

The operation of the hybrid DC/AC microgrid can be explained by several modes, all of those here described. For the explanation of the modes, it is needed first to explain the possible states for the distribution lines.

- **Connection to the main AC grid.** When the main AC grid is connected, the energy to the distribution system can be provided either by the AC grid or by the central energy storage connected to the solid-state transformer. When the AC grid is disconnected, the distribution system works in islanded mode using

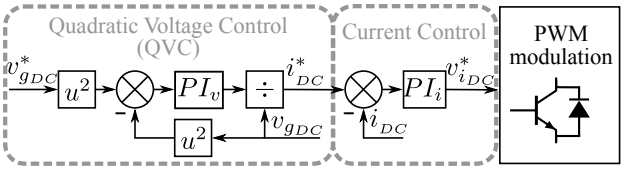

(a) DC/DC stage from 375 Vdc bus to 48 Vdc.

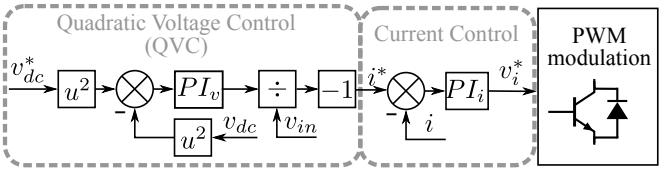

(b) Boost from 375 to 750 V.

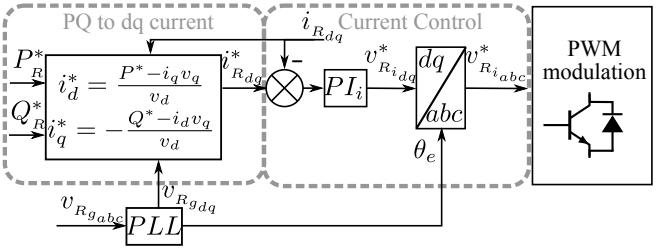

(c) DC/AC stage, from 375 Vdc to 400 Vac (PQ mode).

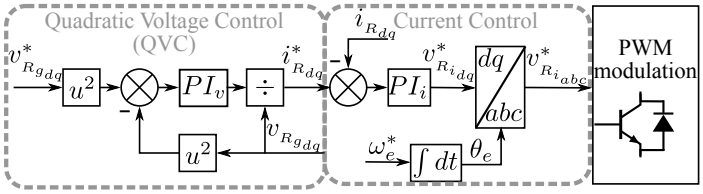

(d) DC/AC stage, from 375 Vdc to 400 Vac (slack mode).

Figure 3.4: Ring converter control diagram.

the energy stored at the central energy storage and the internal generation and energy storage systems.

- **DC/AC main feeders**. The two AC and the two DC feeders can operate simultaneously or independently when a contingency occurs. Under any event condition, all the loads have to be operate normally. Alternative energy path are provided for the different loads by the ring and tail converters and from the local energy storage installed at the 48 V distribution.

According to this, the following modes are considered:

- **HPEC fully operational.** In this case, the two AC and DC feeders are operational. The HPEC behaves like a dual slack converter, generating the two AC feeders voltages. Both NPC converters participate in the balancing of the dual DC link. The two ring converters work in P,Q mode, being a complementary path for supplying the loads when needed. The TPEC could be either in operational mode or disconnected.
- **HPEC AC outputs not operational.** One or the two AC outputs could be disconnected for a variety of reasons. Whenever an AC output is disconnected, the corresponding Ring converter change its operation mode from P,Q to slack. The TPEC converter is in operational mode providing alternative paths for the energy. DC feeders continue fully operational.
- **Fault in the DC feeders.** One or two of the DC feeders could have a contingency. In that case, the corresponding RPEC can not operate. AC feeders continue its normal operation. 48 V bus is generated internally from the dESS.
- **Disconnection of the main DC link.** The main 750 Vdc link is generated by the output port of the solid-state transformer. If a fault occurs in there, both in the connection to the mains and in the central energy storage, the HPEC and the RPEC cannot operate. In that case, the TPEC with the local storage and the dESS connected to the 48 V link are the responsible for the grid generation.

3.4 Simulation Results

For testing the proper operation of the proposed architecture, two of the proposed modes have been simulated using MATLAB/Simulink.

The simulations are based on the scheme shown in Fig. 3.1 with some simplifications for the initial evaluation: 1) the 750 Vdc bus is generated from a bi-directional DC/DC converter, 2) the tail converters are not considered.

All the converters are connected to its corresponding output through a LC filter, whose values are shown in Table 3.1, together with control loop bandwidths and DC bus capacitance of each converter.

3.4.1 HPEC fully operational

Each of the two parallel-connected 3-level NPC converter operates in slack mode, being responsible for the voltage control in Feeder #1 and Feeder #2 respectively (to a fixed value of 400 Vrms), apart from the aforementioned balancing of the DC buses in which both converters are participating.

The two ring converters are connected to the two 400 Vac feeders (operating in P,Q mode) and to the 48 Vdc internal building grid (operating in DC slack mode).

Table 3.1: Converter parameters.

Converter	HPEC - AC	RPEC - AC	RPEC - DC
L_{filter} (mH)	1.68	3.37	1.47
R_{filter} (mΩ)	35.3	70.5	30.7
C_{filter} (mF)	0.5	0.1	5
C_{bus} (mF)	5	5	5
BW_i (Hz)	500	500	500
BW_v (Hz)	50	50	50

In this sequence, there will be three different load cases. First, changes in the references and in the loads will be balanced for both feeders and the ring converters, having the same power demand in both DC link rails. Second, changes in the reference commands and in the loads will be applied only to Building block #2, thus generating a difference between power demand in both DC link rails which induces an unbalance that has to be compensated by the HPEC NPC converters. Third, a single-phase load will be connected at Feeder #2, generating an unbalance in that AC grid.

The time intervals for the complete sequence are as follows:

- At t = 0.1 s, P reference in DC/AC stage of both ring converters changes from 0 to −8 kW.
- At t = 0.2 s, a 4 kW load is connected in each 48 Vdc internal building grid.
- At t = 0.3 s, Q reference in DC/AC stage of both ring converters changes from 0 to 12 kvar.
- At t = 0.5 s, a 12 kW load is connected in each 400 Vac feeder.
- At t = 0.7 s, P reference in DC/AC stage of Building block #2 ring converter changes from −8 to 10 kW.
- At t = 0.8 s, Q reference in DC/AC stage of Building block #2 ring converter changes from 12 to −4 kvar.
- At t = 1.1 s, load connected in Building block #2 48 Vdc grid changes from 4 to 1 kW.
- At t = 1.2 s, load connected in Building block #2 400 Vac feeder changes from 12 to 2 kW.
- At t = 1.4 s, a single-phase 4 kW load is connected in Building block #2 400 Vac feeder.

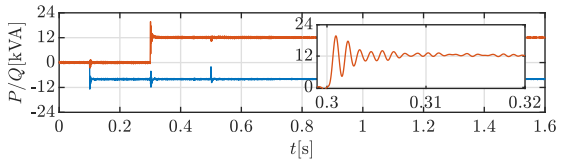

(a) Ring converter in building block #1.

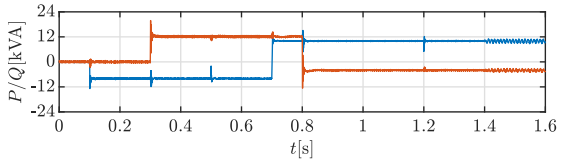

(b) Ring converter in building block #2.

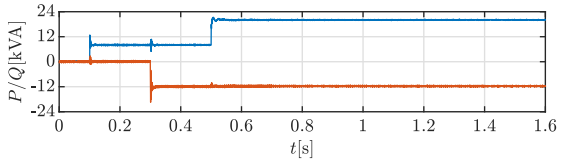

(c) HPEC connected to Feeder #1.

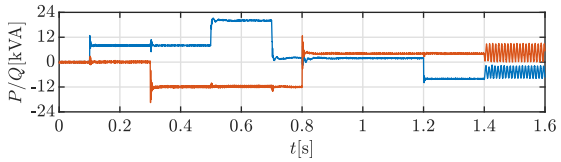

(d) HPEC connected to Feeder #2.

Figure 3.5: active and reactive power output (red, active power; red, reactive power).

In Fig. 3.5a and 3.5b, the active and reactive power output for the DC/AC stage of each ring converter is shown. It can be seen that the control system is able to follow the references with a fast response but with some overshoot (as it can be seen in the zoom area). It also has deviations from the reference values when loads are connected in the corresponding feeder, causing some oscillations, but the control is able to fast recovery.

In Fig. 3.5c and 3.5d, the active and reactive power delivered by the HPEC to each of the 400 Vac feeders is shown. Since they operate in slack mode, they have to provide all the feeder net consumption (sum of all loads consumption, considering ring converters as loads, since they operate in P,Q mode) to maintain an stiff voltage value. The response in all the changes of demand is really fast.

The effect of a single-phase load is shown in Fig. 3.5d. In there, a single-phase load is connected to Feeder #2. As expected, a pulsating power demand at twice the

fundamental frequency appears in the active and reactive power components delivered by the HPEC.

Fig. 3.6 shows HPEC voltage output in dq reference frame. Despite the transient oscillations when the load changes, the control is able to keep the voltage really close to the reference value ($230\sqrt{2} = 325$ V for the d-axis; 0 V for the q-axis).

Besides that, it can be seen that the connection of single-phase loads causes a 100 Hz oscillation to appear in the steady-state. This is the -50 Hz negative-sequence component resulting from the unbalanced single-phase load (when represented in the synchronous reference frame, it is seen as 100 Hz).

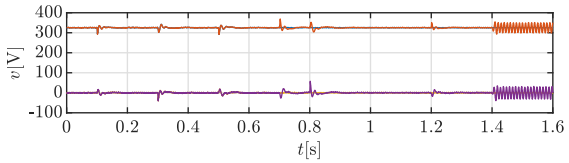

Figure 3.6: HPEC voltage output in dq reference frame for both AC feeders (red and red, d voltage for Feeder #1 and #2; yellow and purple, q voltage for Feeder #1 and #2).

Fig. 3.7 shows the voltage output in the two 48 Vdc internal building grids. It can be seen that the DC/DC stage of the ring converters is able to control the voltage. The sags appearing when a new load is connected is recovered in short-time and the variation of the voltage value is acceptable, considering that they appear after a sudden connection of a load of 80% of the rated power of that converter.

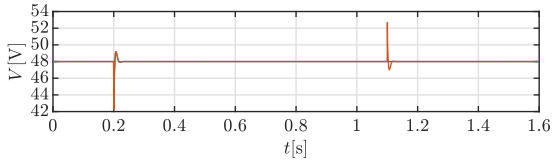

Figure 3.7: DC/DC stage of ring converters voltage output for both 48 Vdc internal building grids (red and red, voltage for Building block #1 and#2).

Fig. 3.8 shows the 750 Vdc link voltage in both ring converters. The control is able to control the voltage properly, only with some deviations (not very significant) when changes in the power reference for the corresponding ring converter are applied. It also has some ripple but the peak-to-peak value is really small compared with the rated voltage.

In Fig. 3.9, voltage in both 375 Vdc buses is shown. It can be seen that the balancing control implemented at the NPC is able to keep both buses stable, even though a small voltage sag can be seen when a load of 12 kW is connected to each AC feeder (at t = 0.5 s).

In Fig. 3.10a, current output of HPEC converter connected to Feeder #2 is shown. When there is no unbalance in the load, the current has low THD (1.31 %), close to

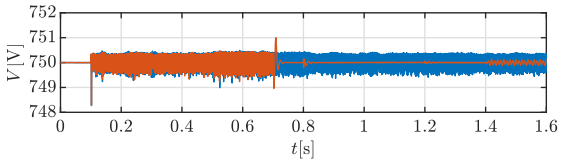

Figure 3.8: Voltage after intermediate step for boosting from 375 to 750 Vdc to connect DC bus with AC feeder (red and red, voltage for Building block #1 and#2).

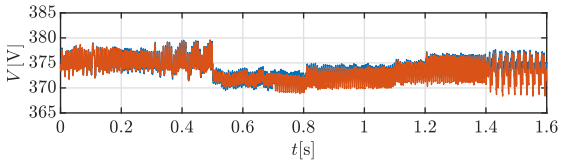

Figure 3.9: Voltage in both DC buses (red and red, voltage in DC bus 1 and 2).

a perfect balanced-sinusoidal system, with negligible current flowing through neutral conductor. Once the single-phase load is connected, an important amount of current is flowing through the neutral conductor and currents no longer form a balanced system.

The consequences of this load unbalance can be seen in Fig. 3.10b. At t = 1.4 s (single-phase load connection) the current in the inverter becomes unbalanced due to the negative sequence component that appear in the voltage controlled by the HPEC.

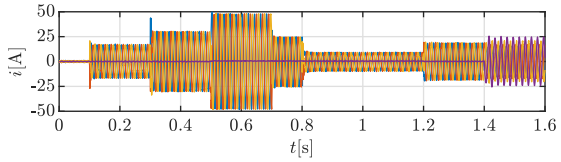

(a) HPEC connected to Feeder #2.

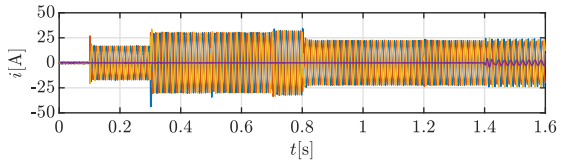

(b) Ring converter connected to Feeder #2.

Figure 3.10: Current output (red, red, yellow and purple for phase a, b, c and n).

3.4.2 Disconnection of one HPEC AC outputs

In this second simulation, the situation with the HPEC AC output disconnected from one of the feeders (#2) is studied. In this case, the ring converter connected to that feeder should act in slack mode to keep the voltage level of the feeder to the

reference value. Apart from that, only one of the two HPEC NPC converters can contribute to balance the DC buses.

The simulation conditions (reference changes, load connections,...) are the same than in the previous simualation except for those regarding to Feeder #2. The sequence in that feeder now is: connection of a 10 kvar capacitive load at t = 0.1 s; connection of a 6 kW resistive load at t = 0.3 s; reduction of resistive load from 6 to 2 kW at t = 0.8 s; reduction of capactive load from 10 to 4 kvar at t = 1 s and connection of a 2 kW single-phase resistive load at t = 1.4 s.

In Fig. 3.11 the active and reactive power delivered by ring converter #2 are shown. Since this converter acts as the slack bus of this feeder now, it has to provide all the power demand to keep the voltage level of the feeder. The effect of the single-phase load can be appreciated as a pulsating power demand with twice the fundamental frequency.

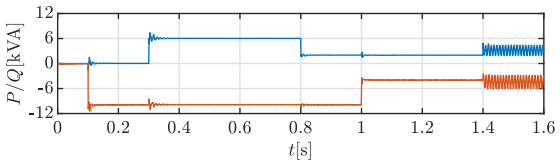

Figure 3.11: Ring converter in building block #2 active and reactive power output (red, active power; red, reactive power).

In Fig. 3.12 voltages in both AC feeders are shown. It can be seen that oscillations in Feeder #2 are much more significant. This is normal since the converter acting as a slack for that feeder has less rated power so it is more affected by the sudden changes in power demand.

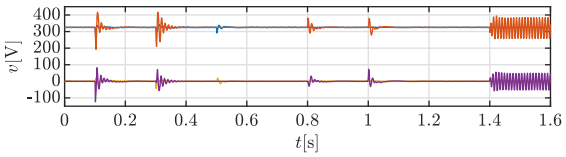

Figure 3.12: HPEC voltage output in dq reference frame for both AC feeders (red and red, d voltage for Feeder #1 and #2; yellow and purple, q voltage for Feeder #1 and #2).

In Fig. 3.13 voltage in both DC buses is shown. It can be seen that even though only one of the HPEC NPC converters is now working for balancing the DC buses, it is able to maintain a value close to the reference level with almost no difference between the voltage of each bus.

Finally, in Fig. 3.14 current output for the ring converter connected to Feeder #2 is shown. The system is able to provide balanced currents with low distortion, except when the single-phase load is connected (the currents become clearly unbalanced and current flows through neutral conductor because of this single-phase load).

The results related to Feeder #1 and the 48 Vdc internal building grid were really similar to the ones obtained in the previous simulation, so they are not shown.

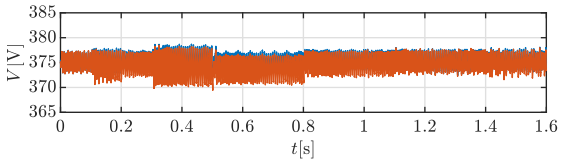

Figure 3.13: Voltage in both DC buses (red and red, voltage in DC bus 1 and 2).

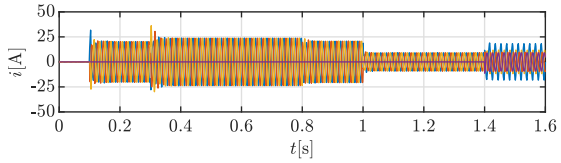

Figure 3.14: Ring converter current output (red, red, yellow and purple for phase a, b, c and n).

3.5 Conclusion

In this chapter, a novel architecture for a hybrid DC/AC microgrid, including the power converters topologies and control has been analyzed. A technique for the balancing of the two DC feeders, provided by the 3-level multiport converter has been successfully tested. Different operating modes, having reliability as the key design factor have been stated. Two of them have been successfully demonstrated by simulation. In all the cases a good dynamic response under balanced/unbalanced load has been demonstrated.

Only solutions found in the literature have been considered for this first stage of the demand, although the proposed topology will be used as reference for the contributions in the thesis. However, only the part of the microgrid involved in each contribution will be considered and not always the complete structure of the microgrid.

Next chapters will will include collaborative operation for the different converters, considering droop control instead of slack mode. Secondary control will be studied too to exploit the different alternatives provided by the mesh structures inside the microgrid. Control with no specific islanded detection for the transition between operation modes is intended to be considered too.

References

[3.1] P. García, P. Arboleya, B. Mohamed, and A. A. C. Vega, "Implementation of a Hybrid Distributed/Centralized Real-Time Monitoring System for a DC/AC Microgrid With Energy Storage Capabilities," *IEEE Transactions on Industrial Informatics*, vol. 12, no. 5, pp. 1900–1909, Oct. 2016.

[3.2] Á. Navarro-Rodríguez, P. García, R. Georgious, and J. García, "Adaptive Active Power Sharing Techniques for DC and AC Voltage Control in a Hybrid DC/AC Microgrid," *IEEE Transactions on Industry Applications*, vol. 55, no. 2, pp. 1106–1116, Mar. 2019.

[3.3] C. Wang, Z. Li, X. Si, and H. Xin, "Control of neutral-point voltage in three-phase four-wire three-level NPC inverter based on the disassembly of zero level," *CPSS Transactions on Power Electronics and Applications*, vol. 3, no. 3, pp. 213–222, Sep. 2018.

Chapter 4

Flexible secondary control for droop control strategies in hybrid AC/DC microgrids

4.1 Introduction

As explained in the state of the art, droop techniques are clearly the most widespread solution for primary control. As a drawback, they present a voltage (and frequency in most of the AC applications) deviation from nominal values, with a compromise between power sharing accuracy and this deviation. If droop coefficients are chosen to achieve an accurate power sharing, this would result in higher deviations from nominal values.

In DC, P/V droop is used, as well as for AC in LV distribution levels, due to the fact that the grid impedance in LV networks is mainly resistive [4.1]. Normally, a Q/f droop is then used for reactive power sharing, although reactive power sharing is normally less critical. Thus avoiding the necessity of this droop could be of interest, especially due to the fact that frequency is often a source of instabilities.

Secondary control is used to eliminate the deviations caused by the droop. Secondary control typically relies on integrators or PI regulators to eliminate the voltage deviation, both in AC [4.2] and DC [4.3]. This requires periodic calculations for the integrator to operate, gradually reducing the error every cycle.

This type of secondary control is normally divided into three categories: centralized, distributed and decentralized [4.4]. Centralized control has a central controller with communications with the control of each involved converter and measures the area voltage in order to eliminate its deviation, normally with a PI regulator, sending

the same reference to all the converters. Distributed control operates in a similar way, but the PI regulator is implemented on each converter control, but with communication among all the converters. Decentralized control does not require neither central controller nor communications.

Secondary control can also be used to achieve accurate power sharing in P/V droops [4.5]. However, these methods add some extra complexity to the secondary control, with an extra control loop with a PI regulator and they are not suitable for decentralized secondary control, since they use some communication between PECs.

This thesis shows a proposal of a hybrid AC/DC microgrid and the coordinated control of all the involved converters (AC/DC and DC/DC). The coordinated control is composed of a P/V droop control for the primary control and a novel approach for the secondary control. The proposed secondary control is applied to P/V droop, but it could be easily adapted to $P/f + Q/V$ droop or other alternatives.

The proposed secondary control is able to eliminate the voltage deviation due to droop controllers based on a single calculation of the optimum power flow, shifting the droop characteristic of each converter according to voltage and power obtained from the power flow. This proposed solution has two main advantages compared to the aforementioned ones (centralized, distributed and decentralized).

Firstly, it is capable of achieving power sharing accuracy for the P/V droop without extra complexity. Besides, it is very flexible allowing any power sharing among the converters to be implemented, meanwhile the solutions in centralized and distributed controls to correct power sharing are designed for achieving one specific power sharing among the converters. The capability of the proposed secondary control to implement any power sharing allows the integration of any criteria for the power sharing, providing a high flexibility. For example, the secondary control can be combined with optimization problems, like the use of ESS contributing to the grid stability working in droop mode, meanwhile the secondary control optimizes its use in terms of cost. The proposed secondary control is also able to easily fix any reactive AC power sharing criteria, including active power loads that can contribute to the reactive power production if interfaced with a PEC, without additional droop control (Q/f droop is not required).

Secondly, since it requires only one calculation for operating point optimization, it has lower communication requirements and higher robustness against communication delays, high communication latency or loss of transmitted data compared to distributed and, especially, centralized secondary controls [4.5]. Decentralized secondary control does not require communications. However, considering communications infrastructure is always needed for coordination of distributed generation units during black start and microgrid real-time monitoring [4.4], the possibility of total lack of communications given by decentralized secondary control is not critical.

These differences are summarized in Table 4.1.

This secondary control also provides the capability of compensating the voltage drop of virtual impedance techniques at the steady-state, [4.6–4.10]. As stated in [4.6] the

Table 4.1: Comparison between the proposed secondary control and alternatives in the literature based on PI regulators: centralized (CSC), distributed (DISC) and decentralized (DESC) secondary control [4.4].

	Proposed	CSC	DISC	DESC
Central controller required	Yes	Yes	No	No
Communication required	Yes	Yes	Yes	No
Robustness against data loss, comm. delays or high latency	High	Low	Medium	Complete
Power sharing accuracy	Yes	Extra PI	Extra PI	No
Flexibility to change the power sharing	Yes	No	No	No

virtual impedance can be used for many different purposes like active stabilization and disturbance rejection or, in the case of droop controllers, for making the line impedance more resistive/inductive, depending on the type of droop used.

However, this virtual impedance causes a voltage drop, that makes the effective total voltage drop greater, since the real output voltage of the converter is lower than the reference one (assuming that the converter is producing power). Some solutions can be found in the literature, like the use of a high-pass filter in the virtual impedance [4.7] to eliminate the effect of the virtual impedance in steady-state. However, this solution is only valid when the use of the virtual impedance is needed because of its transient effect (like the active stabilization aforementioned). When the steady-state effects of the virtual impedance are also needed, this solution is not valid. It is shown in this thesis, how the designed secondary control can take into account this virtual impedance and eliminate the effect of its voltage droop. This is done by adding extra nodes to the optimum power flow calculation and selecting the physical connection of the converter, after the virtual impedance, to be the node having 1 p.u. voltage.

This chapter is organized as follows. In Section 4.2, the proposed hybrid microgrid topology and the power converters topologies are described. In Section 4.3, the control strategy is explained, with a special focus in the proposed secondary control. Sections 4.4 and 4.5 show the simulation and experimental results respectively. Section 4.6 shows an example of how to integrate the proposed secondary control with optimization problems. Section 4.7 presents the conclusions.

During the rest of the chapter only reference to the voltage deviation will be mentioned, since only the P/V droop will be considered, although the proposed method is adaptable to droops involving frequency.

4.2 Proposed Microgrid Topology

The hybrid AC/DC network architecture [4.11] proposed in this thesis is shown in Fig. 3.2, where the SST connection is simplified as a DC/DC converter in voltage

control mode using QVC, as shown in Fig. 2.12. The AC feeders and the DC lines (both ±375 and 48 Vdc) are modeled as purely resistive lines, assuming a maximum voltage drop of 5 % at the end of the line for the rated power.

Being the lines purely resistive, if reactive power loads and references were set to 0, the AC part of the microgrid could be studied as if it was DC. Being the q-axis component of the voltages equal to 0 in steady-state, the d-axis component is equivalent to a DC voltage for the calculations.

For this reason, the analysis done in the chapter starts with the DC case, since it is also a simplified study of the AC part. From DC solution, some modifications are done in order to include reactive power and possible non purely resistive impedances in the calculations for the AC complete solution.

As explained in Section 4.1, virtual impedance can be used for different purposes, introducing an induced voltage drop. Virtual impedance is used for the converters in the AC feeders and is taken into account too for compensating its voltage drop.

4.3 Coordinated control

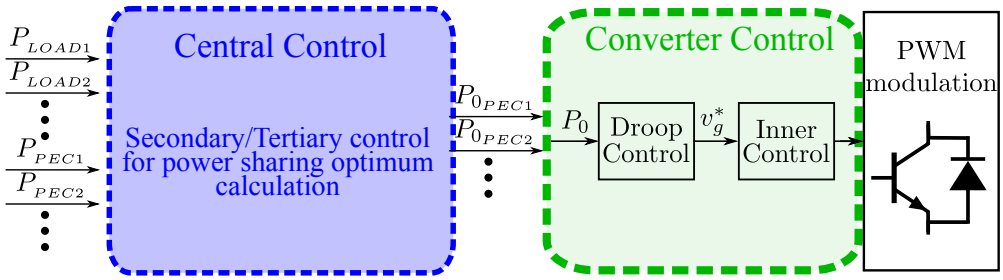

Figure 4.1: General control diagram for converters in the 48 Vdc network. P_{LOADi} is the aggregate load connected to node i, P_{PECi} is the measured power output of the converter and P_{0PECi} is the power offset for the converter connected to node i.

As explained in the previous sections, the coordinate control of the power converters is done with a P/V droop control, both for the AC feeders and the 48 Vdc network.

This droop control acts as a primary control, making possible that all the converters which can deliver power, either coming from the connection to the main AC grid or from ESS, contribute to the power sharing.

The power sharing at the primary control level is achieved without requiring communication among the power converters. However, communication among them is used for upper level control, namely secondary and tertiary control for enhanced power sharing.

4.3.1 ±375 Vdc grid control

In the ±375 Vdc grid, the SST provides connection to the mains supply and to the central ESS. In the present thesis, this is simplified as a DC/DC converter connected to a DC voltage source since the focus is in the hybrid microgrid. This DC/DC converter controls the voltage difference between the positive and the negative bus (750 Vdc) as shown in Fig. 3.1.

Header PEC (HPEC), connected to node 1, is in charge of the DC bus balancing [4.12], due to its neutral point clamped topology, assuring that the voltage in both buses is 375 Vdc (one positive and one negative with respect to the neutral).

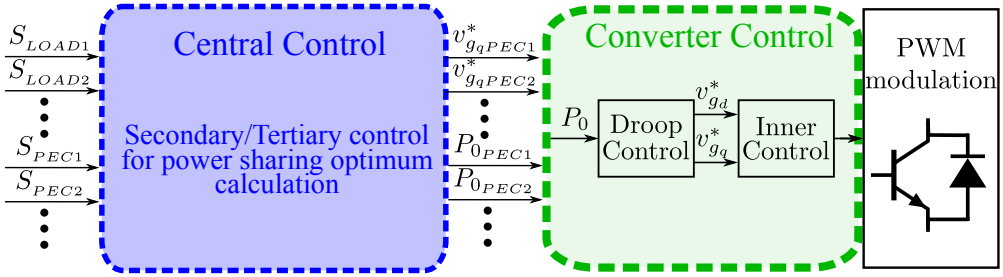

Figure 4.2: General control diagram for converters in the AC feeder. S_{LOADi} is the aggregate load connected to node i, S_{PECi} is the measured power output of the converter and P_{0PECi} is the active power offset for the converter connected to node i. Both S_{LOADi} and S_{PECi} mean P and Q are required (being $S = P + jQ$).

These two buses are distributed so that loads can be directly connected to these DC buses. They can be connected to either bus, so loads can be strongly unbalanced. Apart from that, Ring#1 PEC is connected to +375 Vdc bus and Ring#2 PEC is connected to −375 Vdc bus.

These two buses are distributed, so that loads can be directly connected to them. Due to the different loads at each of the buses (Ring#1 PEC at the +375 Vdc and Ring#2 PEC to the −375 Vdc bus respectively), they could become strongly unbalanced thus making much needed the balancing control implemented at the HPEC.

4.3.2 48 Vdc network control

In Fig. 4.1 the control diagram for the 48 Vdc grid is shown. The control system is separated into two main blocks; 1) the internal converter control and 2) the central control. The internal control implements the voltage control using a quadratic approximation [4.13] and relies on a cascaded-architecture with an internal current controller. The references for the voltage control are given by a P/V droop. Connected to the internal control, the central controller provides the power offsets (P_0) to the different converters based on the secondary control, whose effect is to shift the droop curve.

The droop characteristic equation is shown in (4.1), where V is the resulting voltage from the droop control; m_V is the droop coefficient; P, the measured power output; P_0 and V_0 the offset power and voltage (equal to rated voltage in the study case).

$$V = m_V(P_0 - P) + V_0 \tag{4.1}$$

4.3.3 400 Vac feeder control

The general control scheme for the converters in the AC feeder is shown in Fig. 4.2, which is completely equivalent to the 48 Vdc network case except from the decomposition in the synchronous dq reference frame. Details about cross-coupling and feedforward terms shown in [4.13] are omitted due to space constraints. The reference for the d axis voltage control is given by a P/V droop. The central controller plays the same role as in the case of the 48 Vdc network. In here, also the q-axis voltage reference is provided to the different converters.

4.3.4 Secondary control

For the secondary control, a new strategy has been used. The idea consists on changing the P/V droop characteristics of each converter, by modifying the offset power P_0 in (4.1), so that they match the desired solution. For this explanation, the chosen solution is to have a power sharing among the droop controlled converters proportional to each converter power rating and a voltage of 1 p.u. at a given specific node. In general, the output of the main converter of the corresponding grid is used as the 1 p.u. reference.

This secondary control is applied to the 400 Vac feeder and the 48 Vdc network. Considering the proposed grid topology in each case, the loads at each node and the reference output power of each converter, the power flow can be calculated, resulting in the voltage profile at each node considering one of the nodes is set to 1 p.u. For these calculations, only droop-controlled converters participating in the power sharing are taken into account as controllable converters, the remaining are seen as bidirectional loads.

The reference power output of each converter can be selected with different criteria. For the calculations presented hereafter, the sharing among the converters is proportional to the power rating of each converter. If any other criteria is used, this method could easily accommodate to it without further implications.

In this case, as shown in Fig. 3.1 both studied cases, the AC feeder or the 48 Vdc network, are radial networks, without rings inside. This eases the calculation of the power flow. Different grid topologies, including mesh and ring networks could also be considered, thus increasing the computational burden for the power flow calculations [4.14].

Calculations required for DC and AC case are very similar, but DC case is presented before, since it is simpler and more straightforward because it does not include reactive power. After presenting both cases, the possibility of including virtual impedance is presented too.

4.3.4.1 Secondary control in DC

Knowing the reference power and the voltage at each converter, obtained from the power flow, P_0 can be calculated so that the droop characteristic, whose equation is shown in (4.1), meets the requirements. The method is explained using network shown in Fig. 4.3.

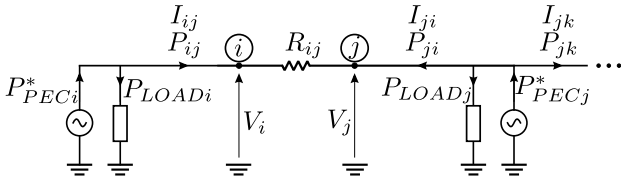

Figure 4.3: Power flow diagram. P_{ij} (I_{ij}) is the power (current) flow from node i to j, P_{ji} (I_{ji}) from j to i and P_{jk} (I_{jk}) from j to k. P^*_{PECi}: reference power for converter at node i, P_{LOADi}: total connected load in that node and V_i: voltage in that node. R_{ij} is the equivalent impedance connecting node i and j (it should include both wires impedance in DC).

In Fig. C.1 (Appendix C), the flowchart for the method is shown. Starting assuming no losses, an iteration of the power flow algorithm is done. Total load, including losses, is summed and its share between the droop-controlled converters is calculated, assuming they are proportional to their rated power. Although this criteria has been chosen for the power sharing, any other could be used, making that this method can be used for tertiary control too. The power flow solution for that power sharing is calculated. This might include more than one iteration, as power flow algorithms are normally iterative. A stop criterion for the power flow is checked to decide if more iterations are required. An analysis of power flow convergence is shown later in Subsection 4.3.5. When the power flow calculation finishes, the proposed control calculates the offset power for each converter, P_{0PECi}, so that the droop curve of each converter matches the solution from the power flow, as shown in Fig. 4.4. This offset power is sent back to the converter control to modify their droop (see Fig. 4.1).

4.3.4.2 Secondary control in AC

The implementation of the secondary control in AC resembles the DC case but power (S, in this case), voltage, impedance (Z) and currents are complex magnitudes.

Fig. C.2 show the corresponding calculations for AC. The only significant difference is in the last step. Since the droop is applied to P and V_d (real part of S and V complex vectors), the equation for calculating the active power offset relies on the real

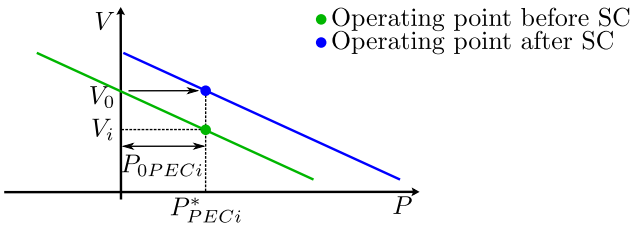

Figure 4.4: Droop curve shift for fulfilling power flow solution. Green: base case with $P_{0PECi} = 0$ and blue: final solution.

V component (d-axis), while imaginary (q-axis) component is sent as a direct reference to the converters.

Apart from the differences due to the use of complex variables in AC, the voltage drop for the DC case is calculated as $RI = R\frac{P}{V}$ meanwhile in AC it is $ZI = Z\frac{\overline{S}}{\sqrt{3}\cdot\overline{V}}$, because the AC network is three-phase.

4.3.4.3 Secondary control including virtual impedance

As explained in Section 4.2, when virtual impedance is considered, the proposed secondary control allows for the compensation of the induced voltage drop. The compensation is achieved by adding virtual nodes to the power flow calculation shown in Fig. C.2.

In the example shown in Fig. C.2, voltage in physical node 1, V_1, is selected to be 1 p.u., obtaining this voltage at the physical connection of the PEC to that node. A virtual node is added before the virtual impedance voltage drop. This can be seen in Fig. 4.5 with an example of a circuit including virtual impedance, $Z_{vir,i}$. The voltage in the node in which each converter is physically connected is V_i and it is the one obtained from the power flow explained before. The voltage before the virtual impedance, $V_{PEC,i}$, can be obtained from V_i, adding the voltage drop in the virtual impedance. This calculation is shown in (4.2).

$$V_{PECi} = V_i + Z_{vir,i}\frac{\overline{S^*_{PECi}}}{\sqrt{3}\cdot\overline{V_i}} \tag{4.2}$$

The calculated V_{PECi} should be used instead of V_i in last step in Fig. C.2. So in Fig. 4.5, the virtual voltage $V_{PEC,i}$ is the one used for the droop calculations, while V_i is the reference voltage for the physical node, achieving $V_1 = 1$ p.u.

The calculation presented in (4.2) is done considering a three-phase AC system, while extension to the DC case only requires to use real instead of complex variables for the impedance and power and without the $1/\sqrt{3}$ factor for the voltage drop calculation.

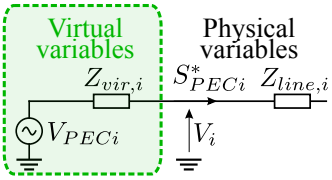

Figure 4.5: Example of circuit including virtual impedance. V_i is the voltage at the physical connection of the corresponding PEC and $Z_{line,i}$, the coupling impedance. $Z_{vir,i}$ is the virtual impedance of the PEC and $V_{PEC,i}$, the (virtual) voltage before the voltage drop in the virtual impedance.

4.3.5 Power flow calculation convergence

The proposed secondary control is based on the calculation of the power flow solution. This power flow solution is an iterative process, thus an stop criteria is needed. It can be both a fixed number of iterations, a threshold for the difference of some calculated variables between consecutive iterations of the algorithm or a combination of both.

In this case, for analyzing the convergence of the method, the difference between the losses obtained at the end of the iteration (step 6 in Fig. C.1 and Fig. C.2) and the ones calculated in the step before is used. When this difference is below a threshold, the solution can be considered precise enough.

The convergence time can be improved if instead of assuming zero losses in the first iteration, the losses in the situation prior to secondary control execution are used. This can be done simply by using the power production of each converter (P_{PECi}) for calculating the total needed production in step 2 for the first iteration. Using P_{PECi} instead of P_{LOADi} for this first iteration will make the losses of the previous situation to be included. Although P_{PECi} is not required for the rest of the algorithm, this is normally an information that the central controller can easily have.

To check the convergence, a simulation for the proposed microgrid is performed. The results are shown in Table 4.2, where DC and AC cases are shown. The effect of using P_{PEC} for the first iteration is also included. It can be seen that the power flow converges in few steps, leading to an error below 0.8 ‰ in all the cases. The use of P_{PEC} for the initialization reduces the error of this first iteration, although no difference is seen from the second one onwards. For this thesis, due to the fast convergence of the power flow solution, a fixed and small number of iterations (5) has been chosen for the stop criterion, although comparing the difference between losses calculated in consecutive iterations with a threshold would work similarly.

4.4 Simulation results

The presented solution has been simulated using MATLAB/Simulink. The complete hybrid microgrid is depicted in Fig. 3.1, including node numbers and code colors

Table 4.2: Error for different number of iterations (n) of the algorithm. First and second columns: DC network; third and fourth: AC feeder. First and third columns: results using P_{LOADi} for the first iteration; second and fourth columns: using P_{PECi}.

n	DC: P_{LOAD}	DC: P_{PEC}	AC: P_{LOAD}	AC: P_{PEC}
1	0.78 ‰	0.17 ‰	2.34 ‰	0.21 ‰
2	0.17 ‰	0.17 ‰	0.18 ‰	0.18 ‰
3	0.17 ‰	0.17 ‰	0.18 ‰	0.18 ‰

for the different sections: green for AC feeder; purple for 48 Vdc network; black for the ±375 Vdc buses.

In the AC feeder, nodes 1 and 2 are connected to the HPEC and to the AC output of the Ring PEC (RPEC-AC) respectively, by implementing a droop control strategy. Loads are connected to nodes 2 and 3, where the TPEC works in PQ mode. Both the HPEC and RPEC-AC have a virtual impedance of 5 times the line impedance in the AC feeder.

In the 48 Vdc, the DC output of the RPEC (RPEC-DC) works in droop control, together with a 1.25 kW DC/DC converter operating as a distributed Energy Storage System (dESS-PEC). Constant Power Load (CPL) is connected to node 2. In the ±375 Vdc grid, HPEC connected to node 1, is in charge of the DC bus balancing [4.12], while loads are connected both to 2 (positive DC bus) and 3 (negative DC bus). The details of the rated power of each converter and droop coefficients (m_V) are shown in Table 4.3. Droop low pass filter (LPF) cutoff frequency are also shown. Cutoff frequency for DC is small because of the low communication speed in the experimental setup.

Table 4.3: Converter Parameters.

Converter	HPEC	RPEC-AC	RPEC-DC	dESS-PEC
S_n / P_n	7.5 kVA	3.75 kVA	1.25 kW	1.25 kW
k_p (p.u.)	0.1	0.1	0.05	0.05
f_c (Hz)	50	50	0.5	0.5

The simulation results are shown in Fig. 4.6. Before vertical lines marked with 1 (for 48 Vdc network) and 2 (AC feeder), the secondary control algorithm is disabled, thus having only a classical droop control. It can be seen the operation of the droop, which has two undesirable results. First, the power sharing among the converters is different from the desired one. In the AC feeder, the active power sharing ratio should be 2 : 1, proportional to their power ratings, but it is not even though the droop coefficient has the same per unit value. In AC, for the reactive power no droop is being used, so the sharing without secondary control is not controlled anyway

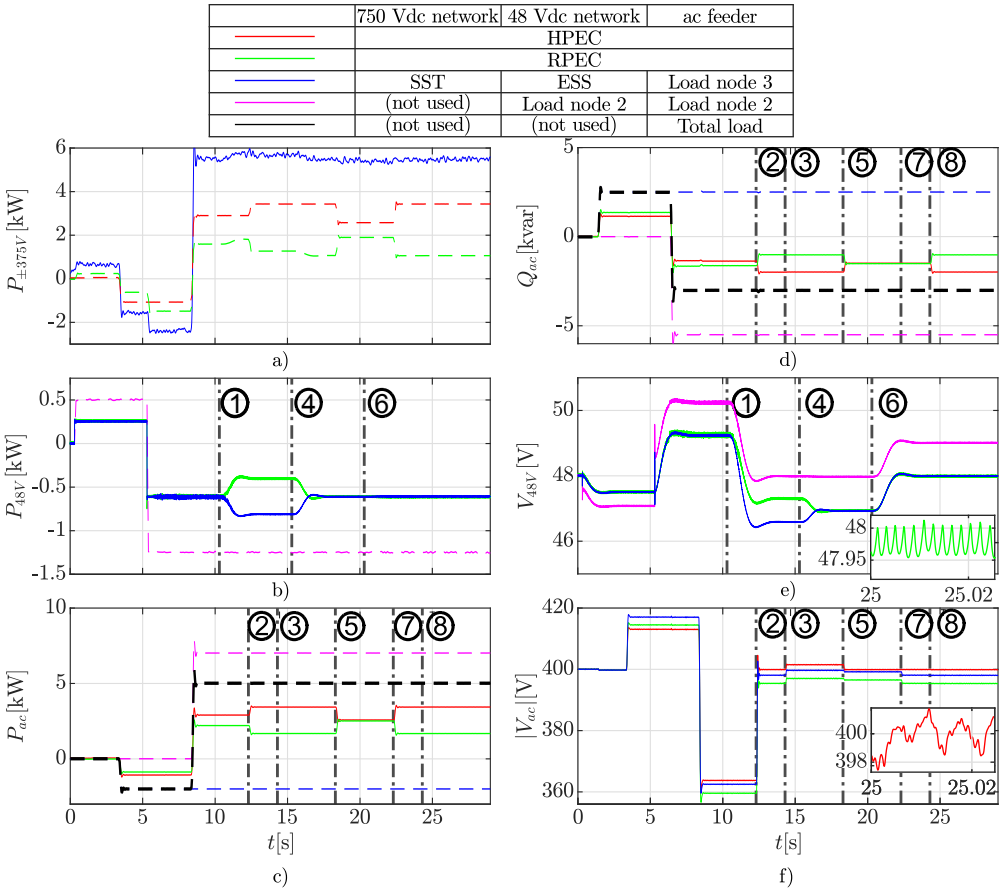

Figure 4.6: Simulation results. a) Power in ±375 Vdc network. b) Power in 48 Vdc network. c) Active power in AC feeder. d) Reactive power in AC feeder. e) Voltage in 48 Vdc network, with a zoom to show the ripple. f) Filtered voltage in AC feeder (10 Hz LPF), zoom to show the ripple with unfiltered signal. For active/reactive power plots, load consumption is shown in dashed lines and converter production is shown in continuous lines. RPEC and HPEC are considered loads in the ±375 Vdc network.

and depends only on grid configuration and load demand. In the 48 Vdc network it matches the desired 1 : 1 ratio because the network is completely symmetrical. Second, the droop causes a voltage deviation, making all the nodes far from 1 pu value (48 Vdc and 400 Vac respectively). Once the secondary control is enabled, these two effects are eliminated. Proposed secondary control algorithm is performed once per vertical line in Fig. 4.6. The sequence of power reference changes in the simulation are the following:

- At $t = 0.3$ s, power reference for CPL in node 2 of 48 Vdc network is set to 0.5 kW.

- At $t = 1.3$ s, reactive power reference for CPL in node 3 of AC feeder is set to 2.5 kvar.
- At $t = 3.3$ s, active power reference for CPL in node 3 of AC feeder is set to -2 kW.
- At $t = 5.3$ s, power reference for CPL in node 2 of 48 Vdc network is set to -1.25 kW.
- At $t = 6.3$ s, reactive power reference for CPL in node 2 of AC feeder is set to -5.5 kvar.
- At $t = 8.3$ s, active power reference for CPL in node 2 of AC feeder is set to 7 kW.

Sequence of changes in secondary control references (power sharing ratio and node with 1 pu voltage) is listed below. Changes in power sharing ratio are carried out by modifying step 3 in Fig. C.1 and C.2, with the desired proportion (the algorithm presented the case as if the desired proportion was proportional to the rated power).

1. At $t = 10.3$ s, secondary control is activated in 48 Vdc network, setting node 2 (load) to have 1 pu voltage (48 V) and sharing of power production among the two droop-controlled power electronic converters with $2:1$ ratio (ESS and RPEC output).
2. At $t = 12.3$ s, secondary control is activated in AC feeder, setting node 1 (HPEC) to have 1 pu voltage (400 V) and sharing of active and reactive power production among the two droop-controlled power electronic converters (HPEC and RPEC) proportional to their rated power ($2:1$ ratio). Is is worth to remark that 1 pu voltage is achieved in node 1, which has a converter with virtual impedance, being able to compensate the voltage drop in this virtual impedance.
3. At $t = 14.3$ s, 1 pu voltage reference in AC feeder is changed to node 3. The change is reversed in next update of secondary control in AC feeder.
4. At $t = 15.3$ s, power sharing ratio of converters in 48 Vdc network is set to $1:1$ ratio.
5. At $t = 18.3$ s, active and reactive power sharing ratio of converters in AC feeder is set to $1:1$ ratio.
6. At $t = 20.3$ s, 1 pu voltage reference in 48 Vdc network is changed to node 1 (RPEC output).
7. At $t = 22.3$ s, active power sharing ratio of converters in AC feeder is set back to $2:1$ ratio.
8. At $t = 24.3$ s, reactive power sharing ratio of converters in AC feeder is set back to $2:1$ ratio.

4.4.1 Effect of grid parameters estimation mismatch

In order to check the accuracy of the method under parameter estimation mismatches, a simulation has been performed forcing these estimation errors. The simulation has been done both for the AC feeder and the 48 Vdc network, in the same configuration explained previously in this section. For both cases, the network situation, including load consumptions, is exactly the same that there is at the end of the simulation shown in Fig. 4.6, only changing the situation of the load consumption in the AC feeder, where two nodes have loads. Apart from that, the only difference is in the performance of the secondary control.

The results are shown in Fig. 4.7. A variable error between ±30 % has been included in the grid resistances estimation used for the secondary control. Both the AC feeder and the 48 Vdc network have the same configuration: R_{12} and R_{23} connecting nodes 1, 2 and 3 in a radial manner. For all the cases, the proposed variation for R_{12} estimation error has been added. Three different cases are considered for R_{23}: no error and same magnitude error as in R_{12} with same or opposite sign.

As commented before, the AC loads at the end of simulation shown in Fig. 4.6 are connected to nodes 2 and 3. In order to check which load configuration is more sensitive to estimation mismatches, two simulations have been performed. The sum of both loads in Fig. 4.6 is connected to one of the nodes. The results for the load connected to node 2 are the same for the three cases for the R_{23} error. This is a logical result, since if no load or PEC is connected to node 3, current does not flow in R_{23} and the estimation of that value has no effect. Similar results are obtained when all the load connected to node 3 with no error in R_{23}. Since no PEC is connected to node 3, for the secondary control, R_{23} and the node 3 load can be considered as a load connected to node 2, with a small variability due to the R_{23} losses. If the value of R_{23} is estimated properly, the losses are calculated exactly and there is no significant difference with the case where the load is directly connected to node 2.

In the results for the 48 Vdc network, it can be seen that the worst scenario is when the estimation has errors with opposite sign being the effect almost negligible for both power and voltage when the same sign estimation error occurs. The maximum deviation in absolute value is: 13.85 % for P_1 and P_3 and 0.35 % for v_1.

For the AC feeder, the worst scenario for active power and voltage occurs for same and opposite sign error respectively. For the reactive power, all the cases show almost identical results. The maximum deviation in absolute value is: 2.80 % for P_2, 5.51 % for Q_2 and 0.18 % for v_1. The errors for P_1 and Q_1 are in all cases smaller than those for P_2 and Q_2.

It can be seen that in all cases the error in terms of voltage is really small, meanwhile for all the other variables (active/reactive power), the maximum error in all the scenarios is 13.85 %. Considering that this error occurs for a very significant error (30 %), the method can be considered robust enough referring to parameters estimation mismatches. Taking into account that these important errors only appear for power sharing and not for voltage magnitude, the method can be considered as a valid

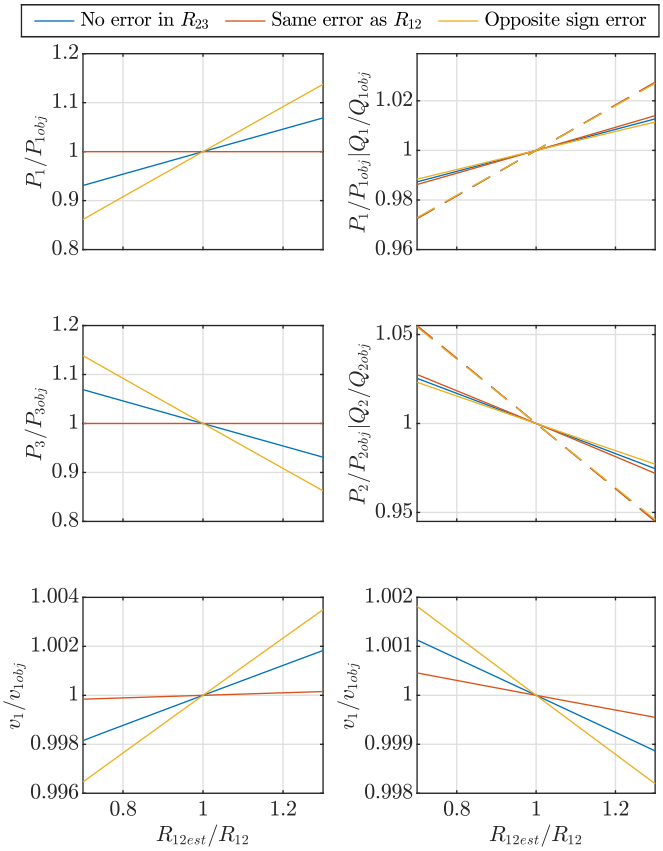

Figure 4.7: Estimation mismatch simulation results. Left column: DC network; right column: AC feeder. First two rows indicate both PECs power production compared to the reference one for the secondary control (two PECs in each case, DC and AC; for AC, dashed lines indicate reactive power). Third row indicates deviation in the voltage in the node whose voltage is chosen to have 1 pu voltage.

alternative to other secondary control alternatives, which normally correct the voltage deviation of the droop controllers but have no capability of varying the power sharing in a flexible way.

The application of this secondary control is thought for microgrids, coordinated by a central controller with access to measurements in the different nodes. In this scenario, a proper estimation of all the required parameters can be worthy for multiple reasons, including an optimum operation of the microgrid (like losses optimization). Online parameter estimation methods are found in the literature and some of them use the same variables required for the secondary control, to perform an inverse power flow problem, estimating impedances from current and voltages in the different nodes [4.15]. This strategy for online parameter estimation is very convenient to be run in parallel with the secondary control, when offline estimation is not possible.

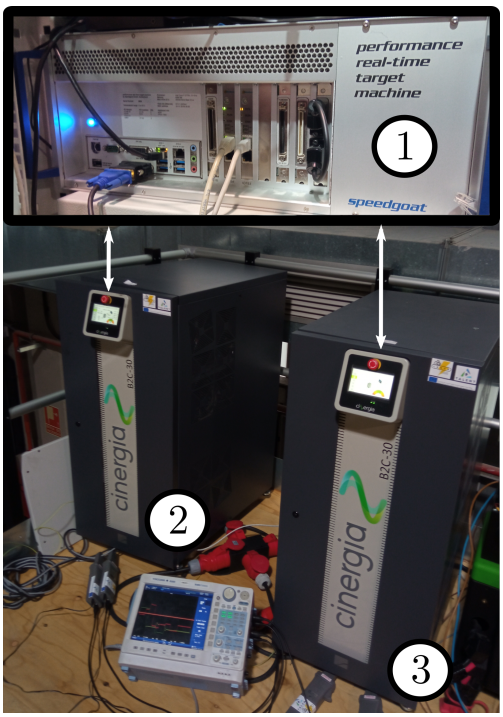

Figure 4.8: Setup for experimental validation. Speedgoat real-time simulator (1): implements the AC feeder and controls two Cinergia B2C-30 converters, one for the 750 Vdc network (2) and the other for the 48 Vdc network (3). White arrows indicate Modbus/TCP communication channels for the real-time simulator to send references to and receive measurements from the converters.

4.5 Experimental validation

The proposed method has been validated experimentally with the setup shown in Fig 4.8. The microgrid shown in Fig. 3.1 is partially implemented. The ±375 Vdc grid is simplified to a unipolar 750 Vdc bus and only one AC feeder and one 48 Vdc network are used.

The two Cinergia B2C-30 converters shown in Fig. 4.8 are controlled through the Speedgoat real-time simulation platform, sending power references to outputs operating as constant power loads and voltage references to the droop-controlled converters, with the droop calculations inside the real-time simulator. Real measurements from the converter outputs, using Modbus/TCP communications, are fed back for the calculation inside Speedgoat. The AC feeder is implemented in the real-time simulator. The interconnection of the AC feeder and the 48 Vdc network with the 750 Vdc bus is implemented as a load in the 750 Vdc, whose demand is updated with the production of the corresponding converter: RPEC in 48 Vdc network (real power measurements)

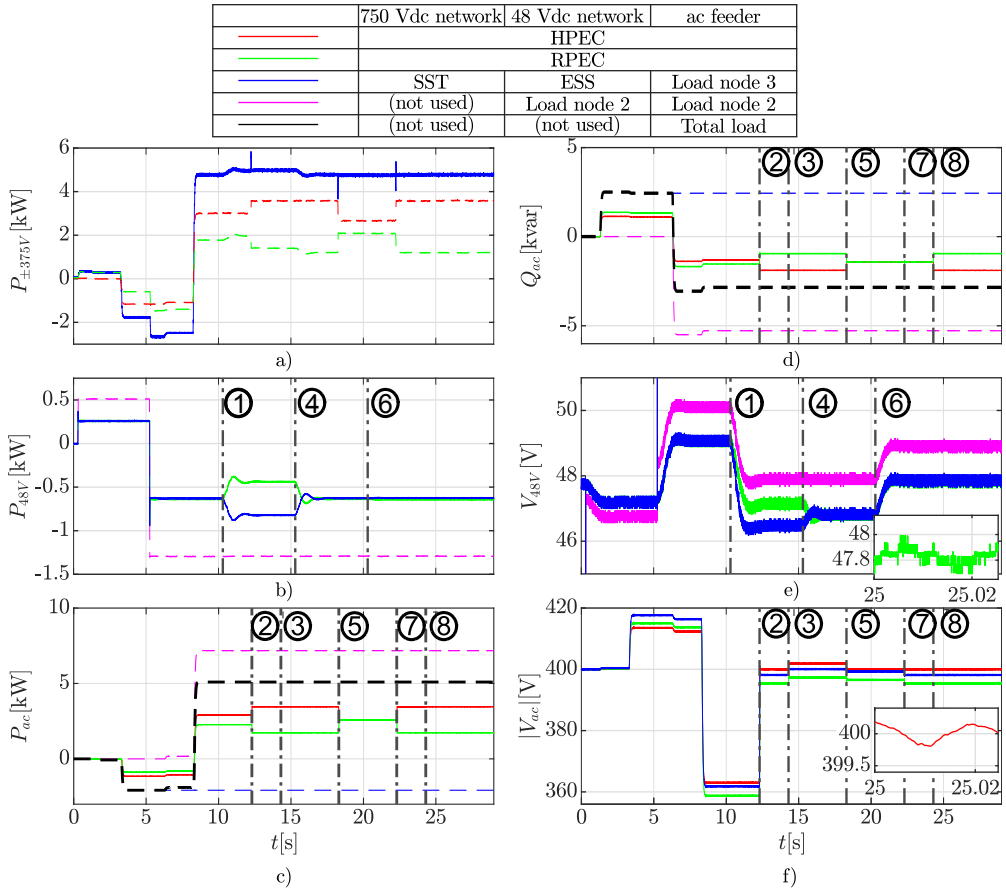

Figure 4.9: Experimental results. a) Power in ±375 Vdc network. b) Power in 48 Vdc network. c) Active power in AC feeder. d) Reactive power in AC feeder. e) Voltage in 48 Vdc network, with a zoom to show the ripple. f) Voltage in AC feeder, with a zoom to show the ripple. For active/reactive power plots, load consumption is shown in dashed lines and converter production is shown in continuous lines. RPEC and HPEC are considered loads in the ±375 Vdc network.

and RPEC and HPEC in the AC feeder (real-time simulation data).

In Fig. 4.9, the results from the experimental setup validation are shown, with the same sequence of changes in load and secondary control references explained in Section 4.4 for the Simulink simulation. It can be seen that the experimental results agree with the simulated ones, thus validating the proposed secondary control.

4.6 Combination with power sharing optimization criteria

In the previous sections, the power sharing was determined as a constant proportion between both converters production.

In this section, this power sharing selection is chosen for optimizing a given cost function, thus illustrating the versatility of the proposed method. This application belongs to the tertiary control layer, since economic variables are also considered. Besides that, commands from the main grid tertiary control layer could be easy incorporated too. This does not require a slower regulator, as normally required when secondary and tertiary control are based on PI regulators.

Optimization problems including power flows normally require iterative processes, for the same reason power flow solutions are normally iterative. For this reason, the iterative process explained in Fig. C.1 can be used for calculating the optimization problem at the same time the power flow is being solved, being the study case for the optimization problem is in DC.

The cost function to be minimized is (4.3), where P_l are the losses in the network, P_{load} and P_b the power consumed by the load and the battery used as ESS, C_0 is the cost of energy at the moment of optimization and C_1 is the expected cost of energy in a future moment of the day.

$$C = C_0 P_g - C_1 P_b = C_0(P_l + P_b + P_{load}) - C_1 P_b \tag{4.3}$$

This cost function represents the cost per unit time of the consumed energy, $C_0 P_g = C_0(P_l + P_b + P_{load})$, minus the expected revenues from the energy stored in the battery for a future sell, $C_1 P_b$. P_b is considered with load convention, so a positive value means it is being charged, thus having a positive future revenues (reducing cost). The two costs, C_0 and C_1 are thought for tariff with hour discrimination, in which the price for peak and valley moments of the day can be known and used for estimating the possible earns with battery usage.

For the losses calculation, only the losses in the lines in the 48 Vdc network are considered, neglecting the losses in PEC and assuming RPEC is directly connected to the grid (so grid variables from now on indicate RPEC output). The same procedure applied here can be used for more complete losses calculation, as it can be used including other parts of the grid, but it complicates the problem and is considered as future work out of the scope of the thesis.

Losses can be calculated as shown in (4.4), where R is the resistance of the line connecting to the load, indicating subscript g and b grid or battery side, and V is the voltage at grid/battery PEC output.

$$P_l = \frac{R_b}{V_b^2} P_b^2 + \frac{R_g}{V_g^2} P_g^2 = \frac{R_b}{V_b^2}(1-r)^2 P_T^2 + \frac{R_g}{V_g^2} r^2 P_T^2 \tag{4.4}$$

Where P_g and P_b are expressed as a function of total production that the battery and grid must share ($P_T = P_l + P_{load}$): $P_g = rP_T$ and $P_b = (1-r)P_T$, being r the proportion of this demand supplied by the grid (P_{TOTAL} in Fig. C.1).

Substituting (4.4) in (4.3) and differentiating with respect to r, the condition for the minimum of the function is obtained, as shown in (4.5).

$$C' = C_0 \frac{2R_b}{V_b^2}(r-1)P_T^2 + C_0 \frac{2R_g}{V_g^2} r P_T^2 - (C_1 - C_0)P_T = 0 \tag{4.5}$$

Defining $B_x = 2P_T R_x / V_x^2$ (where x can be either g or b) and $C_{diff} = (C_1 - C_0)/C_0$, and dividing by $P_T C_0$ condition shown in (4.5) can be rewritten as shown in (4.6).

$$B_b(r-1) + B_g r - C_{diff} = 0 \rightarrow r = \frac{B_b + C_{diff}}{B_b + B_g} \tag{4.6}$$

Losses (used for obtaining P_T) and voltage in each node are assumed as constants for this calculation, although they depend on the solution. This means that the optimum will not be found with one single calculation, since the value of r, whose optimum is being calculated, is affecting the parameters needed for its calculation. However, this optimum calculation can be added to the iterative nature of power flow algorithms (used in the proposed secondary control), recalculating the constants for every iteration. This process does not fully guarantee the convergence to the optimum point, but it will be seen that the deviation is generally small.

Due to this possible deviation from the optimum solution, and in order to make the method valid for more complex problems in which an expression for r might be impossible to obtain, another method for the optimum calculation is proposed. For this method, the iterations of the secondary control are done with steps in the different values of r, doing a sweep among the possible values. For every value of r, the cost function is calculated. If the calculated cost is minimum compared to the previous ones, the value of the cost function is updated to be used in the next steps. The value of the outputs of the secondary control (P_{0PECi} and, in the case of AC, also $v^*_{g_{qPECi}}$) is also stored to avoid recalculating the power flow after the sweep has finished. The explained Sweep Optimization method is shown in Fig. C.3.

Since the steps in r are going to be relatively small, it can be considered that the power flow for each value of r converges in only one iteration, because it is starting from a similar solution. This way, the iterative nature of the power flow solution and the optimization problem is combined.

These two alternatives, which from now on are going to be referred as Optimum Calculation and Sweep Optimization, are going to be compared in order to check its effectiveness.

4.6.1 Simulation validation

The cost optimization problem presented in this thesis is a simple case with a reduced version of the grid infrastructure presented in Fig. 3.1, with only one of the 48 Vdc networks.

The configuration of the study case network is the same used for Sections 4.4 and 4.5, with the RPEC connected to node 1, the ESS to node 3 and load to node 2. The load consumption is fixed to 1.25 kW for all the results presented here.

For validating the proposed optimization algorithm, a simulation has been carried out. For the same network situation, the value of r is varied in order to obtain the cost function for a given range. This is similar to the Sweep Optimization, but in this case the secondary control shown in Fig. C.1 is executed for each value of r during the simulation, the output of the secondary control for each value is sent to the converters and the cost function is obtained with the real values of P_g and P_b measured in the simulation. In the Sweep Optimization, the cost function is calculated in the algorithm, and the secondary control reference is sent to the PEC only when the sweep is finished.

The results can be seen in Fig. 4.10. Minimum values of cost (C) for each curve and corresponding value of r, together with values obtained with both methods for optimization are shown in Table 4.4. For Sweep Optimization a step of 1% for r has been used.

It can be seen that the error in the value of r for the Optimum Calculation is significant in some cases (up to 11.3 % in the worst case). Meanwhile, for Sweep Optimization, is always smaller than 1 %. However, in both methods, the obtained cost is really close to the actual minimum, with a maximum deviation of 0.5 % and less than 0.1 % for Optimum Calculation and Sweep Optimization respectively.

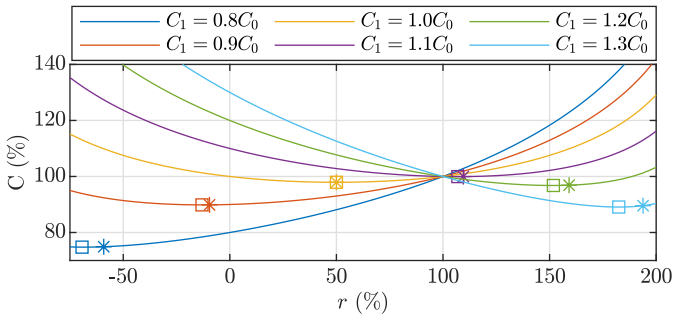

Figure 4.10: Simulation results for different values of future energy cost (C_1) with respect to present value (C_0). r is the proportion of total load supplied by the grid connection and C is the expected cost compared to the case with no ESS (r = 100 %). Asterisks mark the position of the Optimum Calculation, meanwhile squares mark the minimum obtained by Sweep Optimization. Minimum values of C and r for each curve and values obtained with both methods for optimization are shown in Table 4.4.

Table 4.4: Minimum value of cost function for different values of C_1 and values obtained by both methods for optimization.

	Real value		Opt. Calculation		Sweep Opt.	
	r (%)	C (%)	r (%)	C (%)	r (%)	C (%)
$C_1 = 0.8C_0$	−68.5	74.8	−59.1	74.9	−69.3	74.8
$C_1 = 0.9C_0$	−12.5	89.9	−9.5	89.9	−13.1	89.9
$C_1 = 1.0C_0$	50.0	97.9	50.0	97.9	50.0	97.9
$C_1 = 1.1C_0$	106.9	100.0	109.5	100.0	107.0	100.0
$C_1 = 1.2C_0$	151.3	96.8	159.1	96.9	151.8	96.8
$C_1 = 1.3C_0$	182.5	89.1	193.8	89.6	182.5	89.1

This indicates that the deviation in the Optimum Calculation from the actual minimum is not important, since although it can be significant in terms of the chosen r value, the obtained cost is close to the minimum one. This makes that this method is more suitable for the proposed scenario, since less iterations will be required. However, the validity of the Sweep Optimization method is also proved as an alternative for more complex problems in which the value of r minimizing the cost function cannot be directly calculated. This could be the case of considering efficiency curves in PECs, more than one interconnected networks or multi-variable optimization (for example, if the sharing is between three instead of two PECs, adding one degree of freedom).

4.7 Conclusions

This chapter has shown an approach for the sharing control scheme in a hybrid AC/DC microgrid. The proposed method enables the different converters to contribute to the power sharing by a droop control implementation. The proposed secondary control eliminates the voltage deviation due to the droop characteristic. It also eliminates the voltage droop caused by the virtual impedance.

The proposed secondary control applied in AC allows the reactive power sharing among the converters with no specific droop control. This also eases the integration of converters which are seen as active power loads, but whose reactive power can be controlled to contribute to the sharing, as it can be the case of a converter feeding a load or a STATCOM. All the droop-controlled converters can achieve any active/reactive power production, thus achieving different power sharing scenarios, including shared conditions among the different networks in the hybrid microgrid if the secondary control of these different networks is coordinated. The proposed method has been validated both in simulation and in an experimental setup.

The secondary control is also flexible, allowing to introduce any criteria for the power flow solution, like any method for deciding the power sharing among the converters (minimize losses, saturation of converters for its rated power,...) or the possibility of easily changing the node whose voltage is fixed to 1 p.u. This flexibility has been

proven with a simplified optimization problem, using the secondary control combined to the minimization of a cost function, with an application that can be considered in the teriary control layer. Two alternatives were presented and validated through simulation, both with similar performance in terms of obtained cost. Cost Optimization approach is more suitable for simpler problems that can be solved analytically, whereas Sweep Optimization is a better option under complex scenarios. This could be the case of considering efficiency curves in PECs, more than one interconnected networks or multi-variable optimization.

References

[4.1] J. Rocabert, A. Luna, F. Blaabjerg, and P. Rodríguez, "Control of Power Converters in AC Microgrids," *IEEE Transactions on Power Electronics*, vol. 27, no. 11, pp. 4734–4749, Nov. 2012.

[4.2] J. W. Simpson-Porco, Q. Shafiee, F. Dörfler, J. C. Vasquez, J. M. Guerrero, and F. Bullo, "Secondary Frequency and Voltage Control of Islanded Microgrids via Distributed Averaging," *IEEE Transactions on Industrial Electronics*, vol. 62, no. 11, pp. 7025–7038, 2015.

[4.3] P. Wang, X. Lu, X. Yang, W. Wang, and D. Xu, "An Improved Distributed Secondary Control Method for DC Microgrids With Enhanced Dynamic Current Sharing Performance," *IEEE Transactions on Power Electronics*, vol. 31, no. 9, pp. 6658–6673, 2016.

[4.4] Y. Khayat, Q. Shafiee, R. Heydari, M. Naderi, T. Dragičević, J. W. Simpson-Porco, F. Dörfler, M. Fathi, F. Blaabjerg, J. M. Guerrero, and H. Bevrani, "On the Secondary Control Architectures of AC Microgrids: An Overview," *IEEE Transactions on Power Electronics*, vol. 35, no. 6, pp. 6482–6500, 2020.

[4.5] Q. Shafiee, J. M. Guerrero, and J. C. Vasquez, "Distributed Secondary Control for Islanded Microgrids—A Novel Approach," *IEEE Transactions on Power Electronics*, vol. 29, no. 2, pp. 1018–1031, 2014.

[4.6] X. Wang, Y. W. Li, F. Blaabjerg, and P. C. Loh, "Virtual-Impedance-Based Control for Voltage-Source and Current-Source Converters," *IEEE Transactions on Power Electronics*, vol. 30, no. 12, pp. 7019–7037, 2015.

[4.7] Z. Liu, S. Ouyang, and W. Bao, "An improved droop control based on complex virtual impedance in medium voltage micro-grid," in *2013 IEEE PES Asia-Pacific Power and Energy Engineering Conference (APPEEC)*, 2013, pp. 1–6.

[4.8] A. Micallef, M. Apap, C. Spiteri-Staines, and J. M. Guerrero, "Performance comparison for virtual impedance techniques used in droop controlled islanded microgrids," in *2016 International Symposium on Power Electronics, Electrical Drives, Automation and Motion (SPEEDAM)*, Jun. 2016, pp. 695–700.

[4.9] A. D. Paquette and D. M. Divan, "Virtual Impedance Current Limiting for Inverters in Microgrids With Synchronous Generators," *IEEE Transactions on Industry Applications*, vol. 51, no. 2, pp. 1630–1638, 2015.

[4.10] J. He and Y. W. Li, "Analysis, Design, and Implementation of Virtual Impedance for Power Electronics Interfaced Distributed Generation," *IEEE Transactions on Industry Applications*, vol. 47, no. 6, pp. 2525–2538, 2011.

[4.11] C. Gómez-Aleixandre, A. Navarro-Rodríguez, G. Villa, C. Blanco, and P. García, "Sharing Control Strategies for a Hybrid 48V/375V/400Vac AC/DC Microgrid," in *2020 IEEE Energy Conversion Congress and Exposition (ECCE)*, 2020, pp. 3900–3907.

[4.12] C. Wang, Z. Li, X. Si, and H. Xin, "Control of neutral-point voltage in three-phase four-wire three-level NPC inverter based on the disassembly of zero level," *CPSS Transactions on Power Electronics and Applications*, vol. 3, no. 3, pp. 213–222, Sep. 2018.

[4.13] Á. Navarro-Rodríguez, P. García, R. Georgious, and J. García, "Adaptive Active Power Sharing Techniques for DC and AC Voltage Control in a Hybrid DC/AC Microgrid," *IEEE Transactions on Industry Applications*, vol. 55, no. 2, pp. 1106–1116, Mar. 2019.

[4.14] R. Chai, B. Zhang, J. Dou, Z. Hao, and T. Zheng, "Unified Power Flow Algorithm Based on the NR Method for Hybrid AC/DC Grids Incorporating VSCs," *IEEE Transactions on Power Systems*, vol. 31, no. 6, pp. 4310–4318, 2016.

[4.15] K. Gajula, L. K. Marepalli, X. Yao, and L. Herrera, "Recursive Least Squares and Adaptive Kalman Filter based State and Parameter Estimation for Series Arc Fault Detection on DC Microgrids," *IEEE Journal of Emerging and Selected Topics in Power Electronics*, pp. 1–1, 2021.

Chapter 5

Analysis of a complex-valued droop method in AC microgrids with complete steady-state frequency compensation using *dq*-Decomposition

5.1 Introduction

Droop control is a widely used and well-known solution for power sharing without requiring communication among converters. There are two main variants depending on line impedance: $P/f + Q/V$ for inductive lines or $P/V + Q/f$ for resistive lines [5.1]. In both cases, three considerations are done to obtain the final droop: 1) lines are assumed to be purely inductive/resistive and the other term of the impedance is neglected; 2) phase angle difference, δ, between voltages is small, thus allowing to approximate $\sin\delta \approx \delta$ and $\cos\delta \approx 1$; and 3) frequency and voltage show a steady-state deviation with respect to the rated conditions.

Neglecting resistive/inductive part can worsen the operation when R/X ratio is close to 1, thus the coupling term effect becoming significant. Virtual impedance can be included to increase the resistive/inductive component of the line impedance [5.2, 5.3], but this would cause some unwanted side effects, like the voltage loss capability in the control system due to this virtual impedance.

Some solutions can be found in the literature that consider the coupling terms. In [5.4, 5.5], an orthogonal linear rotational transformation matrix (obtained from impedance phase angle) is used to rotate P and Q so that the coupling terms are avoided. In [5.6, 5.7], the coupling terms are compensated. This is done by introducing in the formula for each droop output (voltage magnitude and frequency) a term to compensate the effect of the deviation of the other output with respect to the nominal value.

However, these two methods still include the $\sin\delta = \delta$ and $\cos\delta = 1$ approximation and use the frequency as one of the droop outputs, thus having a frequency deviation in steady-state. Other solutions are found in the literature using angle instead of frequency as one of the droop outputs [5.7–5.10], thus eliminating frequency deviation.

The method proposed in this chapter also eliminates frequency deviation and takes into account the coupling effect by the orthogonal linear rotational transformation matrix.

Additionally, due to the decomposition of the voltage in the dq-reference frame, it does not require any trigonometric function simplification, thus obtaining a compact formulation using complex numbers and the d- and q- voltage components as the droop outputs. This approach is appealing when dq-composition is used in the control system or for state-space modeling, in which the angle variation introduces a new variable (the angle) with non-linear terms [5.11].

This chapter is organized as follows. In Section 5.2, the proposed droop control is explained. In Section 5.3, the voltage deviation caused by the proposed droop is compared with the $P/f + Q/V$ and $P/V + Q/f$ alternatives. In Section 5.4, the grid used for the study is presented. Section 5.5 shows the simulation results. Firstly, the proposed droop is compared with $P/f + Q/V$ and $P/V + Q/f$ approaches, assuming perfect knowledge of impedance phase angle for orthogonal linear rotational transformation matrix. Then, the effect of mismatches in the estimation of impedance phase angle is analyzed by simulating the different scenarios with significant estimation errors. Finally, section 5.6 presents the conclusions.

5.2 Proposed Droop Control

A diagram for the power flow in a generic line with arbitrary impedance is shown in Fig. 5.1. Classical $P/f + Q/V$ and $P/V + Q/f$ droops are obtained from the same diagram assuming $R \approx 0$ and $X \approx 0$, respectively.

In this thesis, polar expressions for voltage and impedance are replaced with their equivalent rectangular equations in the synchronous dq-reference frame and complex numbers are used for the calculations.

For the following calculations, steady-state situation is considered. However, the outputs of the droop are used as references for instantaneous values of the voltage.

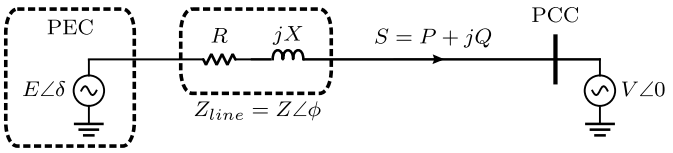

Figure 5.1: Power flow diagram in a line impedance connecting a power electronic converter to the grid.

Apparent power calculation is shown in (5.1), being S, P and Q apparent, active and reactive power flowing to the Point of Common Coupling (PCC) from the power electronic converter (PEC); V_{dq} the voltage vector at the PCC and $\overline{I_{dq}}$ the conjugate of the line current vector. For this thesis, power invariant transformation is considered ($k = 1$). Still the following discussion is equivalent for the magnitude invariant transformation, leading to equivalent expressions.

$$S = P + jQ = kV_{dq}\overline{I_{dq}} \xrightarrow{k=1} S = P + jQ = V_{dq}\overline{I_{dq}} \tag{5.1}$$

The conjugate of the current can be obtained as shown in (5.2) from the converter output voltage, E_{dq}, the voltage at the PCC, V_{dq}, and the impedance of the line connecting them. The voltage expression at the PCC can be simplified as $V_{dq} = V_d = V$, since the d-axis is used as the phase reference.

$$\overline{I_{dq}} = \overline{\left(\frac{E_{dq} - V_{dq}}{Z_{line}}\right)} = \frac{\overline{E_d + jE_q - V}}{\overline{R + jX}} = \frac{E_d - V - jE_q}{R - jX} \tag{5.2}$$

Substituting (5.2) in (5.1), (5.3) is obtained.

$$S = V\frac{E_d - V - jE_q}{R - jX} = V\frac{(E_d - V - jE_q)(R + jX)}{(R - jX)(R + jX)} \tag{5.3}$$

Taking into account that $(R - jX)(R + jX) = Z^2$, the expression shown in (5.4) is obtained, being Z the modulus of the complex impedance.

$$S = \frac{V}{Z^2}(E_d - V - jE_q)(R + jX) \tag{5.4}$$

Splitting (5.4) into real and imaginary components, the expressions for active and reactive power are obtained, as shown in (5.5a) and (5.5b).

$$P = \frac{V}{Z^2}(E_d R + E_q X - VR) \tag{5.5a}$$

$$Q = \frac{V}{Z^2}(E_d X - E_q R - VX) \tag{5.5b}$$

From (5.5a) and (5.5b), $P/f + Q/V$ and $P/V + Q/f$ droops can be obtained by substituting $E_d = E\cos\delta \approx E$ and $E_q = E\sin\delta \approx E\delta$ and considering $R \approx 0$ or $X \approx 0$ respectively, as shown in (5.6) and (5.7).

$$P \approx \frac{V}{X} E\delta \rightarrow \omega - \omega_0 = -m_\omega (P - P_0) \tag{5.6a}$$

$$Q \approx \frac{V}{X}(E - V) \rightarrow E - E_0 = -m_V (Q - Q_0) \tag{5.6b}$$

$$P \approx \frac{V}{R}(E - V) \rightarrow E - E_0 = -m_V (P - P_0) \tag{5.7a}$$

$$Q \approx -\frac{V}{R} E\delta \rightarrow \omega - \omega_0 = m_\omega (Q - Q_0) \tag{5.7b}$$

Equations (5.5a) and (5.5b) can be expressed in matrix form as shown in (5.8).

$$\begin{pmatrix} P \\ Q \end{pmatrix} = \frac{V}{Z^2} \left[\begin{pmatrix} R & X \\ X & -R \end{pmatrix} \begin{pmatrix} E_d \\ E_q \end{pmatrix} - \begin{pmatrix} R \\ X \end{pmatrix} V \right] \tag{5.8}$$

From (5.8), applying a droop coefficient, m_V, to relate E_d and E_q variations with both P and Q, the proposed droop formula shown in (5.9) is obtained in the same way $P/f + Q/V$ and $P/V + Q/f$ are obtained in (5.6) and (5.7) [5.1].

$$\begin{pmatrix} E_d - E_{d0} \\ E_q - E_{q0} \end{pmatrix} = -m_V \begin{pmatrix} R/Z & X/Z \\ X/Z & -R/Z \end{pmatrix} \begin{pmatrix} P - P_0 \\ Q - Q_0 \end{pmatrix} \tag{5.9}$$

This complex-valued droop, obtained from the dq-decomposition, takes into account the coupling between P and Q. It only requires knowledge on the lines R/X ratio and, by applying the droop to both voltage components instead of magnitude and frequency, enables no frequency deviation in steady-state.

Considering the analyzed droop alternatives, the complete converter control scheme is shown in Fig. 5.2, together with the different droop controllers. $P/f + Q/V$ and $P/V + Q/f$ use the structure shown in Fig. 2.17a and 2.17b. Details about cross-coupling and feedforward terms, normalization and nonlinear compensation can be seen in [5.12].

5.3 Complex-valued Droop Steady-state behaviour

Applying a droop related to voltage components will cause a voltage deviation with respect to nominal value in the same way $P/f + Q/V$ and $P/V + Q/f$ alternatives have deviations with respect to frequency and voltage.

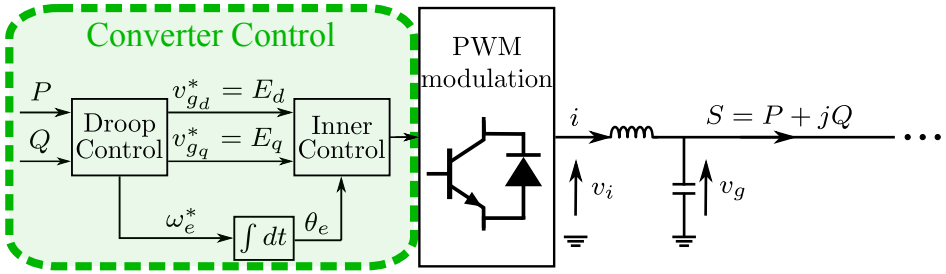

(a) Converter control.

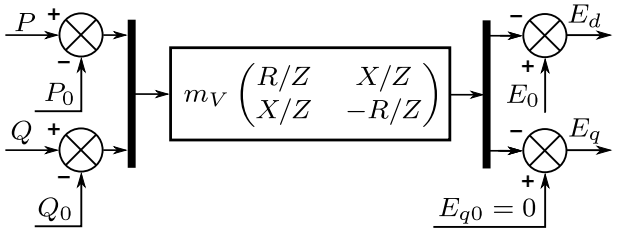

(b) Complex-valued droop.

Figure 5.2: Control scheme including the different droop control methods. For $P/f + Q/V$ and $P/V + Q/f$ droops, E_q reference is set to 0 and for complex-valued droop ω reference is set to 100π rad/s (50 Hz). For the simulations in this chapter $P_0 = Q_0 = 0$.

In our proposal, since both components, E_d and E_q, are involved in the droop calculation, the combined effect of both components shall be analyzed to check if the impact in the voltage deviation is increased.

Considering $\Delta S = \Delta P + j\Delta Q = (P - P_0) + j(Q - Q_0)$ and $\Delta E = \Delta E_d + j\Delta E_q = (E_d - E_{d0}) + j(E_q - E_{q0})$, (5.9) can be rewritten as shown in (5.10).

$$\begin{pmatrix} \Delta E_d \\ \Delta E_q \end{pmatrix} = -m_V \begin{pmatrix} R/Z & X/Z \\ X/Z & -R/Z \end{pmatrix} \begin{pmatrix} \Delta P \\ \Delta Q \end{pmatrix} \tag{5.10}$$

For this demonstration, the PEC is considered to be producing an apparent power S, expressed as a complex number $S = P + jQ = |S|\angle\alpha$. For the simulations in this chapter $P_0 = Q_0 = 0$, resulting in $\Delta S = S$. As shown in Fig. 5.2b, $E_{q0} = 0$ and $E_{d0} = E_0$, that for simplicity will be expressed in per unit as $E_{d0} = 1$ pu. Expressing the matrix equation (5.10) in complex number form, (5.11) is obtained.

$$\Delta E = -m_V(R/Z + jX/Z)(P - jQ) \tag{5.11}$$

$(R/Z + jX/Z)$ is a complex number with modulus 1 and angle ϕ and $(P - jQ)$ is the conjugate of the apparent power. Thus (5.11) can be rewritten as shown in (5.12).

$$\Delta E = -m_V|S|(\cos\beta + j\sin\beta) \tag{5.12}$$

Being β the difference between line impedance phase angle and apparent power angle $(\phi - \alpha)$.

With (5.12) and taking into account that $E_{d0} = 1$ pu, the voltage amplitude is obtained using the formula shown in (5.13).

$$|E| = \sqrt{(1 - m_V|S|\cos\beta)^2 + (m_V|S|\sin\beta)^2} \tag{5.13}$$

Taking into account $\cos^2\beta + \sin^2\beta = 1$, the deviation in the voltage amplitude due to the proposed droop method with respect to nominal value (1 pu) is obtained by (5.14).

$$\Delta|E| = \sqrt{1 - 2m_V|S|\cos\beta + m_V^2|S|^2} - 1 \tag{5.14}$$

It is important to remark here, that for all the demonstration before, the values used for impedance phase angle are not the real ones, but the ones assumed by the droop control. This means that in case that the estimation of the angle is not correct, the one that is involved in the voltage deviation effect is the estimated one (from now on ϕ_{est}).

The maximum deviation in voltage amplitude is obtained for $\beta = 0°$ and $\beta = 180°$, as shown in (5.15a) and (5.15b) respectively.

$$\Delta|E| = \sqrt{1 - 2m_V|S| + m_V^2|S|^2} - 1 = -m_V|S| \tag{5.15a}$$

$$\Delta|E| = \sqrt{1 + 2m_V|S| + m_V^2|S|^2} - 1 = m_V|S| \tag{5.15b}$$

Where m_V is expressed in per unit value. This means that the maximum value for the voltage amplitude deviation is obtained when line impedance and apparent power have opposite phases while the minimum occurs when they have the same phase. In both cases, the deviation from nominal value is $m_V|S|$ in absolute value.

Taking this into account, it can be concluded that the range for voltage amplitude deviation obtained from the proposed droop control for $|S| \leq S_n$ is $(-m_V, m_V)$, as it happens in the $P/f + Q/V$ and $P/V + Q/f$ droops for a variation of P or Q in the range of $(-S_n, S_n)$.

In the case of $P/f + Q/V$ and $P/V + Q/f$ droops, voltage amplitude is only a function of active/reactive power with a linear relationship, meanwhile in the proposed complex-valued droop it depends on both apparent power magnitude and phase difference with respect to line impedance phase angle.

This relationship for a fix value of $|S|$ is shown in Fig. 5.3, with the deviation in output voltage for different values of apparent power angle (α).

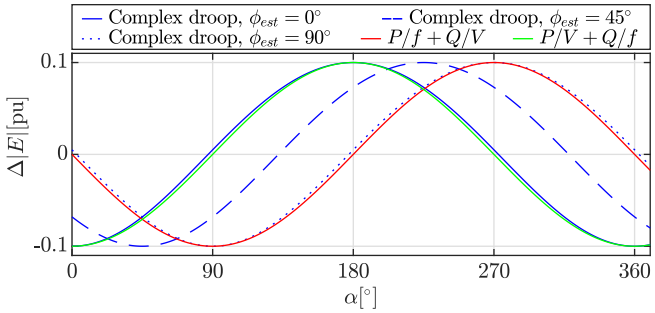

Figure 5.3: Variation of voltage amplitude output for different values of α (apparent power angle), with $m_V|S|$= 0.1 pu.

The curve for $P/f + Q/V$ and $P/V + Q/f$ is a sinusoidal waveform, since for a fixed value of $|S|$, the relationship of voltage variation with respect to the angle is $\Delta|E| = -m_V Q = -m_V|S|\sin(\alpha)$ and $\Delta|E| = -m_V P = -m_V|S|\cos(\alpha)$ respectively.

Since the dependence of voltage deviation with respect to angle shown in (5.14) is for angle $\beta = \phi_{est} - \alpha$, different values of ϕ_{est} result in a horizontal displacement of the corresponding $\Delta|E|$ vs α curve. When $\phi_{est} = 0°$, the corresponding curve (continuous blue) is very similar to the one corresponding to $P/V + Q/f$ droop (continuous green), meanwhile when $\phi_{est} = 90°$ the corresponding curve (dotted blue) is very similar to the one corresponding to $P/f + Q/V$ droop (continuous red). In all the cases, the maximum voltage deviation is $m_V|S|$.

In Fig. 5.4, the variation of voltage amplitude for different values of apparent power is shown for different values of angle β. Taking into account that β was defined as $\phi_{est} - \alpha$ for the proposed droop, it can be defined in a similar way for $P/f + Q/V$ and $P/V + Q/f$ considering $\phi_{est} = 90°$ and $\phi_{est} = 0°$ respectively, since these droops are obtained assuming purely inductive/resistive lines for obtaining the droop equations. With this notation, $\beta = 0°$ implies apparent power to be purely reactive for $P/f + Q/V$ droop and active for $P/V + Q/f$, producing the maximum voltage deviation. For Fig. 5.4, S is considered as a real number, having the apparent power the direction of β and being positive for power production and negative for consumption.

5.3.1 Droop coefficient selection

Taking into account that the proposed droop produces a voltage output variation range equal to the one obtained for $P/f + Q/V$ and $P/V + Q/f$ droops, the starting point for selection of the droop coefficient can be done taking into account the maximum variation of the voltage output.

For this chapter, a maximum voltage deviation of 2.5 % is used for droop coefficient selection. Due to the similar effect in voltage deviation produced by the classical droops ($P/f + Q/V$ and $P/V + Q/f$) and the proposed complex-valued alternative, the same

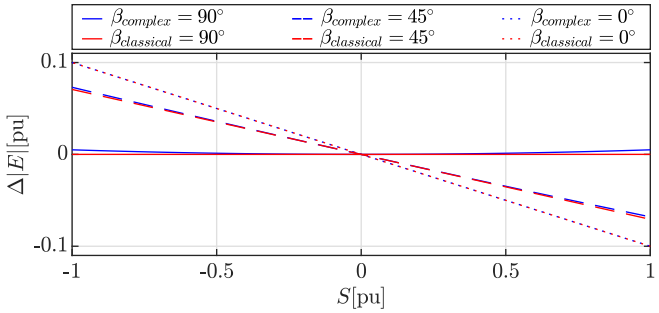

Figure 5.4: Variation of voltage amplitude output for different values of S, with $m_V = 0.1$ pu. Blue lines correspond to the proposed complex droop and red lines to the classical $P/f + Q/V$ and $P/V + Q/f$ alternatives. For $\beta = 0°$, the three droops produce the same variation (red and blue dotted lines coincide).

Table 5.1: Converter Parameters.

S_n	30 kVA	PI_i: P Gain	50
R_{filter}	0.1 Ω	PI_i: I Gain	500
L_{filter}	1.35 mH	PI_v: P Gain	5
C_{filter}	980 μF	PI_v: I Gain	50
Droop: m_ω	$9 \cdot 10^{-5}$	Droop: m_V	$2 \cdot 10^{-4}$

value for the coefficient is used for the three cases and using the same name for this coefficient (m_V).

5.4 Case study

The grid used as case study is shown in Fig. 5.5, where PEC_1 and PEC_2 are droop-controlled power electronic converters connected in node 1 and 3 respectively. Constant impedance loads are connected in node 2 (CIL_1) and 4 (CIL_2) and a converter connected to distributed energy storage system (dESS) is connected to node 5, behaving as a constant power load (CPL).

The used grid is one of the AC feeders from the microgrid shown in [5.13]. For demonstration purposes, both converters are considered to be equal with a rated power of 30 kVA. Converter parameters are shown in Table 5.1.

To compare the performance of the proposed complex-valued droop with respect to $P/f + Q/V$ and $P/V + Q/f$ droops, the impedance phase angle (ϕ) is varied. Three different angles (0°, 45° and 90°) are following considered in the simulation results.

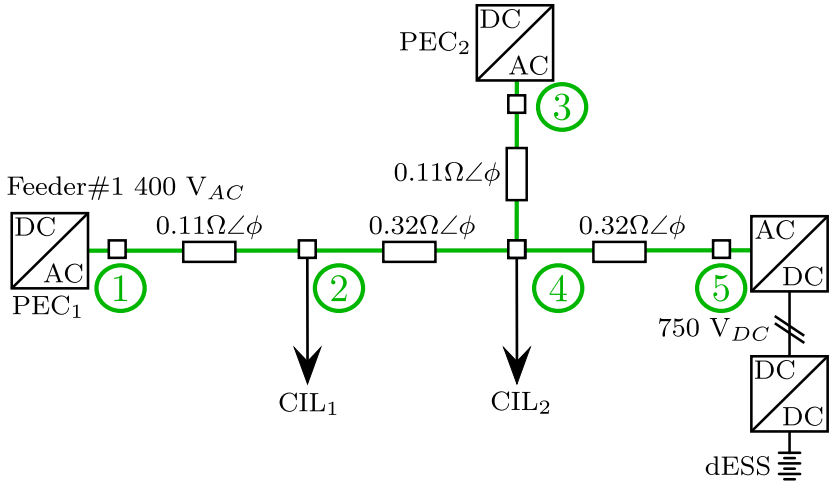

Figure 5.5: Grid used for simulation. Impedance phase angle (ϕ) varies for different simulation scenarios.

5.5 Simulation results

The simulation results are divided in two main parts. In the first one, the proposed droop is compared with the classical $P/f+Q/V$ and $P/V+Q/f$. For these simulations, perfect knowledge of the impedance phase angle is assumed. Impedance estimation [5.14, 5.15] can be used for online estimation. For the second part, the response of the proposed droop when mismatches occur in the impedance phase angle estimation are analyzed.

5.5.1 Comparison of different droop methods

Simulations for the different impedance phase angles are shown in Fig. 5.6. Results for the three different alternatives are shown together for a better comparison between the proposed complex-valued (continuous line) droop and the classical $P/f + Q/V$ (dashed) and $P/V + Q/f$ (dotted).

Starting with no load, at $t = 0.05$ s a CIL of 10 kW, 10 kvar is connected in nodes 2 and 4 (Fig. 5.5). In that situation, the grid is completely symmetric, so both converters have the exact same output. At $t = 0.2$ s another CIL, 10 kW, 10 kvar is connected in node 4. At $t = 0.6$ s the converter in node 5 starts to produce 10 kW, behaving as a CPL.

The proposed droop is able to operate with a good response in all the impedance phase angle range and both for CIL and CPL (bidirectional).

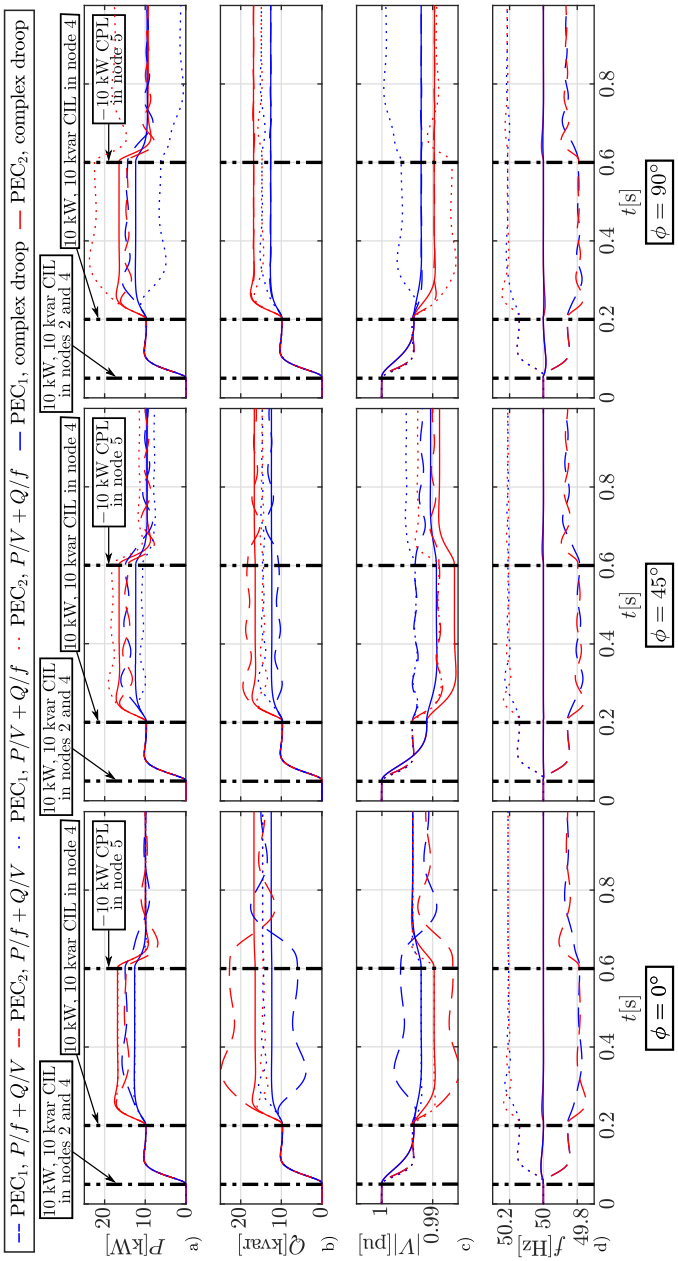

Figure 5.6: Simulation results for different values of impedance phase angle (ϕ) for the three type of droops: a) active power production, b) reactive power productions, c) output voltage magnitude and d) frequency.

It can be seen, that $P/f + Q/V$ and $P/V + Q/f$ droops present some oscillations during the transient after load connections. These oscillations do not appear in the proposed complex-valued droop, reaching the steady-state much quicker. Additionally, frequency deviation in steady-state does not appear in the proposed droop, while the variation during the transients is really small.

Besides that, it can be seen that the complex-valued droop is able to properly decouple active and reactive power, remaining the reactive power share unchanged when at $t = 0.6$ s an active power step is introduced.

5.5.2 Effect of impedance phase angle estimation mismatch

In order to check the effect of impedance phase angle estimation mismatch, simulations with error in the estimation of the angle has been analyzed.

In Fig. 5.7, simulations for different values of the impedance phase angle are shown with three values for the estimation of the impedance phase angle. The load steps are the same used in Fig. 5.6.

It can be seen that the control is not very sensitive to this mismatch, as no significant difference in the performance of the control system can be seen. The major differences are related to the voltage output amplitude and frequency results. The difference in frequency results are not very significant, taking into account that the deviation from nominal value is small and nominal value is recovered quickly.

The difference in the voltage amplitude are due to the use of different rotation matrix. As explained in Section 5.3, the deviation in voltage amplitude with respect to nominal value depends on apparent power magnitude and angle and the angle used for the rotation matrix (ϕ_{est}).

It can be seen that the voltage amplitude result is similar for the same ϕ_{est}, even for different values of the actual line impedance phase angle. The small difference is due to the different power sharing of the PECs when line impedance phase angle changes.

5.6 Conclusions

This chapter has shown a new droop strategy taking into account the coupling terms due to non-purely inductive/resistive lines, using the R/X ratio of the line. This droop, called Complex-Valued droop, does not require to operate with trigonometric functions, using complex formulations and *dq*-decomposition instead.

The variation of voltage amplitude produced by the proposed droop control has been analyzed, demonstrating that the range of variation is equal to the one obtained for $P/f + Q/V$ and $P/V + Q/f$ droops, but depending on apparent power magnitude and phase instead of active/reactive power.

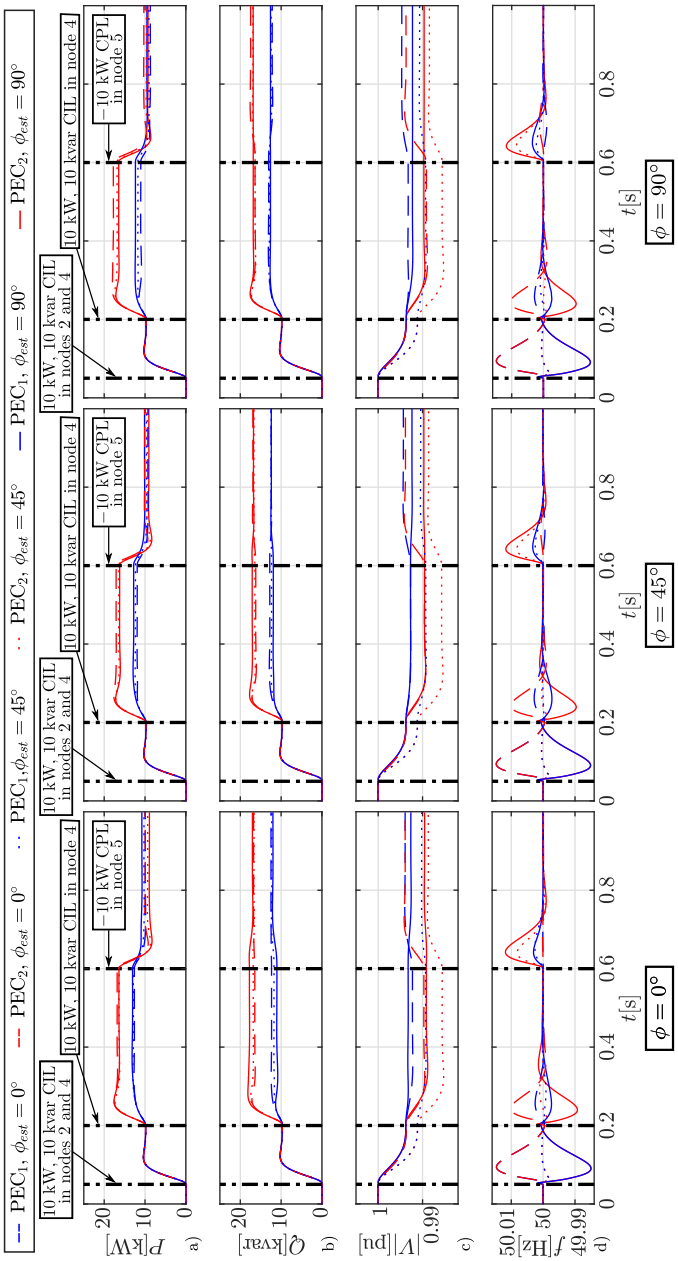

Figure 5.7: Simulation results for different values of impedance phase angle (ϕ) for three values of estimated impedance phase angle (ϕ_{est}).

This similarity in the range of variation allows using this range of output voltage variation as a way of selecting the droop coefficient, as it is often done for $P/f + Q/V$ and $P/V + Q/f$ approaches.

The simulation results have shown the operation of the proposed complex-valued droop, being able to operate at different R/X ratios with a faster response. Besides that, it presents the important advantage of eliminating the frequency deviation inherent to droop-based control in which f is used as one of the droop variables.

The effect of mismatches in the impedance phase angle estimation has been analyzed, showing that the control method is not much affected by these errors for the complete range of R/X values.

References

[5.1] J. Rocabert, A. Luna, F. Blaabjerg, and P. Rodríguez, "Control of Power Converters in AC Microgrids," *IEEE Transactions on Power Electronics*, vol. 27, no. 11, pp. 4734–4749, Nov. 2012.

[5.2] J. C. Vasquez, J. M. Guerrero, M. Savaghebi, J. Eloy-Garcia, and R. Teodorescu, "Modeling, Analysis, and Design of Stationary-Reference-Frame Droop-Controlled Parallel Three-Phase Voltage Source Inverters," *IEEE Transactions on Industrial Electronics*, vol. 60, no. 4, pp. 1271–1280, 2013.

[5.3] E. Lenz, D. J. Pagano, A. Ruseler, and M. L. Heldwein, "Two-Parameter Stability Analysis of Resistive Droop Control Applied to Parallel-Connected Voltage-Source Inverters," *IEEE Journal of Emerging and Selected Topics in Power Electronics*, vol. 8, no. 4, pp. 3318–3332, 2020.

[5.4] K. De Brabandere, B. Bolsens, J. Van den Keybus, A. Woyte, J. Driesen, and R. Belmans, "A Voltage and Frequency Droop Control Method for Parallel Inverters," *IEEE Transactions on Power Electronics*, vol. 22, no. 4, pp. 1107–1115, 2007.

[5.5] T. Qunais and M. Karimi-Ghartemani, "Systematic Modeling of a Class of Microgrids and Its Application to Impact Analysis of Cross-Coupling Droop Terms," *IEEE Transactions on Energy Conversion*, vol. 34, no. 3, pp. 1632–1643, 2019.

[5.6] Z. Peng, J. Wang, D. Bi, Y. Wen, Y. Dai, X. Yin, and Z. J. Shen, "Droop Control Strategy Incorporating Coupling Compensation and Virtual Impedance for Microgrid Application," *IEEE Transactions on Energy Conversion*, vol. 34, no. 1, pp. 277–291, 2019.

[5.7] K. Lao, W. Deng, J. Sheng, and N. Dai, "PQ-Coupling Strategy for Droop Control in Grid-Connected Capacitive-Coupled Inverter," *IEEE access : practical innovations, open solutions*, vol. 7, pp. 31 663–31 671, 2019.

[5.8] R. Majumder, B. Chaudhuri, A. Ghosh, R. Majumder, G. Ledwich, and F. Zare, "Improvement of Stability and Load Sharing in an Autonomous Microgrid Using Supplementary Droop Control Loop," *IEEE Transactions on Power Systems*, vol. 25, no. 2, pp. 796–808, 2010.

[5.9] H. Han, X. Hou, J. Yang, J. Wu, M. Su, and J. M. Guerrero, "Review of Power Sharing Control Strategies for Islanding Operation of AC Microgrids," *IEEE Transactions on Smart Grid*, vol. 7, no. 1, pp. 200–215, 2016.

[5.10] J. M. Guerrero, M. Chandorkar, T. Lee, and P. C. Loh, "Advanced Control Architectures for Intelligent Microgrids—Part I: Decentralized and Hierarchical Control," *IEEE Transactions on Industrial Electronics*, vol. 60, no. 4, pp. 1254–1262, 2013.

[5.11] B. Li, L. Zhou, x. yu, C. Zheng, and J. Liu, "Improved Power Decoupling Control Strategy Based on Virtual Synchronous Generator," *IET Power Electronics*, vol. 10, Dec. 2016.

[5.12] Á. Navarro-Rodríguez, P. García, R. Georgious, and J. García, "Adaptive Active Power Sharing Techniques for DC and AC Voltage Control in a Hybrid DC/AC Microgrid," *IEEE Transactions on Industry Applications*, vol. 55, no. 2, pp. 1106–1116, Mar. 2019.

[5.13] C. Gómez-Aleixandre, A. Navarro-Rodríguez, G. Villa, C. Blanco, and P. García, "Sharing Control Strategies for a Hybrid 48V/375V/400Vac AC/DC Microgrid," in *2020 IEEE Energy Conversion Congress and Exposition (ECCE)*, 2020, pp. 3900–3907.

[5.14] P. García, M. Sumner, Á. Navarro-Rodríguez, J. M. Guerrero, and J. García, "Observer-Based Pulsed Signal Injection for Grid Impedance Estimation in Three-Phase Systems," *IEEE Transactions on Industrial Electronics*, vol. 65, no. 10, pp. 7888–7899, 2018.

[5.15] A. SuÁrez, C. Blanco, P. García, Á. Navarro-Rodríguez, J. Manuel, and C. Rodríguez, "Online Impedance Estimation in AC Grids Considering Parallel-Connected Converters," in *2018 IEEE Energy Conversion Congress and Exposition (ECCE)*, 2018, pp. 5912–5919.

Chapter 6

Weighted DC Virtual Generator for interlinking converters in DC microgrids

6.1 Introduction

Interlinking converters can be used for connecting more than one DC microgrid to increase stability by having the capacity of exchanging power [6.1] or to have different voltage levels in the same microgrid [6.2]. These interlinking converters can contribute to voltage regulation. This chapter presents a DC microgrid with two voltage levels connected by an interlinking converter.

Some solutions can be found in the literature for DC-AC converters interfacing an AC microgrid with a DC link capacitor at the output of a converter connected to an energy source. This is done with a droop relating AC and DC voltage (V_g/V_{dc} droop) [6.3] or a dual droop, adding a DC voltage term to AC droop equations [6.4]. However, apart from being DC-AC converter cases, they can only act as grid-forming units in one of its outputs.

Some solutions are found both for AC-DC [6.5] and DC-DC [6.6] interlinking converters that can act as grid-forming units in either side. This makes that if one of the interconnected networks losses its grid-forming unit, the interlinking converter will give voltage control capability to that network with power coming from the grid-forming unit in the other network. This can be done without control scheme switching and operation mode detection. However, this method requires communications between the interlinking converter and the grid-forming units of each network and it needs a grid-forming unit in one of them.

This chapter proposes a new control strategy based on the well-known DC Virtual Generator (DCVG) concept, whose control scheme is shown in Fig. 6.1.

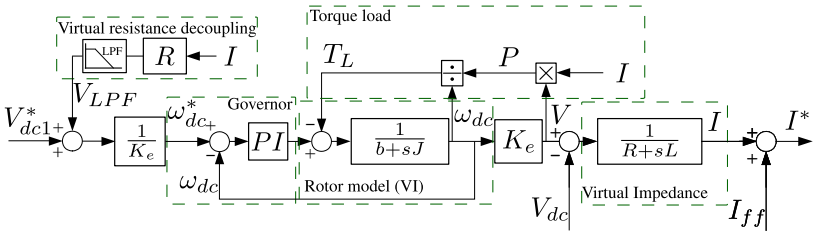

Figure 6.1: DC Virtual Generator control [6.7].

From the DC Virtual Generator scheme, an adaptation is done to make the control reversible, i.e. to use the same voltage control scheme for the controlling the voltage in both converter sides. The proposed modification considers a weighted approach in which a different priority can be given to both converter sides. By considering a weight calculation strategy proportional to the deviation with respect to the rated voltage at each converter side, a simultaneous grid-forming capability in both sides is achieved. The proposed method only requires a grid-feeding converter with a P/V droop in any side to keep the voltage in both grids at reasonable levels and does not demand any communication between the converters.

The chapter is organized as follows. Section 6.2 presents the grid used for the study. Section 6.3 describes the proposed control. Section 6.4 explains the case study, presenting the different grid configurations that are considered for the analysis. Section 6.5 presents the results obtained with OPAL-RT for the validation of the proposed control and Section 6.9 presents the conclusions.

6.2 Proposed DC microgrid topology

The proposed study uses part of the grid shown in [6.8]. The schematic representation is shown in Fig. 6.2. As it can be seen, it includes a ±375 Vdc bus and a 48 Vdc network connected to it using an interlinking power electronic converter. The 48 Vdc network will be referred as converter side 1, while the 375 Vdc bus connection is named side 2.

The converter with the proposed control strategy is labelled as DCVG, meanwhile in each of the DC networks have another DC/DC converter contributing to voltage regulation. PEC2 represents a connection to the mains, simplified here as a DC-DC converter, always operating as grid-forming unit. PEC1 can represent any DER operating either as grid-forming unit or grid-feeding with P/V droop. PEC control is shown in Fig. 6.3.

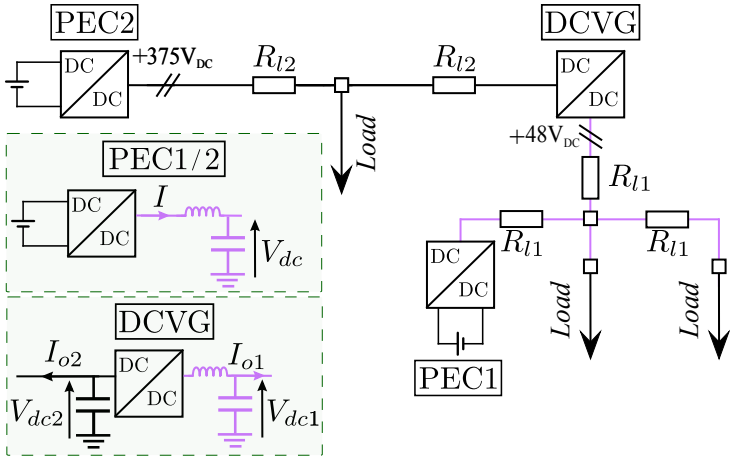

Figure 6.2: Grid used for OPAL-RT validation. Shadowed boxes show the filter configuration and control variables for interlinking (DCVG) and each network converter (PEC1 and PEC2).

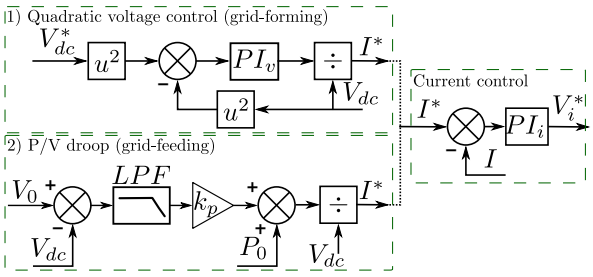

Figure 6.3: PEC1 and PEC2 control control diagram, showing both grid-forming (with quadratic voltage control [6.9]) and grid-feeding alternatives.

6.3 Proposed control

6.3.1 Weighted DC Virtual Generator (WDCVG)

From the conventional DC Virtual Generator scheme shown in Fig. 6.1, important modifications are incorporated to obtain the proposed control, as shown in Fig. 6.4, in order to be able to control the voltage in either side of the converter (V_{dc1} or V_{dc2}) when the DCVG is acting as interlinking converter. Current control, not included due to room constraints, has the same structure as shown in Fig. 6.3 for PEC1 and PEC2.

Starting from the voltage control in side 1 shown in Fig. 6.1, two adaptations are proposed.

Firstly, the voltage in side 2 (V_{dc2}) has to be referred to side 1 voltage level (V'_{dc2}). This is something similar to a change of voltage base, but also changing the sign of

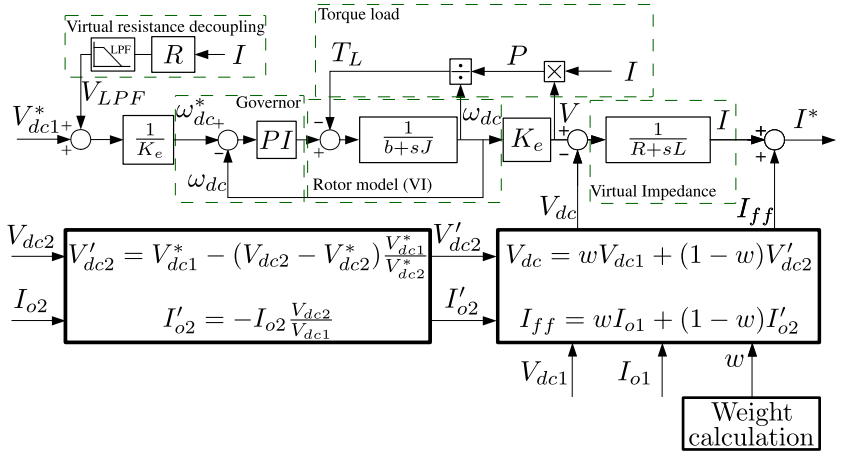

Figure 6.4: Weighted DC Virtual Generator control.

voltage deviation. For example, a voltage level of $(1 + \Delta V_{dc2})V^*_{dc2}$ will be transformed into $V'_{dc2} = (1 - \Delta V_{dc2})V^*_{dc1}$, being ΔV_{dc2} in per unit. The change in sign of the voltage deviation is due to the fact that for increasing voltage in side 2, the required power has opposite direction to the required for increasing voltage in side 1. The required transformation is shown in (6.1).

$$V'_{dc2} = (1 - \Delta V_{dc2})V^*_{dc1} = V^*_{dc1} - (V_{dc2} - V^*_{dc2})\frac{V^*_{dc1}}{V^*_{dc2}} \tag{6.1}$$

Following, an adaptation is required in the current feedforward term. Since in steady-state converter power output is the same in both sides, but with opposite directions, the feedforward term is calculated obtaining the measured current in side 1, from where the side 2 current is derived by using the voltage conversion ratio, i.e, by multiplying the output current I_{o2} by V_{dc2}/V_{dc1} and changing its sign. The corresponding expression is shown in (6.2).

$$I'_{o2} = -I_{o2}\frac{V_{dc2}}{V_{dc1}} \tag{6.2}$$

Once the voltage and current feedforward term are referred to side 1, the voltage and current used as measurements for the control are obtained as a weighted average of both sides values (side 1 and side 2 referred to side 1 levels). (6.3a) and (6.3b) show this weighted average calculation, being w the weight corresponding to side 1 ($0 \leq w \leq 1$).

$$V_{dc} = wV_{dc1} + (1 - w)V'_{dc2} \tag{6.3a}$$

$$I_{ff} = wI_{o1} + (1 - w)I'_{o2} \tag{6.3b}$$

6.3.2 Proportionally Weighted DC Virtual Generator (PWD-CVG)

Weight w can be fixed according to different criteria. An upper control level could set it depending on the grid situation. For example, if only one of the grids has another converter with grid-forming capability, the weight corresponding to that side can be set to 0. By doing this, the DCVG will only control the voltage in the other side, acting as a grid-forming for that network. If both grids have grid-forming units, the weights can be set dynamically, taking into account which grid is closer to reach any saturation limit or has more critical loads.

Another option is to only control the voltage in one of the sides, except if the voltage in the other side exceeds the selected limits, changing in that case the direction of the control. This behaviour is similar to the voltage margin control found in literature [6.10]. The main difference with the proposed strategy being that while in [6.10] the change is from power control to voltage control when one of the output voltages goes beyond the established limits, in the strategy proposed in this chapter it switches from controlling voltage in one side or the other depending on which one gets closer to the maximum/minimum voltage values.

This chapter proposes a weight calculation strategy proportional to the voltage deviation with respect to the rated value in each converter side, as shown in (6.4), where ΔV_{dc1} and ΔV_{dc2} are each side per unit voltage deviation.

$$w = \frac{|V_{dc1} - V^*_{dc1}|}{|V_{dc1} - V^*_{dc1}| + |V'_{dc2} - V^*_{dc1}|} = \frac{|\Delta V_{dc1}|}{|\Delta V_{dc1}| + |\Delta V_{dc2}|} \tag{6.4}$$

By doing this, the control focuses more in the side which is further from nominal voltage, without requiring any upper layer control to infer it from the grid conditions. Additionally, the proposed system avoids any sharp transition between the side whose voltage is being controlled, but a smooth and continuous change in the priority given to each side. This control strategy will be referred as Proportionally Weighted DC Virtual Generator (PWDCVG).

By following this strategy, same per unit voltage deviation is achieved in both converter sides, as it will be shown in the results. This can be proven by finding the value which makes V_{dc} in (6.3a) equal to V^*_{dc1}, since the latter is the voltage reference for the DCVG and the former is the equivalent to the measured voltage for the proposed weighted strategy.

By doing this substitution in (6.3a), (6.5) is obtained. V_{dc1} and V'_{dc2} are expressed in terms of V^*_{dc1}, taking into account V'_{dc2} is obtained by changing the sign of the per unit voltage deviation measured in side 2 as shown in (6.1).

$$V^*_{dc1} = w(1 + \Delta V_{dc1})V^*_{dc1} + (1 - w)(1 - \Delta V_{dc2})V^*_{dc1} \tag{6.5}$$

By simplifying V_{dc1}^{*} and since all terms independent of ΔV_{dc1} and ΔV_{dc2} are cancelled, the formula shown in (6.6) is obtained.

$$w\Delta V_{dc1} = (1-w)\Delta V_{dc2} \tag{6.6}$$

Finally, considering $w/(1-w) = |\Delta V_{dc1}|/|\Delta V_{dc2}|$, the result shown in (6.7) is obtained. This result shows that both per unit voltage deviations will be equal in magnitude and sign in steady-state.

$$|\Delta V_{dc1}|\Delta V_{dc1} = |\Delta V_{dc2}|\Delta V_{dc2} \tag{6.7}$$

As a final remark about the proposed mechanism, it has to be highlighted that with the weighted strategy the interlinking converter can behave as a grid-forming converter for both sides simultaneously, just requiring a grid-feeding with P/V droop control in either side. This aspect will be discussed in the results section.

6.4 Case study

The microgrid used as the case study is shown in Fig. 6.2, with all the grid and converter parameters included in Table 6.1.

For checking the operation of the converter in different scenarios, transitions between different configuration modes of the microgrid are introduced by connecting/disconnecting PEC1 and PEC2 units. The different operation modes of the microgrid are shown in Table 6.2.

Five different scenarios are going to be shown. For the first four, PEC1 operates as grid-forming unit:

- Step in weight (w) setting different values to show how sending weight references can change the way the WDCVG contributes to both networks. Converters in mode A1.
- The strategy based in voltage margin control is followed. Initially, weight is fixed to 1, making the WDCVG only contributes to control in 48 Vdc network. Starting in mode A1, there is a transition to mode B1, making the voltage in side 2 (375 Vdc network) to be uncontrolled. When the voltage in that network goes outside some limits, the weight is changed to 0 so that the WDCVG starts to control the voltage in that side.
- Proportionally WDCVG is used in the same scenario shown for voltage margin control case in order to compare both scenarios.
- A longer OPAL-RT simulation for proportionally WDCVG is shown to demonstrate how transition between different scenarios affects the grid situation.

Table 6.1: System parameters

Grid parameters	Values
Side 1 voltage: V^*_{dc1}	48 Vdc
Side 1 line resistance: R^*_{l1}	6.9 mΩ
Side 2 voltage: V^*_{dc2}	375 Vdc
Side 2 line resistance: R^*_{l2}	105.5 mΩ
PEC1 parameters	Values
Filter inductance: L^*_f	0.73 mH
Filter capacitance: C^*_f	5 mF
Current regulator bandwidth: BW_i	500 Hz
Voltage regulator bandwidth: BW_v	50 Hz
P/V droop constant: k^*_{pv}	8.33 kW/V
PEC2 parameters	Values
Filter inductance: L^*_f	2.5 mH
Filter capacitance: C^*_f	5.04 mF
Current regulator bandwidth: BW_i	500 Hz
Voltage regulator bandwidth: BW_v	50 Hz
WDCVG parameters	Values
Filter inductance: L^*_f	1.47 mH
Filter capacitance (side 1): C^*_f	5.04 mF
DC link capacitance (side 2): C^*_f	5 mF
Current regulator bandwidth: BW_i	500 Hz
Governor regulator bandwidth: BW_ω	50 Hz
Virtual inertia: J_{dc}	0.0002 kg·m^2
Virtual damping: b_{dc}	0.003 N·m·s

Apart from that, an OPAL-RT simulation equal to the last mentioned one is done but changing PEC1 to be a grid-feeding unit with droop control.

6.5 OPAL-RT results

The proposed control has been validated using OPAL-RT real time simulator. The time step for the real time simulation is 245 ns.

6.5.1 Steps in weights

The first scenario is done for the weighted DCVG generator working with different values of weights which is changed by steps. The results are shown in Fig. 6.5. Power is expressed using active sign convention, positive for generation and negative for consumption.

Table 6.2: Different Operating Modes of the Microgrid.

Mode	PEC1	PEC2
A1	Grid-forming	Grid-forming
A2	Grid-feeding with P/V droop	Grid-forming
B1	Grid-forming	Off
B2	Grid-feeding with P/V droop	Off
C	Off	Grid-forming

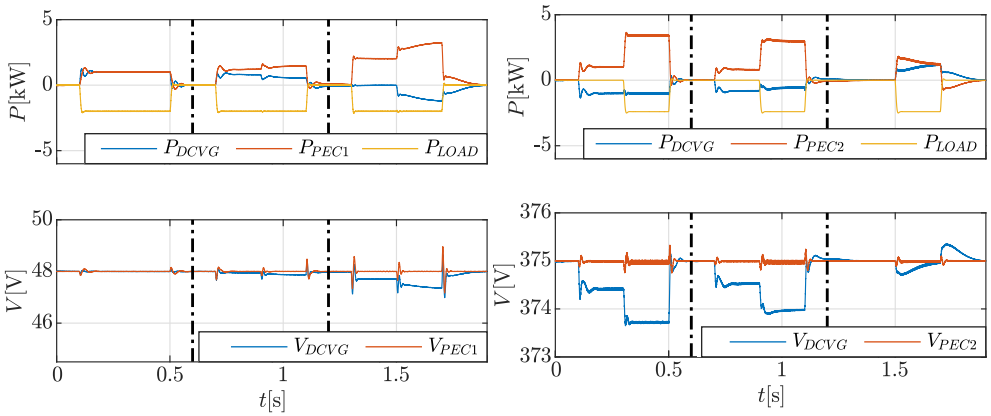

Figure 6.5: OPAL-RT results for step changes in weights with converters in mode A1. Weight is initially set to 1 (only control side 1). First vertical line indicates step change to $w = 0.5$. Second vertical line indicates step change to $w = 0$ (only control side 2). From top to bottom: power in side 1 (48 Vdc network); voltage in side 1; power in side 2 (375 Vdc network); voltage in side 2.

The initial situation is with weight (w) equal to 1. Starting from no load, at $t = 0.1$ s a step of 2 kW in the power demanded by the load in 48 Vdc network. At $t = 0.3$ s a step of 2.4 kW in the power demanded by the load in 375 Vdc network. At $t = 0.5$ s the power demanded by the loads in both networks is set back to 0 kW. The weight is changed to 0.5 at $t = 0.6$ s and to 1 at $t = 1.2$ s. After these two changes, the same steps in demanded power mentioned for $w = 1$ are used.

When weight is equal to 1, the control is focusing only in the voltage control in 48 Vdc network. It can be seen, that in that interval the control of the DCVG is not affected by the power changes in the other side ($t = 0.3$ s).

When $w = 0.5$ (after $t = 0.6$ s), the control is contributing in the same proportion to both sides. It can be seen that, in this case, the control reacts to power changes in both grids ($t = 0.7$ s and $t = 0.9$ s).

After the second vertical line, w is set to 0, having the opposite of the initial situation. The control is only focusing in the 375 Vdc network and not affected by power changes in the other network ($t = 1.3$ s)

6.5.2 Weighted DCVG with voltage margin control

In order to check the capability of controlling voltage by its own when no other converter is controlling voltage in any of the sides, a weight calculation strategy similar to voltage margin control is studied. On it, the weight of the DCVG is set to 1 in normal operation, focusing on controlling voltage in 48 Vdc network. When voltage in 375 Vdc network goes outside some range (370 − 380 Vdc in this case), the weight is changed to 0, starting to control voltage in the other side.

If the margin control strategy is applied to the weighted DCVG, the results shown in Fig. 6.6 are obtained. Starting in mode A1, with PEC1 and PEC2 operating as grid-forming, load reference in each side is changed. At $t = 0.1$ s, load in 48 Vdc network is set to -2 kW (demand) and changed to 3 kW (production) at $t = 0.7$ s. At $t = 0.3$ s, load in 375 Vdc network is set to -2.4 kW and changed to 1.6 kW at $t = 0.5$ s. It can be seen that load changes in 375 Vdc network are totally absorbed by PEC2, since DCVG converter is only focusing on side 1 if voltage in side 2 is within the limits.

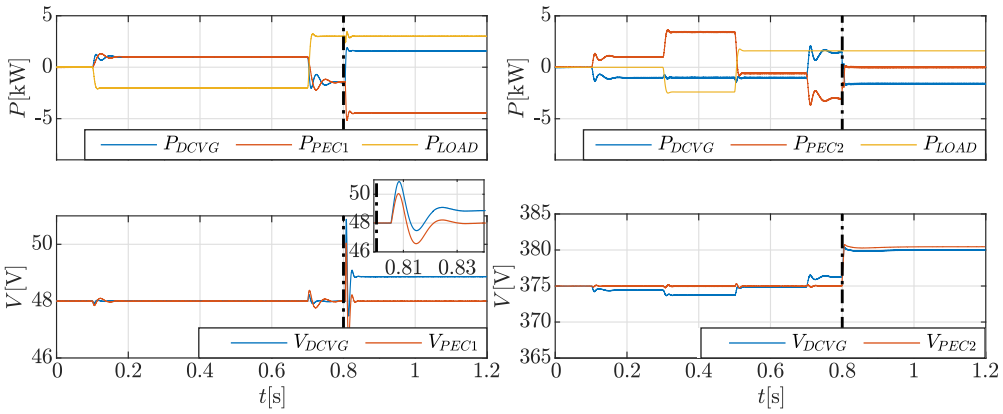

Figure 6.6: OPAL-RT results for weighted DCVG with voltage margin control with PEC1 as grid-forming. Vertical line indicates change from mode A1 to mode B1. From top to bottom: power in side 1 (48 Vdc network); voltage in side 1; power in side 2 (375 Vdc network); voltage in side 2.

After the first vertical line, the only converter controlling voltage in 375 Vdc network (PEC2) is disconnected. When the voltage goes out of the specified limits, the DCVG starts to control voltage in that side, setting the reference to 380 Vdc.

This allows the converter to be able to work in both directions, but producing a sudden change from one control mode to the other, which causes fast voltage variation meanwhile one grid has no converter in voltage control.

Apart from that, in some situations both grids can be in similar conditions and it will be difficult to select which one is given priority.

6.5.3 Proportionally weighted DCVG (with grid-forming converters in both networks)

To solve the previous two problems, the weight calculation strategy proposed calculates each weight proportional to voltage deviation with respect to rated values in each converter side. In that way, the voltage deviation from the rated point is used as a measure of the neediness of each side and the priority is set proportional to it. This makes the weight can take any value between the range 0 to 1, giving the system a smooth operation during grid situation changes.

This can be seen in Fig. 6.7, which is the same situation (configuration and load sequence) of Fig. 6.6 but with the explained weight calculation strategy. The proposed strategy reacts smoothly to PEC2 disconnection, reducing the rate of change of the voltage in the uncontrolled grid.

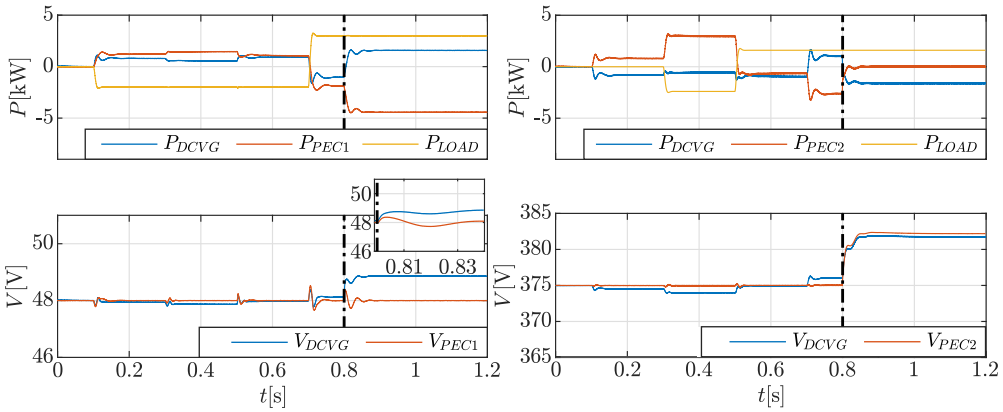

Figure 6.7: OPAL-RT results for proportionally weighted DCVG with PEC1 as grid-forming. Vertical line indicates change from mode A1 to mode B1. From top to bottom: power in side 1 (48 Vdc network); voltage in side 1; power in side 2 (375 Vdc network); voltage in side 2.

Fig. 6.8 shows a longer sequence of changes for a complete demonstration of the operation of the converter in different grid configurations. Starting in mode C (PEC1 off, PEC2 acting as grid-forming), the sequence of changes is the following:

- $t = 0.1$ s: load in 48 Vdc network is set to -2 kW (demand).
- $t = 0.3$ s: load in 375 Vdc network is set to -2.4 kW (demand).
- $t = 0.4$ s: PEC1 is connected, acting as grid-forming, changing operating mode to A1.
- $t = 0.5$ s: load in 375 Vdc network is set to 1.6 kW (production).
- $t = 0.7$ s: load in 48 Vdc network is set to 3 kW (production).

- $t = 0.8$ s: PEC2 is disconnected, changing operating mode to B1.
- $t = 1.0$ s: load in 375 Vdc network is set to -2.4 kW (demand).
- $t = 1.4$ s: PEC2 is connected, acting as grid-forming, changing operating mode to A1.
- $t = 1.6$ s: PEC1 is disconnected, changing operating mode to C.

It can be seen that the control is able to act as grid-forming converter in any of the sides keeping the voltage stable in both sides, even if the other grid-forming converter in the corresponding network is disconnected. Apart from that, when both PEC1 and PEC2 are operating, the DCVG reacts to load changes in both sides, making it possible to each PEC to contribute to the load in the other network.

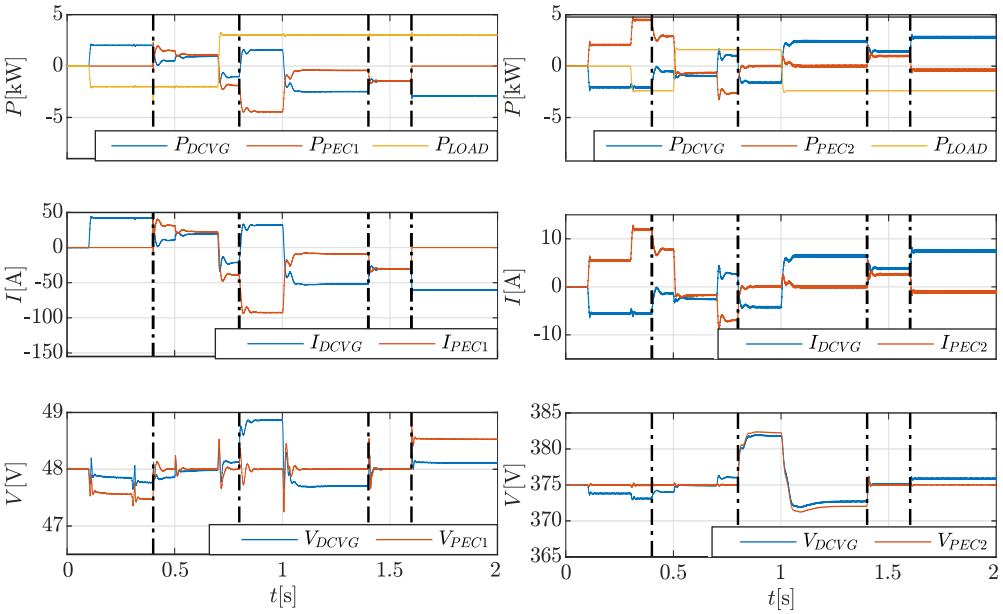

Figure 6.8: OPAL-RT results for proportionally weighted DCVG with PEC1 as grid-forming. Left column show variables referred to side 1 (48 Vdc network) and right column for side 2 (375 Vdc network). From top to bottom: active power; output current; voltage.

Current outputs are shown too, where it can be seen that the ripple in the current is not very significant. The ripple is higher in 375 Vdc network (side 2) because side 1 is the one with LC filter (see Fig. 6.2).

Finally, a comparison in the per unit voltage at each side of the converter is shown. As it was demonstrated mathematically, it can be seen that, in steady-state, the voltage deviation is equal in both sides. This means that it is able to reach a balanced situation in which both networks are in similar neediness as seen from both converter output voltages.

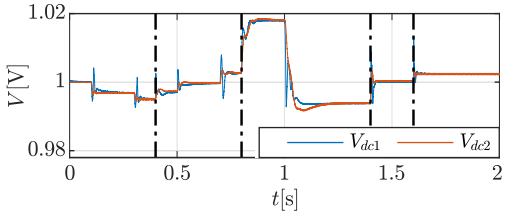

Figure 6.9: OPAL-RT results for proportionally weighted DCVG with PEC1 as grid-forming. Per unit voltage at each side of the WDCVG.

6.5.4 Proportionally weighted DCVG (with grid-feeding)

The proportionally WDCVG has the capability of acting as grid-forming in both networks at the same time, with no need of other grid-forming unit in either side. Only one converter acting as grid-feeding with droop control is required for the proposed control to be able to control voltage in both sides at the same time.

This is shown in Fig. 6.10, with exactly the same scenario shown in Fig. 6.8, but changing the grid-forming unit in 48 Vdc network by a grid-feeding unit with P/V droop. Thus the sequence is the one presented before, but changing modes A1 and B1 for A2 and B2.

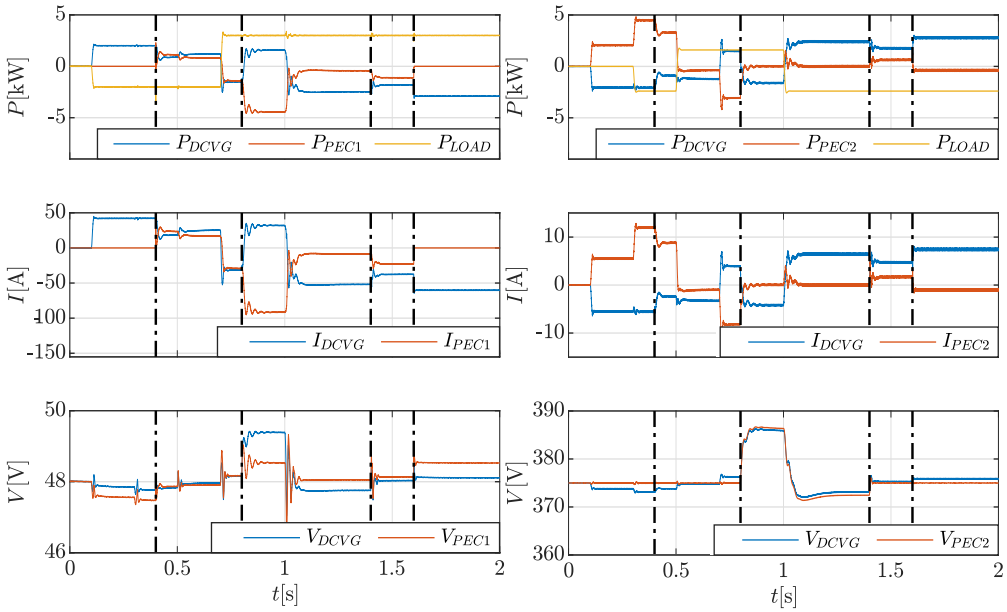

Figure 6.10: OPAL-RT results for proportionally weighted DCVG with PEC1 as grid-feeding with P/V droop. Left column show variables referred to side 1 (48 Vdc network) and right column for side 2 (375 Vdc network). From top to bottom: active power; output current; voltage.

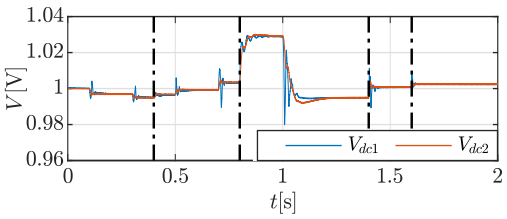

Figure 6.11: OPAL-RT results for proportionally weighted DCVG weighted DCVG with PEC1 as grid-feeding with P/V droop. Per unit voltage at each side of the WDCVG.

It can be seen that even when the only grid-forming unit in the system apart from the DCVG interlinking converter (PEC2) is disconnected after the second vertical line, the interlinking converter is able to reach stable situation forming both grids at the same time.

In this case, the voltage deviation is higher than for the case with grid-forming units in both networks due to the P/V droop required for the grid-feeding unit to contribute. However, this situation will only happen because of contingencies and a secondary control will be able to recover the voltage level.

6.6 State-space modeling

In this section, the state-space modeling of the proposed control is going to be carried out. This model will allow to perform stability analysis and study of parameter variation sensitivity.

6.6.1 WDCVG control equations

First, the control part needs to be modeled. The voltage control scheme of the weighted DCVG is shown in Fig. 6.4. The current controller is just a PI regulator, shown in Fig. 6.12 together with the variables used for the control.

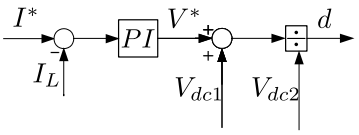

(a) Current control loop, including feedforward and duty calculation.

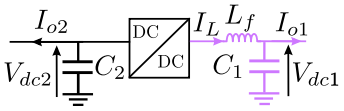

(b) Control variables.

Figure 6.12: Weighted DC Virtual Generator control.

The complete state-space model is shown in (6.8)-(6.12), being T_I^* and V_I^* the integral control action of angular frequency and current PI regulators respectively. In red, the varying matrices are highlighted, as well as the varying terms inside them.

$$\frac{\mathrm{d}}{\mathrm{d}t}\begin{bmatrix}\omega_{dc}\\ I\\ T_I^*\\ V_{LPF}\\ V_I^*\end{bmatrix} = \left[A_x\right]_{5\times5}\begin{bmatrix}\omega_{dc}\\ I\\ T_I^*\\ V_{LPF}\\ V_I^*\end{bmatrix} + \left[\begin{array}{c|c}\left[B_c\right]_{5\times3} & \left[B_x\right]_{5\times3}\end{array}\right]\begin{bmatrix}V_{dc1}^*\\ I_{o1}\\ I_{o2}\\ \hline V_{dc1}\\ V_{dc2}\\ I_L\end{bmatrix} \tag{6.8}$$

$$\left[d\right] = \left[C_x\right]_{1\times5}\begin{bmatrix}\omega_{dc}\\ I\\ T_I^*\\ V_{LPF}\\ V_I^*\end{bmatrix} + \left[\begin{array}{c|c}\left[D_c\right]_{1\times3} & \left[D_x\right]_{1\times3}\end{array}\right]\begin{bmatrix}V_{dc1}^*\\ I_{o1}\\ I_{o2}\\ \hline V_{dc1}\\ V_{dc2}\\ I_L\end{bmatrix} \tag{6.9}$$

$$\left[A_x\right]_{5\times5} = \begin{bmatrix}\frac{-(b+K_{p\omega})}{J} & \frac{-K_e}{J} & \frac{1}{J} & \frac{K_{p\omega}}{K_eJ} & 0\\ \frac{K_e}{L} & \frac{-R}{L} & 0 & 0 & 0\\ -K_{i\omega} & 0 & 0 & \frac{K_{i\omega}}{K_e} & 0\\ 0 & R\omega_{LPF} & 0 & -\omega_{LPF} & 0\\ 0 & K_{ii} & 0 & 0 & 0\end{bmatrix} \tag{6.10}$$

$$[B_c]_{5\times3} = \begin{bmatrix} \frac{K_{p\omega}}{K_e J} & 0 & 0 \\ \frac{-2w_2}{L} & 0 & 0 \\ \frac{K_{i\omega}}{K_e} & 0 & 0 \\ 0 & 0 & 0 \\ 0 & w_1 K_{ii} & \frac{-w_2 V_{dc2}}{V_{dc1}} K_{ii} \end{bmatrix} \tag{6.11}$$

$$[B_x]_{5\times3} = \begin{bmatrix} 0 & 0 & 0 \\ \frac{-w_1}{L} & \frac{w_2 V^*_{dc1}}{L V^*_{dc2}} & 0 \\ 0 & 0 & 0 \\ 0 & 0 & 0 \\ 0 & 0 & -K_{ii} \end{bmatrix}; \quad [C_x]_{1\times5} = \begin{bmatrix} 0 & \frac{K_{pi}}{V_{dc2}} & 0 & 0 & \frac{1}{V_{dc2}} \end{bmatrix} \tag{6.12}$$

$$[D_c]_{1\times3} = \begin{bmatrix} 0 & \frac{w_1 K_{pi}}{V_{dc2}} & \frac{-w_2 K_{pi}}{V_{dc1}} \end{bmatrix}; \quad [D_x]_{1\times3} = \begin{bmatrix} \frac{1}{V_{dc2}} & 0 & \frac{-K_{pi}}{V_{dc2}} \end{bmatrix} \tag{6.13}$$

6.6.2 Power equations

Including the power, now V_{dc1}, V_{dc2} and I_L are states and the state-space model shown in (6.14)-(6.17) is obtained. For doing so, the action of the converter is considered with an average model for each switching period. That means, for example, that the voltage before the filter (i.e., between both IGBTs) is $d \cdot V_{dc2}$ (considering V_{dc2} as the high voltage side). On the other hand, the current input in the side with higher voltage is $d \cdot i_L$, considering no losses in the converter (the active power must be conserved).

$$\frac{\mathrm{d}}{\mathrm{d}t}\begin{bmatrix} V_{dc1} \\ V_{dc2} \\ I_L \end{bmatrix} = [A_p]_{3\times3}\begin{bmatrix} V_{dc1} \\ V_{dc2} \\ I_L \end{bmatrix} + \left[\, [B_p]_{3\times3} \;\middle|\; [B_{pd}]_{3\times1} \,\right] \left[\begin{array}{c} V^*_{dc1} \\ I_{o1} \\ I_{o2} \\ \hline d \end{array}\right] \tag{6.14}$$

$$\begin{bmatrix} V_{dc1} \\ V_{dc2} \\ I_L \end{bmatrix} = [I]_{3\times3}\begin{bmatrix} V_{dc1} \\ V_{dc2} \\ I_L \end{bmatrix} + [0]_{3\times4}\left[\begin{array}{c} V^*_{dc1} \\ I_{o1} \\ I_{o2} \\ \hline d \end{array}\right] \tag{6.15}$$

$$[A_p]_{3\times3} = \begin{bmatrix} 0 & 0 & \frac{1}{C_1} \\ 0 & 0 & 0 \\ \frac{-1}{L_f} & 0 & 0 \end{bmatrix} \tag{6.16}$$

$$[B_p]_{3\times3} = \begin{bmatrix} 0 & \frac{-1}{C_1} & 0 \\ 0 & 0 & \frac{-1}{C_2} \\ 0 & 0 & 0 \end{bmatrix} ; \; [B_{pd}]_{3\times1} = \begin{bmatrix} 0 \\ \frac{-i_L}{C_2} \\ \frac{V_{dc2}}{L_f} \end{bmatrix} \tag{6.17}$$

6.6.3 Complete state-space model

Models of previous two subsections can be merged considering duty cycle, d, is the output of the control part and one of the inputs of the power stage. The state space model shown in (6.18)-(6.23) is obtained. Matrices A and B are shown in Appendix D, in (D.9) and (D.6).

$$[x_c] = \begin{bmatrix} \omega_{dc} \\ I \\ T_I^* \\ V_{LPF} \\ V_I^* \end{bmatrix} ; \; [x_p] = \begin{bmatrix} V_{dc1} \\ V_{dc2} \\ I_L \end{bmatrix} ; \; [u] = \begin{bmatrix} V_{dc1}^* \\ I_{o1} \\ I_{o2} \end{bmatrix} \tag{6.18}$$

$$\frac{\mathrm{d}}{\mathrm{d}t} \left[\begin{array}{c} x_c \\ \hline x_p \end{array}\right] = [A]_{8\times8} \left[\begin{array}{c} x_c \\ \hline x_p \end{array}\right] + [B]_{8\times3} [u] \tag{6.19}$$

$$\begin{bmatrix} V_{dc1} \\ V_{dc2} \\ I_L \end{bmatrix} = \left[\begin{array}{c|c} [0]_{3\times5} & [I]_{3\times3} \end{array}\right] \left[\begin{array}{c} x_c \\ \hline x_p \end{array}\right] + [0]_{3\times3} [u] \tag{6.20}$$

$$[A]_{8\times8} = \left[\begin{array}{c|c} [A_{xx}]_{5\times5} & [A_{xp}]_{5\times3} \\ \hline [A_{px}]_{3\times5} & [A_{pp}]_{3\times3} \end{array}\right] \tag{6.21}$$

$$[A]_{8\times8} = \left[\begin{array}{c|c} [A_x]_{5\times5} & [B_x]_{5\times3} \\ \hline [B_{pd}]_{3\times1}[C_x]_{1\times5} & [A_p]_{3\times3} + [B_{pd}]_{3\times1}[D_x]_{1\times3} \end{array}\right] \tag{6.22}$$

$$[B]_{8\times3} = \left[\begin{array}{c} [B_c]_{5\times3} \\ \hline [B_p]_{3\times3} + [B_{pd}]_{3\times1} [D_c]_{1\times3} \end{array}\right] \tag{6.23}$$

The model has been tested compared with a Simulink simulation to test is validity. The results are shown in Fig. 6.13. It can be seen that the response of all the states completely matches the one obtained with Simulink, as well as the outputs, since, in this case, they are also states. This proves the validity of our model.

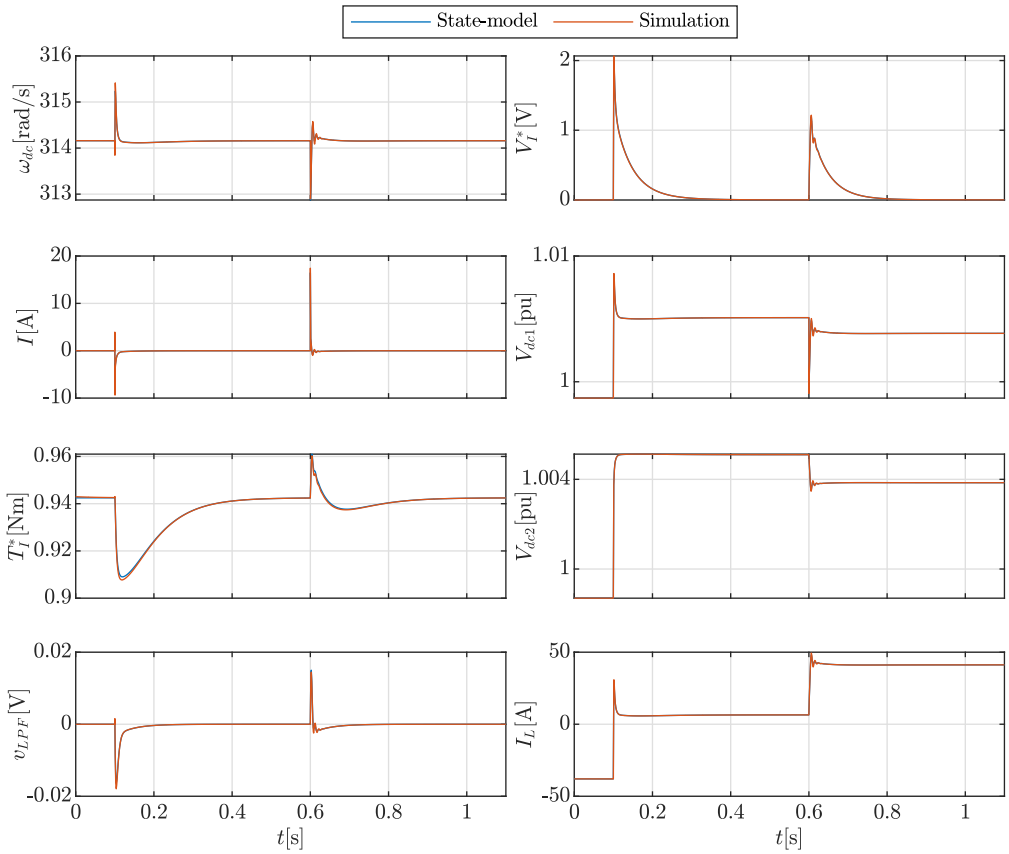

Figure 6.13: Comparison between the results obtained with Simulink electrical model and the state-space equations.

It is worth to remark that, until this point, I_{o1} and I_{o2} were considered as system inputs. However, this will generally not be the case when looking to the complete system. One or both sides of the PEC will normally be connected to a voltage source through a line impedance which provides the required power. In that case, the corresponding input I_{ox} should be replaced by $\frac{V_{dcx} - V_{sx}}{R_x}$, thus affecting both A and B matrices. This change only affects the columns corresponding to that input in matrix B (I_{ox} which changes to V_{s1}) and the corresponding voltage output in A (V_{dcx}, which is also a state).

For example, if both outputs are connected to a voltage source through a purely resistive line impedance the state-space equations would be the ones shown in (6.24)-(6.27), where only the last three columns of A are shown (since the first five, related to control states, do not change).

$$[u_v] = \begin{bmatrix} V_{dc1}^* \\ V_{s1} \\ V_{s2} \end{bmatrix} ; \frac{\mathrm{d}}{\mathrm{d}t} \left[\begin{array}{c} x_c \\ \hline x_p \end{array}\right] = [A_v]_{8\times 8} \left[\begin{array}{c} x_c \\ \hline x_p \end{array}\right] + [B_v]_{8\times 3} [u_v] \tag{6.24}$$

$$\begin{bmatrix} V_{dc1} \\ V_{dc2} \\ I_L \end{bmatrix} = \left[\begin{array}{c|c} [0]_{3\times 5} & [I]_{3\times 3} \end{array}\right] \left[\begin{array}{c} x_c \\ \hline x_p \end{array}\right] + [0]_{3\times 3} [u_v] \tag{6.25}$$

$$[A_v]_{8\times 8}(:, 6:8) = \begin{bmatrix} 0 & 0 & 0 \\ -\frac{w_1}{L} & \frac{V_{dc1}^* w_2}{L V_{dc2}^*} & 0 \\ 0 & 0 & 0 \\ 0 & 0 & 0 \\ \frac{K_{ii} w_1}{R_1} & -\frac{K_{ii} V_{dc2} w_2}{R_2 V_{dc1}} & -K_{ii} \\ -\frac{1}{C_1 R_1} & 0 & \frac{1}{C_1} \\ -\frac{i_L}{C_2 V_{dc2}} - \frac{K_{pi} i_L w_1}{C_2 R_1 V_{dc2}} & \frac{K_{pi} i_L w_2}{C_2 V_{dc1} R_2} - \frac{1}{C_2 R_2} & \frac{K_{pi} i_L}{C_2 V_{dc2}} \\ \frac{K_{pi} w_1}{L_f R_1} & -\frac{K_{pi} V_{dc2} w_2}{L_f R_2 V_{dc1}} & -\frac{K_{pi}}{L_f} \end{bmatrix} \tag{6.26}$$

$$[B_v]_{8\times 3} = \begin{bmatrix} \frac{K_{pw}}{JK_e} & 0 & 0 \\ -\frac{2w_2}{L} & 0 & 0 \\ \frac{K_{iw}}{K_e} & 0 & 0 \\ 0 & 0 & 0 \\ 0 & -\frac{K_{ii}w_1}{R_1} & \frac{K_{ii}V_{dc2}w_2}{R_2V_{dc1}} \\ 0 & \frac{1}{C_1R_1} & 0 \\ 0 & \frac{K_{pi}i_Lw_1}{C_2R_1V_{dc2}} & \frac{1}{C_2R_2} - \frac{K_{pi}i_Lw_2}{C_2V_{dc1}R_2} \\ 0 & -\frac{K_{pi}w_1}{L_fR_1} & \frac{K_{pi}V_{dc2}w_2}{L_fR_2V_{dc1}} \end{bmatrix} \tag{6.27}$$

In all the previous cases, there are variable terms in matrices A and B. For small-signal analysis, the equations have to be linearized around an equilibrium point. A_l and A_{lv} are the linearized versions of A and A_v respectively. These linearized matrices are shown in in Appendix D, in (D.1) and (D.2). On it, all the equilibrium conditions were already introduced so that the matrices depend on the minimum amount of independent variables. Only the last 3 columns are shown since they are the only one that vary when linearizing the original matrices (as the variable state-space matrices A and A_v only depend on the last 3 states: V_{dc1}, V_{dc2} and I_L).

6.7 Stability analysis

Once the model is obtained, it can be used for stability analysis. In this section, the stability of the proposed control is going to be analyzed, comparing it with the conventional DCVG control and other weight calculation strategies. The model sensitivity to parameter variation is going to be studied, in this case, with the variation of virtual inductance, L.

The system is going to be analyzed for two different scenarios. In both of them, one of the PEC outputs is going to be connected to a voltage source (V_{sx}) through a line resistance (R_x), meanwhile the other output is going to be connected to a current source (I_{oy}), representing a bidirectional load. For the first case, output 1 is going to be connected to the voltage source and output 2 to the current, and it will be referred to as case $V_{s1} - I_{o2}$. The second case will be the opposite, being referred to as $I_{o1} - V_{s2}$.

6.7.1 Comparison between methods

Different ways of choosing w were analysed in order to compare their performance. These different w selection criteria are:

- Proposed formula for w: Proportionally Weighted DC Virtual Generator proposed in this chapter ($w = \frac{|\Delta V_{dc1}|}{|\Delta V_{dc1}|+|\Delta V_{dc2}|}$).
- $w = 0$: control only focuses on V_{dc2} control. Behaves similarly to a DCVG control applied to control V_{dc2}.
- $w = 0.5$: since the equilibrium is reached always for $w = 0.5$, the possibility of just having that fixed value for the weight has been studied too.
- $w = 1$: control only focuses on V_{dc1} control. This is conventional DCVG control applied to control V_{dc1}.

Although these cases are the most relevant ones, a sweep for every possible value of w within the range $[0, 1]$ is going to be included for completeness.

6.7.1.1 Case $\mathbf{V_{s1}}$-$\mathbf{I_{o2}}$

In Fig. 6.14, the eigenvalues obtained for the different values of w are shown for case $V_{s1} - I_{o2}$. The most relevant values of w (0, 0.5 and 1) are highlighted. The eigenvalues using the proposed formula, instead of a fixed value of w are shown too (they do not lie in the continuous lines of the w sweep because it is not one fixed value as done in that sweep). In the bottom subplot, only the dominant eigenvalue for each w is shown. It can be seen that, for this case, only $w = 1$ is not stable (eigenvalue equal to 0). This is because, if $w = 1$, control is focusing on side 1, leaving side 2 uncontrolled (and there is no voltage source on that side).

In Fig. 6.15, the step response for the different w selection criteria are shown. In all of them, the settling time for the proposed formula for w is smaller than that for $w = 0.5$. $w = 0$ is less affected by the variation on the inputs and, in general, faster, because the voltage control is focusing on the side which has no voltage source on it. Response for $w = 1$ in the right-side column (step responses for V_{dc2}) cannot be appreciated because the voltage increases/decreases uncontrolled.

It is worth to remark, that even if only $w = 1$ makes the control unstable, the equilibrium point it is not the same for all w values. Some of the values of w may lead to stable solutions with undesired steady-state result.

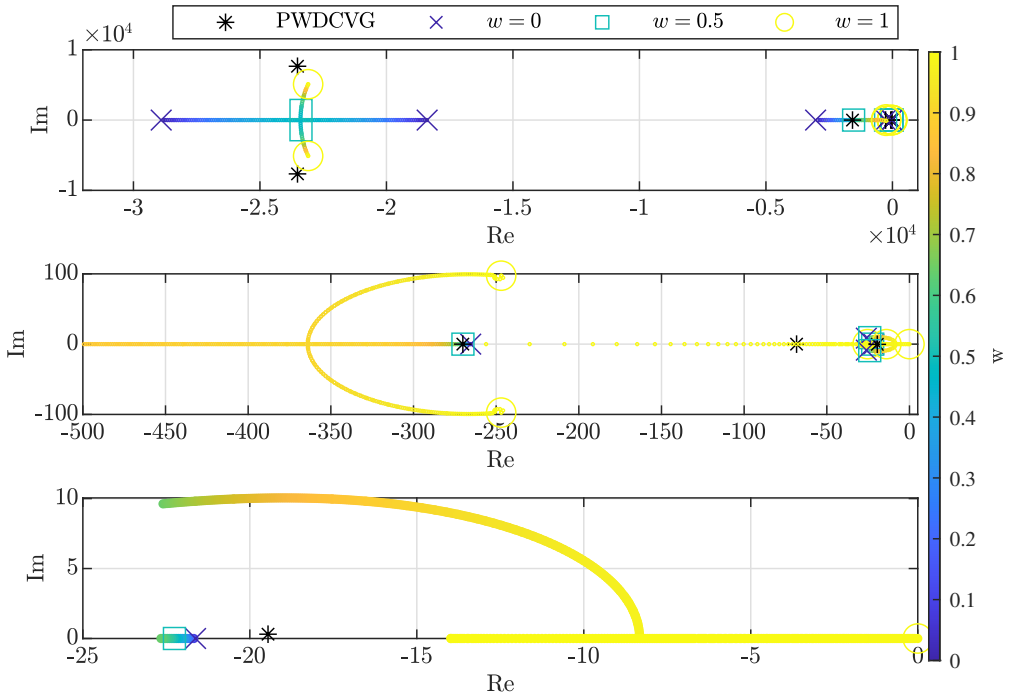

Figure 6.14: Eigenvalues for the different weight values for case $V_{s1} - I_{o2}$. Top: general view. Middle: zoom to the dominant eigenvalues. Bottom: only the dominant eigenvalue is shown.

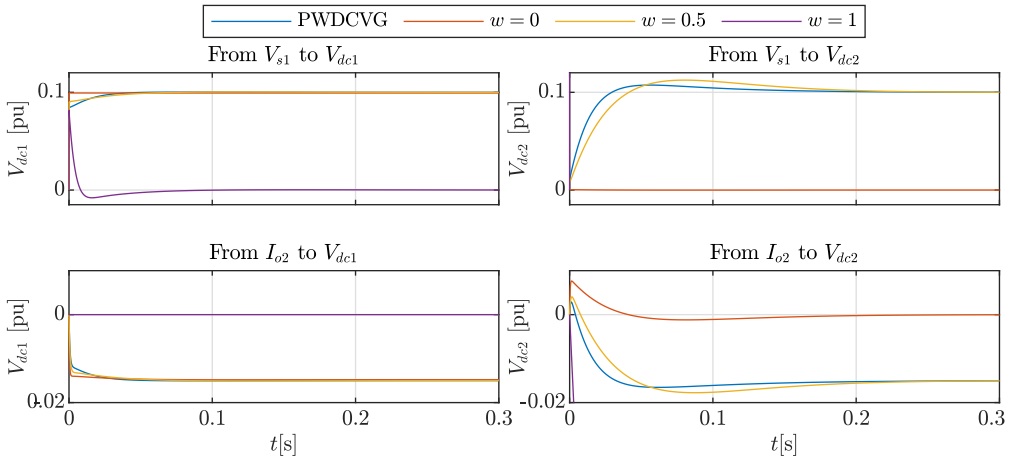

Figure 6.15: Step response for the different weight selection criteria for case $V_{s1} - I_{o2}$.

In Fig. 6.16, the steady-state value of V_{dc2} for different values of w is shown. In

this case, V_{dc2} is shown because there is a voltage source in side V_{s1}, thus ensuring a reasonable steady-state voltage in the corresponding network. The proposed formula for w achieves the same steady-state result as for $w = 0.5$. A zoom can be seen in the bottom graph of Fig. 6.16, for a range of $\pm 10\% V^*_{dc2}$ deviation from reference value. When $w > 0.924$, V_{dc2} steady-state is out of that range.

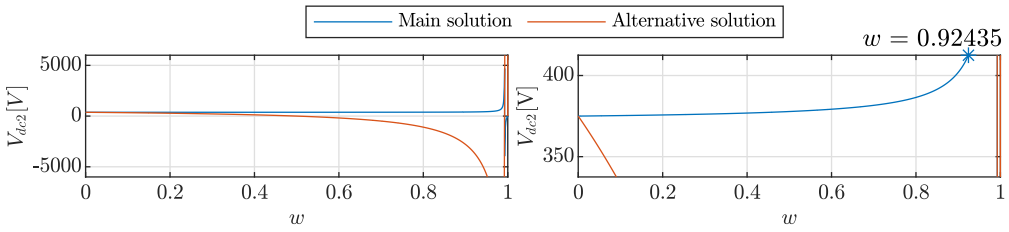

Figure 6.16: V_{dc2} equilibrium value for case $V_{s1} - I_{o2}$ for different weight values. Top: general view, showing the range for the main solution. Bottom: zoom to the range $0.9V^*_{dc2} < V_{dc2} < 1.1V^*_{dc2}$.

6.7.1.2 Case $\mathbf{I_{o1}}$-$\mathbf{V_{s2}}$

Same study has been carried out for $I_{o1} - V_{s2}$. In Fig. 6.17, the eigenvalues obtained for the different values of w. In the bottom figure, only the dominant eigenvalue for each w is shown.

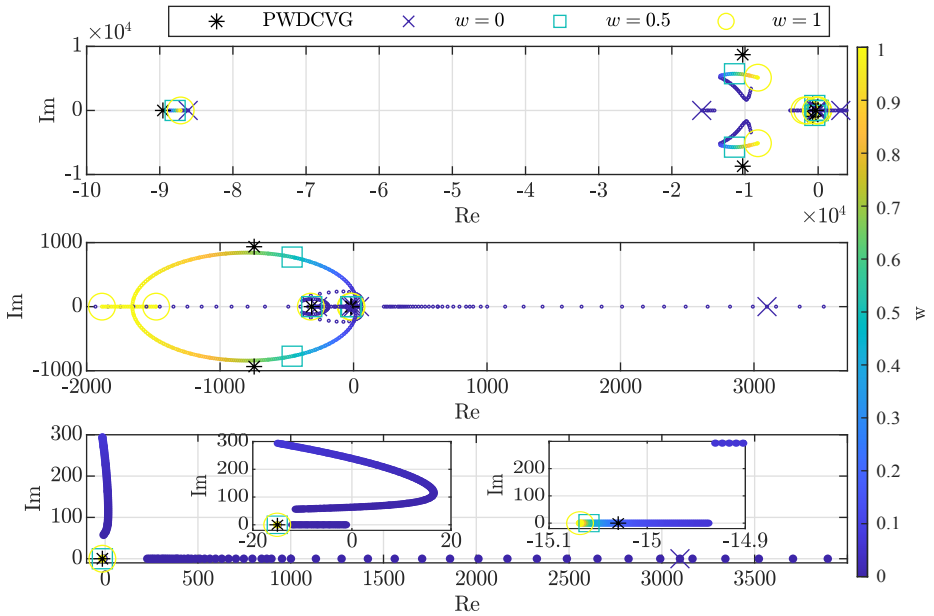

Figure 6.17: Eigenvalues for the different weight values for case $I_{o1} - V_{s2}$. Top: general view. Middle: zoom to the dominant eigenvalues. Bottom: only the dominant eigenvalue is shown.

It can be seen that, for this case, the range $0 \leq w < 0.00188$ and $0.00328 \leq w < 0.04209$, the system is unstable.

In Fig. 6.18, the step response for the different w selection criteria are shown. In all of them, the settling time for the proposed formula for w is smaller than that for $w = 0.5$. $w = 1$ is less affected by the variation on the inputs and faster, because the voltage control is focusing on the side which has no voltage source on it. Response for $w = 0$ is unstable, being most of it out of the range covered by the step responses of the other cases.

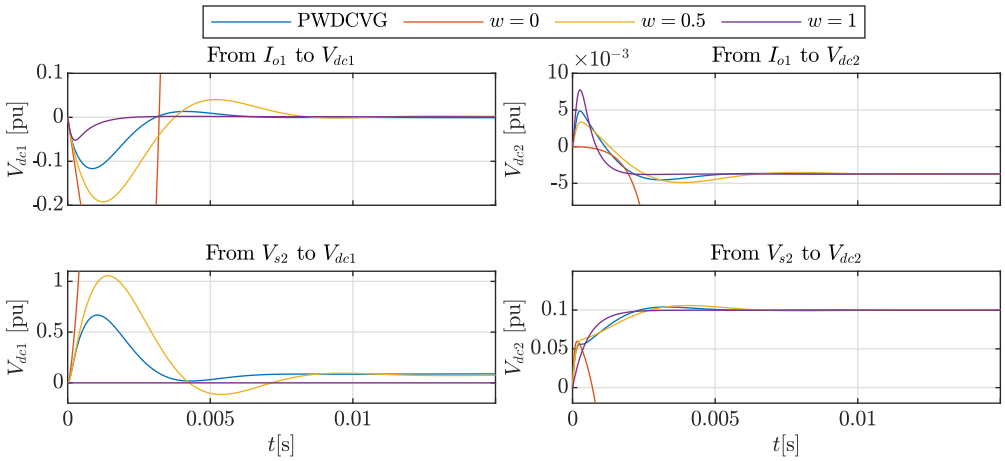

Figure 6.18: Step response for the different weight selection criteria for case $I_{o1} - V_{s2}$.

In Fig. 6.19, the steady-state value of V_{dc1} for different values of w is shown. The proposed formula for w achieves the same steady-state result as for $w = 0.5$. A zoom can be seen in the bottom graph of Fig. 6.19, for a range of $\pm 10\% V^*_{dc1}$ deviation from reference value. When $w < 0.0202$, V_{dc1} steady-state is out of that range.

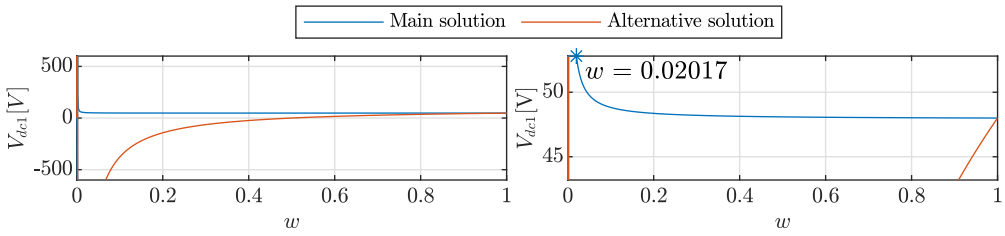

Figure 6.19: V_{dc1} equilibrium value for case $I_{o1} - V_{s2}$ for different weight values. Top: general view, showing the range for the main solution. Bottom: zoom to the range $0.9V^*_{dc1} < V_{dc1} < 1.1V^*_{dc1}$.

6.7.1.3 Conclusion

These results highlight the capacity of the proposed scheme to control voltage in either side of the converter. Although the voltage in each side is more affected to disturbances, if it is compared to the case in which the control focuses only on that side, the performance is not much worse. However, only with the proposed control scheme, the converter is able to operate in both cases presented before, $V_{s1} - I_{o2}$ and $I_{o1} - V_{s2}$.

The proposed formula achieves the same steady-state voltage result that for $w = 0.5$. This steady-result is a good choice for the weight selection criteria due to the fact that same per unit voltage is obtained in both converter outputs, as demonstrated before. The proposed formula, due to the weight calculation strategy based in a formula proportional to the voltage deviation on each side, makes the system faster rather than fixing $w = 0.5$ as shown in Fig. 6.15 and Fig. 6.18.

6.7.2 Parameter variation

In this section, the effect of the variation of a tunable parameter (virtual inductance, L) is shown. In Fig. 6.20, the eigenvalues obtained for different values of L are shown for case $V_{s1} - I_{o2}$.

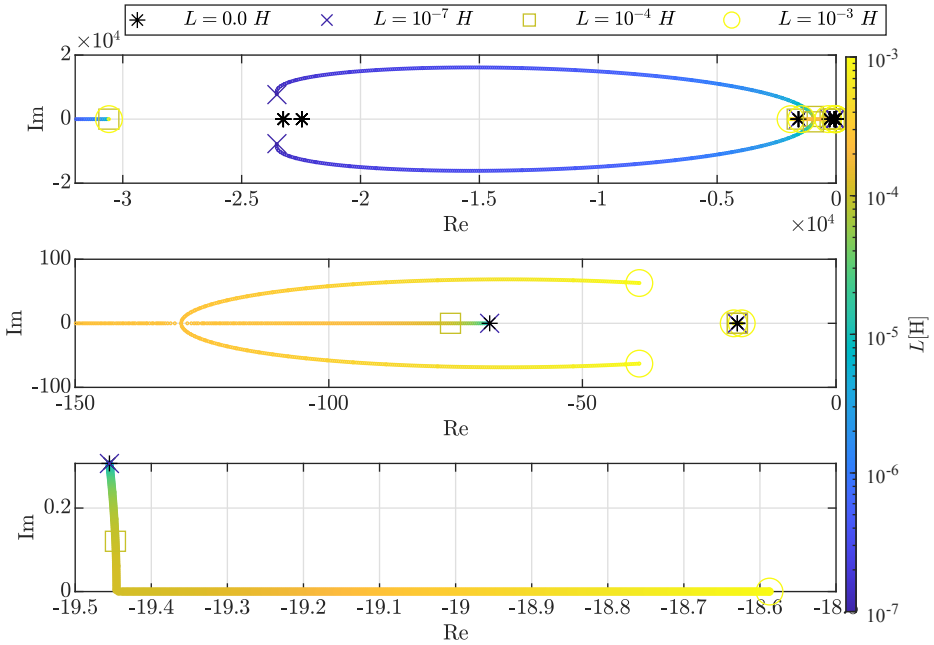

Figure 6.20: Eigenvalues for the different L values for case $V_{s1} - I_{o2}$. Top: general view. Middle: zoom to the dominant eigenvalues. Bottom: only the dominant eigenvalue is shown.

The case for $L = 0$ is included too, although it is important to remark that, for that case, the state number is reduced by 1 and the matrices vary, since I is no longer a state, but a linear combination of other states and the inputs. However, the case for $L = 0$ is almost identical to $L = 10^{-7}$ H. In fact, the dominant poles of $L = 0$ are not appreciable because they coincide with $L = 10^{-7}$ H eigenvalues.

In Fig. 6.21, the step response for the different values of L is shown. It can be seen that, for case $V_{s1} - I_{o2}$, there is no big difference between $L = 10^{-4}$ H and $L = 10^{-7}$ H behaviour, being this last one almost indistinguishable from $L = 0$. The lower the value of L, the faster the response and less overshoot, although there is no big difference from $L = 10^{-4}$ H.

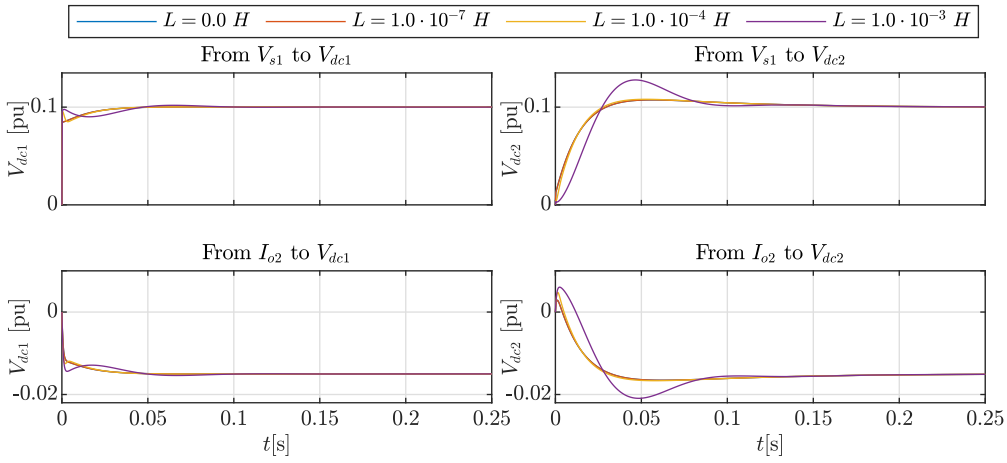

Figure 6.21: Step response for the different L values for case $V_{s1} - I_{o2}$.

Same study has been carried out for $I_{o1} - V_{s2}$. In Fig. 6.22, the eigenvalues obtained for the different values of L. Unlike case $V_{s1} - I_{o2}$, the system is only stable for $L = 0$ and $L = 10^{-7}$ H. The poles in -15 and -20 for $L = 10^{-3}$ H overlap those for the other three cases in almost the same position, being the dominant poles for $L = 10^{-7}$ H and $L = 0$.

In Fig. 6.23, the step response for the different values of L is shown. Those corresponding to $L = 10^{-3}$ H and $L = 10^{-4}$ H are not represented because they are unstable and their big oscillations make difficult to see the stable ones.

The shown results demonstrate that the virtual inductance effect on stability is negative. This is the reason why in most DCVG applications, the virtual impedance is just a resistor [6.11–6.16]. In the case for the present thesis, no virtual inductance is used, although it was considered in the control diagram and steady-state matrices for a more general approach. As shown, and as expected, the difference between $L = 10^{-7}$ H and $L = 0$ was negligible.

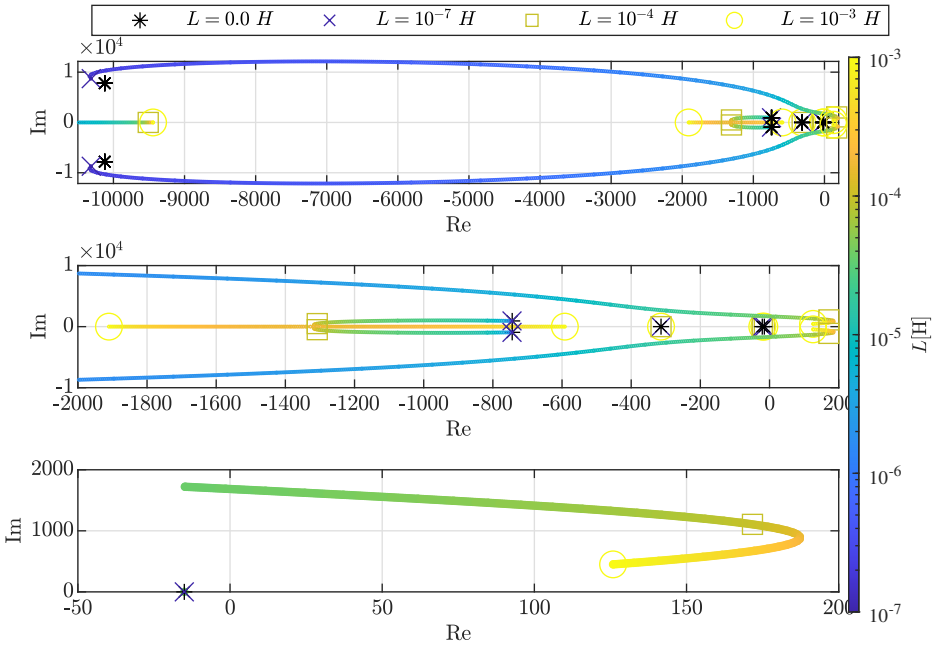

Figure 6.22: Eigenvalues for the different L values for case $I_{o1} - V_{s2}$. Top: general view. Middle: zoom to the dominant eigenvalues. Bottom: only the dominant eigenvalue is shown.

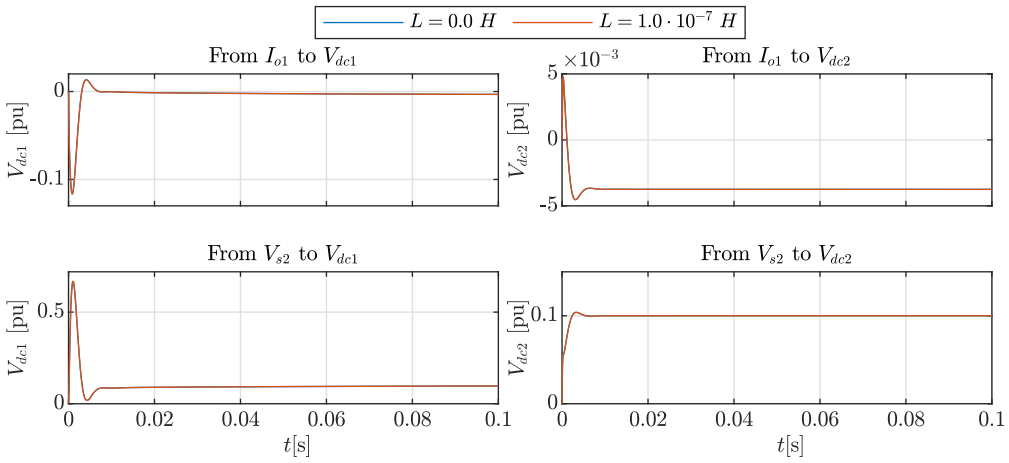

Figure 6.23: Step response for the different L values for case $I_{o1} - V_{s2}$.

6.8 Power sharing using P/V droop

As stated before, the proposed proportionally weighted DCVG achieves equal per unit voltage in both sides of the interlinking converter in steady-state. So, in steady-

state, the effect of the interlinking converter can be understood as an ideal transformer which can operate in DC (and with no short-circuit impedance).

Thus, the equivalent circuit of the complete system can be obtained just expressing everything in per unit values, or referring variables of one side to the voltage base of the other. This allows P/V droop-controlled converters in both networks to collaborate with power sharing even for loads from the other side.

This power sharing mechanism is analysed with a simulation. As shown in Fig. 6.24, when $w = 0$, the droop-controlled converter in side 2 does not collaborate in any change in current load because $w = 0$ makes the voltage control achieve $V_{dc2} = V^*_{dc2}$ in steady-state, acting as a slack for that network. The same happens for $w = 1$ with converter in side 1. However, if $w = 0.5$ or the proposed formula is used, they can share the power as if they were in the same network, being the interlinking converter just a node on it. For a better highlighting of this, the loads were placed symmetrically with respect to both PECs, being the analyzed grid a 3-node network, with two extreme nodes with both droop-controlled converters, V_{s1} and V_{s2}, and loads I_{o1} and I_{o2}, in the converter outputs, which represent one single node in the middle of both droop-controlled converters and with same per unit value for the cable connecting to both of them.

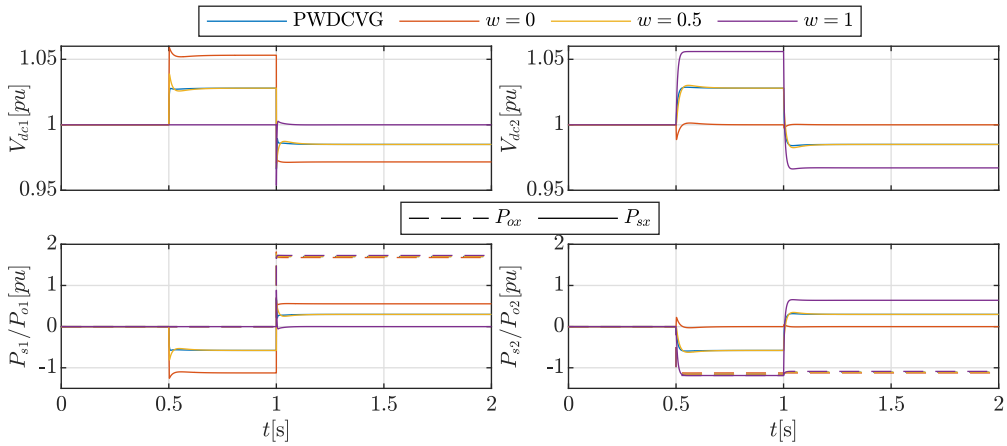

Figure 6.24: Power sharing comparison between the proposed method (PWDCVG) and different fixed values of w. Top row: voltage at the interlinking converter in side 1 (left) and 2 (right). Bottom row: power production/consumption of the elements in side 1 (left) and 2 (right). P_{sx} (continuous) is the power production of the droop control PECs in side x, P_{ox} (dashed) is the power consumption of the loads connected in side x.

Of course, in non-symmetrical scenarios, the power sharing between them would not be perfect, as it always happens for P/V droop. But it allows collaboration between both networks, which is not possible for $w = 0$ or $w = 1$.

The secondary control explained in Chapter 4 can be directly applied to this method, just using the per unit equivalent or referring one of the sides to the volt-

age base of the other one. This is shown in Fig. 6.25, applied to the same scenario of Fig. 6.24 for the PWDCVG. It can be seen that the secondary control is able to obtain 1 pu voltage in both converter outputs, without changing the power sharing between droop-controlled converters in both sides.

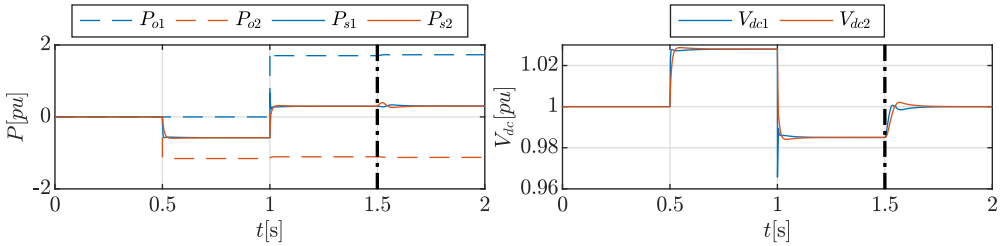

Figure 6.25: Secondary control applied to the proposed P/V droop based mechanism. Vertical line indicates the execution of the proposed secondary control algorithm. Left: per unit power output, P_{sx} (continuous) is the power production of the droop control PECs in side x, P_{ox} (dashed) is the power consumption of the loads connected in side x. Right: per unit voltage output in each side.

6.9 Conclusions

This chapter proposes a new control strategy based on a modification of the DCVG control to adapt the control to make it able to control voltage in either side of the converter, being able of operate as grid-forming unit in either side. A weight is given to each side so that the control focuses more on that side.

The proposed weighted DCVG is controlled using weights proportional to deviation of each converter side voltages from rated point. This makes the control to focus in the grid which is more in need. The results show the capability of the converter of operating any scenario, provided that at least in one of the grids there is a converter providing the required power, either with grid-forming units or grid-feeding with P/V droop. It was shown that, in steady-state, the proposed control achieves the same voltage deviation in both sides, obtaining a good balance between the neediness in both grids.

References

[6.1] T. Dragičević, X. Lu, J. C. Vasquez, and J. M. Guerrero, "DC Microgrids-Part II: A Review of Power Architectures, Applications, and Standardization Issues," *IEEE Transactions on Power Electronics*, vol. 31, no. 5, pp. 3528–3549, 2016.

[6.2] T. Dragičević, J. C. Vasquez, J. M. Guerrero, and D. Skrlec, "Advanced LVDC Electrical Power Architectures and Microgrids: A step toward a new generation of power distribution networks." *IEEE Electrification Magazine*, vol. 2, no. 1, pp. 54–65, 2014.

[6.3] T. L. Vandoorn, B. Renders, L. Degroote, B. Meersman, and L. Vandevelde, "Active Load Control in Islanded Microgrids Based on the Grid Voltage," *IEEE Transactions on Smart Grid*, vol. 2, no. 1, pp. 139–151, 2011.

[6.4] H. Liu, Y. Yang, X. Wang, P. C. Loh, F. Blaabjerg, W. Wang, and D. Xu, "An Enhanced Dual Droop Control Scheme for Resilient Active Power Sharing Among Paralleled Two-Stage Converters," *IEEE Transactions on Power Electronics*, vol. 32, no. 8, pp. 6091–6104, 2017.

[6.5] J. Wang, C. Dong, C. Jin, P. Lin, and P. Wang, "Distributed Uniform Control for Parallel Bidirectional Interlinking Converters for Resilient Operation of Hybrid AC/DC Microgrid," *IEEE Transactions on Sustainable Energy*, vol. 13, no. 1, pp. 3–13, 2022.

[6.6] X. Li, L. Guo, Y. Li, C. Hong, Y. Zhang, Z. Guo, D. Huang, and C. Wang, "Flexible Interlinking and Coordinated Power Control of Multiple DC Microgrids Clusters," *IEEE Transactions on Sustainable Energy*, vol. 9, no. 2, pp. 904–915, 2018.

[6.7] A. Navarro-Rodríguez, P. García, C. Gómez-Aleixandre, and C. Blanco, "Cooperative Primary Control of a Hybrid AC/DC Microgrid based on AC/DC Virtual Generators," *IEEE Transactions on Energy Conversion*, pp. 1–14, 2022.

[6.8] C. Gómez-Aleixandre, A. Navarro-Rodríguez, G. Villa, C. Blanco, and P. García, "Sharing Control Strategies for a Hybrid 48V/375V/400Vac AC/DC Microgrid," in *2020 IEEE Energy Conversion Congress and Exposition (ECCE)*, 2020, pp. 3900–3907.

[6.9] Á. Navarro-Rodríguez, P. García, R. Georgious, and J. García, "Adaptive Active Power Sharing Techniques for DC and AC Voltage Control in a Hybrid DC/AC Microgrid," *IEEE Transactions on Industry Applications*, vol. 55, no. 2, pp. 1106–1116, Mar. 2019.

[6.10] T. K. Vrana, J. Beerten, R. Belmans, and O. B. Fosso, "A classification of DC node voltage control methods for HVDC grids," *Electric Power Systems Research*, vol. 103, pp. 137–144, 2013. [Online]. Available: https://www.sciencedirect.com/science/article/pii/S0378779613001193

[6.11] Y. Guo, J. Meng, Y. Wang, and C. Wang, "A Virtual DC Machine Control Strategy for Dual Active Bridge DC-DC Converter," in *2019 IEEE Innovative Smart Grid Technologies - Asia (ISGT Asia)*, May 2019, pp. 2384–2388.

[6.12] W. Yi, D. Yi, X. Hu, X. Wang, and F. Shi, "Modeling and simulation of DC micro-grid based on virtual motor control," in *2017 IEEE Transportation Electrification Conference and Expo, Asia-Pacific (ITEC Asia-Pacific)*, Aug. 2017, pp. 1–6.

[6.13] H. Hu, M. Zhu, X. Li, and X. Cai, "Virtual DC machine based islanding detection method in DC distribution system and stability enhancement," in *IECON 2020 The 46th Annual Conference of the IEEE Industrial Electronics Society*, Oct. 2020, pp. 3277–3282.

[6.14] N. Zhi, Y. Ding, and L. Du, "Virtual DC Generator Control Strategy Based on Differential Compensation," in *2019 IEEE Energy Conversion Congress and Exposition (ECCE)*, Sep. 2019, pp. 1454–1458.

[6.15] D. Huang, S. Fan, and B. Fan, "Virtual DC Generator Control Strategy for Load DC-DC converter," in *2015 International Symposium on Computers & Informatics*. Atlantis Press, Jan. 2015, pp. 1359–1368.

[6.16] T. Shucheng, D. Ge, Z. Hui, Z. Na, and X. Xi, "Virtual DC machine control strategy of energy storage converter in DC microgrid," in *2016 IEEE Electrical Power and Energy Conference (EPEC)*, Oct. 2016, pp. 1–5.

Chapter 7

Conclusions and future work

7.1 Conclusiones

Esta tesis ha abordado el diseño de una arquitectura de control coordinado para microrredes malladas híbridas AC/DC. Las ventajas de este tipo de microrred se presentaron en el Capítulo 2, junto con los desafíos para su control coordinado. Se ha optado por el control jerárquico como forma de operar la microrred, tratando de evitar la dependencia de las comunicaciones para un funcionamiento estable y tratando de aprovechar los beneficios de la flexibilidad que brinda la configuración en malla. Las principales contribuciones de la tesis están relacionadas con diferentes capas del control jerárquico.

- En el Capítulo 3, se analiza una nueva arquitectura para una microrred híbrida AC/DC, que incluye las topologías y el control de los convertidores de potencia. Se ha probado con éxito una técnica para el equilibrio de los dos alimentadores DC, proporcionada por el convertidor multipuerto de 3 niveles. Se han establecido diferentes modos de funcionamiento, teniendo la fiabilidad como factor de diseño clave. Dos de ellos han sido demostrados con éxito mediante simulación. Los resultados obtenidos derivan de la aportación "Diseño de una microrred híbrida [CP3]".
- En el Capítulo 4 se propuso un control secundario flexible para el control primario basado en droop. El método se caracteriza por su versatilidad, permitiendo explotar el potencial de una configuración de malla como la que se presenta en la microrred diseñada en el Capítulo 3. El método puede lograr cualquier distribución de potencia entre los convertidores de potencia y la tensión nominal en cualquier nodo dado de la microrred. Esto permite el uso del método para tareas que normalmente pertenecen al control secundario (eliminar la desviación de los valores nominales debido al droop y el reparto de potencia según los coeficientes

de droop), pero también para incorporar criterios de reparto de potencia que normalmente pertenecen a la capa de control terciario. , como la optimización económica del uso de Energy Storage Systems considerando las pérdidas y los precios de la electricidad, como se ha demostrado. El método se basa en el cálculo de la solución óptima de flujo de potencia considerando cualquiera de los criterios mencionados y el desplazamiento de las características de caída de cada convertidor para que coincidan con su potencia de salida y el nivel de tensión calculado en la solución. Dado que el método utiliza parámetros de la microrred para su funcionamiento, se ha analizado el efecto de los desajustes de estimación, presentando un buen rendimiento incluso para errores de estimación importantes. La necesidad de estimar los parámetros de la red ya ha sido considerada en la literatura. De las alternativas existentes, se prefieren aquellas basadas en resolver el problema de flujo inverso, ya que requieren los mismos datos necesarios para el método propuesto. Además de eso, el control propuesto solo requiere una aplicación del algoritmo para lograr la solución óptima. Eso lo hace robusto frente a retrasos en la comunicación o pérdidas de datos y con bajos requerimientos de ancho de banda de comunicación si se compara con controles secundarios basados en integradores o reguladores PI que dependen de sucesivas aplicaciones de la ley del algoritmo de control en intervalos regulares debido a la integración. Los resultados obtenidos derivan de la contribución "Control secundario flexible y su uso en optimización [JP1, CP2]".

- En el Capítulo 5 se presentó un control primario para AC sin desviación de frecuencia de estado estable basado en un droop de valor complejo. En lugar de utilizar las fórmulas utilizadas para derivar el clásico droop $P/f + Q/V$, para líneas inductivas, o su variante $P/V + Q/f$ droop, para líneas resistivas, que expresan el flujo de potencia en términos de amplitud y fase de tensión, se consideraron las ecuaciones en descomposición dq. Se derivó un droop que relaciona P y Q con ambas componentes de la tensión, considerando el acoplamiento entre ambas ecuaciones debido a líneas no puramente inductivas/resistivas, que depende de la relación R/X. El droop propuesto ofreció un buen desempeño en comparación con los droops $P/f + Q/V$ y $P/V + Q/f$ para diferentes valores de la relación R/X. Se analizó el desempeño bajo desajustes de estimación para la relación R/X, mostrando un desempeño razonablemente bueno incluso para errores muy grandes en el desajuste. Los resultados obtenidos derivan de la contribución "Control primario para AC sin desviación de frecuencia en estado estacionario [CP1]".

- En el Capítulo 6, se propuso una estrategia de control para interconectar convertidores DC/DC, basada en el concepto de generador virtual DC. El método propuesto fue capaz de proporcionar capacidad de formación de red dual al convertidor, es decir, la capacidad de lograr un nivel de tensión estable en ambos lados del convertidor que solo requiere un gr.

7.2 Conclusions

This thesis has addressed the design of a coordinated control architecture for hybrid AC/DC mesh microgrids. The advantages of such type of microgrid were presented in Chapter 2, together with the challenges for its coordinated control. Hierarchical control has been chosen as a way to operate the microgrid, trying to avoid dependency on communications for stable operation and trying to exploit the benefits of the flexibility given by the mesh configuration. The main contributions of the thesis are related with different layers of the hierarchical control.

- In Chapter 3, a novel architecture for a hybrid AC/DC microgrid, including the power converters topologies and control has been analyzed. A technique for the balancing of the two DC feeders, provided by the 3-level multiport converter has been successfully tested. Different operating modes, having reliability as the key design factor have been stated. Two of them have been successfully demonstrated by simulation. The results obtained derive from contribution "Design of a hybrid microgrid [CP3]".

- A flexible secondary control was proposed in Chapter 4 for droop-based primary control. The method is characterized by its versatility, allowing the exploitation of the potential of a mesh configuration like the one presented in the microgrid designed of Chapter 3. The method can achieve any power sharing among the power converters and nominal voltage in any given node of the microgrid. This allows the use of the method for tasks that normally belong to secondary control (eliminate deviation from nominal values due to the droop and power sharing according to the droop coefficients), but also to incorporate power sharing criteria that normally belong to the tertiary control layer, like economic optimization of the use of Energy Storage Systems considering losses and electricity prices, as it has been demonstrated. The method is based on the calculation of the optimum power flow solution considering any of the mentioned criteria and the displacement of the droop characteristics of each converter so that they match their output power and voltage level calculated in the solution. Since the method uses grid parameters for its operation, the effect of estimation mismatches has been analysed, presenting a good performance even for important estimation errors. The necessity of estimating grid parameters has been already considered in the literature. From the existing alternatives, those based in solving the inverse flow problem are preferred, since they require the same data needed for the proposed method. Besides that, the proposed control only requires one application of the algorithm to achieve the optimum solution. That makes it robust against communication delays or data losses and with low requirements for communication bandwidth if compared with secondary controls based on integrators or PI regulators which depend on successive applications of the control algorithm law in regular intervals due to the integration. The results obtained derive from contribution "Flexible secondary control and its use in optimization [JP1, CP2]".

- A primary control for AC with no steady-state frequency deviation was presented in Chapter 5 based on a complex-valued droop. Instead of using the formulas used for derived the classical $P/f + Q/V$ droop, for inductive lines, or its variant $P/V + Q/f$ droop, for resistive lines, which express power flow in terms of voltage amplitude and phase, the equations in dq decomposition were considered. A droop relating P and Q with both components of the voltage was derived, considering the coupling between both equations due to non purely inductive/resistive lines, which depends on R/X ratio. The proposed droop offered a good performance compared to $P/f + Q/V$ and $P/V + Q/f$ droops for different values of R/X ratio. The performance under estimation mismatches for the R/X ratio was analysed, showing a reasonably good performance even for very large errors in the mismatch. The results obtained derive from contribution "Primary control for AC with no frequency deviation in steady-state [CP1]".

- In Chapter 6, a control strategy for interlinking DC/DC converters was proposed, based on the DC virtual generator concept. The proposed method was able to provide dual grid-forming capability to the converter, i.e., the capability of achieving stable voltage level in both sides of the converter just requiring one grid supporting element in one of the networks (in this case, grid-feeding converter with P/V droop). This lowers the requirement for grid-forming units in the microgrid. The state-space model of the interlinking converter with the proposed control has been derived. Small-signal analysis has been applied to this model, studying the effect of parameter variations and comparing the performance of the proposed method with the already existing DC virtual generator control. The results highlight the capability of the converter to guarantee the stability in a wider variety of grid conditions. Besides that, a power sharing strategy based on the use of the proposed strategy has been demonstrated. This is done by applying a P/V droop to the converter in both sides of the network, allowing the proposed dropp-based control to react to changes in the other network. The secondary control proposed in Chapter 4 was used to eliminate the deviation due to this P/V droop strategy. The results obtained derive from contribution "Interlinking DC/DC converter control with dual grid-forming capability".

7.3 Future work

New research opportunities appear as a possible continuation of the contributions presented for this thesis. The following lines of research are considered:

- In order to improve the coordinated control, an analysis of the limits for the capacity of NPC converters to compensate unbalances in the DC buses should be performed. This would allow the NPC converters to know the margin they have before reaching their limits, so that connection of loads that would exceed the unbalance capacity can be foreseen and avoided. Since their limitation depends

on the current injection in the AC side, the coordinated control can vary their production (especially regarding reactive power) so that they can increase their capability in case of necessity.

- Study of a more complete optimization problem to be applied with the proposed secondary control. The application has been applied to a segment of the microgrid, being an optimization involving just one variable (the power sharing ratio between the involved converters). Further study could analyse more complete problems, like considering losses in the Power Electronic Converters or multivariable optimization (for example, including more converters to share the production).

- Analysis of the feasibility of adapting the proposed complex-valued droop for its use in harmonic and negative-sequence power sharing. Applying the same idea of the complex-valued droop, it should be possible to control the power sharing for harmonics and negative-sequence. However, this is technically demanding due to the difficulty in isolating the non-fundamental components of voltages and currents. Therefore, the challenges are related with the proper filtering of the signals and different filtering alternatives should be analysed to see if they can have a sufficient filtering capability which allows a proper operation of the droop.

- The application of the proposed weighted DC Virtual Generator has been restricted to 2-port DC/DC converters. The adaptation of the proposed method to AC/DC or multiport applications would be of great interest. The detailed state-space study performed during the thesis could ease the study.

- Large-signal stability analysis of the proposed state-space model of the converter might be an interesting tool for the proposed state-space modeling. The analysis of the proposed weighted DC Virtual Generator has been carried out using small-signal stability, which requires a linearization of the system. Although the stability has been verified with simulations considering a wide variety of scenarios showing agreement with the small-signal analysis, large-signal stability can be more reliable since it does not require any approximation. Although its study is more complex, it would complete all the work in that field carried out during the thesis and it can be useful for future work with very nonlinear models, like the ones involving interlinking converters.

- Some of the proposals were validated only with real time simulations or Hardware-in-the-loop results. Experimental validation in the designed microgrid would be of high interest. However, the proposed microgrid has an important size, so the complete construction of it would require several years, although some of the elements do not require the complete microgrid to be validated. For example, although the secondary control proposed in Chapter 4 was validated with a partial implementation of the microgrid, it was done by using Speedgoat real-time simulator as the central controller and using its communication channels. The implementation of this secondary control with our own central controller

and communication architecture can be of important interest, together with the implementation of the online parameter estimation techniques found in the literature.

Appendix A

Journal publications

A.1 Adaptive Droop Controller for a Hybrid 375 Vdc/48 Vdc/400 Vac AC/DC Microgrid

Adaptive Droop Controller for a Hybrid 375Vdc/48Vdc/400Vac AC/DC Microgrid

Carlos Gómez-Aleixandre, Ángel Navarro-Rodríguez, Geber Villa, Cristian Blanco and Pablo García
Dept. of Electrical, Electronics, Systems & Computers Engineering
University of Oviedo, LEMUR Group
Gijón, 33204, Spain
Email: gomeztcarlos@uniovi.es, navarroangel@uniovi.es, villageber@uniovi.es,
blancocristian@uniovi.es, garciafpablo@uniovi.es

***Abstract*—This paper studies the sharing control scheme for a Hybrid 48V/375V/400Vac AC/DC Microgrid, based on classical droop control and a novel approach for secondary control. In this paper, both the dc and ac grids are controlled by a P/V droop strategy. At the ac grid, this assumes a main resistive component in the distribution line impedance. The droop control voltage error in steady state is compensated by a novel and simple secondary control approach. The proposed control strategy is based on the calculation of the optimum power flow in each operating point and the real-time modification of the droop characteristics of the converters involved in the power flow calculation. The proposed control is also capable of eliminating the induced voltage drop when using virtual impedance and incorporating any power sharing criteria for the converters contributing to the power production, being this flexibility one of its more important characteristics.**

***Index Terms*—Microgrids, hybrid power systems, secondary control, voltage control, load flow control.**

I. Introduction

The future electricity grid is gradually moving in the direction of dc distribution, due the envisaged lower distribution losses (compared with ac distribution) and the more efficient integration of renewables and distributed resources [1]–[3]. The evolution in power electronics and control technologies has enabled the development of dc Low-Voltage (LV) microgrids, which eases the integration of Energy Storage Systems (ESS). Although the pathway from traditional ac distribution systems to these new topologies integrating is not clear, it is reasonable to think that the new grids should take advantage of the already existing ac infrastructure, leading to the creation of hybrid ac/dc microgrids [1]. This hybrid approach should use Power Electronic Converters (PEC) in order to provide redundancy of power flows, thus increasing the grid resiliency [4].

Droop techniques are a widely used control strategy to coordinate PECs so that they can share power production. In dc, P/V droop is used, as well as for ac in LV distribution levels, due to the fact that the grid impedance in LV networks is mainly resistive [5]. Droop techniques cause a deviation from nominal values for the variables involved. In the case of P/V droop, a deviation from nominal voltage appears due to the droop operation. Apart from that,for the P/V droop, the active power sharing among the converters is not always accurate, as the converters normally see different voltages. This is the same that happens for reactive power in Q/V droop.

Secondary control is used to eliminate voltage deviation due to the droop. Secondary control typically relies on integrators or PI regulators to eliminate the voltage deviation, both in ac [6] and dc [7]. This requires periodic calculations for the integrator to operate, gradually reducing the error every cycle.

This type of secondary control is normally divided into three categories: centralized, distributed and decentralized [8]. Centralized control has a central controller with communications with the control of each involved converter and measures the area voltage in order to eliminate its deviation, normally with a PI regulator, sending the same reference to all the converters. Distributed control operates in a similar way, but the PI regulator is implemented on each converter control, but with communication among all the converters. Decentralized control does not require neither central controller nor communications.

Secondary control can also be used to achieve accurate power sharing in P/V droops [9]. However, these methods add some extra complexity to the secondary control, with an extra control loop with a PI regulator and they are not suitable for decentralized secondary control, since they use some communication between PECs.

This paper shows a proposal of a hybrid ac/dc microgrid and the coordinated control of all the involved converters (ac/dc and dc/dc). The coordinated control is composed of a P/V droop control for the primary control and a novel approach for the secondary control. The proposed secondary control is applied to P/V droop, but it could be easily adapted to P/f+Q/V droop or other alternatives.

The proposed secondary control is able to eliminate the voltage deviation due to droop controllers based on a single calculation of the optimum power flow, shifting the droop characteristic of each converter according to voltage and power obtained from the power flow. This proposed solution has

The present work has been partially supported by the predoctoral grants program FPU for the formation in university teaching of Spain MECD under the grant IDs FPU16/05313 and FPU16/06829. This work also was supported in part by Spanish Ministry of Science and Innovation under grant MCI-20-PID2019-111051RB-I00 and the European Union's H2020 Research and Innovation programme under Grant Agreement No 864459 (UE-19-TALENT-864459).

TABLE I
COMPARISON BETWEEN THE PROPOSED SECONDARY CONTROL AND ALTERNATIVES IN THE LITERATURE BASED ON PI REGULATORS [8].

	Central controller required	Communication required	Robustness against data loss, communication delays or high latency	Power sharing accuracy	Flexibility to change the power sharing
Proposed	Yes	Yes	High	Yes	Yes
Centralized	Yes	Yes	Low	Extra PI reg.	No
Distributed	No	Yes	Medium	Extra PI reg.	No
Decentralized	No	No	Complete (no communication)	No	No

two main advantages compared to the aforementioned ones (centralized, distributed and decentralized).

Firstly, it is capable of achieving power sharing accuracy for the P/V droop without extra complexity. Besides, it is very flexible allowing any power sharing among the converters to be implemented, meanwhile the solutions in centralized and distributed controls to correct power sharing are designed for achieving one specific power sharing among the converters. The capability of the proposed secondary control to implement any power sharing allows the integration of any criteria for the power sharing, providing a high flexibility. For example, the secondary control can be combined with optimization problems, like the use of ESS contributing to the grid stability working in droop mode, meanwhile the secondary control optimizes its use in terms of cost. The proposed secondary control is also able to easily fix any reactive ac power sharing criteria, including active power loads that can contribute to the reactive power production if interfaced with a PEC, without additional droop control (Q/f droop is not required).

Secondly, since it requires only one calculation for operating point optimization, it has lower communication requirements and higher robustness against communication delays, high communication latency or loss of transmitted data compared to distributed and, especially, centralized secondary controls [9]. Decentralized secondary control does not require communications. However, considering communications infrastructure is always needed for coordination of distributed generation units during black start and microgrid real-time monitoring [8], the possibility of total lack of communications given by decentralized secondary control is not critical.

These differences are summarized in Table I.

This secondary control also provides the capability of compensating the voltage drop of virtual impedance techniques at the steady-state, [10]–[14]. As stated in [10] the virtual impedance can be used for many different purposes like active stabilization and disturbance rejection or, in the case of droop controllers, for making the line impedance more resistive/inductive, depending on the type of droop used.

However, this virtual impedance causes a voltage drop, that makes the effective total voltage drop greater, since the real output voltage of the converter is lower than the reference one (assuming that the converter is producing power). Some solutions can be found in the literature, like the use of a high-pass filter in the virtual impedance [11] to eliminate the effect of the virtual impedance in steady-state. However, this solution is only valid when the use of the virtual impedance is needed because of its transient effect (like the active stabilization aforementioned). When the steady-state effects of the virtual impedance are also needed, this solution is not valid. It is shown in this paper, how the designed secondary control can take into account this virtual impedance and eliminate the effect of its voltage droop. This is done by adding extra nodes to the optimum power flow calculation and selecting the physical connection of the converter, after the virtual impedance, to be the node having 1 p.u. voltage.

This paper extends the contributions in [15] by the same authors, adding the analysis of the power flow calculation convergence used in the proposed control, experimental validation of the proposed method and an example of how to take advantage of the proposed secondary control in optimization problems.

This paper is organized as follows. In Section II, the proposed hybrid microgrid topology and the power converters topologies are described. In Section III, the control strategy is explained, with a special focus in the proposed secondary control. Sections IV and V show the simulation and experimental results respectively. Section VI shows an example of how to integrate the proposed secondary control with optimization problems. Section VII presents the conclusions.

II. PROPOSED MICROGRID TOPOLOGY

The hybrid ac/dc network architecture [15] proposed in this paper is shown in Fig. 1 with the topologies of the converters in the shadowed blocks. The ac feeders and the dc lines (both ± 375 and 48 Vdc) are modeled as purely resistive lines, assuming a maximum voltage drop of 5 % at the end of the line for the rated power.

Being the lines purely resistive, if reactive power loads and references were set to 0, the ac part of the microgrid could be studied as if it was dc. Being the q-axis component of the voltages equal to 0 in steady-state, the d-axis component is equivalent to a dc voltage for the calculations.

For this reason, the analysis done in the paper starts with the dc case, since it is also a simplified study of the ac part. From dc solution, some modifications are done in order to include reactive power and possible non purely resistive impedances in the calculations for the ac complete solution.

As explained in Section I, virtual impedance can be used for different purposes, introducing an induced voltage drop. In this paper, virtual impedance is used for the converters in the ac feeders and is taken into account too for compensating its voltage drop.

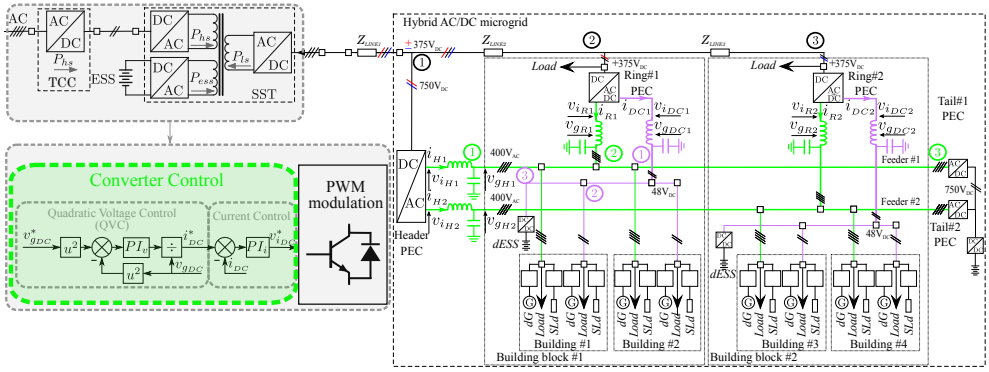

Fig. 1. Proposed system level grid infrastructure [15]. Shadowed blocks in the left side indicates the simplification of the SST connection as a dc/dc converter controlling the voltage.

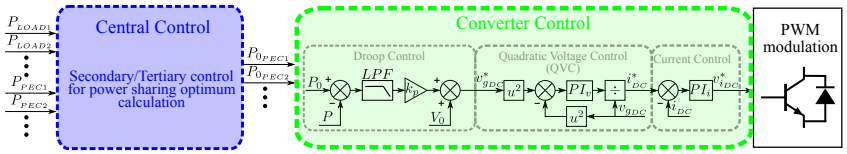

Fig. 2. General control diagram for converters in the 48 Vdc network. P_{LOAD_i} is the aggregate load connected to node i, P_{PEC_i} is the measured power output of the converter and $P_{0_{PEC_i}}$ is the power offset for the converter connected to node i.

III. Coordinated control

As explained in the previous sections, the coordinate control of the power converters is done with a P/V droop control, both for the ac feeders and the 48 Vdc network.

This droop control acts as a primary control, making possible that all the converters which can deliver power, either coming from the connection to the main ac grid or from ESS, contribute to the power sharing.

The power sharing at the primary control level is achieved without requiring communication among the power converters. However, communication among them is used for upper level control, namely secondary and tertiary control for enhanced power sharing. This is later discussed in the paper.

A. ±375 *Vdc grid control*

In the ±375 Vdc grid, the SST provides connection to the mains supply and to the central ESS. In the present paper, this is simplified as a dc/dc converter connected to a dc voltage source since the focus is in the hybrid microgrid. This dc/dc converter controls the voltage difference between the positive and the negative bus (750 Vdc) as shown in Fig. 1.

Header PEC (HPEC), connected to node 1, is in charge of the dc bus balancing [16], due to its neutral point clamped topology, assuring that the voltage in both buses is 375 Vdc (one positive and one negative with respect to the neutral).

These two buses are distributed so that loads can be directly connected to these dc buses. They can be connected to either bus, so loads can be strongly unbalanced. Apart from that, Ring#1 PEC is connected to +375 Vdc bus and Ring#2 PEC is connected to −375 Vdc bus.

These two buses are distributed, so that loads can be directly connected to them. Due to the different loads at each of the buses (Ring#1 PEC at the +375 Vdc and Ring#2 PEC to the −375 Vdc bus respectively), they could become strongly unbalanced thus making much needed the balancing control implemented at the HPEC.

B. 48 *Vdc network control*

In Fig. 2 the control diagram for the 48 Vdc grid is shown. The control system is separated into two main blocks; 1) the internal converter control and 2) the central control. The internal control implements the voltage control using a quadratic approximation [17] and relies on a cascaded-architecture with an internal current controller. The references for the voltage control are given by a P/V droop. Connected to the internal control, the central controller provides the power offsets (P_0) to the different converters based on the secondary control, whose effect is to shift the droop curve.

The droop characteristic equation is shown in (1), where V is the resulting voltage from the droop control; k_p is the droop coefficient; P, the measured power output; P_0 and V_0

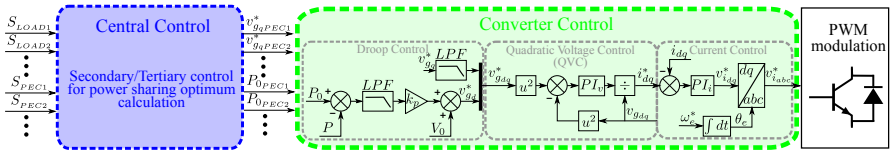

Fig. 3. General control diagram for converters in the ac feeder. S_{LOADi} is the aggregate load connected to node i, S_{PECi} is the measured power output of the converter and $P_{0_{PECi}}$ is the active power offset for the converter connected to node i. Both S_{LOADi} and S_{PECi} mean P and Q are required (being $S = P + jQ$).

the offset power and voltage (equal to rated voltage in the study case).

$$V = k_p(P_0 - P) + V_0 \tag{1}$$

C. 400 Vac feeder control

The general control scheme for the converters in the ac feeder is shown in Fig. 3, which is completely equivalent to the 48 Vdc network case except from the decomposition in the synchronous dq reference frame. Details about cross-coupling and feedforward terms shown in [17] are omitted due to space constraints. The reference for the d axis voltage control is given by a P/V droop. The central controller plays the same role as in the case of the 48 Vdc network. In here, also the q-axis voltage reference is provided to the different converters.

D. Secondary control

For the secondary control, a new strategy has been used. The idea consists on changing the P/V droop characteristics of each converter, by modifying the offset power P_0 in (1), so that they match the desired solution. For this paper, the chosen solution is to have a power sharing among the droop controlled converters proportional to each converter power rating and a voltage of 1 p.u. at a given specific node. In general, the output of the main converter of the corresponding grid is used as the 1 p.u. reference.

This secondary control is applied to the 400 Vac feeder and the 48 Vdc network. Considering the proposed grid topology in each case, the loads at each node and the reference output power of each converter, the power flow can be calculated, resulting in the voltage profile at each node considering one of the nodes is set to 1 p.u. For these calculations, only droop-controlled converters participating in the power sharing are taken into account as controllable converters, the remaining are seen as bidirectional loads.

The reference power output of each converter can be selected with different criteria. For the calculations presented hereafter, the sharing among the converters is proportional to the power rating of each converter. If any other criteria is used, this method could easily accommodate to it without further implications.

In this case, as shown in Fig. 1 both studied cases, the ac feeder or the 48 Vdc network, are radial networks, without rings inside. This eases the calculation of the power flow. Different grid topologies, including mesh and ring networks could also be considered, thus increasing the computational burden for the power flow calculations [18].

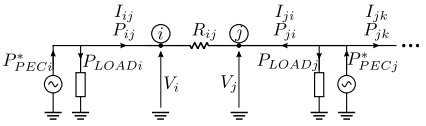

Fig. 4. Power flow diagram. P_{ij} (I_{ij}) is the power (current) flow from node i to j, P_{ji} (I_{ji}) from j to i and P_{jk} (I_{jk}) from j to k. P^*_{PECi}: reference power for converter at node i, P_{LOADi}: total connected load in that node and V_i: voltage in that node. R_{ij} is the equivalent impedance connecting node i and j (it should include both wires impedance in dc).

Calculations required for dc and ac case are very similar, but dc case is presented before, since it is simpler and more straightforward because it does not include reactive power. After presenting both cases, the possibility of including virtual impedance is presented too.

1) Secondary control in dc: Knowing the reference power and the voltage at each converter, obtained from the power flow, P_0 can be calculated so that the droop characteristic, whose equation is shown in (1), meets the requirements. The method is explained using network shown in Fig. 4.

In Fig. 5, the flowchart for the method is shown. Step 1 is for initialization, starting assuming no losses. Step 2 to 6 perform an iteration of the power flow. After step 6, a stop criterion is checked for deciding whether to stop or to continue with the next iteration, for a more precise calculation of the power flow solution. An analysis of power flow convergence is shown later in Subsection III-E. Step 7 calculates the offset power for each converter, P_{0PECi}, so that the droop curve of each converter matches the solution from the power flow, as shown in Fig. 6. This offset power is sent back to the converter control to modify their droop (see Fig. 2).

2) Secondary control in ac: The implementation of the secondary control in ac resembles the dc case but power (S, in this case), voltage, impedance (Z) and currents are complex magnitudes.

Fig. 7 show the corresponding calculations for ac. The only significant difference is in the last step. Since the droop is applied to P and V_d (real part of S and V complex vectors), the equation for calculating the active power offset relies on the real V component (d-axis), while imaginary (q-axis) component is sent as a direct reference to the converters.

Apart from the differences due to the use of complex variables in ac, the voltage drop for the dc case is calculated as $RI = R\dfrac{P}{V}$ meanwhile in ac it is $ZI = Z\dfrac{\overline{S}}{\sqrt{3}\cdot\overline{V}}$, because the ac network is three-phase.

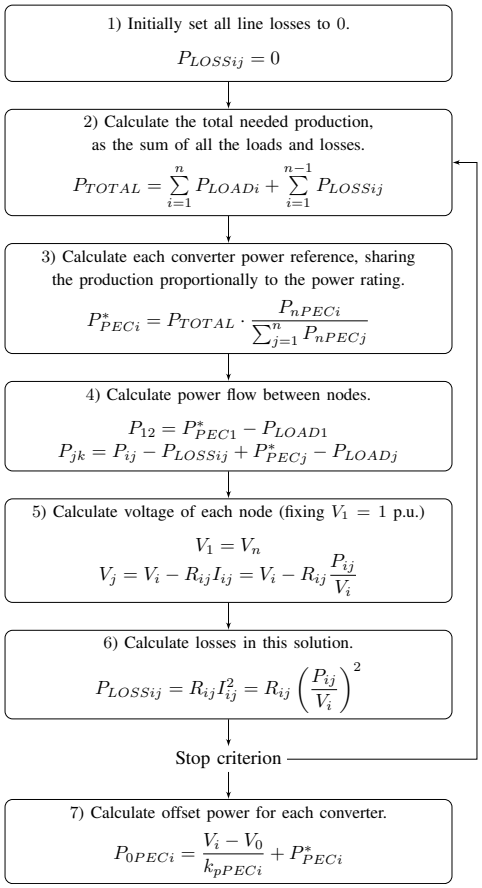

Fig. 5. Flowchart for secondary control in dc. i, j and k denote any three consecutive nodes.

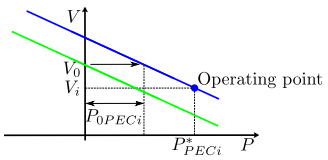

Fig. 6. Droop curve shift for fulfilling power flow solution. Green: base case with $P_{0PECi} = 0$ and blue: final solution.

3) Secondary control including virtual impedance: As explained in Section II, when virtual impedance is considered, the proposed secondary control allows for the compensation of the induced voltage drop. The compensation is achieved by adding virtual nodes to the power flow calculation shown in Fig. 7.

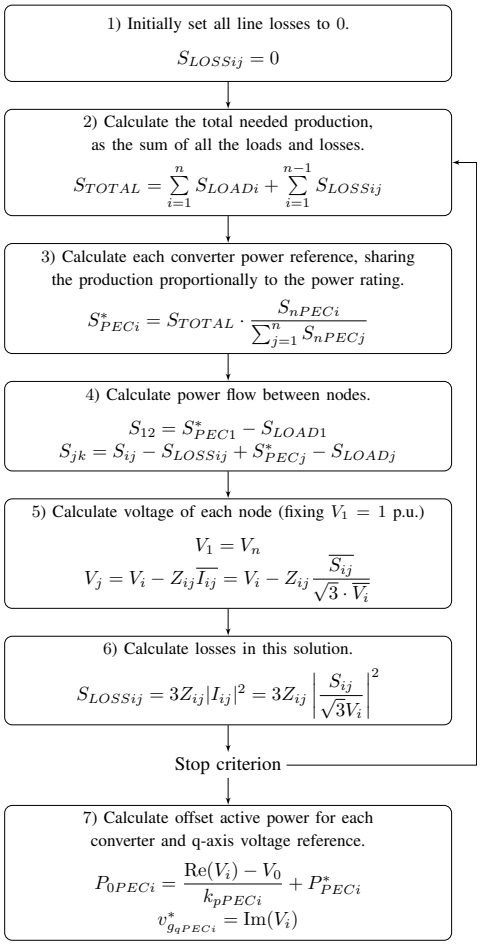

Fig. 7. Flowchart for secondary control in dc. i, j and k denote any three consecutive nodes. For obtaining a more compact expression, active and reactive power equations are presented in its complex form, so they are joint into one equation with $S = P + iQ$, using also $Z = R + iX$. $\overline{x}$, $\mathrm{Re}(x)$ and $\mathrm{Im}(x)$ are the conjugate, real part and imaginary part of a complex vector.

In the example shown in Fig. 7, voltage in physical node 1, V_1, is selected to be 1 p.u., obtaining this voltage at the physical connection of the PEC to that node. A virtual node is added before the virtual impedance voltage drop. This can be seen in Fig. 8 with an example of a circuit including virtual impedance, $Z_{vir,i}$. The voltage in the node in which each converter is physically connected is V_i and it is the one

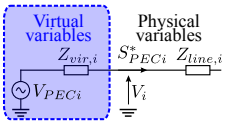

Fig. 8. Example of circuit including virtual impedance. V_i is the voltage at the physical connection of the corresponding PEC and $Z_{line,i}$, the coupling impedance. $Z_{vir,i}$ is the virtual impedance of the PEC and $V_{PEC,i}$, the (virtual) voltage before the voltage drop in the virtual impedance.

obtained from the power flow explained before. The voltage before the virtual impedance, $V_{PEC,i}$, can be obtained from V_i, adding the voltage drop in the virtual impedance. This calculation is shown in (2).

$$V_{PECi} = V_i + Z_{vir,i}\overline{\frac{S^*_{PECi}}{\sqrt{3}\cdot V_i}} \tag{2}$$

The calculated V_{PECi} should be used instead of V_i in last step in Fig. 7. So in Fig. 8, the virtual voltage $V_{PEC,i}$ is the one used for the droop calculations, while V_i is the reference voltage for the physical node, achieving $V_1 = 1$ p.u.

The calculation presented in (2) is done considering a three-phase ac system, while extension to the dc case only requires to use real instead of complex variables for the impedance and power and without the $1/\sqrt{3}$ factor for the voltage drop calculation.

E. Power flow calculation convergence

The proposed secondary control is based on the calculation of the power flow solution. This power flow solution is an iterative process, thus an stop criteria is needed. It can be both a fixed number of iterations, a threshold for the difference of some calculated variables between consecutive iterations of the algorithm or a combination of both.

In this paper, for analyzing the convergence of the method, the difference between the losses obtained at the end of the iteration (step 6 in Fig. 5 and Fig. 7) and the ones calculated in the step before is used. When this difference is below a threshold, the solution can be considered precise enough.

The convergence time can be improved if instead of assuming zero losses in the first iteration, the losses in the situation prior to secondary control execution are used. This can be done simply by using the power production of each converter (P_{PECi}) for calculating the total needed production in step 2 for the first iteration. Using P_{PECi} instead of P_{LOADi} for this first iteration will make the losses of the previous situation to be included. Although P_{PECi} is not required for the rest of the algorithm, this is normally an information that the central controller can easily have.

To check the convergence, a simulation for the proposed microgrid is performed. The results are shown in Table II, where dc and ac cases are shown. The effect of using P_{PEC} for the first iteration is also included. It can be seen that the power flow converges in few steps, leading to an error below 0.8 ‰ in all the cases. The use of P_{PEC} for the initialization

TABLE II
ERROR FOR DIFFERENT NUMBER OF ITERATIONS (n) OF THE ALGORITHM. FIRST AND SECOND COLUMNS: DC NETWORK; THIRD AND FOURTH: AC FEEDER. FIRST AND THIRD COLUMNS: RESULTS USING P_{LOADi} FOR THE FIRST ITERATION; SECOND AND FOURTH COLUMNS: USING P_{PECi}.

n	dc: P_{LOAD}	dc: P_{PEC}	ac: P_{LOAD}	ac: P_{PEC}
1	0.78 ‰	0.17 ‰	2.34 ‰	0.21 ‰
2	0.17 ‰	0.17 ‰	0.18 ‰	0.18 ‰
3	0.17 ‰	0.17 ‰	0.18 ‰	0.18 ‰

TABLE III
CONVERTER PARAMETERS.

Converter	HPEC	RPEC-ac	RPEC-dc	dESS-PEC
S_n / P_n	7.5 kVA	3.75 kVA	1.25 kW	1.25 kW
k_p (p.u.)	0.1	0.1	0.05	0.05
f_c (Hz)	50	50	0.5	0.5

reduces the error of this first iteration, although no difference is seen from the second one onwards. For this paper, due to the fast convergence of the power flow solution, a fixed and small number of iterations (5) has been chosen for the stop criterion, although comparing the difference between losses calculated in consecutive iterations with a threshold would work similarly.

IV. SIMULATION RESULTS

The presented solution has been simulated using Matlab/Simulink. The complete hybrid microgrid is depicted in Fig. 1, including node numbers and code colors for the different sections: green for ac feeder; purple for 48 Vdc network; black for the ±375 Vdc buses.

In the ac feeder, nodes 1 and 2 are connected to the HPEC and to the ac output of the Ring PEC (RPEC-ac) respectively, by implementing a droop control strategy. Loads are connected to nodes 2 and 3, where the TPEC works in PQ mode. Both the HPEC and RPEC-ac have a virtual impedance of 5 times the line impedance in the ac feeder.

In the 48 Vdc, the dc output of the RPEC (RPEC-dc) works in droop control, together with a 1.25 kW dc/dc converter operating as a distributed ESS (dESS-PEC). A constant power load (CPL) is connected to node 2. In the ±375 Vdc grid, HPEC connected to node 1, is in charge of the dc bus balancing [16], while loads are connected both to 2 (positive dc bus) and 3 (negative dc bus). The details of the rated power of each converter and droop coefficients (k_p) are shown in Table III. Droop low pass filter (LPF) cutoff frequency are also shown. Cutoff frequency for dc is small because of the low communication speed in the experimental setup.

The simulation results are shown in Fig. 9. Before vertical lines marked with 1 (for 48 Vdc network) and 2 (ac feeder), the secondary control algorithm is disabled, thus having only a classical droop control. It can be seen the operation of the droop, which has two undesirable results. First, the power sharing among the converters is different from the desired one. In the ac feeder, the active power sharing ratio should be $2:1$, proportional to their power ratings, but it is not even though the droop coefficient has the same per unit value. In ac, for the reactive power no droop is being used, so the sharing without secondary control is not controlled anyway

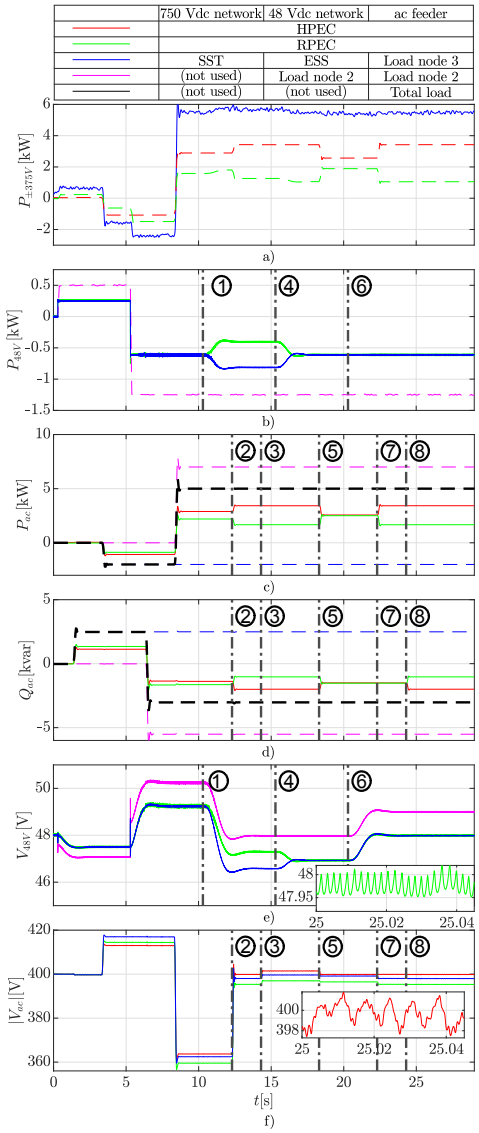

Fig. 9. Simulation results. a) Power in ±375 Vdc network. b) Power in 48 Vdc network. c) Active power in ac feeder. d) Reactive power in ac feeder. e) Voltage in 48 Vdc network, with a zoom to show the ripple. f) Filtered voltage in ac feeder (10 Hz LPF), zoom to show the ripple with unfiltered signal. For active/reactive power plots, load consumption is shown in dashed lines and converter production is shown in continuous lines. RPEC and HPEC are considered loads in the ±375 Vdc network.

and depends only on grid configuration and load demand. In the 48 Vdc network it matches the desired $1:1$ ratio because the network is completely symmetrical. Second, the droop causes a voltage deviation, making all the nodes far from 1 pu value (48 Vdc and 400 Vac respectively). Once the secondary control is enabled, these two effects are eliminated. Proposed secondary control algorithm is performed once per vertical line in Fig. 9. The sequence of power reference changes in the simulation are the following:

- At $t = 0.3$ s, power reference for CPL in node 2 of 48 Vdc network is set to 0.5 kW.
- At $t = 1.3$ s, reactive power reference for CPL in node 3 of ac feeder is set to 2.5 kvar.
- At $t = 3.3$ s, active power reference for CPL in node 3 of ac feeder is set to -2 kW.
- At $t = 5.3$ s, power reference for CPL in node 2 of 48 Vdc network is set to -1.25 kW.
- At $t = 6.3$ s, reactive power reference for CPL in node 2 of ac feeder is set to -5.5 kvar.
- At $t = 8.3$ s, active power reference for CPL in node 2 of ac feeder is set to 7 kW.

Sequence of changes in secondary control references (power sharing ratio and node with 1 pu voltage) is listed below. Changes in power sharing ratio are carried out by modifying step 3 in Fig. 5 and 7, with the desired proportion (the algorithm presented the case as if the desired proportion was proportional to the rated power).

1) At $t = 10.3$ s, secondary control is activated in 48 Vdc network, setting node 2 (load) to have 1 pu voltage (48 V) and sharing of power production among the two droop-controlled power electronic converters with $2:1$ ratio (ESS and RPEC output).
2) At $t = 12.3$ s, secondary control is activated in ac feeder, setting node 1 (HPEC) to have 1 pu voltage (400 V) and sharing of active and reactive power production among the two droop-controlled power electronic converters (HPEC and RPEC) proportional to their rated power ($2:1$ ratio). Is is worth to remark that 1 pu voltage is achieved in node 1, which has a converter with virtual impedance, being able to compensate the voltage drop in this virtual impedance.
3) At $t = 14.3$ s, 1 pu voltage reference in ac feeder is changed to node 3. The change is reversed in next update of secondary control in ac feeder.
4) At $t = 15.3$ s, power sharing ratio of converters in 48 Vdc network is set to $1:1$ ratio.
5) At $t = 18.3$ s, active and reactive power sharing ratio of converters in ac feeder is set to $1:1$ ratio.
6) At $t = 20.3$ s, 1 pu voltage reference in 48 Vdc network is changed to node 1 (RPEC output).
7) At $t = 22.3$ s, active power sharing ratio of converters in ac feeder is set back to $2:1$ ratio.
8) At $t = 24.3$ s, reactive power sharing ratio of converters in ac feeder is set back to $2:1$ ratio.

A. *Effect of grid parameters estimation mismatch*

In order to check the accuracy of the method under parameter estimation mismatches, a simulation has been performed forcing these estimation errors. The simulation has been done both for the ac feeder and the 48 Vdc network, in the same configuration explained previously in this section. For both cases, the network situation, including load consumptions, is exactly the same that there is at the end of the simulation shown in Fig. 9, only changing the situation of the load consumption in the ac feeder, where two nodes have loads. Apart from that, the only difference is in the performance of the secondary control.

The results are shown in Fig. 10. A variable error between ± 30 % has been included in the grid resistances estimation used for the secondary control. Both the ac feeder and the 48 Vdc network have the same configuration: R_{12} and R_{23} connecting nodes 1, 2 and 3 in a radial manner. For all the cases, the proposed variation for R_{12} estimation error has been added. Three different cases are considered for R_{23}: no error and same magnitude error as in R_{12} with same or opposite sign.

As commented before, the ac loads at the end of simulation shown in Fig. 9 are connected to nodes 2 and 3. In order to check which load configuration is more sensitive to estimation mismatches, two simulations have been performed. The sum of both loads in Fig. 9 is connected to one of the nodes. The results for the load connected to node 2 are the same for the three cases for the R_{23} error. This is a logical result, since if no load or PEC is connected to node 3, current does not flow in R_{23} and the estimation of that value has no effect. Similar results are obtained when all the load connected to node 3 with no error in R_{23}. Since no PEC is connected to node 3, for the secondary control, R_{23} and the node 3 load can be considered as a load connected to node 2, with a small variability due to the R_{23} losses. If the value of R_{23} is estimated properly, the losses are calculated exactly and there is no significant difference with the case where the load is directly connected to node 2.

In the results for the 48 Vdc network, it can be seen that the worst scenario is when the estimation has errors with opposite sign being the effect almost negligible for both power and voltage when the same sign estimation error occurs. The maximum deviation in absolute value is: 13.85 % for P_1 and P_3 and 0.35 % for v_1.

For the ac feeder, the worst scenario for active power and voltage occurs for same and opposite sign error respectively. For the reactive power, all the cases show almost identical results. The maximum deviation in absolute value is: 2.80 % for P_2, 5.51 % for Q_2 and 0.18 % for v_1. The errors for P_1 and Q_1 are in all cases smaller than those for P_2 and Q_2.

It can be seen that in all cases the error in terms of voltage is really small, meanwhile for all the other variables (active/reactive power), the maximum error in all the scenarios is 13.85 %. Considering that this error occurs for a very significant error (30 %), the method can be considered robust enough referring to parameters estimation mismatches. Taking into account that these important errors only appear for power sharing and not for voltage magnitude, the method can be considered as a valid alternative to other secondary control alternatives, which normally correct the voltage deviation of the droop controllers but have no capability of varying the power sharing in a flexible way.

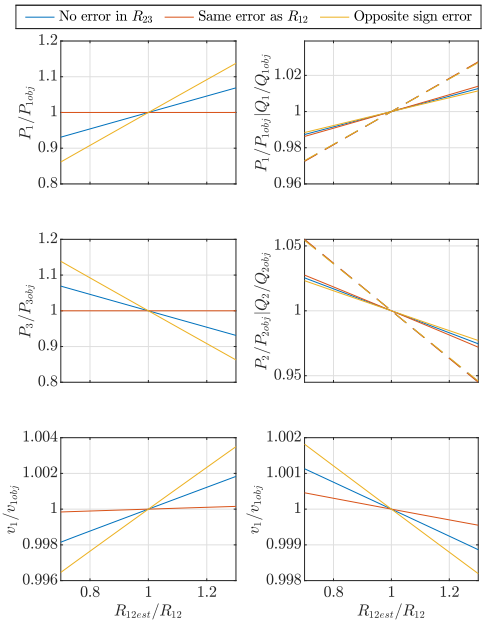

Fig. 10. Estimation mismatch simulation results. Left column: dc network; right column: ac feeder. First two rows indicate both PECs power production compared to the reference one for the secondary control (two PECs in each case, dc and ac; for ac, dashed lines indicate reactive power). Third row indicates deviation in the voltage in the node whose voltage is chosen to have 1 pu voltage.

The application of this secondary control is thought for microgrids, coordinated by a central controller with access to measurements in the different nodes. In this scenario, a proper estimation of all the required parameters can be worthy for multiple reasons, including an optimum operation of the microgrid (like losses optimization). Online parameter estimation methods are found in the literature and some of them use the same variables required for the secondary control, to perform an inverse power flow problem, estimating impedances from current and voltages in the different nodes [19]. This strategy for online parameter estimation is very convenient to be run in parallel with the secondary control, when offline estimation is not possible.

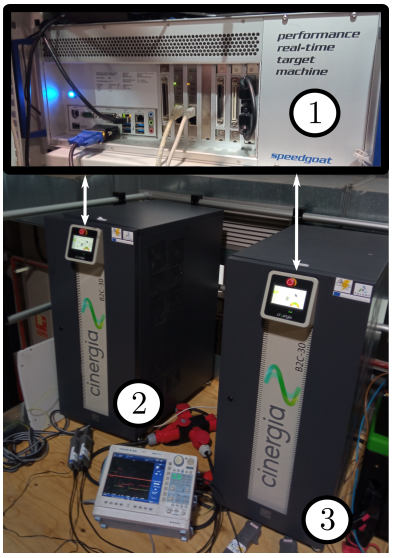

Fig. 11. Setup for experimental validation. Speedgoat real-time simulator (1): implements the ac feeder and controls two Cinergia B2C-30 converters, one for the 750 Vdc network (2) and the other for the 48 Vdc network (3). White arrows indicate Modbus/TCP communication channels for the real-time simulator to send references to and receive measurements from the converters.

V. Experimental validation

The proposed method has been validated experimentally with the setup shown in Fig 11. The microgrid shown in Fig. 1 is partially implemented. The ± 375 Vdc grid is simplified to a unipolar 750 Vdc bus and only one ac feeder and one 48 Vdc network are used.

The two Cinergia B2C-30 converters shown in Fig. 11 are controlled through the Speedgoat real-time simulation platform, sending power references to outputs operating as constant power loads and voltage references to the droop-controlled converters, with the droop calculations inside the real-time simulator. Real measurements from the converter outputs, using Modbus/TCP communications, are fed back for the calculation inside Speedgoat. The ac feeder is implemented in the real-time simulator. The interconnection of the ac feeder and the 48 Vdc network with the 750 Vdc bus is implemented as a load in the 750 Vdc, whose demand is updated with the production of the corresponding converter: RPEC in 48 Vdc network (real power measurements) and RPEC and HPEC in the ac feeder (real-time simulation data).

In Fig. 12, the results from the experimental setup validation are shown, with the same sequence of changes in load and secondary control references explained in Section IV for the Simulink simulation. It can be seen that the experimental results agree with the simulated ones, thus validating the proposed secondary control.

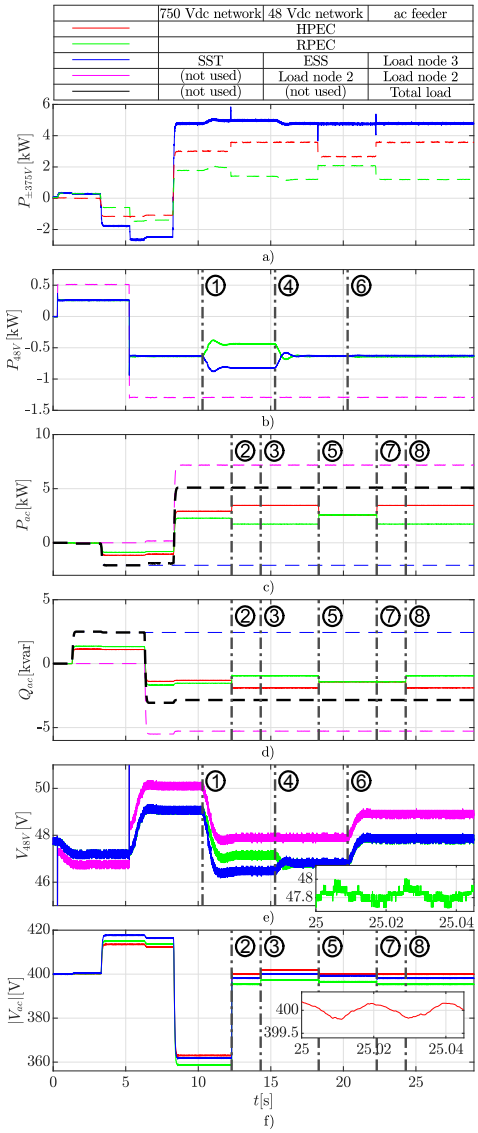

Fig. 12. Experimental results. a) Power in ± 375 Vdc network. b) Power in 48 Vdc network. c) Active power in ac feeder. d) Reactive power in ac feeder. e) Voltage in 48 Vdc network, with a zoom to show the ripple. f) Voltage in ac feeder, with a zoom to show the ripple. For active/reactive power plots, load consumption is shown in dashed lines and converter production is shown in continuous lines. RPEC and HPEC are considered loads in the ± 375 Vdc network.

VI. Combination with power sharing optimization criteria

In the previous sections, the power sharing was determined as a constant proportion between both converters production.

In this section, this power sharing selection is chosen for optimizing a given cost function, thus illustrating the versatility of the proposed method.

Optimization problems including power flows normally require iterative processes, for the same reason power flow solutions are normally iterative. For this reason, the iterative process explained in Fig. 5 can be used for calculating the optimization problem at the same time the power flow is being solved, being the study case for the optimization problem is in dc.

The cost function to be minimized is (3), where P_l are the losses in the network, P_{load} and P_b the power consumed by the load and the battery used as ESS, C_0 is the cost of energy at the moment of optimization and C_1 is the expected cost of energy in a future moment of the day.

$$C = C_0 P_g - C_1 P_b = C_0(P_l + P_b + P_{load}) - C_1 P_b \quad (3)$$

This cost function represents the cost per unit time of the consumed energy, $C_0 P_g = C_0(P_l + P_b + P_{load})$, minus the expected revenues from the energy stored in the battery for a future sell, $C_1 P_b$. P_b is considered with load convention, so a positive value means it is being charged, thus having a positive future revenues (reducing cost). The two costs, C_0 and C_1 are thought for tariff with hour discrimination, in which the price for peak and valley moments of the day can be known and used for estimating the possible earns with battery usage.

For the losses calculation, only the losses in the lines in the 48 Vdc network are considered, neglecting the losses in PEC and assuming RPEC is directly connected to the grid (so grid variables from now on indicate RPEC output). The same procedure applied here can be used for more complete losses calculation, as it can be used including other parts of the grid, but it complicates the problem and is considered as future work out of the scope of the paper.

Losses can be calculated as shown in (4), where R is the resistance of the line connecting to the load, indicating subscript g and b grid or battery side, and V is the voltage at grid/battery PEC output.

$$P_l = \frac{R_b}{V_b^2} P_b^2 + \frac{R_g}{V_g^2} P_g^2 = \frac{R_b}{V_b^2}(1-r)^2 P_T^2 + \frac{R_g}{V_g^2} r^2 P_T^2 \quad (4)$$

Where P_g and P_b are expressed as a function of total production that the battery and grid must share ($P_T = P_l + P_{load}$): $P_g = r P_T$ and $P_b = (1-r)P_T$, being r the proportion of this demand supplied by the grid (P_{TOTAL} in Fig. 5).

Substituting (4) in (3) and differentiating with respect to r, the condition for the minimum of the function is obtained, as shown in (5).

$$C' = C_0 \frac{2R_b}{V_b^2}(r-1)P_T^2 + C_0 \frac{2R_g}{V_g^2} r P_T^2 - (C_1 - C_0)P_T = 0 \quad (5)$$

Defining $B_x = 2P_T R_x / V_x^2$ (where x can be either g or b) and $C_{diff} = (C_1 - C_0)/C_0$, and dividing by $P_T C_0$ condition shown in (5) can be rewritten as shown in (6).

$$B_b(r-1) + B_g r - C_{diff} = 0 \rightarrow r = \frac{B_b + C_{diff}}{B_b + B_g} \quad (6)$$

Losses (used for obtaining P_T) and voltage in each node are assumed as constants for this calculation, although they depend on the solution. This means that the optimum will not be found with one single calculation, since the value of r, whose optimum is being calculated, is affecting the parameters needed for its calculation. However, this optimum calculation can be added to the iterative nature of power flow algorithms (used in the proposed secondary control), recalculating the constants for every iteration. This process does not fully guarantee the convergence to the optimum point, but it will be seen that the deviation is generally small.

Due to this possible deviation from the optimum solution, and in order to make the method valid for more complex problems in which an expression for r might be impossible to obtain, another method for the optimum calculation is proposed. For this method, the iterations of the secondary control are done with steps in the different values of r, doing a sweep among the possible values. For every value of r, the cost function is calculated. If the calculated cost is minimum compared to the previous ones, the value of the cost function is updated to be used in the next steps. The value of the outputs of the secondary control (P_{0PECi} and, in the case of ac, also $v^*_{g_{qPECi}}$) is also stored to avoid recalculating the power flow after the sweep has finished. The explained Sweep Optimization method is shown in Fig. 13.

Since the steps in r are going to be relatively small, it can be considered that the power flow for each value of r converges in only one iteration, because it is starting from a similar solution. This way, the iterative nature of the power flow solution and the optimization problem is combined.

These two alternatives, which from now on are going to be referred as Optimum Calculation and Sweep Optimization, are going to be compared in order to check its effectiveness.

A. Simulation validation

The cost optimization problem presented in this paper is a simple case with a reduced version of the grid infrastructure presented in Fig. 1, with only one of the 48 Vdc networks.

The configuration of the study case network is the same used for Sections IV and V, with the RPEC connected to node 1, the ESS to node 3 and load to node 2. The load consumption is fixed to 1.25 kW for all the results presented here.

For validating the proposed optimization algorithm, a simulation has been carried out. For the same network situation, the value of r is varied in order to obtain the cost function for a given range. This is similar to the Sweep Optimization, but

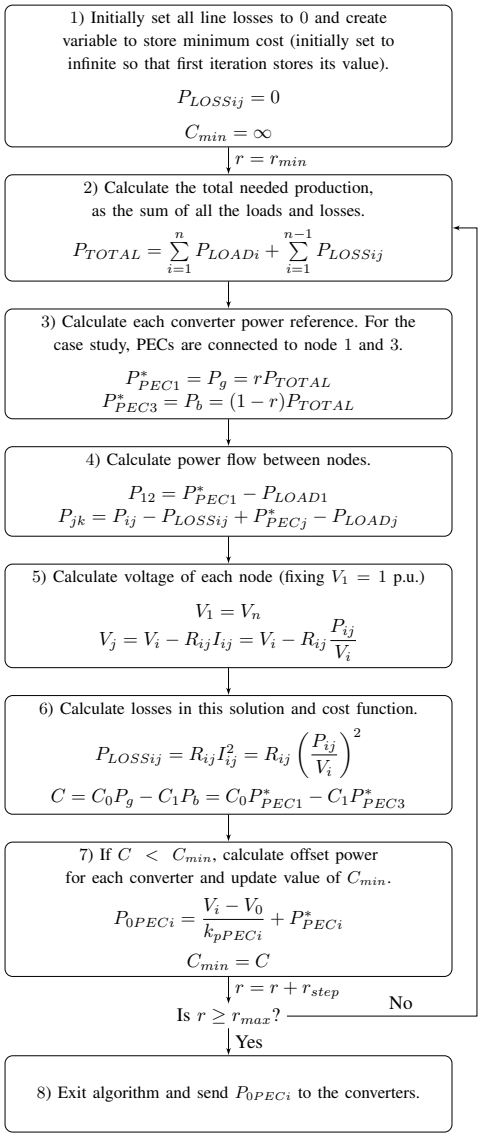

Fig. 13. Flowchart for secondary control with cost optimization in dc. i, j and k denote any three consecutive nodes. r_{min} and r_{max} are the minimum and maximum value of r for the sweep, and r_{step} is the step in r between iterations.

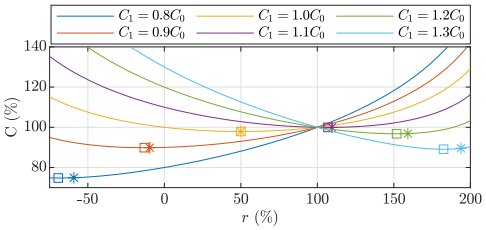

Fig. 14. Simulation results for different values of future energy cost (C_1) with respect to present value (C_0). r is the proportion of total load supplied by the grid connection and C is the expected cost compared to the case with no ESS ($r = 100$ %). Asterisks mark the position of the Optimum Calculation, meanwhile squares mark the minimum obtained by Sweep Optimization. Minimum values of C and r for each curve and values obtained with both methods for optimization are shown in Table IV.

TABLE IV
MINIMUM VALUE OF COST FUNCTION FOR DIFFERENT VALUES OF C_1 AND VALUES OBTAINED BY BOTH METHODS FOR OPTIMIZATION.

	Real value		Opt. Calculation		Sweep Opt.	
	r (%)	C (%)	r (%)	C (%)	r (%)	C (%)
$C_1 = 0.8C_0$	−68.5	74.8	−59.1	74.9	−69.3	74.8
$C_1 = 0.9C_0$	−12.5	89.9	−9.5	89.9	−13.1	89.9
$C_1 = 1.0C_0$	50.0	97.9	50.0	97.9	50.0	97.9
$C_1 = 1.1C_0$	106.9	100.0	109.5	100.0	107.0	100.0
$C_1 = 1.2C_0$	151.3	96.8	159.1	96.9	151.8	96.8
$C_1 = 1.3C_0$	182.5	89.1	193.8	89.6	182.5	89.1

in this case the secondary control shown in Fig. 5 is executed for each value of r during the simulation, the output of the secondary control for each value is sent to the converters and the cost function is obtained with the real values of P_g and P_b measured in the simulation. In the Sweep Optimization, the cost function is calculated in the algorithm, and the secondary control reference is sent to the PEC only when the sweep is finished.

The results can be seen in Fig. 14. Minimum values of cost (C) for each curve and corresponding value of r, together with values obtained with both methods for optimization are shown in Table IV. For Sweep Optimization a step of 1% for r has been used.

It can be seen that the error in the value of r for the Optimum Calculation is significant in some cases (up to 11.3 % in the worst case). Meanwhile, for Sweep Optimization, is always smaller than 1 %. However, in both methods, the obtained cost is really close to the actual minimum, with a maximum deviation of 0.5 % and less than 0.1 % for Optimum Calculation and Sweep Optimization respectively.

This indicates that the deviation in the Optimum Calculation from the actual minimum is not important, since although it can be significant in terms of the chosen r value, the obtained cost is close to the minimum one. This makes that this method is more suitable for the proposed scenario, since less iterations will be required. However, the validity of the Sweep Optimization method is also proved as an alternative for more complex problems in which the value of r minimizing the

cost function cannot be directly calculated. This could be the case of considering efficiency curves in PECs, more than one interconnected networks or multi-variable optimization (for example, if the sharing is between three instead of two PECs, adding one degree of freedom).

VII. Conclusions

This paper has shown an approach for the sharing control scheme in a hybrid ac/dc microgrid. The proposed method enables the different converters to contribute to the power sharing by a droop control implementation. The proposed secondary control eliminates the voltage deviation due to the droop characteristic. It also eliminates the voltage droop caused by the virtual impedance.

The proposed secondary control applied in ac allows the reactive power sharing among the converters with no specific droop control. This also eases the integration of converters which are seen as active power loads, but whose reactive power can be controlled to contribute to the sharing, as it can be the case of a converter feeding a load or a STATCOM. All the droop-controlled converters can achieve any active/reactive power production, thus achieving different power sharing scenarios, including shared conditions among the different networks in the hybrid microgrid if the secondary control of these different networks is coordinated. The proposed method has been validated both in simulation and in an experimental setup.

The secondary control is also flexible, allowing to introduce any criteria for the power flow solution, like any method for deciding the power sharing among the converters (minimize losses, saturation of converters for its rated power,...) or the possibility of easily changing the node whose voltage is fixed to 1 p.u. This flexibility has been proven with a simplified optimization problem, using the secondary control combined to the minimization of a cost function. Two alternatives were presented and validated through simulation, both with similar performance in terms of obtained cost. Cost Optimization approach is more suitable for simpler problems that can be solved analytically, whereas Sweep Optimization is a better option under complex scenarios. This could be the case of considering efficiency curves in PECs, more than one interconnected networks or multi-variable optimization.

References

[1] P. Wang, L. Goel, X. Liu, and F. H. Choo, "Harmonizing AC and DC: A Hybrid AC/DC Future Grid Solution," *IEEE Power and Energy Magazine*, vol. 11, no. 3, pp. 76–83, May 2013.

[2] P. Fairley, "DC Versus AC: The Second War of Currents Has Already Begun [In My View]," *IEEE Power and Energy Magazine*, vol. 10, no. 6, pp. 104–103, Nov 2012.

[3] A. Bindra, "Projecting the Evolution of Power Electronics: Highlights from FEPPCON VIII," *IEEE Power Electronics Magazine*, vol. 3, no. 1, pp. 32–44, March 2016.

[4] C. Marnay, H. Aki, K. Hirose, A. Kwasinski, S. Ogura, and T. Shinji, "Japan's Pivot to Resilience: How Two Microgrids Fared After the 2011 Earthquake," *IEEE Power and Energy Magazine*, vol. 13, no. 3, pp. 44–57, May 2015.

[5] J. Rocabert, A. Luna, F. Blaabjerg, and P. Rodríguez, "Control of Power Converters in AC Microgrids," *IEEE Transactions on Power Electronics*, vol. 27, no. 11, pp. 4734–4749, Nov 2012.

[6] J. W. Simpson-Porco, Q. Shafiee, F. Dörfler, J. C. Vasquez, J. M. Guerrero, and F. Bullo, "Secondary Frequency and Voltage Control of Islanded Microgrids via Distributed Averaging," *IEEE Transactions on Industrial Electronics*, vol. 62, no. 11, pp. 7025–7038, 2015.

[7] P. Wang, X. Lu, X. Yang, W. Wang, and D. Xu, "An Improved Distributed Secondary Control Method for DC Microgrids With Enhanced Dynamic Current Sharing Performance," *IEEE Transactions on Power Electronics*, vol. 31, no. 9, pp. 6658–6673, 2016.

[8] Y. Khayat, Q. Shafiee, R. Heydari, M. Naderi, T. Dragičević, J. W. Simpson-Porco, F. Dörfler, M. Fathi, F. Blaabjerg, J. M. Guerrero, and H. Bevrani, "On the secondary control architectures of ac microgrids: An overview," *IEEE Transactions on Power Electronics*, vol. 35, no. 6, pp. 6482–6500, 2020.

[9] Q. Shafiee, J. M. Guerrero, and J. C. Vasquez, "Distributed secondary control for islanded microgrids—a novel approach," *IEEE Transactions on Power Electronics*, vol. 29, no. 2, pp. 1018–1031, 2014.

[10] X. Wang, Y. W. Li, F. Blaabjerg, and P. C. Loh, "Virtual-Impedance-Based Control for Voltage-Source and Current-Source Converters," *IEEE Transactions on Power Electronics*, vol. 30, no. 12, pp. 7019–7037, 2015.

[11] Z. Liu, S. Ouyang, and W. Bao, "An improved droop control based on complex virtual impedance in medium voltage micro-grid," in *2013 IEEE PES Asia-Pacific Power and Energy Engineering Conference (APPEEC)*, 2013, pp. 1–6.

[12] A. Micallef, M. Apap, C. Spiteri-Staines, and J. M. Guerrero, "Performance comparison for virtual impedance techniques used in droop controlled islanded microgrids," in *2016 International Symposium on Power Electronics, Electrical Drives, Automation and Motion (SPEEDAM)*, June 2016, pp. 695–700.

[13] A. D. Paquette and D. M. Divan, "Virtual Impedance Current Limiting for Inverters in Microgrids With Synchronous Generators," *IEEE Transactions on Industry Applications*, vol. 51, no. 2, pp. 1630–1638, 2015.

[14] J. He and Y. W. Li, "Analysis, Design, and Implementation of Virtual Impedance for Power Electronics Interfaced Distributed Generation," *IEEE Transactions on Industry Applications*, vol. 47, no. 6, pp. 2525–2538, 2011.

[15] C. Gómez-Aleixandre, A. Navarro-Rodríguez, G. Villa, C. Blanco, and P. García, "Sharing control strategies for a hybrid 48v/375v/400vac ac/dc microgrid," in *2020 IEEE Energy Conversion Congress and Exposition (ECCE)*, 2020, pp. 3900–3907.

[16] C. Wang, Z. Li, X. Si, and H. Xin, "Control of neutral-point voltage in three-phase four-wire three-level NPC inverter based on the disassembly of zero level," *CPSS Transactions on Power Electronics and Applications*, vol. 3, no. 3, pp. 213–222, Sep. 2018.

[17] A. Navarro-Rodríguez, P. García, R. Georgious, and J. García, "Adaptive Active Power Sharing Techniques for DC and AC Voltage Control in a Hybrid DC/AC Microgrid," *IEEE Transactions on Industry Applications*, vol. 55, no. 2, pp. 1106–1116, March 2019.

[18] R. Chai, B. Zhang, J. Dou, Z. Hao, and T. Zheng, "Unified Power Flow Algorithm Based on the NR Method for Hybrid AC/DC Grids Incorporating VSCs," *IEEE Transactions on Power Systems*, vol. 31, no. 6, pp. 4310–4318, 2016.

[19] K. Gajula, L. K. Marepalli, X. Yao, and L. Herrera, "Recursive least squares and adaptive kalman filter based state and parameter estimation for series arc fault detection on dc microgrids," *IEEE Journal of Emerging and Selected Topics in Power Electronics*, pp. 1–1, 2021.

Carlos Gómez-Aleixandre (S'19) received the B.Sc. degree in electrical engineering and the B.Sc. degree in industrial electronic and automatic engineering from the University of Oviedo, Gijón, Spain, in 2015 and 2018, respectively. He received the M.Sc. degree in sustainable transportation and electrical power systems from the University of Oviedo, University of Nottingham, Sapienza Università di Roma and Instituto Superior de Engenharia de Coimbra in 2017. He is currently working toward the Ph.D. degree in electrical engineering with the LEMUR Research Team, University of Oviedo.

He has coauthored 2 IEEE journals and 7 IEEE international conference papers. His research interests include microgrids, coordinated control, and modeling and control of islanded and grid-connected converters

Mr. Gómez-Aleixandre received a Spanish Predoctoral Grant for the formation in university teaching (Formación de Profesorado Universitario) in 2017.

Ángel Navarro-Rodríguez (S'15-M'20) is "Cum Laude" Ph.D in Energy and Process Control. He received the B.Sc. degree in Telecommunications Engineering with honours from the University of Castilla La-Mancha, Spain in 2012, the M.Sc. degree in Electrical Energy Conversion and Power Systems, and the Ph.D. degree in Energy and Process Control from the University of Oviedo, Spain, in July 2014 and June 2019, respectively, granted by the government of Principado de Asturias. Nowadays, he is an Assistant Professor in the Department of Electrical, Electronics, Comunications, and Systems Engineering in the University of Oviedo since October 2019. In 2016/17 he was a Visitor Researcher with the PEMC Research Group in The University of Nottingham, U.K.

He has authored or co-authored 8 IEEE journals and more than 20 IEEE conferences, with a 7 h-index. He received the Outstanding Young EPE Member Award in 2018 and the University of Oviedo Outstanding Ph.D. Thesis Award in 2020. He is part of the LEMUR research group in the University of Oviedo since July 2014 and his current research interests include microgrids control and modelling, grid-tied converters, energy storage systems, control systems applied to electrical energy conversion, sustainable transportation and electric traction, power quality and renewable energies integration.

Geber Villa received the B.Sc. degree in electronics and control engineering, the M.Sc. degree in electrical energy conversion and power systems, and the M.Sc. degree in industrial engineering from the University of Oviedo, Gijón, Spain, in 2011, 2016, and 2017, respectively. He is currently working toward the Ph.D. degree in electrical engineering with the LEMUR Research Team, University of Oviedo.

He has coauthored several IEEE international conference and journals papers. His research interests include analysis and control of power converters, energy storage systems, and microgrids.

Mr. Villa received the Spanish National Award for the Outstanding Graduate of the Year in 2014 and 2021, and a Spanish Predoctoral Grant for the formation in university teaching (Formación de Profesorado Universitario) in 2017.(S'17) received the B.Sc. degree in electronics and control engineering, the M.Sc. degree in electrical energy conversion and power systems, and the M.Sc. degree in industrial engineering from the University of Oviedo, Gijón, Spain, in 2011, 2016, and 2017, respectively. He is currently working toward the Ph.D. degree in electrical engineering with the LEMUR Research Team, University of Oviedo.

Cristian Blanco (S10'-M'16) was born in Villablino, Leon, Spain. He received a B.S Degree in Telecommunications Engineering, a M.S. degree, and a PhD in Electrical Engineering from the University of Oviedo, Gijon, Spain, in 2010, 2011, and 2015 respectively.

In 2011, he was awarded a fellowship of the Personnel Research Training Program funded by the Regional Ministry of Education and Science of the Principality of Asturias. From Sep. 2012 to Feb. 2013 he was a PhD Guest at Aalborg University (Denmark). From Jul. to Dec. 2019 he was Visiting Faculty at the University of British Columbia (Canada). He is currently Associate Professor with the Department of Electrical, Computer, and Systems Engineering (University of Oviedo). At the same time, he works with the LEMUR research group; his research capabilities include modeling and control of islanded and grid-connected converters including storage systems, synchronization, islanding detection and power quality, microgrids and digital signal processing.

Dr. Blanco was the recipient of an IEEE Energy Conversion Congress and Exposition second prize paper award in 2013. At the same time, he received the University of Oviedo Outstanding Ph.D. Thesis Award in 2016.

Pablo García was born in Luanco, Asturias, Spain. He received a M.S. degree, and a PhD in Electrical Engineering from the University of Oviedo, Gijon, Spain, in 2001 and 2006 respectively.

From 2002 to 2006 he was awarded with a fellowship for the national research and training program by the Ministry of Science and Technology in Spain. In 2004 he was a visiting Scholar at the University of Wisconsin-Madison, USA. In 2013 he was a visiting Scholar at The University of Nottingham, UK. He is currently a Full Professor within the Department of Electrical, Electronics, Communications and Systems Engineering, University of Oviedo. From 2022 he works with the Spanish Research Agency as the manager for international projects in the Energy and Transport division area. He is a member of the LEMUR research group. His research interest include control of grid-tied power converters for distributed resources integration and particularly for the control of grid-tied battery energy storage systems, parameter estimation, optimization of distributed resources and digital signal processing for real-time embedded systems. He is the co-author of near 40 journal papers and 80 conference papers. He has been the Principal Investigator of 50 projects with companies, 1 European H2020 and 4 national funded projects. He is the co-founder of the ENFASYS startup, focused on the development of solutions for the integration of energy storage and collaborative self-consumption applications.

He was a recipient of the 2005 IEEE Transactions on Industry Applications, Third Place Prize Paper Award, three IEEE Industry Applications Society Conference prize paper awards in 2006, 2010 and 2016, respectively and one EPE Conference Award in 2018.

Appendix B

Conference publications

B.1 Analysis of a Complex-Valued Droop Method in AC Microgrids with Complete Steady-State Frequency Compensation Using dq-Decomposition

Analysis of a Complex-Valued Droop Method in AC Microgrids with Complete Steady-State Frequency Compensation Using *dq*-Decomposition

Carlos Gómez-Aleixandre, Cristian Blanco, Andrés Suárez-González, Ángel Navarro-Rodríguez and Pablo García
Dept. of Electrical, Electronics, Computers & Systems Engineering
University of Oviedo
Gijón, 33204, Spain
Email: gomeztcarlos@uniovi.es, blancocristian@uniovi.es, suarezandres@uniovi.es, navarroangel@uniovi.es, garciafpablo@uniovi.es

***Abstract*—This paper proposes a novel droop technique for AC microgrids with no frequency deviation in steady-state. This droop implementation replaces the classical $P/f + Q/V$ used for inductive lines or the alternative $P/V + Q/f$ for resistive lines with a S/V_{dq} droop in which the coupling terms that appear when the line is not purely inductive/resistive are considered. The proposed droop departs from the classical approach; instead of calculating P and Q expressions considering voltage polar equation which requires sine and cosine terms, the dq-decomposition is used. This allows to create a droop combining both components of the voltage versus P and Q, without requiring small-signal simplification of the trigonometric functions ($\sin\delta \approx \delta$ and $\cos\delta \approx 1$) and taking into account the coupling terms, so that the designed droop is valid for any R/X value.**

I. Introduction

Droop control is a widely used and well-known solution for power sharing without requiring communication among converters. There are two main variants depending on line impedance: $P/f + Q/V$ for inductive lines or $P/V + Q/f$ for resistive lines [1]. In both cases, three considerations are done to obtain the final droop: 1) lines are assumed to be purely inductive/resistive and the other term of the impedance is neglected; 2) phase angle difference, δ, between voltages is small, thus allowing to approximate $\sin\delta \approx \delta$ and $\cos\delta \approx 1$; and 3) frequency and voltage show a steady-state deviation with respect to the rated conditions.

Neglecting resistive/inductive part can worsen the operation when R/X ratio is close to 1, thus the coupling term effect becoming significant. Virtual impedance can be included to increase the resistive/inductive component of the line impedance [2], [3], but this would cause some unwanted side effects, like the voltage loss capability in the control system due to this virtual impedance.

The present work has been partially supported by the predoctoral grants program FPU for the formation in university teaching of Spain MECD under the grant ID FPU16/05313. This work also was supported in part by the European Union's H2020 Research and Innovation programme under Grant Agreement No 864459 (UE-19-TALENT-864459) and by the Spanish Ministry of Innovation and Science uder Grant MCI-20-PID2019-111051RB-I00.

Some solutions can be found in the literature that consider the coupling terms. In [4], [5], an orthogonal linear rotational transformation matrix (obtained from impedance phase angle) is used to rotate P and Q so that the coupling terms are avoided. In [6], [7], the coupling terms are compensated. This is done by introducing in the formula for each droop output (voltage magnitude and frequency) a term to compensate the effect of the deviation of the other output with respect to the nominal value.

However, these two methods still include the $\sin\delta = \delta$ and $\cos\delta = 1$ approximation and use the frequency as one of the droop outputs, thus having a frequency deviation in steady-state. Other solutions are found in the literature using angle instead of frequency as one of the droop outputs [7]–[10], thus eliminating frequency deviation.

The method proposed in this paper also eliminates frequency deviation and takes into account the coupling effect by the orthogonal linear rotational transformation matrix.

Additionally, due to the decomposition of the voltage in the dq-reference frame, it does not require any trigonometric function simplification, thus obtaining a compact formulation using complex numbers and the d- and q- voltage components as the droop outputs. This approach is appealing when dq-composition is used in the control system or for state-space modeling, in which the angle variation introduces a new variable (the angle) with non-linear terms [11].

This paper is organized as follows. In Section II, the proposed droop control is explained. In Section III, the voltage deviation caused by the proposed droop is compared with the $P/f + Q/V$ and $P/V + Q/f$ alternatives. In Section IV, the grid used for the study is presented. Section V shows the simulation results. Firstly, the proposed droop is compared with $P/f + Q/V$ and $P/V + Q/f$ approaches, assuming perfect knowledge of impedance phase angle for orthogonal linear rotational transformation matrix. Then, the effect of mismatches in the estimation of impedance phase angle is analyzed by simulating the different scenarios with significant estimation errors. Finally, section VI presents the conclusions.

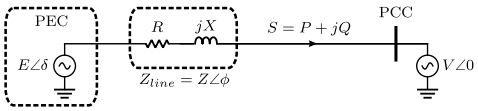

Fig. 1. Power flow diagram in a line impedance connecting a power electronic converter to the grid.

II. Proposed Droop Control

A diagram for the power flow in a generic line with arbitrary impedance is shown in Fig. 1. Classical $P/f + Q/V$ and $P/V + Q/f$ droops are obtained from the same diagram assuming $R \approx 0$ and $X \approx 0$, respectively.

In this paper, polar expressions for voltage and impedance are replaced with their equivalent rectangular equations in the synchronous dq-reference frame and complex numbers are used for the calculations.

For the following calculations, steady-state situation is considered. However, the outputs of the droop are used as references for instantaneous values of the voltage.

Apparent power calculation is shown in (1), being S, P and Q apparent, active and reactive power flowing to the point of common coupling (PCC) from the power electronic converter (PEC); V_{dq} the voltage vector at the PCC and $\overline{I_{dq}}$ the conjugate of the line current vector. For this paper, power invariant transformation is considered ($k = 1$). Still the following discussion is equivalent for the magnitude invariant transformation, leading to equivalent expressions.

$$S = P + jQ = kV_{dq}\overline{I_{dq}} \xrightarrow{k=1} S = P + jQ = V_{dq}\overline{I_{dq}} \quad (1)$$

The conjugate of the current can be obtained as shown in (2) from the converter output voltage, E_{dq}, the voltage at the PCC, V_{dq}, and the impedance of the line connecting them. The voltage expression at the PCC can be simplified as $V_{dq} = V_d = V$, since the d-axis is used as the phase reference.

$$\overline{I_{dq}} = \overline{\left(\frac{E_{dq} - V_{dq}}{Z_{line}}\right)} = \frac{\overline{E_d + jE_q - V}}{\overline{R + jX}} = \frac{E_d - V - jE_q}{R - jX} \quad (2)$$

Substituting (2) in (1), (3) is obtained.

$$S = V\frac{E_d - V - jE_q}{R - jX} = V\frac{(E_d - V - jE_q)(R + jX)}{(R - jX)(R + jX)} \quad (3)$$

Taking into account that $(R - jX)(R + jX) = Z^2$, the expression shown in (4) is obtained, being Z the modulus of the complex impedance.

$$S = \frac{V}{Z^2}(E_d - V - jE_q)(R + jX) \quad (4)$$

Splitting (4) into real and imaginary components, the expressions for active and reactive power are obtained, as shown in (5a) and (5b).

$$P = \frac{V}{Z^2}(E_d R + E_q X - VR) \quad (5a)$$

$$Q = \frac{V}{Z^2}(E_d X - E_q R - VX) \quad (5b)$$

From (5a) and (5b), $P/f + Q/V$ and $P/V + Q/f$ droops can be obtained by substituting $E_d = E\cos\delta \approx E$ and $E_q = E\sin\delta \approx E\delta$ and considering $R \approx 0$ or $X \approx 0$ respectively, as shown in (6) and (7).

$$P \approx \frac{V}{X}E\delta \rightarrow \omega - \omega_0 = -m_\omega(P - P_0) \quad (6a)$$

$$Q \approx \frac{V}{X}(E - V) \rightarrow E - E_0 = -m_V(Q - Q_0) \quad (6b)$$

$$P \approx \frac{V}{R}(E - V) \rightarrow E - E_0 = -m_V(P - P_0) \quad (7a)$$

$$Q \approx -\frac{V}{R}E\delta \rightarrow \omega - \omega_0 = m_\omega(Q - Q_0) \quad (7b)$$

Equations (5a) and (5b) can be expressed in matrix form as shown in (8).

$$\begin{pmatrix} P \\ Q \end{pmatrix} = \frac{V}{Z^2}\left[\begin{pmatrix} R & X \\ X & -R \end{pmatrix}\begin{pmatrix} E_d \\ E_q \end{pmatrix} - \begin{pmatrix} R \\ X \end{pmatrix}V\right] \quad (8)$$

From (8), applying a droop coefficient, m_V, to relate E_d and E_q variations with both P and Q, the proposed droop formula shown in (9) is obtained in the same way $P/f + Q/V$ and $P/V + Q/f$ are obtained in (6) and (7) [1].

$$\begin{pmatrix} E_d - E_{d0} \\ E_q - E_{q0} \end{pmatrix} = -m_V\begin{pmatrix} R/Z & X/Z \\ X/Z & -R/Z \end{pmatrix}\begin{pmatrix} P - P_0 \\ Q - Q_0 \end{pmatrix} \quad (9)$$

This complex-valued droop, obtained from the dq-decomposition, takes into account the coupling between P and Q. It only requires knowledge on the lines R/X ratio and, by applying the droop to both voltage components instead of magnitude and frequency, enables no frequency deviation in steady-state.

Considering the analyzed droop alternatives, the complete converter control scheme is shown in Fig. 2, together with the different droop controllers. Details about cross-coupling and feed-forward terms, normalization and nonlinear compensation can be seen in [12].

III. Complex-valued Droop Steady-state behaviour

Applying a droop related to voltage components will cause a voltage deviation with respect to nominal value in the same way $P/f + Q/V$ and $P/V + Q/f$ alternatives have deviations with respect to frequency and voltage.

In our proposal, since both components, E_d and E_q, are involved in the droop calculation, the combined effect of both components shall be analyzed to check if the impact in the voltage deviation is increased.

Considering $\Delta S = \Delta P + j\Delta Q = (P - P_0) + j(Q - Q_0)$ and $\Delta E = \Delta E_d + j\Delta E_q = (E_d - E_{d0}) + j(E_q - E_{q0})$, (9) can be rewritten as shown in (10).

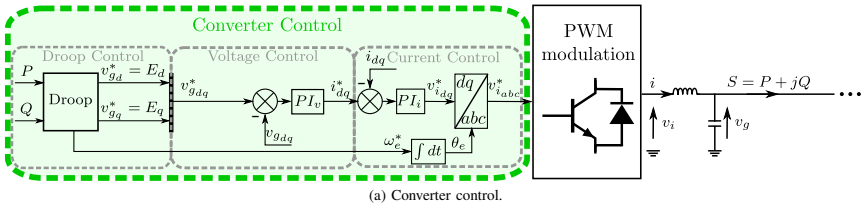

(a) Converter control.

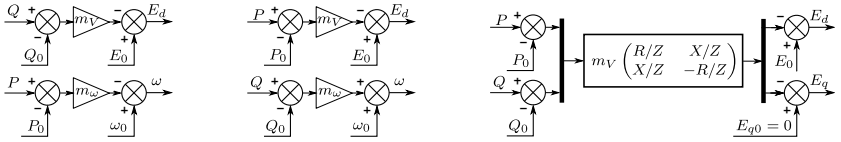

(b) $P/f + Q/V$ droop. (c) $P/V + Q/f$ droop. (d) Complex-valued droop.

Fig. 2. Control scheme including the different droop control methods. For $P/f+Q/V$ and $P/V+Q/f$ droops, E_q reference is set to 0 and for complex-valued droop ω reference is set to 100π rad/s (50 Hz). For the simulations in this paper $P_0 = Q_0 = 0$.

$$\begin{pmatrix}\Delta E_d\\ \Delta E_q\end{pmatrix} = -m_V \begin{pmatrix}R/Z & X/Z\\ X/Z & -R/Z\end{pmatrix}\begin{pmatrix}\Delta P\\ \Delta Q\end{pmatrix} \tag{10}$$

For this demonstration, the PEC is considered to be producing an apparent power S, expressed as a complex number $S = P + jQ = |S|\angle\alpha$. For the simulations in this paper $P_0 = Q_0 = 0$, resulting in $\Delta S = S$. As shown in Fig. 2d, $E_{q0} = 0$ and $E_{d0} = E_0$, that for simplicity will be expressed in per unit as $E_{d0} = 1$ pu. Expressing the matrix equation (10) in complex number form, (11) is obtained.

$$\Delta E = -m_V(R/Z + jX/Z)(P - jQ) \tag{11}$$

$(R/Z + jX/Z)$ is a complex number with modulus 1 and angle ϕ and $(P - jQ)$ is the conjugate of the apparent power. Thus (11) can be rewritten as shown in (12).

$$\Delta E = -m_V|S|(\cos\beta + j\sin\beta) \tag{12}$$

Being β the difference between line impedance phase angle and apparent power angle $(\phi - \alpha)$.

With (12) and taking into account that $E_{d0} = 1$ pu, the voltage amplitude is obtained using the formula shown in (13).

$$|E| = \sqrt{(1 - m_V|S|\cos\beta)^2 + (m_V|S|\sin\beta)^2} \tag{13}$$

Taking into account $\cos^2\beta + \sin^2\beta = 1$, the deviation in the voltage amplitude due to the proposed droop method with respect to nominal value (1 pu) is obtained by (14).

$$\Delta|E| = \sqrt{1 - 2m_V|S|\cos\beta + m_V^2|S|^2} - 1 \tag{14}$$

It is important to remark here, that for all the demonstration before, the values used for impedance phase angle are not the real ones, but the ones assumed by the droop control. This means that in case that the estimation of the angle is not correct, the one that is involved in the voltage deviation effect is the estimated one (from now on ϕ_{est}).

The maximum deviation in voltage amplitude is obtained for $\beta = 0°$ and $\beta = 180°$, as shown in (15a) and (15b) respectively.

$$\Delta|E| = \sqrt{1 - 2m_V|S| + m_V^2|S|^2} - 1 = -m_V|S| \tag{15a}$$

$$\Delta|E| = \sqrt{1 + 2m_V|S| + m_V^2|S|^2} - 1 = m_V|S| \tag{15b}$$

Where m_V is expressed in per unit value. This means that the maximum value for the voltage amplitude deviation is obtained when line impedance and apparent power have opposite phases while the minimum occurs when they have the same phase. In both cases, the deviation from nominal value is $m_V|S|$ in absolute value.

Taking this into account, it can be concluded that the range for voltage amplitude deviation obtained from the proposed droop control for $|S| \leq S_n$ is $(-m_V, m_V)$, as it happens in the $P/f + Q/V$ and $P/V + Q/f$ droops for a variation of P or Q in the range of $(-S_n, S_n)$.

In the case of $P/f+Q/V$ and $P/V+Q/f$ droops, voltage amplitude is only a function of active/reactive power with a linear relationship, meanwhile in the proposed complex-valued droop it depends on both apparent power magnitude and phase difference with respect to line impedance phase angle.

This relationship for a fix value of $|S|$ is shown in Fig. 3, with the deviation in output voltage for different values of apparent power angle (α).

The curve for $P/f + Q/V$ and $P/V + Q/f$ is a sinusoidal waveform, since for a fixed value of $|S|$, the relationship of voltage variation with respect to the angle is $\Delta|E| = -m_V Q = -m_V|S|\sin(\alpha)$ and $\Delta|E| = -m_V P = -m_V|S|\cos(\alpha)$ respectively.

Since the dependence of voltage deviation with respect to angle shown in (14) is for angle $\beta = \phi_{est} - \alpha$, different values of ϕ_{est} result in a horizontal displacement of the corresponding $\Delta|E|$ vs α curve. When $\phi_{est} = 0°$, the corresponding curve

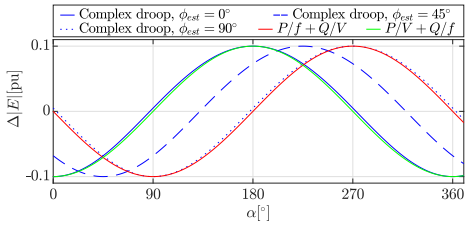

Fig. 3. Variation of voltage amplitude output for different values of α (apparent power angle), with $m_V|S| = 0.1$ pu.

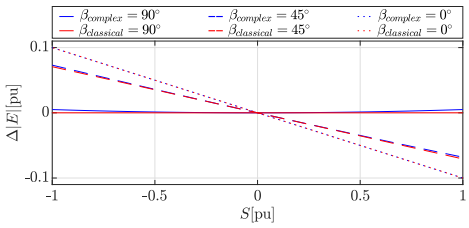

Fig. 4. Variation of voltage amplitude output for different values of S, with $m_V = 0.1$ pu. Blue lines correspond to the proposed complex droop and red lines to the classical $P/f + Q/V$ and $P/V + Q/f$ alternatives. For $\beta = 0°$, the three droops produce the same variation (red and blue dotted lines coincide).

(continuous blue) is very similar to the one corresponding to $P/V + Q/f$ droop (continuous green), meanwhile when $\phi_{est} = 90°$ the corresponding curve (dotted blue) is very similar to the one corresponding to $P/f+Q/V$ droop (continuous red). In all the cases, the maximum voltage deviation is $m_V|S|$.

In Fig. 4, the variation of voltage amplitude for different values of apparent power is shown for different values of angle β. Taking into account that β was defined as $\phi_{est} - \alpha$ for the proposed droop, it can be defined in a similar way for $P/f + Q/V$ and $P/V + Q/f$ considering $\phi_{est} = 90°$ and $\phi_{est} = 0°$ respectively, since these droops are obtained assuming purely inductive/resistive lines for obtaining the droop equations. With this notation, $\beta = 0°$ implies apparent power to be purely reactive for $P/f + Q/V$ droop and active for $P/V + Q/f$, producing the maximum voltage deviation. For Fig. 4, S is considered as a real number, having the apparent power the direction of β and being positive for power production and negative for consumption.

A. Droop coefficient selection

Taking into account that the proposed droop produces a voltage output variation range equal to the one obtained for $P/f + Q/V$ and $P/V + Q/f$ droops, the starting point for selection of the droop coefficient can be done taking into account the maximum variation of the voltage output.

For this paper, a maximum voltage deviation of 2.5 % is used for droop coefficient selection. Due to the similar effect in voltage deviation produced by the classical droops

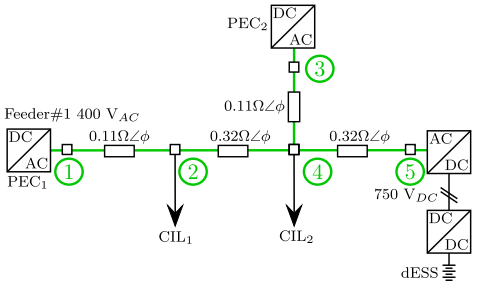

Fig. 5. Grid used for simulation. Impedance phase angle (ϕ) varies for different simulation scenarios.

TABLE I
CONVERTER PARAMETERS.

S_n	30 kVA	PI$_i$: P Gain	50
R_{filter}	0.1 Ω	PI$_i$: I Gain	500
L_{filter}	1.35 mH	PI$_v$: P Gain	5
C_{filter}	980 μF	PI$_v$: I Gain	50
Droop: m_ω	$9 \cdot 10^{-5}$	Droop: m_V	$2 \cdot 10^{-4}$

($P/f + Q/V$ and $P/V + Q/f$) and the proposed complex-valued alternative, the same value for the coefficient is used for the three cases and using the same name for this coefficient (m_V).

IV. CASE STUDY

The grid used as case study is shown in Fig. 5, where PEC$_1$ and PEC$_2$ are droop-controlled power electronic converters connected in node 1 and 3 respectively. Constant impedance loads are connected in node 2 (CIL$_1$) and 4 (CIL$_2$) and a converter connected to distributed energy storage system (dESS) is connected to node 5, behaving as a constant power load (CPL).

The used grid is one of the ac feeders from the microgrid shown in [13]. For demonstration purposes, both converters are considered to be equal with a rated power of 30 kVA. Converter parameters are shown in Table I.

To compare the performance of the proposed complex-valued droop with respect to $P/f + Q/V$ and $P/V + Q/f$ droops, the impedance phase angle (ϕ) is varied. Three different angles (0°, 45° and 90°) are following considered in the simulation results.

V. SIMULATION RESULTS

The simulation results are divided in two main parts. In the first one, the proposed droop is compared with the classical $P/f + Q/V$ and $P/V + Q/f$. For these simulations, perfect knowledge of the impedance phase angle is assumed. Impedance estimation [14], [15] can be used for online estimation. For the second part, the response of the proposed droop when mismatches occur in the impedance phase angle estimation are analyzed.

A. Comparison of different droop methods

Simulations for the different impedance phase angles are shown in Fig. 6. Results for the three different alternatives are shown together for a better comparison between the proposed complex-valued (continuous line) droop and the classical $P/f + Q/V$ (dashed) and $P/V + Q/f$ (dotted).

Starting with no load, at $t = 0.05$ s a CIL of 10 kW, 10 kvar is connected in nodes 2 and 4 (Fig. 5). In that situation, the grid is completely symmetric, so both converters have the exact same output. At $t = 0.2$ s another CIL, 10 kW, 10 kvar is connected in node 4. At $t = 0.6$ s the converter in node 5 starts to produce 10 kW, behaving as a CPL.

The proposed droop is able to operate with a good response in all the impedance phase angle range and both for CIL and CPL (bidirectional).

It can be seen, that $P/f + Q/V$ and $P/V + Q/f$ droops present some oscillations during the transient after load connections. These oscillations do not appear in the proposed complex-valued droop, reaching the steady-state much quicker. Additionally, frequency deviation in steady-state does not appear in the proposed droop, while the variation during the transients is really small.

Besides that, it can be seen that the complex-valued droop is able to properly decouple active and reactive power, remaining the reactive power share unchanged when at $t = 0.6$ s an active power step is introduced.

B. Effect of impedance phase angle estimation mismatch

In order to check the effect of impedance phase angle estimation mismatch, simulations with error in the estimation of the angle has been analyzed.

In Fig. 7, simulations for different values of the impedance phase angle are shown with three values for the estimation of the impedance phase angle. The load steps are the same used in Fig. 6.

It can be seen that the control is not very sensitive to this mismatch, as no significant difference in the performance of the control system can be seen. The major differences are related to the voltage output amplitude and frequency results. The difference in frequency results are not very significant, taking into account that the deviation from nominal value is small and nominal value is recovered quickly.

The difference in the voltage amplitude are due to the use of different rotation matrix. As explained in Section III, the deviation in voltage amplitude with respect to nominal value depends on apparent power magnitude and angle and the angle used for the rotation matrix (ϕ_{est}).

It can be seen that the voltage amplitude result is similar for the same ϕ_{est}, even for different values of the actual line impedance phase angle. The small difference is due to the different power sharing of the PECs when line impedance phase angle changes.

VI. Conclusions

This paper has shown a new droop strategy taking into account the coupling terms due to non-purely inductive/resistive lines, using the R/X ratio of the line. This droop, called Complex-Valued droop, does not require to operate with trigonometric functions, using complex formulations and dq-decomposition instead.

The variation of voltage amplitude produced by the proposed droop control has been analyzed, demonstrating that the range of variation is equal to the one obtained for $P/f + Q/V$ and $P/V + Q/f$ droops, but depending on apparent power magnitude and phase instead of active/reactive power.

This similarity in the range of variation allows using this range of output voltage variation as a way of selecting the droop coefficient, as it is often done for $P/f + Q/V$ and $P/V + Q/f$ approaches.

The simulation results have shown the operation of the proposed complex-valued droop, being able to operate at different R/X ratios with a faster response. Besides that, it presents the important advantage of eliminating the frequency deviation inherent to droop-based control in which f is used as one of the droop variables.

The effect of mismatches in the impedance phase angle estimation has been analyzed, showing that the control method is not much affected by these errors for the complete range of R/X values.

References

[1] J. Rocabert, A. Luna, F. Blaabjerg, and P. Rodríguez, "Control of power converters in ac microgrids," *IEEE Transactions on Power Electronics*, vol. 27, no. 11, pp. 4734–4749, 2012.

[2] J. C. Vasquez, J. M. Guerrero, M. Savaghebi, J. Eloy-Garcia, and R. Teodorescu, "Modeling, analysis, and design of stationary-reference-frame droop-controlled parallel three-phase voltage source inverters," *IEEE Transactions on Industrial Electronics*, vol. 60, no. 4, pp. 1271–1280, 2013.

[3] E. Lenz, D. J. Pagano, A. Ruseler, and M. L. Heldwein, "Two-parameter stability analysis of resistive droop control applied to parallel-connected voltage-source inverters," *IEEE Journal of Emerging and Selected Topics in Power Electronics*, vol. 8, no. 4, pp. 3318–3332, 2020.

[4] K. De Brabandere, B. Bolsens, J. Van den Keybus, A. Woyte, J. Driesen, and R. Belmans, "A voltage and frequency droop control method for parallel inverters," *IEEE Transactions on Power Electronics*, vol. 22, no. 4, pp. 1107–1115, 2007.

[5] T. Qunais and M. Karimi-Ghartemani, "Systematic modeling of a class of microgrids and its application to impact analysis of cross-coupling droop terms," *IEEE Transactions on Energy Conversion*, vol. 34, no. 3, pp. 1632–1643, 2019.

[6] Z. Peng, J. Wang, D. Bi, Y. Wen, Y. Dai, X. Yin, and Z. J. Shen, "Droop control strategy incorporating coupling compensation and virtual impedance for microgrid application," *IEEE Transactions on Energy Conversion*, vol. 34, no. 1, pp. 277–291, 2019.

[7] K. Lao, W. Deng, J. Sheng, and N. Dai, "PQ-coupling strategy for droop control in grid-connected capacitive-coupled inverter," *IEEE Access*, vol. 7, pp. 31 663–31 671, 2019.

[8] R. Majumder, B. Chaudhuri, A. Ghosh, R. Majumder, G. Ledwich, and F. Zare, "Improvement of stability and load sharing in an autonomous microgrid using supplementary droop control loop," *IEEE Transactions on Power Systems*, vol. 25, no. 2, pp. 796–808, 2010.

[9] H. Han, X. Hou, J. Yang, J. Wu, M. Su, and J. M. Guerrero, "Review of power sharing control strategies for islanding operation of ac microgrids," *IEEE Transactions on Smart Grid*, vol. 7, no. 1, pp. 200–215, 2016.

[10] J. M. Guerrero, M. Chandorkar, T. Lee, and P. C. Loh, "Advanced control architectures for intelligent microgrids—part i: Decentralized and hierarchical control," *IEEE Transactions on Industrial Electronics*, vol. 60, no. 4, pp. 1254–1262, 2013.

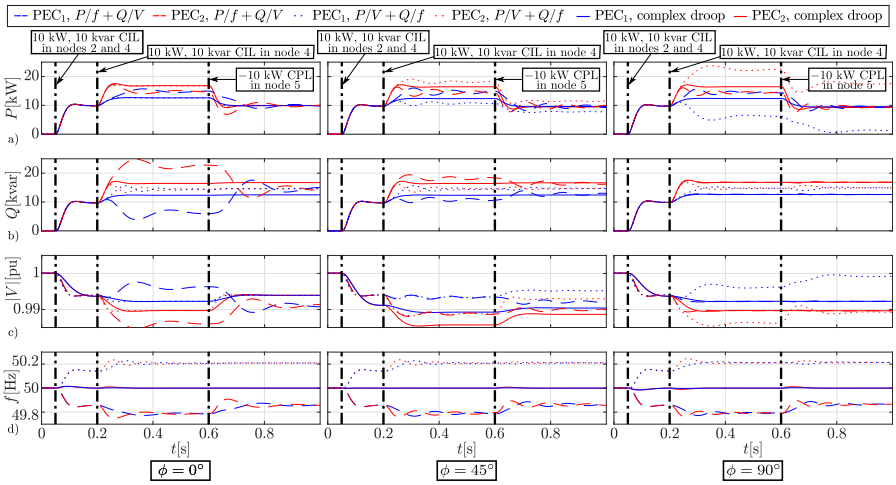

Fig. 6. Simulation results for different values of impedance phase angle (ϕ) for the three type of droops: a) active power production, b) reactive power productions, c) output voltage magnitude and d) frequency.

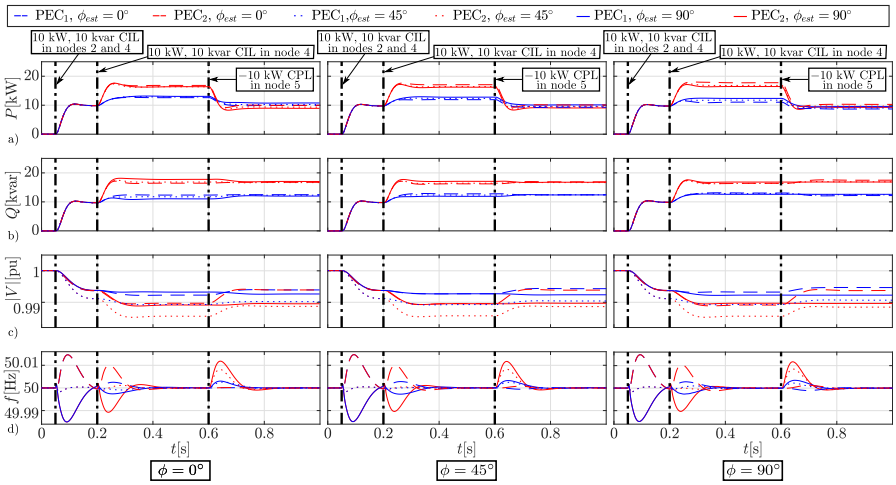

Fig. 7. Simulation results for different values of impedance phase angle (ϕ) for three values of estimated impedance phase angle (ϕ_{est}).

[11] B. Li, L. Zhou, x. yu, C. Zheng, and J. Liu, "Improved power decoupling control strategy based on virtual synchronous generator," *IET Power Electronics*, vol. 10, 12 2016.

[12] Á. Navarro-Rodríguez, P. García, R. Georgious, and J. García, "Adaptive active power sharing techniques for dc and ac voltage control in a hybrid dc/ac microgrid," *IEEE Transactions on Industry Applications*, vol. 55, no. 2, pp. 1106–1116, March 2019.

[13] C. Gómez-Aleixandre, Á. Navarro-Rodríguez, G. Villa, C. Blanco, and P. García, "Sharing control strategies for a hybrid 48V/375V/400Vac AC/DC microgrid," in *2020 IEEE Energy Conversion Congress and Exposition (ECCE)*, 2020, pp. 3900–3907.

[14] P. García, M. Sumner, Á. Navarro-Rodríguez, J. M. Guerrero, and J. García, "Observer-based pulsed signal injection for grid impedance estimation in three-phase systems," *IEEE Transactions on Industrial Electronics*, vol. 65, no. 10, pp. 7888–7899, 2018.

[15] A. Suárez, C. Blanco, P. García, Á. Navarro-Rodríguez, J. Manuel, and C. Rodríguez, "Online impedance estimation in ac grids considering parallel-connected converters," in *2018 IEEE Energy Conversion Congress and Exposition (ECCE)*, 2018, pp. 5912–5919.

B.2 Sharing Control Strategies for a Hybrid 48V/375V/400Vac AC/DC Microgrid

Sharing Control Strategies for a Hybrid 48V/375V/400Vac AC/DC Microgrid

Carlos Gómez-Aleixandre, Ángel Navarro-Rodríguez, Geber Villa, Cristian Blanco and Pablo García
Dept. of Electrical, Electronics, Systems & Computers Engineering
University of Oviedo, LEMUR Group
Gijón, 33204, Spain
Email: gomeztcarlos@uniovi.es, navarroangel@uniovi.es, villageber@uniovi.es,
blancocristian@uniovi.es, garciafpablo@uniovi.es

***Abstract*—This paper studies the sharing control scheme for a Hybrid 48V/375V/400Vac AC/DC Microgrid, considering reliability as one of the key factors. For that purpose, different possible paths for energy flow provide redundancy to the grid. However, this redundancy leads to the need of enhanced coordinated control systems that can enable these alternative paths for the energy flow. In this paper, both the dc and ac grids are controlled by a P/V droop strategy. At the ac grid, this assumes a main resistive component in the distribution line impedance. The droop control voltage error in steady state is compensated by a novel and simple secondary control approach. The proposed control strategy is based on the calculation of the optimum power flow in each operating point and the real-time modification of the droop characteristics of the converters involved in the power flow calculation. The proposed control is also capable of eliminating the induced voltage drop when using virtual impedance and incorporating any power sharing criteria for the converters contributing to the power production.**

I. Introduction

The future electricity grid is gradually moving in the direction of dc distribution, due the envisaged lower distribution losses (compared with ac distribution) and the more efficient integration of renewables and distributed resources [1]–[3]. The evolution in power electronics and control technologies has enabled the development of dc Low-Voltage (LV) microgrids, which eases the integration of Energy Storage Systems (ESS). Although the pathway from traditional ac distribution systems to these new topologies integrating is not clear, it is reasonable to think that the new grids should take advantage of the already existing ac infrastructure, leading to the creation of hybrid ac/dc microgrids [1]. This hybrid approach should use Power Electronic Converters (PEC) in order to provide redundancy of power flows, thus increasing the grid resiliency [4].

This paper shows a proposal of a hybrid ac/dc microgrid that can be built up over the existence ac infrastructure by adding the corresponding dc energy paths. The coordinated control of all the involved interlinking (ac/dc and dc/dc) converters is also provided, considering a P/V droop control for the primary control and a novel approach for the secondary control.

Secondary control typically relies on integrators or PI regulators to eliminate the voltage deviation, both in ac [5] and dc [6]. This requires periodic calculations for the integrator to operate, gradually reducing the error every cycle. The proposed secondary control is able to eliminate the voltage deviation due to droop controllers based on a single calculation of the optimum power flow, shifting the droop characteristic of each converter according to voltage and power obtained from the power flow, in which any criteria for the power sharing can be used. This proposed solution, requiring only one calculation for optimizing the operating point, has lower communication requirements and robustness against communication delays or loss of transmitted data.

This secondary control also provides the capability of compensating the voltage drop of virtual impedance techniques at the steady-state, [7]–[11]. As stated in [7] the virtual impedance can be used for many different purposes like active stabilization and disturbance rejection or, in the case of droop controllers, for making the line impedance more resistive/inductive, depending on the type of droop used.

However, this virtual impedance causes a voltage drop, that makes the effective total voltage drop greater, since the real output voltage of the converter is lower than the reference one (assuming that the converter is producing power). Some solutions can be found in the literature, like the use of a high-pass filter in the virtual impedance [8] to eliminate the effect of the virtual impedance in steady-state. However, this solution is only valid when the use of the virtual impedance is needed because of its transient effect (like the active stabilization aforementioned). When the steady-state effects of the virtual impedance are also needed, this solution is not valid. It is shown in the paper, how the designed secondary control can take into account this virtual impedance and eliminate the effect of its voltage droop. This is done by adding extra nodes to the optimum power flow calculation and selecting the physical connection of the converter, after the virtual impedance, to be the node having 1 p.u. voltage.

This paper is organized as follows. In Section II, the proposed hybrid microgrid topology and the power converters topologies are described. In Section III, the control strategy

The present work has been partially supported by the predoctoral grants program FPU for the formation in university teaching of Spain MECD under the grant IDs FPU16/05313 and FPU16/06829. This work also was supported in part by the European Union's H2020 Research and Innovation programme under Grant Agreement No 864459 (UE-19-TALENT-864459).

is explained, with a special focus in the proposed secondary control. Section IV shows the simulation results and Section V presents the conclusions.

II. Proposed Microgrid Topology

The hybrid ac/dc network architecture [12] proposed in this paper is shown in Fig. 1 with the topologies of the converters in the shadowed blocks. The ac feeders and the dc lines (both ± 375 and 48 Vdc) are modeled as purely resistive lines, assuming a maximum voltage drop of 5 % at the end of the line for the rated power.

The use of P/V droop control in the ac part of the microgrid is due to the fact that the grid impedance in LV networks is mainly resistive [13]. Being the lines purely resistive, if reactive power loads and references were set to 0, the ac part of the microgrid could be studied as if it was dc. Being the q-axis component of the voltages equal to 0 in steady-state, the d-axis component is equivalent to a dc voltage for the calculations.

For this reason, the analysis done in the paper starts with the dc case, since it is also a simplified study of the ac part. From dc solution, some modifications are done in order to include reactive power and possible non purely resistive impedances in the calculations for the ac complete solution.

As explained in Section I, virtual impedance can be used for different purposes, introducing an induced voltage drop. In this paper, virtual impedance is used for the converters in the ac feeders and is taken into account too for compensating its voltage drop.

III. Coordinated control

As explained in the previous sections, the coordinate control of the power converters is done with a P/V droop control, both for the ac feeders and the 48 Vdc network.

This droop control acts as a primary control, making possible that all the converters which can deliver power, either coming from the connection to the main ac grid or from ESS, contribute to the power sharing.

The power sharing at the primary control level is achieved without requiring communication among the power converters. However, communication among them is used for upper level control, namely secondary and tertiary control for enhanced power sharing. This is later discussed in the paper.

A. ± 375 Vdc grid control

In the ± 375 Vdc grid, the SST provides connection to the mains supply and to the central ESS. In the present paper, this is simplified as a dc/dc converter connected to a dc voltage source since the focus is in the hybrid microgrid. This dc/dc converter controls the voltage different between the positive and the negative bus (750 Vdc) as shown in Fig. 2.

Header PEC (HPEC), connected to node 1, is in charge of the dc bus balancing [14], due to its neutral point clamped topology, assuring that the voltage in both buses is 375 Vdc (one positive and one negative with respect to the neutral).

These two buses are distributed so that loads can be directly connected to these dc buses. They can be connected to either bus, so loads can be strongly unbalanced. Apart from that, Ring#1 PEC is connected to $+375$ Vdc bus and Ring#2 PEC is connected to -375 Vdc bus.

These two buses are distributed, so that loads can be directly connected to them. Due to the different loads at each of the buses (Ring#1 PEC at the $+375$ Vdc and Ring#2 PEC to the -375 Vdc bus respectively), they could become strongly unbalanced thus making much needed the balancing control implemented at the HPEC.

B. 48 Vdc network control

In Fig. 3 the control diagram for the 48 Vdc grid is shown. The control system is separated into two main blocks; 1) the internal converter control and 2) the central control. The internal control implements the voltage control using a quadratic approximation [15] and relies on a cascaded-architecture with an internal current controller. The references for the voltage control are given by a P/V droop. Connected to the internal control, the central controller provides the power references to the different converters based on the secondary control, whose effect is to shift the droop curve.

The droop coefficient for each converter is calculated according to its power rating, corresponding the rated power to a voltage deviation of 10 %. The droop characteristic equation is shown in (1), where k_p is the droop coefficient; P, the measured power output; P_0, the offset power (the one that would correspond to voltage V_0, equal to rated voltage for this paper); V_n and P_n, the rated voltage and power; and V, the output of the droop control.

$$V = k_p(P_0 - P) + V_0 \rightarrow k_p = 0.1 \cdot \frac{V_n}{P_n} \tag{1}$$

C. 400 Vac feeder control

The general control scheme for the converters in the ac feeder is shown in Fig. 4, which is completely equivalent to the 48 Vdc network case except from the decomposition in the synchronous dq reference frame. Details about cross-coupling and feedforward terms shown in [15] are omitted due to space constraints. The reference for the d axis voltage control is given by a P/V droop. The central controller plays the same role as in the case of the 48 Vdc network. In here, also the q-axis voltage reference is provided to the different converters.

D. Secondary control

For the secondary control, a new strategy has been used. The idea consists on changing the P/V droop characteristics of each converter, by modifying offset power P_0 in (1), so that they match the desired solution. For this paper, the chosen solution is to have a power sharing among the droop controlled converters proportional to each converter power rating and a voltage of 1 p.u. at a given specific node. In general, the output of the main converter of the corresponding grid is used as the 1 p.u. reference.

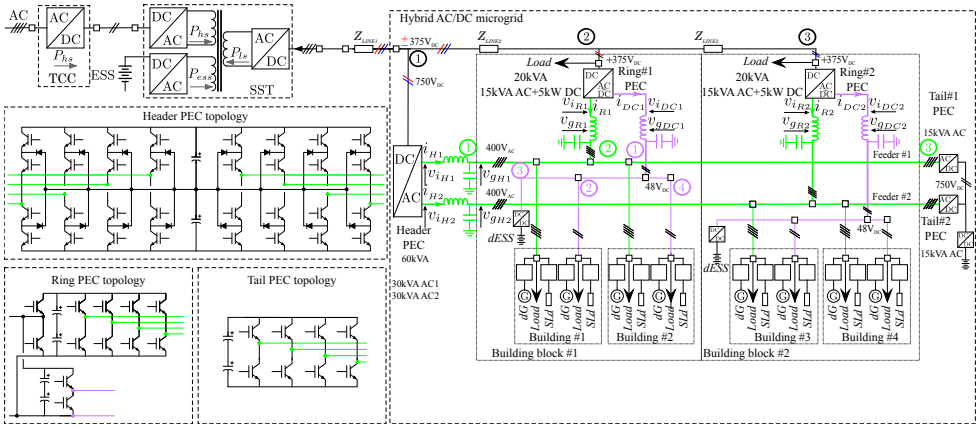

Fig. 1. Proposed system level grid infrastructure [12].

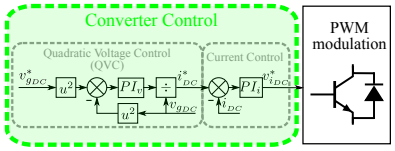

Fig. 2. Control diagram for dc/dc converter used as a simplification for the SST connection to the mains supply and to the central ESS.

This secondary control is applied to the 400 ac feeder and the 48 Vdc network. Considering the proposed grid topology in each case, the loads at each node and the reference output power of each converter, the power flow can be calculated, resulting in the voltage profile at each node considering one of the nodes is set to 1 p.u. For these calculations, only droop-controlled converters participating in the power sharing are taken into account as controllable converters, the remaining are seen as bidirectional loads.

The reference power output of each converter can be selected with different criteria. For the calculations presented hereafter, the sharing among the converters is proportional to the power rating of each converter. If any other criteria is used, this method could easily accommodate to it without further implications.

In this case, as shown in Fig. 1 both studied cases, the ac feeder or the 48 Vdc network, are radial networks, without rings inside. This eases the calculation of the power flow. Different grid topologies, including mesh and ring networks could also be considered, thus increasing the computational burden for the power flow calculations [16].

Calculations required for dc and ac case are very similar, but dc case is presented before, since it is simpler and more straightforward because it does not include reactive power and decomposition of voltage in dq-axis. After presenting both cases, the possibility of including virtual impedance is presented too.

1) Secondary control in dc: Knowing the reference power and the voltage at each converter, obtained from the power flow, P_0 can be calculated so that the droop characteristic, whose equation is shown in (1), meets the requirements. The method is explained using as example a completely linear network, as shown in Fig. 5. The variables shown there have the same names used in the method equations later explained.

In Fig. 6, the flowchart for the method is shown. Step 1 is for initialization, starting assuming no losses. Step 2 to 6 perform an iteration of the power flow. After step 6, a stop criterion is checked for deciding whether to stop or to continue with the next iteration. The stop criterion can be a limit for the difference between the power losses used for the power flow calculation and the ones calculated in step 6, a maximum number of iterations or a mix of both. Step 7 calculates the offset power for each converter, P_{0PECi}, so that the droop curve of each converter matches the solution from the power flow, as shown in Fig. 7. This offset power is sent back to the converter control to modify their droop (see Fig. 3).

2) Secondary control in ac: The implementation of the secondary control in ac is really similar to the dc case but power (S, in this case), voltage, impedance (Z) and currents should all be complex, except for S_{nPECj} which is the nominal power of each converter.

Fig. 8 show the corresponding calculations for ac. The only significant difference is in the last step. Since the droop is applied to P and V_d (real part of S and V complex vectors), the equation for calculating the active power offset only change is to use real part of V. V_q (imaginary part of V for each node) is an output and is sent to the converters as a reference.

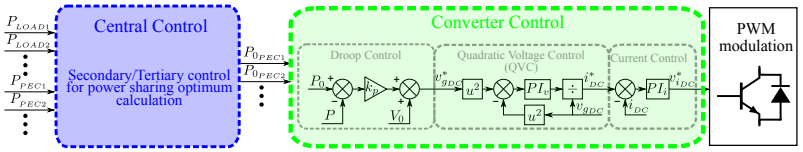

Fig. 3. General control diagram for converters in the 48 Vdc network. P_{LOADi} is the aggregate load connected to node i, P_{PECi} is the measured power output of the converter and $P_{0_{PECi}}$ is the power offset for the converter connected to node i.

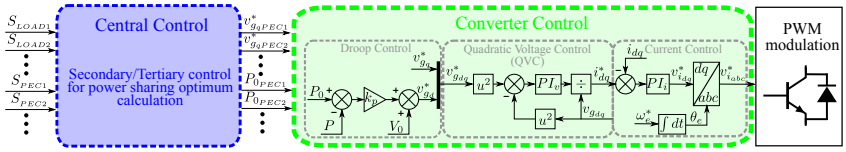

Fig. 4. General control diagram for converters in the ac feeder. S_{LOADi} is the aggregate load connected to node i, S_{PECi} is the measured power output of the converter and $P_{0_{PECi}}$ is the active power offset for the converter connected to node i. Both S_{LOADi} and S_{PECi} mean P and Q are required (being $S = P + jQ$).

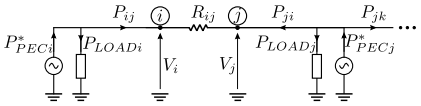

Fig. 5. Power flow diagram. P_{ij} is the power flow from node i to j, P_{ji} from j to i and P_{jk} from j to k. P^*_{PECi}: reference power for converter at node i, P_{LOADi}: total connected load in that node and V_i: voltage in that node.

Apart from the differences due to the use of complex variables in ac, the voltage drop for the dc case is calculated as $2RI = 2R\frac{P}{V}$ meanwhile in ac it is $ZI = Z\frac{\overline{S}}{\sqrt{3}\cdot\overline{V}}$, because the ac network is three-phase.

3) Secondary control including virtual impedance: As explained in Section II, the aim of the secondary control when virtual impedance is considered is the compensation of the induced voltage drop. Compensating its voltage drop is straightforward with the proposed secondary control, adding extra nodes to the power flow calculations in Fig. 8.

In the example shown in Fig. 8, voltage in physical node 1, V_1, is selected to be 1 p.u., obtaining this voltage at the physical connection of the PEC to that node. A virtual node is added before the virtual impedance voltage drop. This can be seen in Fig. 9 with an example of a circuit including virtual impedance, $Z_{vir,i}$. The voltage in the node in which each converter is physically connected is V_i and it is the one obtained from the power flow explained before. The voltage before the virtual impedance, $V_{PEC,i}$, can be obtained from V_i, adding the voltage drop in the virtual impedance. This calculation is shown in (2).

$$V_{PECi} = V_i + Z_{vir,i}\frac{\overline{S^*_{PECi}}}{\sqrt{3}\cdot\overline{V_i}} \tag{2}$$

The calculated V_{PECi} should be used instead of V_i in last step in Fig. 8. So in Fig. 9, $V_{PEC,i}$, which is a virtual voltage, is the voltage used for the droop calculations but voltage V_i is the one fixed to 1 p.u.

The calculation presented in (2) is done considering a three-phase ac system, but to extend it to dc case is straightforward, by using real (R, P) instead of complex variables (Z, S) and changing the factor of $1/\sqrt{3}$ by factor of 2 for the voltage drop calculation.

IV. Simulation Results

The presented solution has been simulated using Matlab/Simulink. The complete circuit is the one depicted in Fig. 1, with node numbers for each part of the microgrid: green for ac feeder; purple for 48 Vdc network; black for the ±375 Vdc buses.

In the ac feeder, nodes number 1 and 2 have HPEC and the ac output of the Ring PEC (RPEC-AC) with droop control and loads are connected to 2 and 3, where TPEC works in PQ mode.

In the 48 Vdc, the dc output of the RPEC (RPEC-DC) works in droop control, together with a dc/dc converter of 2 kW connected to distributed ESS (dESS-PEC). Loads are connected to nodes 2 and 4.

In the ±375 Vdc grid, HPEC, connected to node 1, are in charge of the dc bus balancing [14] and loads are connected to 2 (positive dc bus) and 3 (negative dc bus).

The details of the different converter rated power and output LC filter parameters as well as the control loop bandwidths and gains are shown in Table I, where PI_i and PI_v are the PI regulators for current and voltage and k_p, the droop coefficient, as shown in Fig. 3 and 4.

The simulation results are presented in two different sections. First, a general result, with different step changes in the loads at each subgrid (48 Vdc/375 Vdc/ 400 Vac), is

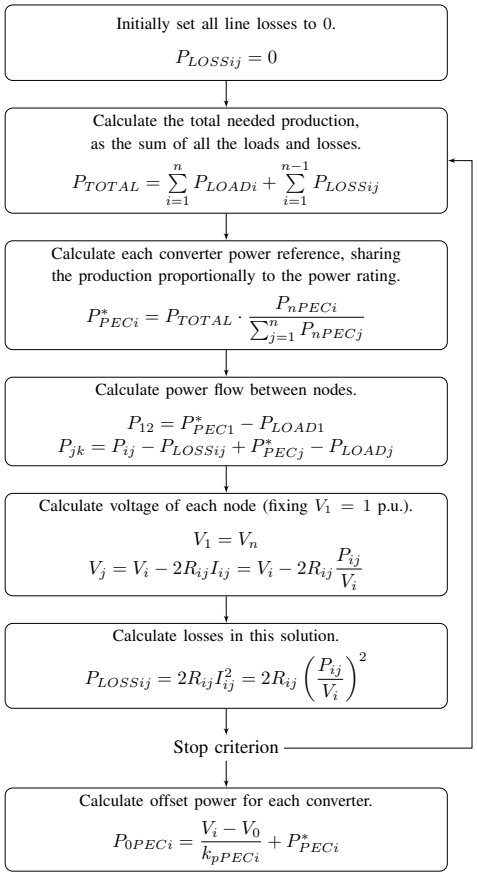

Fig. 6. Flowchart for secondary control in dc. i, j and k denote any three consecutive nodes.

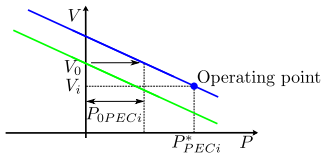

Fig. 7. Droop curve shift for fulfilling power flow solution. Green: base case with $P_{0PECi} = 0$ and blue: final solution.

presented. In this point, the general operation of the grid is shown, together with the activation of the secondary control. Following, a continuation of the simulation for the general

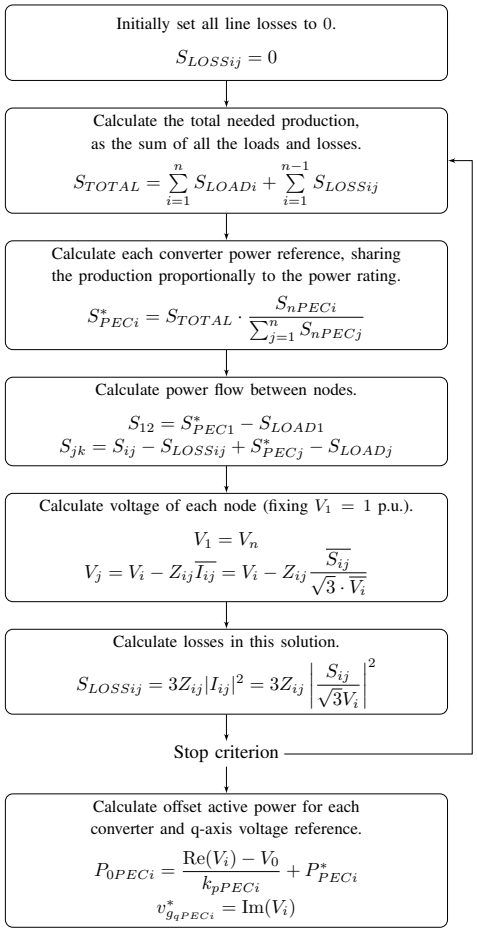

Fig. 8. Flowchart for secondary control in dc. i, j and k denote any three consecutive nodes. For obtaining a more compact expression, active and reactive power equations are presented in its complex form, so they are joint into one equation with $S = P + iQ$, using also $Z = R + iX$. $\overline{x}$, $\mathrm{Re}(x)$ and $\mathrm{Im}(x)$ are the conjugate, real part and imaginary part of a complex vector.

operation of the grid is shown, focusing more in the operation of the secondary control. Different changes are introduced to this secondary control, so that the flexibility of the method is proved.

A. General simulation result

The results for the ±375 Vdc buses are shown in Fig 10. The balancing method from [14] is able to maintain the balance of the dc buses even when having very different demands.

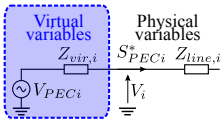

Fig. 9. Example of circuit including virtual impedance. V_i is the voltage at the physical connection of the corresponding PEC and $Z_{line,i}$, the coupling impedance. $Z_{vir,i}$ is the virtual impedance of the PEC and $V_{PEC,i}$, the (virtual) voltage before the voltage drop in the virtual impedance.

TABLE I
CONVERTER PARAMETERS.

Converter	HPEC	RPEC-AC	RPEC-DC	dESS-PEC
S_n / P_n	30 kVA	15 kVA	5 kW	2 kW
L_{filter} (mH)	1.68	3.37	1.47	3.67
R_{filter} (mΩ)	35.3	70.5	30.7	76.8
C_{filter} (mF)	0.5	0.1	5	5
C_{bus} (mF)	5	5	5	5
PI_i: P Gain	5.29	10.58	4.61	11.52
PI_i: I Gain	20.94	20.94	20.94	20.94
PI_i: BW (Hz)	500	500	500	500
PI_v: P Gain	0.111	0.022	1.111	1.111
PI_v: I Gain	222.14	222.14	222.14	222.14
PI_v: BW (Hz)	50	50	50	50
k_p (p.u.)	0.1	0.1	0.1	0.1

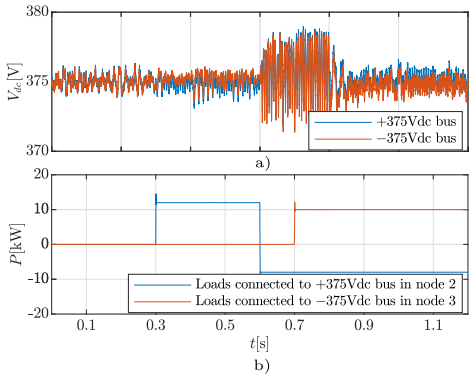

Fig. 10. ±375 Vdc buses simulation result. a) voltage for positive and negative dc buses. b) loads directly connected to both buses.

Fig. 11 and 12 show the results for LV dc network and ac feeder. In both cases, before the vertical line, secondary control is not activated. A sequence of step loads is introduced so that the primary control operation of the system is shown. The vertical line indicates the activation of the secondary control.

LV dc network results are shown in Fig. 11. As expected, the droop control causes a deviation from the nominal voltage. However, when the secondary control is activated, this voltage deviation is eliminated, being the voltage 48.00 V in the end of the simulation, with less than 0.002 % error. This is achieved for node 1, since it was the one selected to have voltage of 1

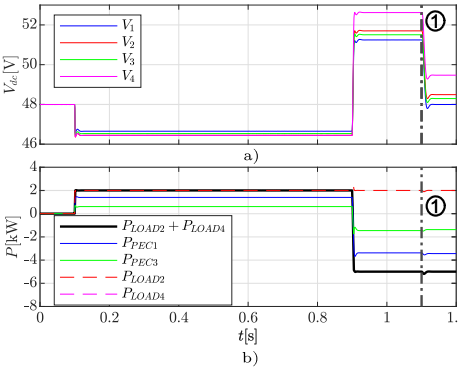

Fig. 11. 48 Vdc grid simulation results. Line 1: activation of secondary control. a) voltage at each node. b) active power production of each converter and active power consumption of each load

p.u. in the power flow solution for this example.

Apart from that, the power sharing between the two converters, gets closer to the theoretical value of 2.5, which is the ratio between both converters rated power. The relationship between power production by converter in node 1 and by converter in node 3 is 2.31 before the secondary control and 2.50 after measured at the end of Fig. 11, with less than 0.04 % error.

The results for the ac feeder are shown in Fig. 12. As commented for the LV dc case, the voltage deviation is eliminated when the secondary control is activated, being 1.00 p.u. at the end of the simulation, with less than 0.06 %. In the ac feeder, the droop-controlled converter uses a virtual impedance approach. As it can be seen, the effect of its voltage drop is also compensated. This is clearly visible since the voltage shown in the figures are measured at the physical converter nodes.

For the power sharing, both active and reactive power have a ratio between both converters of 2, corresponding to the ratio between their rated power. The relationship between active and reactive power production of the converters before the secondary control is activated is 1.28 and 0.86 respectively. After activating the secondary control, it becomes 1.98 for active power (less than 0.95 % error) and 2.03 for reactive power (less than 1.6 % error).

It is worth to remark here that for the reactive power no droop is being used, so the sharing without secondary control is not controlled anyway and depends only on grid configuration and load demand and its distribution in the grid. So, meanwhile P/V droop is able to have an approximation for the active power sharing, which is corrected with the secondary control, no droop is used for the reactive power and the power sharing is controlled only by the secondary control.

In the presented case, the secondary control reference calculation is only done once and the references are sent to the converters. This shows the validity of the method

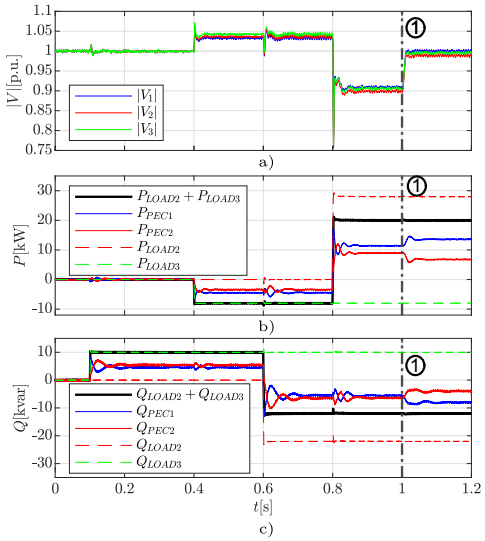

Fig. 12. 400 Vac feeder simulation results. Line 1: activation of secondary control. a) voltage at each node. b) active power production of each converter and active power consumption of each load. c) reactive power production of each converter and active power consumption of each load.

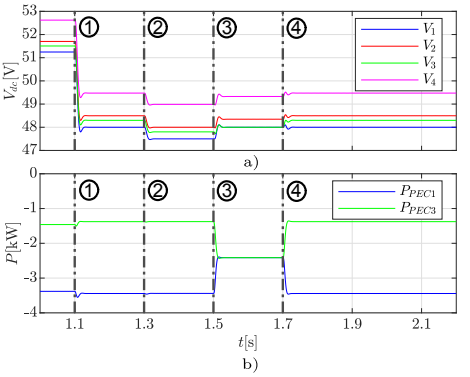

Fig. 13. 48 Vdc grid simulation results for secondary control. Line 1: activation of secondary control. Line 2: change of node whose voltage is set to 48 V, from node 1 to 2 (the change is undone in the line 3). Line 3: change in the power sharing by the converters, from a ratio of 2.5 (proportional to each converter power) to 1 (the change is undone in line 4). Line 4: return to initial situation. a) voltage at each node. b) active power output of each converter.

even for low communication speeds and its robustness against communication delays or loss of transmitted data. However, this is only an example for showing its operation. In a real operation, for taking advantage of the proposed secondary control, the reference calculation and update should be done every time a change in the operating point of the network is detected. Considering low communication speeds, even if significant changes happen between two consecutive checks, the primary control is able to control the operation until the solution is optimized again.

B. Secondary control

For proving the flexibility of the secondary control, an extension of the simulations shown before is presented. Fig. 13 is a continuation of Fig. 11 and Fig. 14 is a continuation of Fig. 12. Power demanded by the loads is not shown, but it remains unchanged from the situation presented in Fig. 11 and 12 when the secondary control is activated.

In both cases, first vertical line indicates the activation of secondary control, that was already shown in the previous figures. The next vertical lines indicate changes in the application of the secondary control, like changes in the node whose voltage is chosen to be 1 p.u. or in the power sharing between the converters. Secondary control reference calculation and transmission is only performed at the time instant represented by a vertical line.

In Fig. 13, starting from the original situation when the secondary control becomes active, a first change is introduced, setting node 2 to have 1 p.u. (48 V) and returning to control voltage in node 1 in the next reference calculation. The second change consists on changing the power sharing among the converters, from a ratio of 2.5, proportional to each converter rated power, to 1, returning to 2.5 in the next reference calculation, thus returning to the initial situation.

It is important to remark here that, when both converters share the power equally, converter in node 3 is working above its rated power. This operating condition is allowed in the simulation for illustrative purposes. With the flexibility shown by the method, it is possible to add more conditions for the power sharing, like these limits for rated power or any other criteria, like ESS State of Charge (SoC).

In Fig. 14, a similar sequence of changes if performed. Starting from the original situation when the secondary control becomes active, a first change is introduced, setting node 3 to have 1 p.u. and returning to control voltage in node 1 in the next reference calculation. For visualizing properly this changes, the original voltage signals are filtered (10 Hz second order filter).

The second change consists on changing the power sharing among the converters, from a ratio of 2, proportional to each converter rated power, to 1, both for active and reactive power. In the next reference calculation, the original power sharing is reestablished for active power and for the last reference calculation it is reestablished for reactive power, returning to the original situation. This shows the flexibility of the method also for having different criteria for both active and reactive power. For example, STATCOM or PEC whose active power is

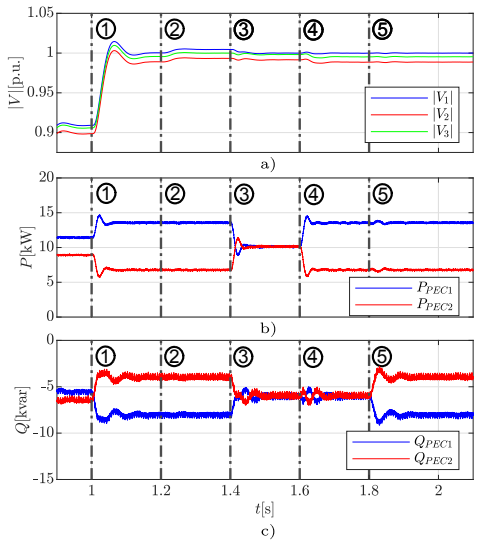

Fig. 14. 400 Vac feeder simulation results for secondary control. Line 1: activation of secondary control. Line 2: change of node whose voltage is set to 1 p.u., from node 1 to 3 (the change is undone in line 3). Line 3: change in the power sharing by the converters, from a ratio of 2 (proportional to each converter power) to 1, both for active and reactive power. Line 4: return to the original power sharing only for the active power. Line 5: return to initial situation. a) voltage at each node. b) active power output of each converter. c) reactive power output of each converter.

fixed for the load they have to feed but whose reactive power can be controlled independently, can participate in the reactive power sharing.

V. Conclusions

This paper has shown a preliminary approach for the sharing control scheme in a novel hybrid ac/dc microgrid. The proposed method enables the different converters to contribute to the power sharing by a droop control implementation. The proposed secondary control eliminates the voltage deviation due to the droop characteristic. It also eliminates the voltage droop caused by the virtual impedance.

Besides that, the secondary control applied in ac allows the reactive power sharing among the converters with no specific droop control. This also eases the integration of converters which are seen as active power loads, but whose reactive power can be controlled to contribute to the sharing, as it can be the case of a converter feeding a load or a STATCOM.

This secondary control is also flexible, because it is easy to introduce any criteria for the power flow solution, like any method for deciding the power sharing among the converters (minimize losses, saturation of converters for its rated power,...) or the possibility of easily changing the node whose voltage is fixed to 1 p.u.

The flexibility of the proposed secondary control allows to introduce new criteria for the power flow solution, like alternative power sharing methods (loss minimization, power limit saturation,...) or the possibility of easily exchange the node with voltage fixed to 1 p.u.

This flexibility eases the integration of additional power sharing mechanism that considers ESS SoC, or the integration of the proposed control system with the tertiary control level.

References

[1] P. Wang, L. Goel, X. Liu, and F. H. Choo, "Harmonizing AC and DC: A Hybrid AC/DC Future Grid Solution," *IEEE Power and Energy Magazine*, vol. 11, no. 3, pp. 76–83, May 2013.

[2] P. Fairley, "DC Versus AC: The Second War of Currents Has Already Begun [In My View]," *IEEE Power and Energy Magazine*, vol. 10, no. 6, pp. 104–103, Nov 2012.

[3] A. Bindra, "Projecting the Evolution of Power Electronics: Highlights from FEPPCON VIII," *IEEE Power Electronics Magazine*, vol. 3, no. 1, pp. 32–44, March 2016.

[4] C. Marnay, H. Aki, K. Hirose, A. Kwasinski, S. Ogura, and T. Shinji, "Japan's Pivot to Resilience: How Two Microgrids Fared After the 2011 Earthquake," *IEEE Power and Energy Magazine*, vol. 13, no. 3, pp. 44–57, May 2015.

[5] J. W. Simpson-Porco, Q. Shafiee, F. Dörfler, J. C. Vasquez, J. M. Guerrero, and F. Bullo, "Secondary Frequency and Voltage Control of Islanded Microgrids via Distributed Averaging," *IEEE Transactions on Industrial Electronics*, vol. 62, no. 11, pp. 7025–7038, 2015.

[6] P. Wang, X. Lu, X. Yang, W. Wang, and D. Xu, "An Improved Distributed Secondary Control Method for DC Microgrids With Enhanced Dynamic Current Sharing Performance," *IEEE Transactions on Power Electronics*, vol. 31, no. 9, pp. 6658–6673, 2016.

[7] X. Wang, Y. W. Li, F. Blaabjerg, and P. C. Loh, "Virtual-Impedance-Based Control for Voltage-Source and Current-Source Converters," *IEEE Transactions on Power Electronics*, vol. 30, no. 12, pp. 7019–7037, 2015.

[8] Z. Liu, S. Ouyang, and W. Bao, "An improved droop control based on complex virtual impedance in medium voltage micro-grid," in *2013 IEEE PES Asia-Pacific Power and Energy Engineering Conference (APPEEC)*, 2013, pp. 1–6.

[9] A. Micallef, M. Apap, C. Spiteri-Staines, and J. M. Guerrero, "Performance comparison for virtual impedance techniques used in droop controlled islanded microgrids," in *2016 International Symposium on Power Electronics, Electrical Drives, Automation and Motion (SPEEDAM)*, June 2016, pp. 695–700.

[10] A. D. Paquette and D. M. Divan, "Virtual Impedance Current Limiting for Inverters in Microgrids With Synchronous Generators," *IEEE Transactions on Industry Applications*, vol. 51, no. 2, pp. 1630–1638, 2015.

[11] J. He and Y. W. Li, "Analysis, Design, and Implementation of Virtual Impedance for Power Electronics Interfaced Distributed Generation," *IEEE Transactions on Industry Applications*, vol. 47, no. 6, pp. 2525–2538, 2011.

[12] C. Gómez-Aleixandre, P. García, A. Navarro-Rodríguez, and G. Villa, "Design and Control of a Hybrid 48V/375V/400Vac AC/DC Microgrid," in *IECON 2019 - 45th Annual Conference of the IEEE Industrial Electronics Society*, vol. 1, Oct 2019, pp. 3977–3982.

[13] J. Rocabert, A. Luna, F. Blaabjerg, and P. Rodríguez, "Control of Power Converters in AC Microgrids," *IEEE Transactions on Power Electronics*, vol. 27, no. 11, pp. 4734–4749, Nov 2012.

[14] C. Wang, Z. Li, X. Si, and H. Xin, "Control of neutral-point voltage in three-phase four-wire three-level NPC inverter based on the disassembly of zero level," *CPSS Transactions on Power Electronics and Applications*, vol. 3, no. 3, pp. 213–222, Sep. 2018.

[15] A. Navarro-Rodríguez, P. García, R. Georgious, and J. García, "Adaptive Active Power Sharing Techniques for DC and AC Voltage Control in a Hybrid DC/AC Microgrid," *IEEE Transactions on Industry Applications*, vol. 55, no. 2, pp. 1106–1116, March 2019.

[16] R. Chai, B. Zhang, J. Dou, Z. Hao, and T. Zheng, "Unified Power Flow Algorithm Based on the NR Method for Hybrid AC/DC Grids Incorporating VSCs," *IEEE Transactions on Power Systems*, vol. 31, no. 6, pp. 4310–4318, 2016.

B.3 Design and Control of a Hybrid 48V/375V/400Vac AC/DC Microgrid

Design and Control of a Hybrid 48V/375V/400Vac AC/DC Microgrid

Carlos Gómez-Aleixandre, Pablo García, Ángel Navarro-Rodríguez and Geber Villa
Dept. of Electrical, Electronics, Systems & Computers Engineering
University of Oviedo, LEMUR Group, Gijón, 33204, Spain
Email: gomeztcarlos@uniovi.es, garciafpablo@uniovi.es, navarroangel@uniovi.es, villageber@uniovi.es

***Abstract*—This paper presents a novel design and control for a hybrid 48 Vdc / 375 Vdc / 400 Vac AC/DC hybrid microgrid for a terminal distribution system. The proposed paper includes the selection of the topologies for the different power electronic converters involved in the hybrid microgrid as well as the proposed control system. Special attention is paid to the balance of the bipolar $\pm$375 Vdc-grid when unbalanced loads are applied, both in the AC and DC grids. Different scenarios are considered in order to evaluate the effect of contingencies in the different converters used for the energy distribution. Two different scenarios are evaluated by simulation results, focusing in the transient response under different loads and distributed generation elements.**

I. Introduction

The future electricity grid is gradually moving in the direction of DC distribution, due the envisaged lower distribution losses (as compared with AC distribution) and the more efficient integration of renewables and distributed resources [1]–[3]. Due to the random behavior of such renewable generation units, a major challenge for a reliable grid performance is to increase the wind/solar power share, while achieving power balance and voltage and frequency stability. Such intermittent behavior of the renewable generators can be effectively compensated by the inclusion of Energy Storage Systems (ESS) in the distribution grid [3]. The evolution in power electronics and control technologies has enabled the development of DC Low-Voltage (LV) microgrids. This eases the integration of ESS, also enhancing the performance of DC grids at building level, by reducing costs and increasing reliability [3], [4]. However, it is still unclear the pathway from AC conventional distribution systems to these modern DC or DC/AC grids. Table I shows the main conclusions arising from the current situation about DC distribution, given by regulations and directives, also considering associations and committees, as well as the experiences in some key facilities.

Therefore, it is reasonable to think that the change is not going to be a drastic switch from a contrasted AC system, with a history over 100 years, to a completely new distribution paradigm. The most feasible solution seems to be the adoption of hybrid AC/DC power system schemes with both AC and DC subsystems based on current AC infrastructures [1]. This hybrid approach has the following objectives: 1) use of PEC in order to provide redundancy of power flows and thus increasing the grid resiliency [5], 2) reducing the number of required power conversion stages for the connection of loads and distributed resources, thus increasing the efficiency. So far, a manifold of purely AC or DC microgrid topologies have been proposed, as well as some experiences dealing with hybrid topologies. In [6], DC and some existing hybrid microgrid topologies are analyzed. The most common hybrid structure is the typical AC/DC hybrid microgrid in which two different buses (AC and DC) are connected through one or more converters. DC loads and generators are connected to

TABLE I
DC distribution alternatives.

Standard	DC voltage (V)	Application
EMerge Alliance Standard for commercial buildings	24	DC power distribution in commercial buildings
EMerge Alliance Standard for data centres	380	Hybrid use of AC and DC power within data centres and telecom central offices
EU Telecom Standard ETSI EN 300 132-3-1	400	Distribution networks supplying telecom and datacom equipment
IEEE 802.3 Standard	50	Applications that receive both power and high-speed data through the same RJ45 connector
European directive EU LDV 2006/95EC	75 - 1500	Encourages manufacturers and other agents for harmonisation but without fixing any voltage level
SEG4 group, IEC60038	12/48/380	Provides a recommendation for different voltage levels
National Electrical Code (NEC) NFPA70	60	Low voltage low power devices like sensors or led lighting
MIL-STD-1399	28/155/270/375/650	Shipboard applications

The present work has been partially supported by the predoctoral grants program FPU for the formation in university teaching of Spain MECD under the grant IDs FPU16/05313 and FPU16/06829 and program Severo Ochoa for the formation in research and university teaching of Principado de Asturias PCTI-FICYT under the grant ID BP14-135. This work also was supported in part by the Research, Technological Development and Innovation Program Oriented to the Society Challenges of the Spanish Ministry of Economy and Competitiveness under grant ENE2016-77919-R and by the European Union through ERFD Structural Funds (FEDER).

the DC bus, while AC loads and generators are coupled with the AC line. Usually, in these kinds of schemes, the AC line is connected to the main grid. Other proposals consider AC rings connected to a substation and AC/DC converters connected to this outer AC rings feeding DC small microgrids. There are few experiences considering complex topologies combining AC and DC structures [4], [6], [7]. The use of these kind of networks inside buildings is another trend that could lead to the massive use of such hybrid technologies. For instance in [8], the building main network is AC but there is a small DC radial microgrid for connecting the PV generation, ESS and also dedicated DC loads. Regarding the control implementation in hybrid microgrids, it is critical to analyze the transient response and the power sharing among the DC and AC buses [9], [10].

II. Proposed Hybrid DC/AC microgrid

The hybrid AC/DC network architecture proposed in this paper is shown in Fig. 1. In there, the hybrid distribution system departures from the output port of a three-port solid state transformer with one input port connected to the main AC grid and the other to a central energy storage system [11]. From there, a ± 375 Vdc distribution line is connected. In parallel, a power converter (Header PEC, 60 kVA) generates two parallel 400 Vac feeders, which distribute the power downstream. The Header PEC (HPEC) is built by two parallel-connected 3-level NPC converters which are also responsible of keeping the two DC-buses (375 V each) balanced. All the elements from the high-frequency transformer up to the HPEC are envisaged to be installed in the next generation transformation center. From the main DC-line two identical Ring PEC (RPEC) are connected, providing an alternative path for the AC distribution but also generating a 48 V DC bus for the internal DC distribution inside a building block. These two RPEC shall be installed in the main connection of a set of buildings to the grid. Finally, the Tail PEC (TPEC) allows for generating a ring between the two feeders, thus enabling an alternative distribution path in the case the other feeder is disabled. The converters could be installed at the next transformation center in the distribution grid.

The DC line connecting the point of connection of the HPEC to the RPEC is considered as a pure resistive line with three identical conductors: one for the $+375$ DC-bus rail of 500 m length and two for ground and -375 DC-bus rail of 1000 m length. They are modelled for a maximum voltage drop of 3 % at the end of the 1000 m line, assuming Ring #2 PEC is working at full power. Both AC feeders are modelled for 1000 m length and for a maximum voltage drop of 3 % at the end of the line, assuming and X/R ratio of 5.

A. Header PEC

The header power electronic converter is the coordination converter for the hybrid DC/AC microgrid. Its functions include: 1) to provide a distributed ± 375 Vdc for the main DC grid path; 2) to generate two different 4-wire 3-phase 400 V lines for the main AC grid distribution; 3) to deal with the load disturbances, both in the AC and DC grids. It will be of critical importance for the converter to be able to deal with unbalances in the distributed DC-link, which is connected to the two Rings, Ring#1 and Ring#2 converters, shown in Fig. 1. As it can be seen these two converters provide an alternative path for the 400 Vac grid as well as they are the responsible of generating the 48 Vdc links. Considering the two converter can have different loads, the demanded energy from the two DC-link rails, $+375$/gnd and gnd/-375 will be different. The reason of the dual DC-link distribution instead of a single 750 Vdc link is to have a more reliable energy link path, being possible that even if one of the DC-links presents a fault condition, the other to continue working.

According to the design constraints, the selected topology for the HPEC is a dual 3-level 4-wire 3-phase NPC converter. The reason about this topology is that is has a reasonable cost for the target power (60 kVA), it provides a split DC-link to generate the two distribution 375 Vdc links and it allows for a balancing control method able to deal both with 3-phase and single phase loads and generation units.

The control system is shown in Fig. 2. Details about cross-coupling and feedforward terms, normalization and non-linear compensation [9] for the duty calculation are omitted due to space constraints. The DC-link balancing scheme is implemented according to the one developed in [12].

B. Ring converter

The two ring converters shown in Fig. 1 have the same rated power, 20 kVA, and they generate, from the two different main DC-grid, a connection to the two 400 Vac feeders and two independent 48 Vdc grids. The converter has an internal bidirectional stage for generating a 750V DC-link from the 375Vdc, a 2-level 4-wire 3-phase DC/AC stage for the interconnection with the AC grid and a bidirectional DC/DC $375/48$ V for the generation of the 48 V internal building grid. Regarding the control system, Fig. 3 shows the required control loops. As it can be seen, the converter has to be able to synchronize with the AC grid generated by the HPEC, contributing to the energy demands. For the case of the 48 Vdc link, the control system generates an stiff bidirectional link, able to deal with the integration of small distributed generation and energy storage systems.

C. Tail converter

The TPEC shown in Fig. 1 is a 2-level 4-wire 3-phase back-to-back converter used for the interconnection of the two AC feeders, thus generating a ringed distribution system. It is worth noting that the operation of that converter, considers the isolated operation of the grid because of the shown local energy storage.

III. Microgrid operation modes

The operation of the hybrid DC/AC microgrid can be explained by several modes, all of those here described. For the explanation of the modes, it is needed first to explain the possible states for the distribution lines.

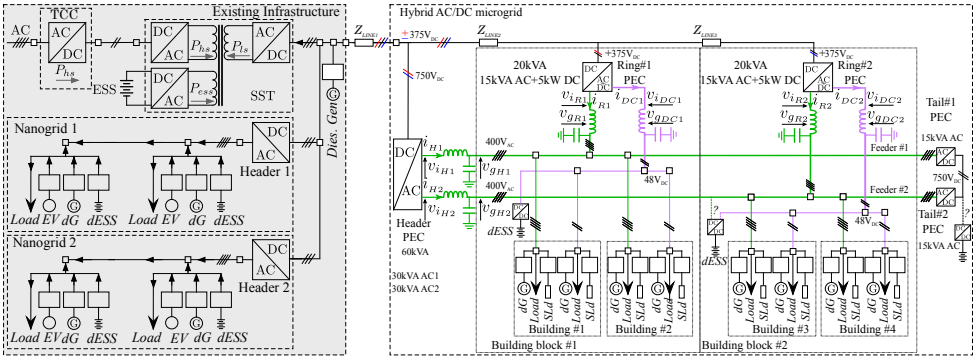

Fig. 1. Proposed system level grid infrastructure.

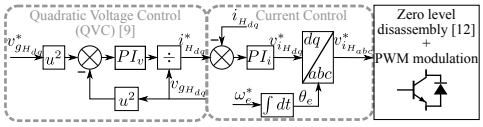

Fig. 2. Header converter control diagram.

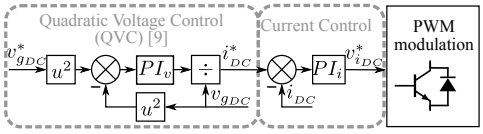

(a) DC/DC stage from 375 Vdc bus to 48 Vdc.

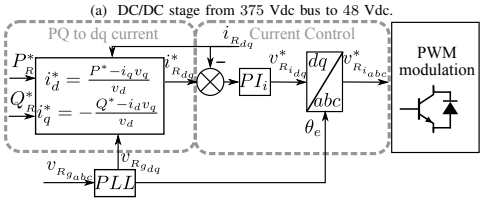

(b) DC/AC stage, from 375 Vdc to 400 Vac (PQ mode).

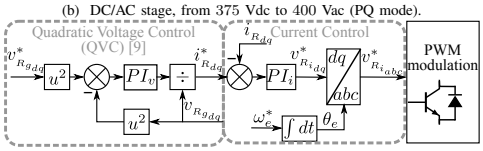

(c) DC/AC stage, from 375 Vdc to 400 Vac (slack mode).

Fig. 3. Ring converter control diagram.

- **Connection to the main AC grid.** When the main AC grid is connected, the energy to the distribution system can be provided by the AC grid or by the central energy storage connected to the solid-state transformer. When disconnected, the distribution system works in islanded mode using the central energy storage, the internal generation and the distributed energy storage systems.
- **DC/AC main feeders**. The two AC and the two DC feeders can operate simultaneously or independently when a contingency occurs. Under any event condition, all the loads have to be operate normally. Alternative energy path are provided for the different loads by the ring and tail converters and from the local energy storage installed at the 48 V distribution.

According to this, the following modes are considered:

- **HPEC fully operational.** In this case, the two AC and DC feeders are operational. The HPEC behaves like a dual slack converter, generating the two AC feeders voltages. Both NPC converters participate in the balancing of the dual DC-link. The two ring converters work in P/Q mode, being a complementary path for supplying the loads when needed. The TPEC could be either in operational mode or disconnected.
- **HPEC AC outputs not operational.** One or the two AC outputs could be disconnected for a variety of reasons. Whenever an AC output is disconnected, the corresponding Ring converter changes its operation mode from P/Q to slack. The TPEC converter is in operational mode providing alternative paths for the energy. DC feeders continue fully operational.
- **Fault in the DC feeders.** One or two of the DC feeders could have a contingency. In that case, the corresponding RPEC can not operate. AC feeders continue its normal operation. 48 V bus is generated internally from the dESS.
- **Disconnection of the main DC-link.** The main 750 V dc link is generated by the output port of the solid-state transformer. If a fault occurs in there, both in the connection to the mains and in the central energy storage, the HPEC and the RPEC can not operate. In that case, the TPEC with the local storage and the dESS connected to the 48 V link are the responsible for the grid generation.

TABLE II
CONVERTER PARAMETERS.

Converter	HPEC - AC	RPEC - AC	RPEC - DC
L_{filter} (mH)	1.68	3.37	1.47
R_{filter} (mΩ)	35.3	70.5	30.7
C_{filter} (mF)	0.5	0.1	5
C_{bus} (mF)	5	5	5
BW_i (Hz)	500	500	500
BW_v (Hz)	50	50	50

IV. SIMULATION RESULTS

For testing the proper operation of the proposed architecture, two of the proposed modes have been simulated using Simulink/Matlab.

The simulations are based on the scheme shown in Fig. 1, with some simplifications for the initial evaluation: 1) the 750 Vdc bus is generated from a bi-directional DC/DC converter, 2) the tail converters are not considered.

The details of the different converter output LC filter parameters as well as the control loop bandwidths are shown in Table II.

A. HPEC fully operational

Each of the two parallel-connected 3-level NPC converter operates in slack mode, being responsible for the voltage control in Feeder #1 and Feeder #2 respectively (to a fixed value of 400 Vrms), apart from the aforementioned DC-bus balancing in which both converters are participating.

The two ring converters are connected to the two 400 Vac feeders (operating in P/Q mode) and to the 48 Vdc internal building grid (operating in DC slack mode).

Three different load cases are analyzed: 1) Balanced case. Changes in the references and in the loads are balanced for both feeders and the ring converters, having the same power demand in both DC-link rails. 2) Unbalanced DC-bus. Changes in the reference commands and in the loads are applied only to Building block #2, thus generating a difference between the power demand in both DC-link rails which induces an unbalance that has to be compensated by the HPEC NPC converter. 3) Unbalanced AC-load. A single-phase load is connected at Feeder #2, generating an unbalance in that AC grid.

The time intervals for the complete sequence are as follows: 1) **t = 0.1 s**, P reference in DC/AC stage of both ring converters changes from 0 to −8 kW, 2) **t = 0.2 s**, a 4 kW load is connected in each 48 Vdc internal building grid, 3) **t = 0.3 s**, Q reference in DC/AC stage of both ring converters changes from 0 to 12 kvar, 4) **t = 0.5 s**, a 12 kW load is connected in each 400 Vac feeder, 5) **t = 0.7 s**, P reference in DC/AC stage of Building block #2 ring converter changes from −8 to 10 kW, 6) **t = 0.8 s**, Q reference in DC/AC stage of Building block #2 ring converter changes from 12 to −4 kvar, 7) **t = 1.1 s**, load connected in Building block #2 48 Vdc grid changes from 4 to 1 kW, 8) **t = 1.2 s**, load connected in Building block #2 400 Vac feeder changes from 12 to 2 kW, 9) **t = 1.4 s**, a single-phase 4 kW load is connected in Building block #2 400 Vac feeder.

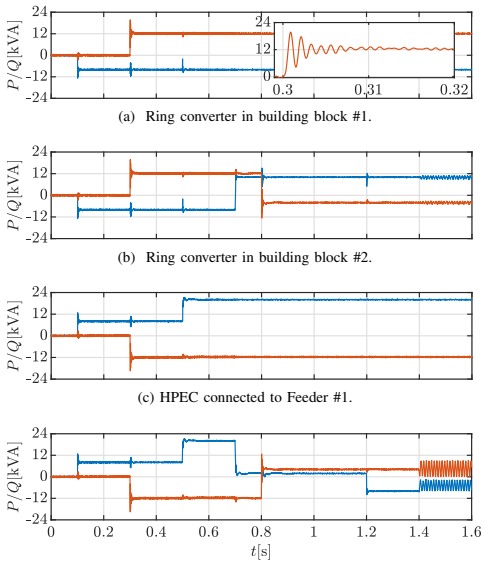

(a) Ring converter in building block #1.

(b) Ring converter in building block #2.

(c) HPEC connected to Feeder #1.

(d) HPEC connected to Feeder #2.

Fig. 4. Active and reactive power output (blue, active power; red, reactive power).

In Fig. 4a and 4b, the active and reactive power output for the DC/AC stage of each ring converter is shown. It can be seen that the control system is able to follow the references with a fast response but with some overshoot (as shown in the zoom area). It also has deviations from the reference values when loads are connected in the corresponding feeder, causing some oscillations, but the control is able to fast recovery.

In Fig. 4c and 4d, the active and reactive power delivered by the HPEC to each of the 400 Vac feeders is shown. Since they operate in slack mode, they have to provide all the feeder net consumption (sum of all loads consumption, considering ring converters as loads, since they operate in P/Q mode) to maintain an stiff voltage value. The response in all the demand changes is really fast.

The effect of a single-phase load is shown in Fig. 4d. In there, a single-phase load is connected to Feeder #2. As expected, a pulsating power demand at twice the fundamental frequency appears in the active and reactive power components delivered by the HPEC.

Fig. 5 shows HPEC voltage output in dq reference frame. Despite the transient oscillations when the load changes, the control is able to keep the voltage really close to the reference value ($230\sqrt{2} = 325$ V for the $d-axis$; 0 V for the $q-axis$).

Besides that, it can be seen that the connection of single-

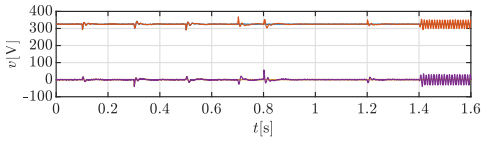

Fig. 5. HPEC voltage output in dq reference frame for both AC feeders (blue and red, d voltage for Feeder #1 and #2; yellow and purple, q voltage for Feeder #1 and #2).

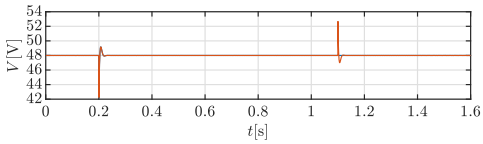

Fig. 6. DC/DC stage of ring converters voltage output for both 48 Vdc internal building grids (blue and red, voltage for Building block #1 and #2).

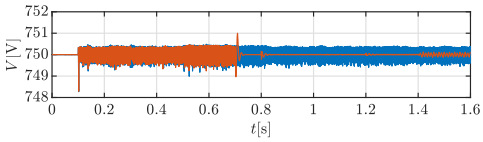

Fig. 7. Voltage after intermediate step for boosting from 375 to 750 Vdc to connect DC-bus with AC-feeder (blue and red, voltage for Building block #1 and #2).

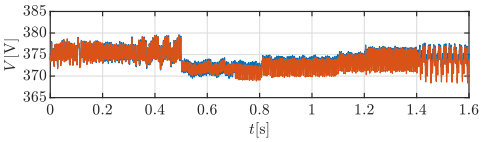

Fig. 8. Voltage in both DC-buses (blue and red, voltage in DC-bus 1 and 2).

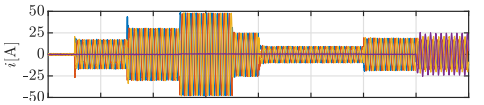

(a) HPEC connected to Feeder #2.

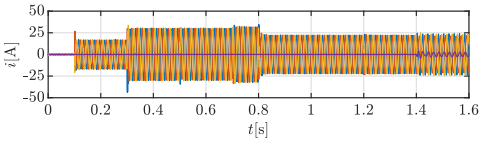

(b) Ring converter connected to Feeder #2.

Fig. 9. Current output (blue, phase a; red, phase b; yellow, phase c; purple, neutral conductor).

phase loads causes a 100 Hz oscillation to appear in the steady-state. This is the -50 Hz negative-sequence component resulting from the unbalanced single-phase load (when represented in the synchronous reference frame, is seen as 100 Hz).

Fig. 6 shows the voltage output in the two 48 Vdc internal building grids. It can be seen that the DC/DC stage of the ring converters is able to control the voltage. The sags appearing when a new load is connected is recovered in short-time and the variation of the voltage value is acceptable, considering that they appear after a sudden connection for a 80% load of the power converter.

Fig. 7 shows the 750 Vdc DC-link voltage in both ring converters. The control is able to control the voltage properly, only with some deviations (not very significant) when changes in the power reference for the corresponding ring converter are applied. The shown ripple has a small peak-to-peak value when compared with the rated voltage (around 1 V for a rated voltage of 750 V).

In Fig. 8, voltage in both 375 DC-buses is shown. It can be seen that the balancing control implemented at the NPC is able to keep both buses stable, even though a small voltage sag can be seen when a load of 12 kW is connected to each AC feeder (at t = 0.5 s).

In Fig. 9a, current output of HPEC converter connected to Feeder #2 is shown. When there is no unbalance in the load, the current has low THD (1.31 %), close to a perfect balanced-sinusoidal system, with negligible current flowing through neutral conductor. Once the single-phase load is connected, an important amount of current is flowing through the neutral conductor and currents no longer form a balanced system.

After the single-phase load is connected, the current flows through the neutral conductor and the system is not longer balanced. The consequences of this load unbalance can be seen in 9b. At t = 1.4 s (single-phase load connection), the current in the inverter becomes unbalanced due to the negative sequence component in the voltage controlled by the HPEC.

B. Disconnection of one HPEC ac outputs

In this second simulation, the disconnection of one of the HPEC AC feeders (#2) is studied. In this case, the ring converter connected to that feeder switches to slack mode control to keep the voltage level of the feeder at the reference valuee. Apart from that, only one of the two HPEC NPC converters can contribute to balance the DC-buses.

The simulation conditions (reference changes, load connections,...) are the same than in the previous simulation except for those regarding to Feeder #2. The sequence in that feeder now is: 1) **t = 0.1 s**, connection of a 10 kvar capacitive load, 2) **t = 0.3 s**,, connection of a 6 kW resistive load, 3) **t = 0.8 s**, reduction of resistive load from 6 to 2 kW, 4) **t = 1 s**, reduction of capacitive load from 10 to 4 kvar, 5) **t = 1.4 s**, connection of a 2 kW single-phase resistive load.

In Fig. 10, the active and reactive power delivered by ring converter #2 are shown. Since this converter is now the slack bus of this feeder, it has to provide all the power demand to keep the voltage level of the feeder. The effect of the single-

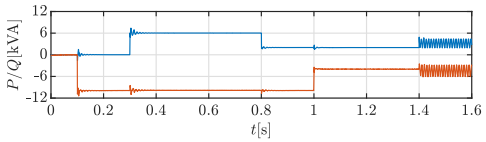

Fig. 10. Ring converter in building block #2 active and reactive power output (blue, active power; red, reactive power).

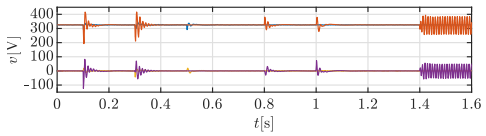

Fig. 11. HPEC voltage output in dq reference frame for both AC feeders (blue and red, d voltage for Feeder #1 and #2; yellow and purple, q voltage for Feeder #1 and #2).

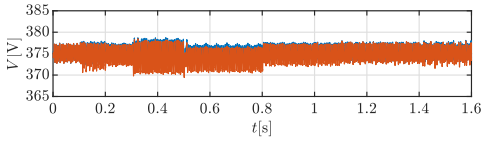

Fig. 12. Voltage in both DC-buses (blue and red, voltage in DC-bus 1 and 2).

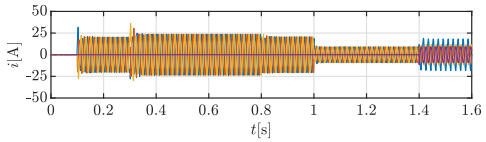

Fig. 13. Ring converter current output (blue, phase a; red, phase b; yellow, phase c; purple, neutral conductor).

phase load can be appreciated as a pulsating power demand with twice the fundamental frequency.

In Fig. 11, voltages in both AC feeders are shown. It can be seen that oscillations in Feeder #2 are much more significant. This is normal since the converter acting as a slack for that feeder has less rated power so it is more affected by the sudden changes in power demand.

In Fig. 12, voltage in both DC-buses is shown. It can be seen that even though only one of the HPEC NPC converters is now working for balancing the DC-buses, it is able to maintain a value close to the reference level with almost no difference between the voltage of each bus.

Finally, in Fig. 13, current output for the ring converter connected to Feeder #2 is shown. The system is able to provide balanced currents with low distortion, except when the single-phase load is connected (the currents become clearly unbalanced and current flows through neutral conductor).

The results related to Feeder #1 and the 48 Vdc internal building grid are really similar to the ones obtained in the previous simulation, so they are not shown.

V. Conclusion

In this paper, a novel architecture for a hybrid DC/AC microgrid, including the power converters topologies and control has been analyzed. A technique for the balancing of the two DC feeders, provided by a 3-level multiport converter has been successfully tested. Different operating modes, having reliability as the key design factor have been identified. From those, two have been successfully demonstrated by simulation. In all the cases, a good dynamic response under balanced/unbalanced loads has been demonstrated.

Future works will include a complete study for all the proposed operating modes as well as the analysis of the transition between them. Collaborative operation for the different converters, considering droop control instead of slack mode is also aim of future developments. An experimental test rig is currently being built for the validation of proposed hybrid distribution system.

References

[1] P. Wang, L. Goel, X. Liu, and F. H. Choo, "Harmonizing ac and dc: A hybrid ac/dc future grid solution," *IEEE Power and Energy Magazine*, vol. 11, no. 3, pp. 76–83, May 2013.

[2] P. Fairley, "Dc versus ac: The second war of currents has already begun [in my view]," *IEEE Power and Energy Magazine*, vol. 10, no. 6, pp. 104–103, Nov 2012.

[3] A. Bindra, "Projecting the evolution of power electronics: Highlights from feppcon viii," *IEEE Power Electronics Magazine*, vol. 3, no. 1, pp. 32–44, March 2016.

[4] N. Eghtedarpour and E. Farjah, "Power control and management in a hybrid ac/dc microgrid," *IEEE Transactions on Smart Grid*, vol. 5, no. 3, pp. 1494–1505, May 2014.

[5] C. Marnay, H. Aki, K. Hirose, A. Kwasinski, S. Ogura, and T. Shinji, "Japan's pivot to resilience: How two microgrids fared after the 2011 earthquake," *IEEE Power and Energy Magazine*, vol. 13, no. 3, pp. 44–57, May 2015.

[6] L. Jia, Y. Zhu, and Y. Wang, "Architecture design for new ac-dc hybrid micro-grid," in *2015 IEEE First International Conference on DC Microgrids (ICDCM)*, June 2015, pp. 113–118.

[7] A. A. Eajal, E. F. El-Saadany, M. F. Shaaban, and K. Ponnambalam, "Stochastic energy coordination in hybrid ac/dc smart grids," in *2015 IEEE Electrical Power and Energy Conference (EPEC)*, Oct 2015, pp. 158–163.

[8] P. Arboleya, P. Garcia, B. Mohamed, and C. Gonzalez-Moran, "Distributed resources coordination inside nearly-zero energy buildings providing grid voltage support from a symmetrical component perspective," *Electric Power Systems Research*, vol. 144, pp. 208 – 214, 2017. [Online]. Available: http://www.sciencedirect.com/science/article/pii/S0378779616304862

[9] A. Navarro-Rodríguez, P. García, R. Georgious, and J. García, "Adaptive active power sharing techniques for dc and ac voltage control in a hybrid dc/ac microgrid," *IEEE Transactions on Industry Applications*, vol. 55, no. 2, pp. 1106–1116, March 2019.

[10] A. Navarro-Rodríguez, P. García, C. Blanco, R. Georgious, and J. García, "Cooperative control in a hybrid dc/ac microgrid based on hybrid dc/ac virtual generators," in *2018 IEEE Energy Conversion Congress and Exposition (ECCE)*, Sep. 2018, pp. 1156–1163.

[11] P. García, P. Arboleya, B. Mohamed, and A. A. C. Vega, "Implementation of a hybrid distributed/centralized real-time monitoring system for a dc/ac microgrid with energy storage capabilities," *IEEE Transactions on Industrial Informatics*, vol. 12, no. 5, pp. 1900–1909, Oct 2016.

[12] C. Wang, Z. Li, X. Si, and H. Xin, "Control of neutral-point voltage in three-phase four-wire three-level npc inverter based on the disassembly of zero level," *CPSS Transactions on Power Electronics and Applications*, vol. 3, no. 3, pp. 213–222, Sep. 2018.

Appendix C

Proposed secondary control flowcharts

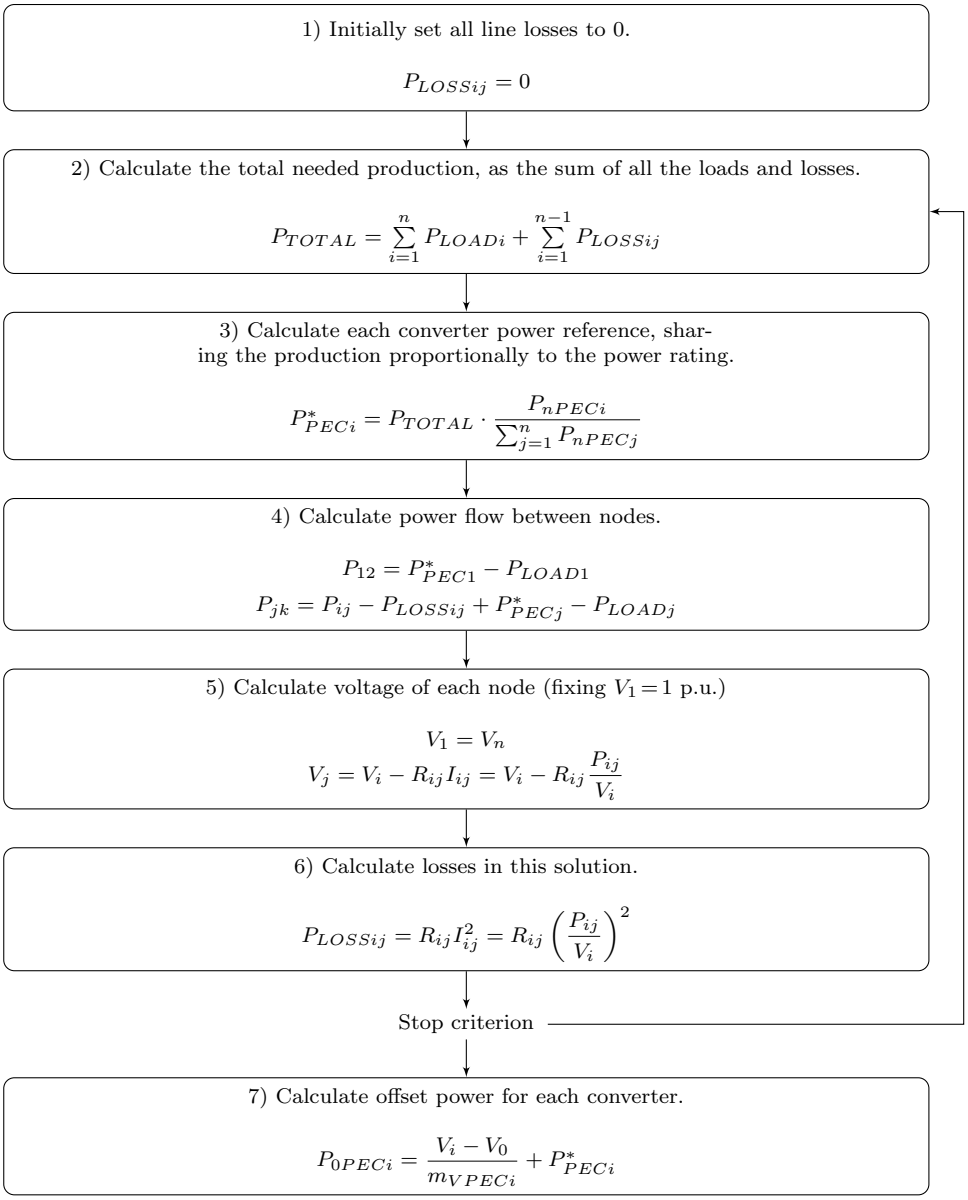

Figure C.1: Flowchart for secondary control in DC. i, j and k denote any three consecutive nodes.

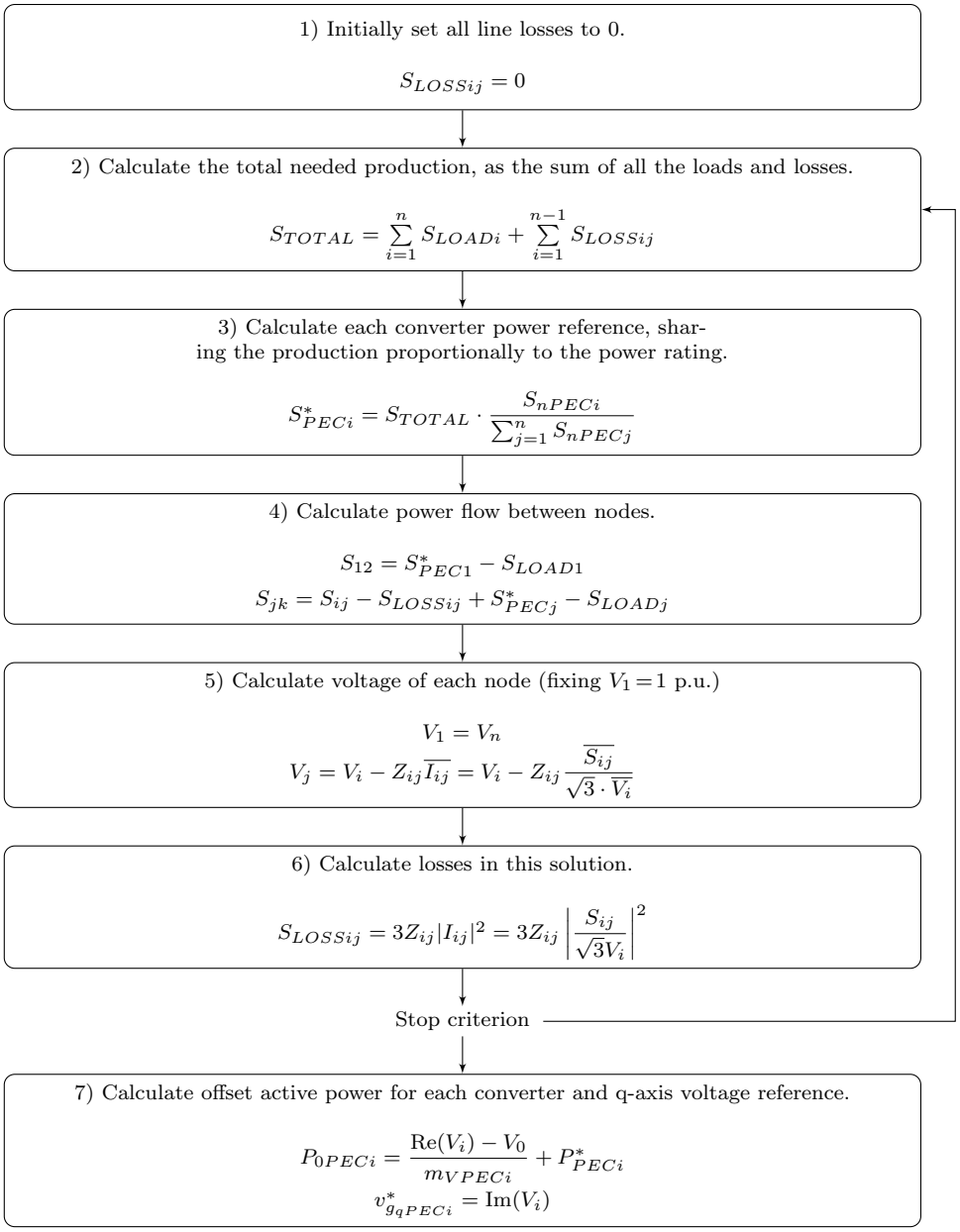

Figure C.2: Flowchart for secondary control in AC. i, j and k denote any three consecutive nodes. For obtaining a more compact expression, active and reactive power equations are presented in its complex form, so they are joint into one equation with $S = P + iQ$, using also $Z = R + iX$. $\overline{x}$, $\mathrm{Re}(x)$ and $\mathrm{Im}(x)$ are the conjugate, real part and imaginary part of a complex vector.

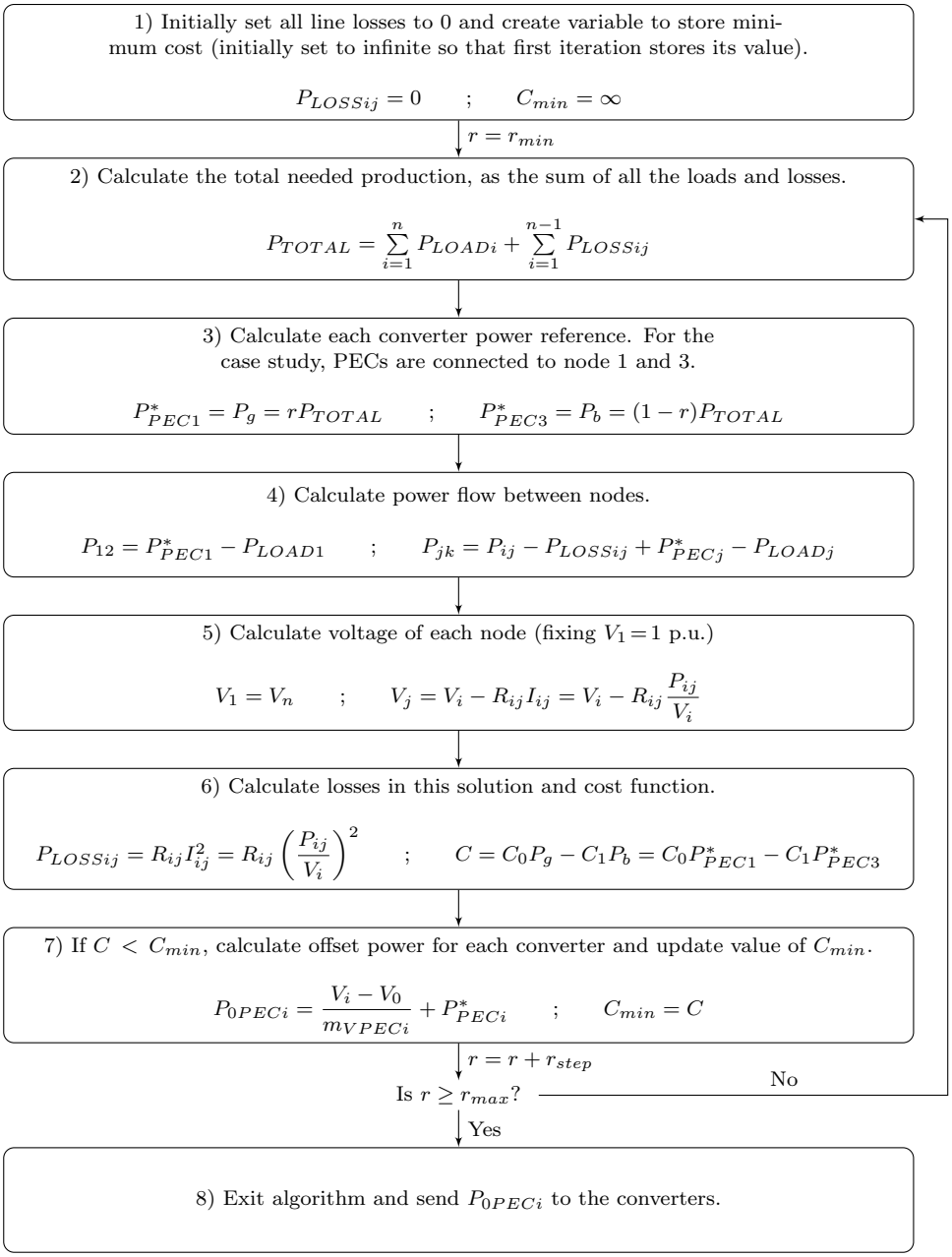

Figure C.3: Flowchart for secondary control with cost optimization in DC. i, j and k denote any three consecutive nodes. r_{min} and r_{max} are the minimum and maximum value of r for the sweep, and r_{step} is the step in r between iterations.

Appendix D

State-space matrices

D.1 Case $\mathbf{I_{o1}}$-$\mathbf{I_{o2}}$

The basic case considers both inputs to be in form of current. In red, the varying matrices are highlighted, as well as the varying terms inside them. The equations and matrices are the following:

$$[x_c] = \begin{bmatrix} \omega_{dc} \\ I \\ T_I^* \\ V_{LPF} \\ V_I^* \end{bmatrix} ; \; [x_p] = \begin{bmatrix} V_{dc1} \\ V_{dc2} \\ I_L \end{bmatrix} ; \; [u] = \begin{bmatrix} V_{dc1}^* \\ I_{o1} \\ I_{o2} \end{bmatrix} \tag{D.1}$$

$$\frac{\mathrm{d}}{\mathrm{d}t} \left[\begin{array}{c} x_c \\ \hline x_p \end{array}\right] = [A]_{8\times 8} \left[\begin{array}{c} x_c \\ \hline x_p \end{array}\right] + [B]_{8\times 3} [u] \tag{D.2}$$

$$\begin{bmatrix} V_{dc1} \\ V_{dc2} \\ I_L \end{bmatrix} = \left[\begin{array}{c|c} [0]_{3\times5} & [I]_{3\times3} \end{array}\right] \left[\begin{array}{c} x_c \\ \hline x_p \end{array}\right] + [0]_{3\times3}\,[u] \tag{D.3}$$

$$[A]_{8\times8} = \left[\begin{array}{c|c} [A_{xx}]_{5\times5} & [A_{xp}]_{5\times3} \\ \hline [A_{px}]_{3\times5} & [A_{pp}]_{3\times3} \end{array}\right] \tag{D.4}$$

$$[A]_{8\times8} = \left[\begin{array}{c|c} [A_x]_{5\times5} & [B_x]_{5\times3} \\ \hline [B_{pd}]_{3\times1}[C_x]_{1\times5} & [A_p]_{3\times3} + [B_{pd}]_{3\times1}[D_x]_{1\times3} \end{array}\right] \tag{D.5}$$

$$[B]_{8\times3} = \begin{bmatrix} \frac{K_{pw}}{JK_e} & 0 & 0 \\ -\frac{2w_2}{L} & 0 & 0 \\ \frac{K_{iw}}{K_e} & 0 & 0 \\ 0 & 0 & 0 \\ 0 & K_{ii}w_1 & -\frac{K_{ii}V_{dc2}w_2}{V_{dc1}} \\ 0 & -\frac{1}{C_1} & 0 \\ 0 & -\frac{K_{pi}i_Lw_1}{C_2V_{dc2}} & \frac{K_{pi}i_Lw_2}{C_2V_{dc1}} - \frac{1}{C_2} \\ 0 & \frac{K_{pi}w_1}{L_f} & -\frac{K_{pi}V_{dc2}w_2}{L_fV_{dc1}} \end{bmatrix} \tag{D.6}$$

$$\left[\begin{array}{c}[A_{xx}]_{5\times5}\\ \hline [A_{px}]_{3\times1}\end{array}\right]=\left[\begin{array}{ccccc}-\frac{K_{pw}+b}{J} & -\frac{K_e}{J} & \frac{1}{J} & \frac{K_{pw}}{JK_e} & 0\\ \frac{K_e}{L} & -\frac{R}{L} & 0 & 0 & 0\\ -K_{iw} & 0 & 0 & \frac{K_{iw}}{K_e} & 0\\ 0 & R\omega_{LPF} & 0 & -\omega_{LPF} & 0\\ 0 & K_{ii} & 0 & 0 & 0\\ 0 & 0 & 0 & 0 & 0\\ 0 & -\frac{K_{pi}i_L}{C_2V_{dc2}} & 0 & 0 & -\frac{i_L}{C_2V_{dc2}}\\ 0 & \frac{K_{pi}}{L_f} & 0 & 0 & \frac{1}{L_f}\end{array}\right] \tag{D.7}$$

$$\left[\begin{array}{c}[A_{xp}]_{5\times3}\\ \hline [A_{pp}]_{3\times3}\end{array}\right]=\left[\begin{array}{ccc}0 & 0 & 0\\ -\frac{w_1}{L} & \frac{V^*_{dc1}w_2}{LV^*_{dc2}} & 0\\ 0 & 0 & 0\\ 0 & 0 & 0\\ 0 & 0 & -K_{ii}\\ 0 & 0 & \frac{1}{C_1}\\ -\frac{i_L}{C_2V_{dc2}} & 0 & \frac{K_{pi}i_L}{C_2V_{dc2}}\\ 0 & 0 & -\frac{K_{pi}}{L_f}\end{array}\right] \tag{D.8}$$

$$
[A]_{8\times 8} = \begin{bmatrix}
-\frac{K_{pv}+b}{J} & -\frac{K_e}{J} & \frac{1}{J} & \frac{K_{pv}}{JK_e} & 0 & 0 & 0 & 0 \\
\frac{K_e}{L} & -\frac{R}{L} & 0 & 0 & 0 & -\frac{w_1}{L} & \frac{V_{dc1}^* w_2}{LV_{dc2}^*} & 0 \\
-K_{iw} & 0 & 0 & \frac{K_{iw}}{K_e} & 0 & 0 & 0 & 0 \\
0 & R\omega_{LPF} & 0 & -\omega_{LPF} & 0 & 0 & 0 & 0 \\
0 & K_{ii} & 0 & 0 & 0 & 0 & 0 & -K_{ii} \\
0 & 0 & 0 & 0 & 0 & 0 & 0 & \frac{1}{C_1} \\
0 & -\frac{K_{pi} i_L}{C_2 V_{dc2}} & 0 & 0 & -\frac{i_L}{C_2 V_{dc2}} & -\frac{i_L}{C_2 V_{dc2}} & 0 & \frac{K_{pi} i_L}{C_2 V_{dc2}} \\
0 & \frac{K_{pi}}{L_f} & 0 & 0 & \frac{1}{L_f} & 0 & 0 & -\frac{K_{pi}}{L_f}
\end{bmatrix} \tag{D.9}
$$

The linearization of the matrices only affects the three last columns of matrix A, since all the non-linearities are related to the last 3 state variables. Thus only the change of the corresponding columns is shown. A_l indicates the linearized version:

$$[A_l]_{8\times 8}(:, 6:8) = \begin{bmatrix} 0 & 0 & \frac{K_{pi}{i_L}^2}{2C_2{V_{dc1}}^2 n} - \frac{i_L}{C_2 V_{dc1} n} \\ -\frac{1}{L} & \frac{1}{Ln} & \frac{i_L}{C_2 V_{dc1} n^2} - \frac{K_{pi}{i_L}^2}{2C_2{V_{dc1}}^2 n^2} \\ 0 & 0 & -\frac{K_{pi} i_L}{2L_f V_{dc1} n} \\ 0 & 0 & -\frac{K_{ii} i_L}{2V_{dc1}} \\ -\frac{K_{ii} i_L}{2V_{dc1}} & \frac{K_{ii} i_L}{2V_{dc1} n} & -K_{ii} \\ 0 & 0 & \frac{1}{C_1} \\ \frac{K_{pi}{i_L}^2}{2C_2{V_{dc1}}^2 n} - \frac{i_L}{C_2 V_{dc1} n} & \frac{i_L}{C_2 V_{dc1} n^2} - \frac{K_{pi}{i_L}^2}{2C_2{V_{dc1}}^2 n^2} & \frac{K_{pi} i_L}{C_2 V_{dc1} n} - \frac{K_{pi}}{L_f} \\ -\frac{K_{pi} i_L}{2L_f V_{dc1}} & \frac{K_{pi} i_L}{2L_f V_{dc1} n} & -\frac{1}{C_2 n} \end{bmatrix} \tag{D.10}$$

D.2 Case $\mathbf{V_{s1}}$-$\mathbf{V_{s2}}$

It is worth to remark that, until this point, I_{o1} and I_{o2} were considered as system inputs. However, this will generally not be the case when looking to the complete system. One or both sides of the PEC will normally be connected to a voltage source through a line impedance which provides the required power. In that case, the corresponding input I_{ox} should be replaced by $\dfrac{V_{dcx} - V_{sx}}{R_x}$, thus affecting both A and B matrices. That will affect to the column corresponding to that input, both in matrix A and B.

The following matrices are obtained substituting both inputs with voltage sources, although other combinations could be done. If only one of the current inputs is substituted by a voltage source, only the changes in its corresponding column would be necessary. Both current and voltage sources connected at the inputs could be considered too, resulting on a linear combination of both matrices.

The matrix corresponding to the linearized model is presented too A_{lv}. Both for A_v and A_{lv} only the last 3 columns are shown since they are the only one which change compared to the case presented before (case $I_{o1} - I_{o2}$ in Section D.1).

$$[u_v] = \begin{bmatrix} V^*_{dc1} \\ V_{s1} \\ V_{s2} \end{bmatrix} \; ; \; \frac{\mathrm{d}}{\mathrm{d}t} \left[\begin{array}{c} x_c \\ \hline x_p \end{array}\right] = [A_v]_{8\times 8} \left[\begin{array}{c} x_c \\ \hline x_p \end{array}\right] + [B_v]_{8\times 3} [u_v] \tag{D.11}$$

$$\begin{bmatrix} V_{dc1} \\ V_{dc2} \\ I_L \end{bmatrix} = \left[\begin{array}{c|c} [0]_{3\times 5} & [I]_{3\times 3} \end{array}\right] \left[\begin{array}{c} x_c \\ \hline x_p \end{array}\right] + [0]_{3\times 3} [u_v] \tag{D.12}$$

$$[A_v]_{8\times 8}(:,6:8) = \begin{bmatrix} 0 & 0 & 0 \\ -\frac{w_1}{L} & \frac{V^*_{dc1}w_2}{LV^*_{dc2}} & 0 \\ 0 & 0 & 0 \\ 0 & 0 & 0 \\ \frac{K_{ii}w_1}{R_1} & -\frac{K_{ii}V_{dc2}w_2}{R_2V_{dc1}} & -K_{ii} \\ -\frac{1}{C_1R_1} & 0 & \frac{1}{C_1} \\ -\frac{i_L}{C_2V_{dc2}} - \frac{K_{pi}i_Lw_1}{C_2R_1V_{dc2}} & \frac{K_{pi}i_Lw_2}{C_2V_{dc1}R_2} - \frac{1}{C_2R_2} & \frac{K_{pi}i_L}{C_2V_{dc2}} \\ \frac{K_{pi}w_1}{L_fR_1} & -\frac{K_{pi}V_{dc2}w_2}{L_fR_2V_{dc1}} & -\frac{K_{pi}}{L_f} \end{bmatrix} \tag{D.13}$$

$$[B_v]_{8\times 3} = \begin{bmatrix} \frac{K_{pw}}{JK_e} & 0 & 0 \\ -\frac{2w_2}{L} & 0 & 0 \\ \frac{K_{iw}}{K_e} & 0 & 0 \\ 0 & 0 & 0 \\ 0 & -\frac{K_{ii}w_1}{R_1} & \frac{K_{ii}V_{dc2}w_2}{R_2V_{dc1}} \\ 0 & \frac{1}{C_1R_1} & 0 \\ 0 & \frac{K_{pi}i_Lw_1}{C_2R_1V_{dc2}} & \frac{1}{C_2R_2} - \frac{K_{pi}i_Lw_2}{C_2V_{dc1}R_2} \\ 0 & -\frac{K_{pi}w_1}{L_fR_1} & \frac{K_{pi}V_{dc2}w_2}{L_fR_2V_{dc1}} \end{bmatrix} \tag{D.14}$$

$$
[A_{lv}](:,6:8) = \begin{bmatrix}
0 & 0 & 0 \\
-\frac{1}{L} & \frac{1}{Ln} & 0 \\
0 & 0 & 0 \\
0 & 0 & 0 \\
\frac{K_{ii}}{2R_1} - \frac{K_{ii} i_L}{2V_{dc1}} & \frac{K_{ii} i_L}{2V_{dc2}} - \frac{K_{ii} n}{2R_2} & -K_{ii} \\
-\frac{1}{C_1 R_1} & 0 & \frac{1}{C_1} \\
\frac{K_{pi} i_L (i_L n R_1 - V_{dc2})}{2 C_2 {V_{dc2}}^2 R_1} - \frac{i_L}{C_2 V_{dc2}} & \frac{i_L n}{C_2 V_{dc2}} - \frac{1}{C_2 R_2} + \frac{K_{pi} i_L}{2 C_2 V_{dc1} R_2} - \frac{K_{pi} {i_L}^2}{2 C_2 {V_{dc2}}^2} & \frac{K_{pi} i_L}{C_2 V_{dc2}} - \frac{1}{C_2 n} \\
\frac{K_{pi}}{2 L_f R_1} - \frac{K_{pi} i_L}{2 L_f V_{dc1}} & \frac{K_{pi} i_L}{2 L_f V_{dc1} n} - \frac{K_{pi} V_{dc2}}{2 L_f R_2 V_{dc1}} & -\frac{K_{pi}}{L_f}
\end{bmatrix} \tag{D.15}
$$